5102-89

DOE/JPL-1060-6
Distribution Category UC-62

# Thermal Power Systems
# Advanced Solar Thermal Technology Project

# Advanced Subsystems Development
## Second Semi-Annual Progress Report
April 1, 1978 to October 1, 1978

November 15, 1978

Prepared for
U.S. Department of Energy
by
Jet Propulsion Laboratory
California Institute of Technology
Pasadena, California
and
NASA Lewis Research Center
Cleveland, Ohio

(JPL PUBLICATION 79-24)

5102-89

DOE/JPL-1060-6
Distribution Category UC-62

# Thermal Power Systems
# Advanced Solar Thermal Technology Project

# Advanced Subsystems Development
## Second Semi-Annual Progress Report
April 1, 1978 to October 1, 1978

November 15, 1978

Prepared for
U.S. Department of Energy
by
Jet Propulsion Laboratory
California Institute of Technology
Pasadena, California
and
NASA Lewis Research Center
Cleveland, Ohio

(JPL PUBLICATION 79-24)

Prepared by the Jet Propulsion Laboratory, California Institute of Technology, for the U.S. Department of Energy through an agreement with the National Aeronautics and Space Administration.

The JPL Solar Thermal Power Systems Project is sponsored by the U.S. Department of Energy and forms a part of the Solar Thermal Program to develop low-cost solar thermal electric generating plants.

This report was prepared as an account of work sponsored by the United States Government. Neither the United States nor the United States Department of Energy, nor any of their employees, nor any of their contractors, subcontractors, or their employees, makes any warranty, express or implied, or assumes any legal liability or responsibility for the accuracy, completeness or usefulness of any information, apparatus, product or process disclosed, or represents that its use would not infringe privately owned rights.

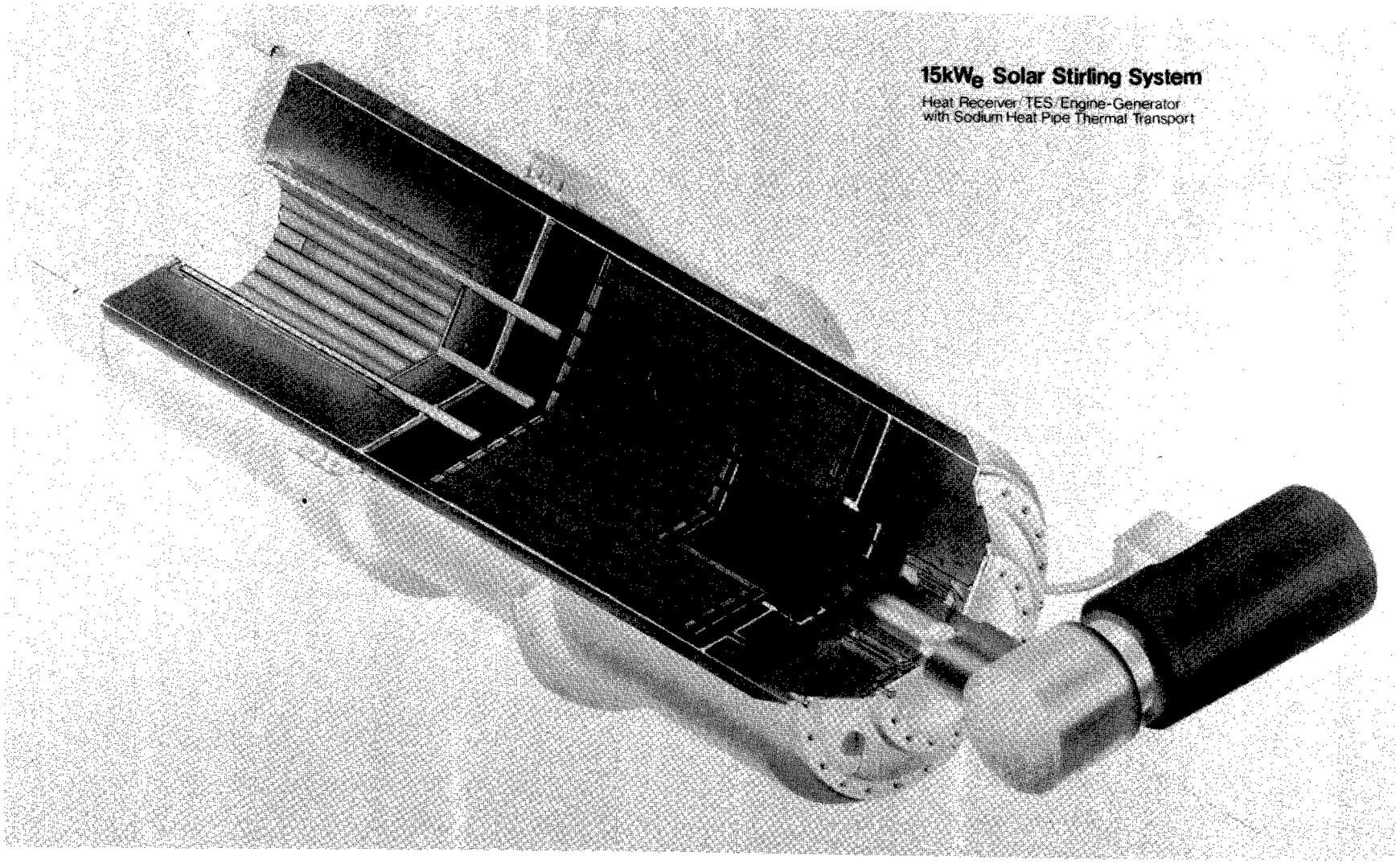
15kW$_e$ Solar Stirling System
Heat Receiver/TES/Engine-Generator
with Sodium Heat Pipe Thermal Transport

## ABSTRACT

This document summarizes the results of the work performed by the Advanced Subsystems Development Task of the Advanced Solar Thermal Technology Project. The activities described were carried out by the Jet Propulsion Laboratory, California Institute of Technology and the Lewis Research Center for the U.S. Department of Energy during the period beginning in April 1978 and ending in October 1978.

During this reporting period, the concept design for a small (less than 10 MWe) solar thermal electric generating plant was completed using projected 1985 technology. The systems requirements were defined and specified. The components, including an engineering prototype for one 15 kWe module of the generating plant, were conceptually designed. Significant features of the small solar thermal power plant were identified as the following:

(1) 15-kWe Stirling-cycle engine/alternator with constant power output

(2) 10-meter point-focusing paraboloidal concentrator with cantilevered cellular glass reflecting panels

(3) Primary heat pipe with 800°C output solar cavity receiver

(4) Secondary heat pipe with molten salt thermal energy storage unit

(5) Electric energy transport system

(6) Advanced battery energy storage capability

The present emphasis for achieving cost reduction goals centers on improving conversion efficiency and reducing the cost of key components.

# FOREWORD

The advanced thermal technology subprogram is a part of the Thermal Power Systems activity of the Department of Energy Division of Solar Technology. The primary objective of the subprogram is to support development of advanced, high-performance, low-cost, long-life and reliable solar thermal power components and subsystems.

The Jet Propulsion Laboratory (JPL) and the NASA Lewis Research Center (LeRC) were selected in 1977 to assist in managing and coordinating this subprogram. These two organizations, working with universities, government agencies, industry, and the scientific community in general, are to lead in developing new concepts and establishing a broad technology base in advanced small power systems which can be used to accelerate the development of cost-effective power systems.

This Semi-Annual Progress Report is the second to be issued (the first was released in June, 1978). It covers the second six months (April to October, 1978) of work on the JPL/LeRC advanced subsystems development task. It is intended as a means of publishing the results of the work on advanced concepts and widely disseminating the technology. It is hoped that the open approach of NASA in providing easy access to the results, procedures, and the data base developed in this task will stimulate early adaptation of the most promising concepts. Considerable detail is provided in some sections and in appendices so that the report may be used by a wide variety of organizations. If additional information is needed or if the reader wishes to discuss any items, please contact Floyd Livingston, the Advanced Subsystems Development Task Manager, at Jet Propulsion Laboratory, FTS 792-9416, Commercial (213) 577-9416 or write him at Jet Propulsion Laboratory, Mail Stop 506-328, 4800 Oak Grove Drive, Pasadena, California 91103.

CONTENTS


I. INTRODUCTION ---------- 1-1

A. GENERAL ---------- 1-1

B. OBJECTIVE AND BACKGROUND ---------- 1-1

C. THIS REPORT ---------- 1-3

D. SUMMARY ---------- 1-4

II. SYSTEMS INTEGRATION STUDIES ---------- 2-1

A. BACKGROUND ---------- 2-1

1. The Dish-Stirling Concept ---------- 2-1

2. Advanced Technology Demonstration ---------- 2-3

B. APPLICATIONS REQUIREMENTS ---------- 2-3

1. Public Utility Loads ---------- 2-3

2. Remote Operation ---------- 2-4

3. Systems Energy Storage ---------- 2-4

C. SOLAR COLLECTION ---------- 2-6

1. Solar Insolation ---------- 2-7

2. Solar Concentration ---------- 2-7

3. Thermal Storage ---------- 2-9

D. ENERGY CONVERSION ---------- 2-9

1. Stirling Engine-Generator Alternatives ---------- 2-9

2. Control Concepts ---------- 2-11

III. POWER CONVERSION ---------- 3-1

A. THERMAL ENERGY STORAGE AND TRANSPORT ---------- 3-1

1. Introduction ---------- 3-1

2. System Alternatives ---------- 3-3

3. Thermal Design ---------- 3-11

4. Mechanical Design Description ---------- 3-29

5. Mass and Cost Analysis ---------- 3-41

B. STIRLING SOLAR ENGINE ---------- 3-45

1. Development Plan ---------- 3-45

IV. POWER PROCESSING, POWER MANAGEMENT AND UTILITY INTERFACE ---------- 4-1

A. INTRODUCTION ---------- 4-1

B. SYSTEM DEFINITION ---------- 4-2

1. Objectives ---------- 4-2

2. Problem Definition ---------- 4-4

3. Assumptions ---------- 4-5

4. System Output Specifications ---------- 4-6

C. POWER PROCESSING (15 kWe) ---------- 4-7

1. Introduction ---------- 4-7

2. Various Generation Unit Concepts ---------- 4-7

3. Component Characterization ---------- 4-11

4. Selection of Two Viable Options ---------- 4-16

D. POWER COLLECTION ---------- 4-18

1. Selection of Viable Options ---------- 4-18

2. Analyses of Options ---------- 4-20

3. Performance and Cost Comparison ---------- 4-24

4. Equipment Selection ---------- 4-25

5. Layout Considerations ---------- 4-26

6. Stability, Paralleling and Load Sharing ---------- 4-29

E. POWER MANAGEMENT ---------- 4-30

F. UTILITY INTERFACE ---------- 4-31

1. Equipment Descirptions ---------- 4-31

2. Additional Utility Interface Issues ---------- 4-32

G. CONCLUSION ---------- 4-33

V. ADVANCED CONCENTRATOR SUBSYSTEM ---------- 5-1

A. INTRODUCTION ---------- 5-1

B. CONCEPT DESCRIPTION ---------- 5-1

C. PROTOTYPE ADVANCED CONCENTRATOR ---------- 5-1

D. STRUCTURAL DEFORMATION ANALYSIS ---------- 5-4

E. PERFORMANCE OF REFLECTIVE SURFACES ---------- 5-10

1. Introduction ---------- 5-10

2. Efficiency of Solar Concentrator Reflective Surfaces ---------- 5-10

3. Effect of Dust and Contamination Accumulation --- 5-10

4. Stability of Reflective Coatings ---------- 5-13

5. Environmental Effects ---------- 5-13

6. Cleaning of Reflective Surfaces ---------- 5-13

7. Price Estimates ---------- 5-13

F. CELLULAR GLASS GORE ENGINEERING TEST UNIT DEVELOPMENT ---------- 5-14

1. Introduction ---------- 5-14

2. Preliminary Cellular Glass Gore Design ---------- 5-14

3. Fabrication Concepts ---------- 5-14

4. Prototype Hardware ---------- 5-14

VI. ADVANCED RECEIVER ---------- 6-1

A. INTRODUCTION ---------- 6-1

B. TECHNICAL APPROACH ---------- 6-1

1. Receiver Computer Program Development ---------- 6-1

2. Preliminary Heat Exchanger Design ---------- 6-2

3. Cavity and Insulation Design ---------- 6-3

C. FUTURE PLANS ---------- 6-5

1. Receiver Performance Analysis ---------- 6-6

2. Final Establishment of Interface Requirements with the Concentrator and the Power Conversion Subsystem ---------- 6-6

3. Formulation of Prototype Test Plan ---------- 6-6

4. Development of a Terminal Concentrator for the Enhancement of Receiver Efficiency ---------- 6-7

5. Development of Support Technology Program ------- 6-7

VII. TRACKING AND CONTROL ANALYSIS ---------- 7-1

VIII. OPTICAL ANALYSIS ---------- 8-1

A. INTRODUCTION ---------- 8-1

B. PARABOLOIDAL REFLECTOR ---------- 8-1

C. CAVITY FLUX COMPUTATIONS ---------- 8-2

D. FUTURE PLANS ---------- 8-11

IX. HEAT TRANSFER ANALYSIS ---------- 9-1

A. HEAT ENERGY ANALYSIS PROGRAM ---------- 9-1

APPENDIXES

A. EVALUATION OF RECENT DATA ON SOLAR CONCENTRATOR REFLECTIVE SURFACES ---------- A-1

B. TRACKING AND CONTROL STUDIES

- EFFICIENCY DEGRADATION DUE TO TRACKING ERRORS FOR POINT-FOCUSING SOLAR COLLECTORS ---------- B-1

- OPTIMAL CONTROL OF SUN TRACKING SOLAR COLLECTORS B-9

C. OPTICAL ANALYSIS

- OFFSET PARABOLOIDAL CONCENTRATOR ---------- C-1

- CPC PARABOLOID AND CPC-FRESNEL CONCENTRATOR SYSTEMS ---------- C-9

- CASSEGRAINIAN SYSTEM ---------- C-18

D. HEAT TRANSFER ANALYSIS

- RECEIVER SENSITIVITY ANALYSIS ---------- D-1

- GENERALIZED FORMAT FOR SOLAR RECEIVERS ---------- D-11

- RECEIVER - ENGINE COUPLING OPTIMIZATION --------- D-16

Figures

1-1. Effect of Improvements in System Efficiency on Achievement of Energy Cost Reductions ---------- 1-2

1-2. Advanced Subsystems Development Schedule ---------- 1-7

2-1. Solar Thermal-Electric System Block Diagram -------- 2-2

2-2. City of Burbank Electric Load Profile ---------- 2-5

2-3. Direct Solar Insolation, Lancaster, California, 1976, No Cloud Cover ---------- 2-8

2-4. Stirling Engine-Generator Operating Efficiency Estimate ---------- 2-10

2-5. Dish-Stirling System Control, Fixed Power Level Operation Concept ---------- 2-12

2-6. Dish-Stirling System Control, Variable Power Level Operation Concept ---------- 2-13

3-1. TES Mass Required Versus Storage Time ---------- 3-6

3-2. Physical Description of Heat Receiver Thermal Flux Analysis Model ---------- 3-13

3-3. Local Impinging Heat Flux along Heat Receiver Cooled Wall ---------- 3-15

3-4. Cummulative Impinging Thermal Energy along Heat Receiver Cylindrical Cooled Wall ---------- 3-15

3-5. Two-Hour Latent Heat TES Requirements at 39.68 $kW_t$ for 67 NaF - 33 $MgF_2$ ---------- 3-17

3-6. Stirling Engine Heat Exchanger Optimization Curves -- 3-20

3-7. Temperature Drop Across the Solidified Salt Layer at Various Power Extraction Levels ---------- 3-28

3-8. Suggested Temperatures in the Thermal Energy Storage Sodium Vapor Space (and at the Stirling Engine) During Charging and Discharging of the TES ---------- 3-30

3-9. Sodium Vapor Pressure vs Temperature ---------- 3-36

3-10. Thickness Required for TES Heat Pipe Forward Head vs Operating Temperature ---------- 3-39

3-11. Allowable Design Stresses ---------- 3-40

3-12. 15 kW Combined Solar Stirling Engine Program -------- 3-48

4-1. Conceptual Block Diagram for a Solar Generation Unit -- Case 1. DC Generation/DC Link ---------- 4-8

4-2. Conceptual Block Diagram for a Solar Generation Unit -- Case 2. Conventional AC Generation/ DC Link ---------- 4-9

4-3. Conceptual Block Diagram for a Solar Generation Unit -- Case 3. Conventional AC Generation/ AC Link ---------- 4-10

4-4. Conceptual Block Diagram for a Solar Generation Unit -- Case 4. Special AC Generation/AC Link ------ 4-11

4-5. Conceptual Block Diagram for a Solar Generation Unit -- Case 5. Regenerative Battery Charger ------- 4-12

4-6. Basic 12 Pulse Current-Fed Line Commutated Inverter ---------- 4-15

4-7. Phase Shift Modulation Inverter ---------- 4-15

4-8. Block Diagram of a Solar Generation Unit (SGU) for the AC-Link Approach Using a Conventional AC Generator ---------- 4-17

4-9. Block Diagram of a Solar Generation Unit for the DC-Link Approach Using a Conventional AC Generator -- 4-18

4-10. Conceptual Block Diagram for an AC-Link Plant ------- 4-19

4-11. A Single Line Diagram for a Four-Group 10 MWe Plant Using AC Link ---------- 4-21

4-12. Conceptual Block Diagram for a DC-Link Plant -------- 4-22

4-13. A Single Line Diagram for a Four-Group 10 MWe Plant Using DC Link ---------- 4-23

4-14. A Group Layout for a 10 MWe Plant with DC Link ------ 4-27

4-15. A Group Layout for a 10 MWe Plant with AC Link ------ 4-28

4-16. Plant Layouts ---------- 4-28

4-17. Control Hierarchy ---------- 4-32

5-1. Deep-Dish, Point-Focusing Concentrator ---------- 5-2

5-2. Concave Bubble Fresnel Lens Configuration ---------- 5-3

5-3. Surface Grid Point Geometry for Structural Deformation Analysis ---------- 5-5

5-4. Displacement of Reflected Rays Due to Structural Deformation ---------- 5-6

5-5. Ray Intercepts at Displaced Focal Point ---------- 5-7

5-6. Ray Intercepts at Displaced Focal Point ---------- 5-8

5-7. Ray Intercepts at Displaced Focal Point ---------- 5-9

5-8. Preliminary Design of Cellular Glass Gore ---------- 5-15

5-9. Cellular Glass Gore Mirror Fabrication ---------- 5-16

8-1. Distribution of Normalized Concentration Ratio, F/D = 0.6 (For a Perfect Paraboloidal Reflector) ---- 8-3

8-2. Intercept Factor as a Function of R/D, F/D = 0.6 (For a Perfect Paraboloidal Reflector) ---------- 8-4

8-3. Distribution of Normalized Concentration Ratio, F/D = 0.6 (For a Paraboloid with Different Slope Errors) ---------- 8-5

8-4. Intercept Factor as a Function of R/D, F/D - 0.6 (For a Paraboloid for Different Slope Errors) ------- 8-6

8-5. Distribution of Normalized Concentration Ratio, F/D = 0.6 (For a Paraboloid for Different Tracking Errors) ---------- 8-7

8-6. Distribution of Normalized Concentration Ratio Along Planes Perpendicular to the Optical Axis as a Function of Distance from Optical Axis --------- 8-9

8-7. Distribution of Normalized Concentration Ratio Along Cylindrical Surfaces for Various Radii as a Function of Distance Beyond Focal Plane ------- 8-10

8-8. Solar Receiver Isoflux Surfaces ---------- 8-12

9-1. Node Representation of a Receiver ---------- 9-3

9-2. HEAP Simulated Program ---------- 9-4

Tables


3-1. Design Guidelines ---------- 3-2

3-2. Preliminary Design Options ---------- 3-4

3-3. System Losses Through Pipe Insulation ---------- 3-8

3-4. 15-Minute Thermal Energy Storage Using No Heat Transport ---------- 3-10

3-5. Initial TES System Definition ---------- 3-18

3-6. Primary Heat Pipe Data ---------- 3-23

3-7. Radial Wicking Capabilities of Wire Screen and Fiber Metal Wicks for 0.46 m (18 in.) Effective Pumping Length ---------- 3-25

3-8. TES Secondary Heat Pipe Wicking ---------- 3-26

3-9. Heat Storage and System Temperature Profiles -------- 3-31

3-10. Parts List for the Focal-Mounted System Basic Design 3-33

3-11. Summary Mass Table ---------- 3-42

4-1. Compenent Sizes and Expected Performance of 15 kWe Solar Generation Unit ---------- 4-19

4-2. Electrical Component Size and Expected Performance for 10 MWe Plants ---------- 4-24

4-3. Parts List for a 10 MWe Plant with AC Link --------- 4-25

4-4. Parts List for a 10 MWe Plant with DC Link --------- 4-26

5-1. Summary of Reflective Surfaces Solar Concentrator --- 5-11

5-2. Summary of Additional Data on Solar Concentrator Mirrors ---------- 5-12

6-1. Preliminary Receiver Design Parameters ---------- 6-3

6-2. Thermal Conductivities of Insulation Material for High Temperature ---------- 6-5

# SECTION I

# INTRODUCTION

# SECTION I

# INTRODUCTION

## A. GENERAL

The general goal of the Advanced Solar Thermal Technology subprogram is to accelerate the availability of cost effective solar thermal power systems for a variety of applications by reducing the cost of components and improving system performance. These cost and performance improvements will be achieved through the application of advanced technology to the design, construction, and operation of solar thermal power systems.

The specific goals of the program are to:

(1) Demonstrate by the mid-1980's the technical viability of advanced large and small solar thermal systems having the potential for energy costs 25 to 50 percent lower than systems based on current or near-term technology.

(2) Identify new, economically viable applications of solar thermal power to help reduce the nation's dependence on critical fossil fuels.

In line with the above goals, a task was initiated to complete a cost-effective dish-Stirling subsystem integration experiment by FY 1983, with subsequent transfer of the technology to the applications projects.

Energy costs of solar thermal power systems may be reduced through the use of lower-cost, longer-life surfaces and components, by increasing system operating efficiencies, and by reducing the requirements for maintenance. At this time, emphasis is being placed on improving conversion efficiencies and reducing costs of the key components. Figure 1-1 shows the effect on energy costs of improved system efficiency and decreased collector costs.

## B. OBJECTIVE AND BACKGROUND

The task undertaken by JPL/LeRC for the Advanced Thermal Technology subprogram is to develop advanced technology to improve life cycle costs of solar thermal electric power plants.

As a result of the systems and advanced studies activities, a point-focusing concentrator, Stirling engine/alternator solar thermal

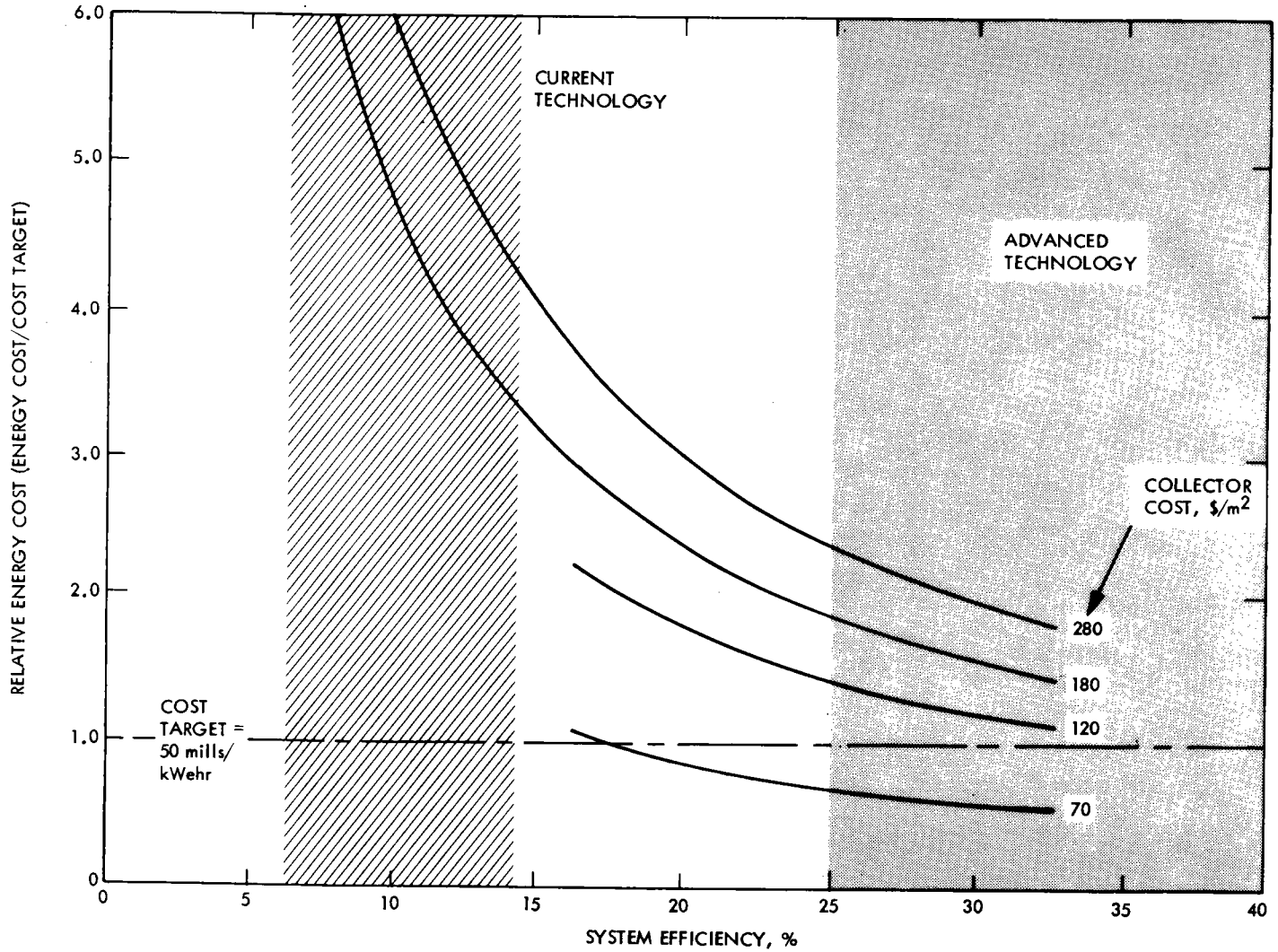


Figure 1-1. Effect of Improvements in System Efficiency on Achievement of Energy Cost Reductions

electric power plant concept was identified in FY 1977 as the most likely cost-effective candidate system to be developed for future small solar power applications.* The dish-Stirling advanced technology development task was initiated in October 1977 with the goal of demonstrating the feasibility of the concept through a single prototype module test program within six years. Greater than 25 percent system efficiency in generating electricity with a module direct cost of less than $700 (1978 dollars) per peak kilowatt of electricity (kWe) at the generator is the 1984 objective. A somewhat longer-term goal is to reduce the module cost to less than $600 per peak kilowatt of electricity at the generator.

## C. THIS REPORT

This report covers work during the last six months on the task of design, fabrication, assembly and test of a paraboloidal dish Stirling engine, alternator module. Since the beginning of the task in October 1977, a selected conceptual design has emerged from many alternatives. During the fiscal year 1979, the preliminary design of all subsystems will be completed. After detail design, fabrication, assembly and test, all components and subsystems will be assembled for system test and proof-of-concept demonstration in fiscal year 1982/1983.

Throughout the course of this task, progress will be reported at monthly task meetings, quarterly Advanced Solar Thermal Technology Project meetings held at the Jet Propulsion Laboratory, Pasadena, California and at semi-annual reviews of the Advanced Solar Thermal Power System subprogram held in conjunction with the Solar Energy Research Institute, in Denver, Colorado. A preliminary issue of this report was published to coincide with the second semi-annual review to be held on November 15-17, 1978. The purpose of this report is not only to meet programmatic objectives, but also to disseminate information about key technical innovations which may be of value or interest to technological corporations engaged in research and development of solar thermal electricity generating plants. Therefore, initial distribution of a preliminary version was made to attendees at the meeting, to be followed later by publication and widespread dissemination by DOE-TIC.

Task members at the Jet Propulsion Laboratory and the Lewis Research Center have defined the basic conceptual design, and will specify the major system requirements and direct system test and operations. Industry will be utilized in the performance of technical work to the maximum extent feasible to develop detailed designs, fabricate and test components, and eventually to produce the subsystems and systems for applications.

A small (less than 10 MWe) solar-thermal electric generating plant design concept was completed using projected 1985 technology.

---

*T. Fujita, et al, "Projection of Disbributed-Collector Solar-Thermal Electric Power Plant Economics to Years 1980-2000." Report DOE/JPL 1060-77/1, Dec. 19

This concept, when in mass production, should meet the solar thermal electric plant capital cost target of $600 per kWe (1978 dollars). Operations and maintenance costs should be sufficiently low so that the cost of electricity from the plant would be about 50-60 mills per kilowatt-hour (1978 dollars). An engineering prototype model of one 15 kWe module of the small solar thermal electric generating plant was conceptually designed. The results of the conceptual design phase are the substance of this semi-annual progress report. Implementing the conceptual design through preliminary design, detail design, fabrication, assembly, and component test by industry will be the thrust of the FY 1979 effort on this task. These current and forthcoming procurement actions, as well as some of the results of ongoing contractual conceptual design efforts, are described in the present report.

For convenience this report is divided into sections relating to systems integration, component design, and analytical methodology employed. These sections are as follows:

I. Introduction

II. Systems Integration

III. Power Conversion

A. Thermal Energy Storage and Transport

B. Stirling Solar Engine

IV. Electrical Processing Power Management and Utility Interface

V. Advanced Concentrator Subsystem

VI. Advanced Receiver

VII. Tracking and Control Analysis

VIII. Optical Analysis

IX. Heat Transfer Analysis

## D. SUMMARY

The past year's activity in the advanced subsystems development task was centered on the conceptual design of components for a small solar thermal electricity generating plant. The dish-Stirling solar thermal electric generating plant was singled out through prior system studies as the candidate most likely to provide cost-competitive generation of electricity. The significant features of this small solar power plant were identified as the following:

(1) 15-kW Stirling cycle engine driver alternator

(2) 10-meter diameter point-focusing solar concentrator

(3) ∿800°C (1500°F) input to the engine

(4) Electric energy transport system

(5) Advanced battery energy storage capability

With these features in mind, designers and analysts at the Jet Propulsion Laboratory and the Lewis Research Center further defined the small solar thermal electric generating plant and specified the system requirements during the first half of FY 1978. During this first part of the system definition task, the major subsystems were selected as follows:

(1) Cantilevered, cellular-glass reflecting panel

(2) Ten-meter diameter paraboloidal concentrator

(3) Liquid-metal heat pipe 800°C output solar cavity receiver

During the latter part of FY 1978, the subsystems of the small solar thermal electric generating plant were further refined. These refinements were needed to define accurately the control and operations of the solar plant. A key feature of the design was to control the engine by an on/off switch and operate it in an essentially fixed power mode. The present baseline design for the power package contains the following:

(1) Primary heat pipe, 800°C output solar cavity receiver

(2) Secondary heat pipe, molten-salt, thermal energy storage unit

(3) Constant power output, 15kW, Stirling-cycle engine

(4) Rectified AC alternator

All of these conceptual design innovations will be implemented through industry. Industry has also been asked to contribute conceptual design innovations with regard to solar Stirling-cycle engines and alternators, cellular-glass reflecting panels, heat pipe receivers, thermal energy storage, and non-heat pipe receivers.

Procurement activities during the last six months of FY 1978 included signing a contract in August with Mechanical Technology, Inc. for conceptual design studies of both a free-piston/linear alternator Stirling-cycle engine and a kinematic, rotating Stirling-cycle engine alternator combination. General Electric, Company Advanced Energy Programs, has been contracted to study the applications of liquid metals in these small power plant applications. In addition, General Electric, has been engaged to conceptually design a primary heat pipe solar cavity receiver, with secondary heat pipe molten salt thermal energy storage subsystem for the small power plant application. A request for proposal was recently issued for a non-heat-pipe solar receiver that could be directly coupled to a solar Stirling engine. A contract for conceptual design, preliminary design, detail design, fabrication, assembly and testing

this non-heat pipe receiver is expected to be executed in January 1979. A schedule of ongoing technical activity is shown in Figure 1-2. The time covered in this schedule covers the period from April 1978 through July 1979. The procurement actions pertaining to the advanced concentrator, the cellular-glass panel, the dish-Stirling receiver, the Stirling engine/alternator and liquid metal heat exchanger were described above. A very low cost Fresnel lens concentrator design will be addressed in FY 1979, with an RFP due to be released in early CY 1979. A Brayton engine/alternator concept study with AiResearch Division will result in alternate engine options being defined.

In order to design a representative engineering prototype module, consisting of the concentrator, receiver, liquid metal heat exchanger and Stirling engine/alternator, the electrical power processing subsystem for a typical 10 MW solar thermal electricity generating plant has to be conceptually designed. It was found that the controls required for the Stirling engine and the electrical alternator were highly dependent upon the complete plant operating mode. Both alternating current and direct current electrical power processing subsystems were considered, with the DC link being the interim choice for the engineering prototype module because of the simplified engine control.

At the present time, means other than advanced batteries for after sunlit hours operations, such as thermal energy storage are also being studied.

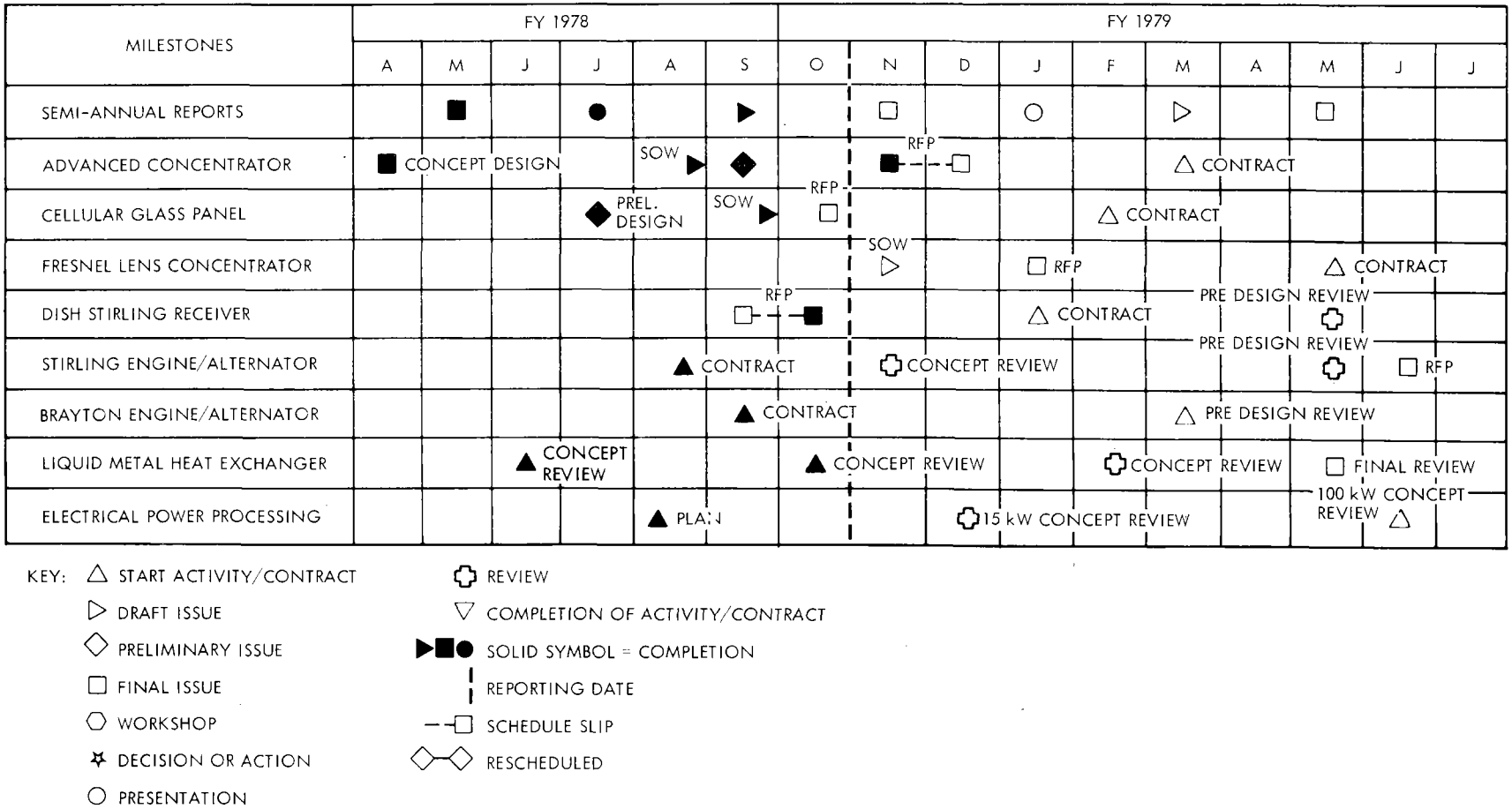


Figure 1-2. Advanced Subsystems Development Schedule

# SECTION II

# SYSTEMS INTEGRATION

## SECTION II

## SYSTEMS INTEGRATION

### A. BACKGROUND

Limited scope, preliminary systems integration studies were completed to identify and assess the sybsystems interface requirements and control alternatives for a dish-Stirling solar thermal electric system. The purpose of this work was to determine important systems factors which should be considered in the component and subsystem design and optimization studies. No attempt has been made to search for applications or engage in any detailed systems or applications studies.

Evaluation was made of the requirements of interfacing a public utility as well as an evaluation of the component interfaces within a dish-Stirling system. Control options were considered and some estimation was made of component operating parameters. Component and subsystem design and development is to be accomplished by contractors. System integration and interface definition will continue as an iterative process with advanced technology development through FY 1979.

#### 1. The Dish-Stirling Concept

Use of a precision tracking parabolic concentrator with a high-temperature, high-efficiency power conversion subsystem is an economical approach to low-cost electric power. Temperature constraints of presently available low-cost materials establish the maximum power conversion operating temperature at approximately 800°C (1500°F). Recent analyses indicating a superior efficiency of the Stirling-cycle at this temperature provide a major incentive to undertake an advanced technology development with an early demonstration date.

The system block diagram is shown in Figure 2-1. The basic solar collection system consists of the solar concentrator, receiver, thermal energy storage, heat transport, Stirling engine and electric generator. The power processing, battery storage and power distribution are primarily identified with the load application. These latter items will still have a significant impact on system design and must, therefore, be treated realistically if not specifically. The primary emphasis of the ASTT effort is in the basic solar collection and energy conversion system elements. The particular technology advance that is to be emphasized in this system concept is a high performance, low-cost, solar concentrator with a high-efficiency Stirling engine power conversion.

The system concept is defined only to the extent necessary to ensure adequate technology direction at the component level. Versatility and scaleability of the technology is emphasized. Principal system application is assumed to be public utility loads at the 1-10 MWe power level, where a large field of small modular units (15-25 kWe) is envisioned. Secondary application is expected to be the remote stand-alone system. Further detail, of the dish-Stirling concept will be

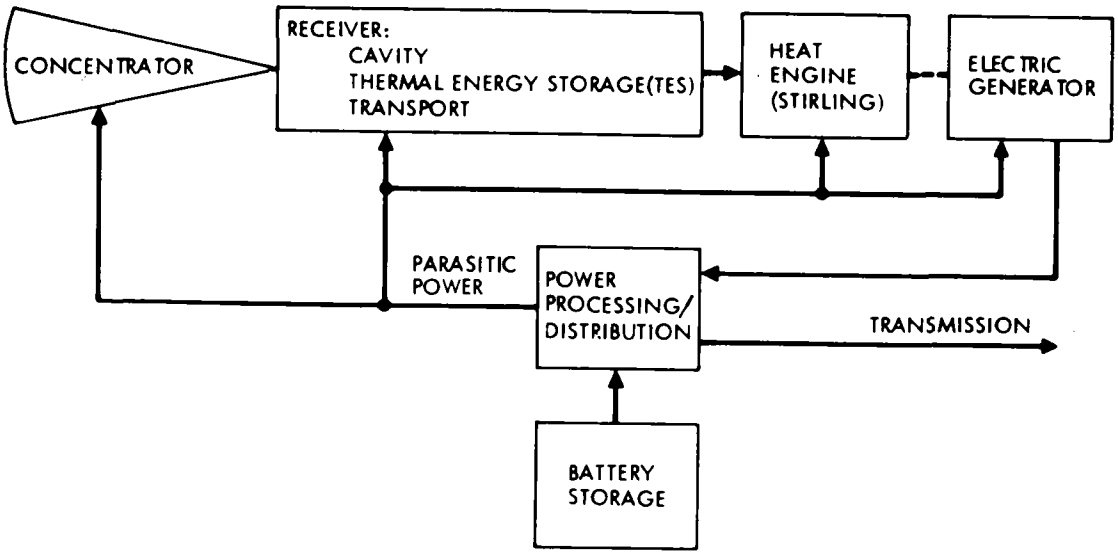


Figure 2-1. Solar Thermal-Electric System Block Diagram

presented in the following discussions of applications requirements, solar collection and energy conversion.

## 2. Advanced Technology Demonstration

The dish-Stirling system is to be the first in a series of advanced technology development and demonstration units. The system is designated Advanced Development System No. 1 (ADS-1). Its purpose is to provide prototype demonstration of a cost-effective technology for future systems application. Component testing at the JPL (Edwards Test Site) Point-Focusing Solar Test Site (PFSTS) is expected to start by FY 1981 with the delivery of the dish-Stirling solar receiver (DSSR). This will be followed by delivery and test of the Stirling engine and the advanced concentrator. During FY 1982/1983, the system will be transferred to the Point Focusing Applications Project for prototype systems integration and testing.

Module demonstration is to be accomplished at a peak electric generator power output level of 15 kWe. Selection of this power level is the result of preliminary studies in FY 1977/1978. Based on this power level, a contract has now been let to consider the options for the Stirling engine-generator, the most critical element of the system. First module generator efficiency is estimated at 0.90, while Stirling engine efficiency is estimated at 0.40. Required peak thermal input to the Stirling engine will therefore be 42 kWth. Depending on collection efficiency and thermal storage requirements, a concentrator diameter of approximately 10 meters will be needed.

ADS-1 will provide prototype technology demonstration. Definition of the technology to be developed is a preliminary task involving system integration studies that cover a full range of power levels and applications.

# B. APPLICATIONS REQUIREMENTS

As noted above, the first application to be considered is the public utility load. The second application is the remote operation. In both applications, the load demand is not constant. Typically, one might expect load peaking to occur about mid-afternoon, with a more pronounced peak in the summer than in the winter. Highest load peak for the year may be expected between mid-August and mid-September.

## 1. Public Utility Loads

With its dependence on sunlight for input energy, solar power generation is not well suited for the conventional public utility generation serviced by fossil-fuel or nuclear-fuel systems. The potential value of solar thermal power plants to a utility system is dependent on energy and capacity. The energy value is approximately equal to the

value of the fuel that is displaced or saved. Capacity value is approximately equal to the value of capital equipment displaced or saved. Busbar energy cost today is slightly under 30 mills/kWe-hr, which is lower than most projections of solar thermal power plant costs.

The conditions for load capacity displacement are quite different for different localities. This is because the load will be a variable mix of "industrial", "residential" and "commercial" loads. The loads that are primarily industrial provide the best match for solar power. Typical of this is the city of Burbank, as shown by the 1976 load profile in Figure 2-2. The load is classified as approximately 44% industrial, 25% residential and 20-25% commercial. The characteristic secondary peaking of residential load in the 6:00-9:00 p.m. range is not too pronounced in Figure 2-2. Approximately half of the load capacity of Burbank appears just between the hours of 6:00 a.m. and midnight.

## 2. Remote Operation

Self-contained power systems capable of remote operation may be able to satisfy special requirements which are not easily met by public utilities. However, there may be a significant specific market for such systems for military applications. In addition, considerable interest exists in foreign marketplaces for self-contained power systems for remote operation.

The potential value of systems for these applications will usually be higher than for a public utility. Relatively large amounts of energy storage are often needed, and reliability is often more important than cost or performance. Diesel systems are already available for this application at power levels of several MWe, where energy storage is effectively provided by the fuel storage, and reliability is provided through standby redundancy in multi-unit power conversion systems.

The character of the remote loads can be quite variable. In general, a baseline of fairly high residential type load is identifiable. This load may then be overlaid with a special-purpose load, sometimes culminating in a high, constant base-load requirement.

Applications of solar thermal remote operation are not yet well defined. Such applications will generally require increased energy storage over public utility applications and/or augmentation by base-load power systems. In certain cases, fuel supply logistics present serious problems where solar power may be the only solution.

## 3. Systems Energy Storage

Solar thermal systems must achieve a significant capacity value rating in order to become cost effective. To do this, energy storage is needed. If the city of Burbank load is taken as a typical industrial-type load, the capability to operate reliably between the hours of 6:00 a.m. and 12 midnight can produce nearly a maximum solar thermal capacity value. Optimization of economic and capacity value of solar power generation will depend greatly on equipment life cycle costs and alternative generation

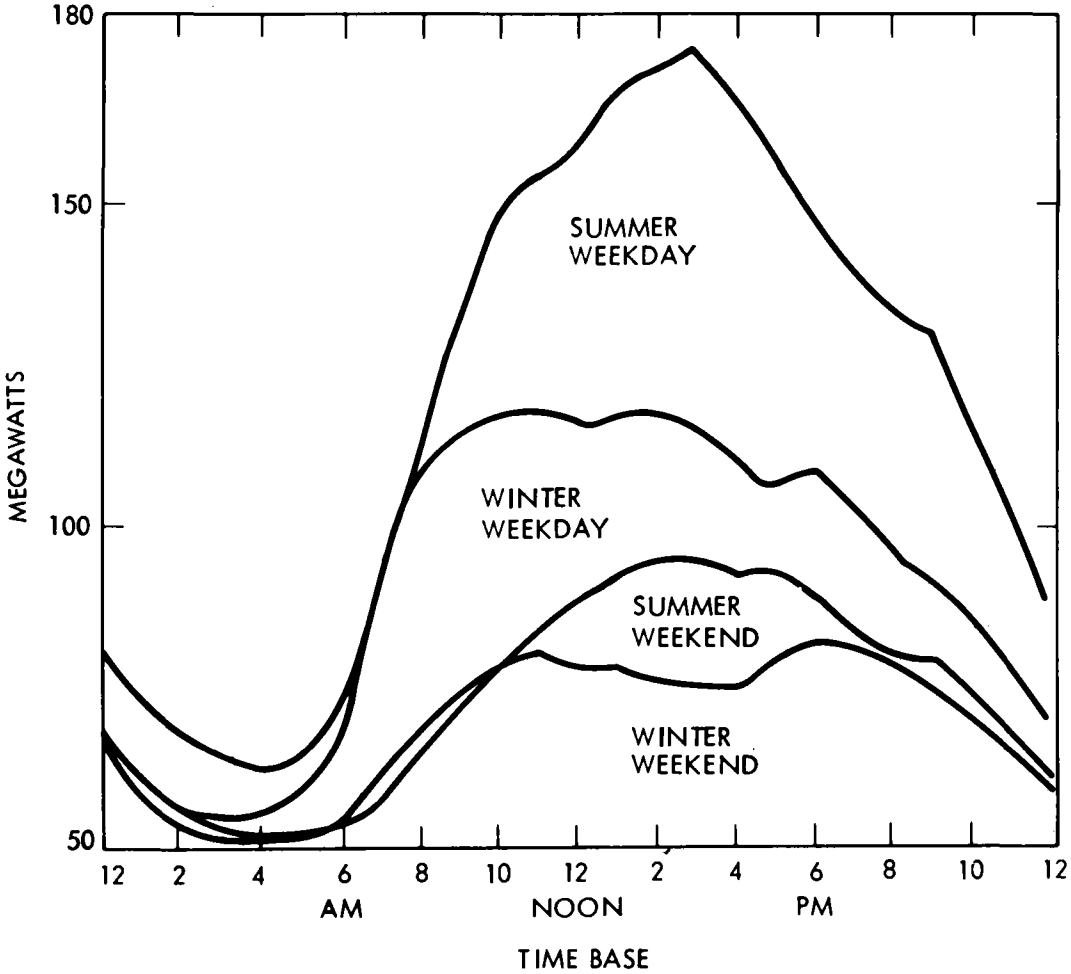


Figure 2-2. City of Burbank Electric Load Profile

resources utilized (i.e., generating systems mix of fossil fuel, nuclear, hydroelectric, etc.). During peak summertime operation, almost all capacity is placed on line, with very limited backup redundancy or reserve capacity. During the winter, when load requirements are minimum and reserves are maximum, downtime for maintenance and equipment modifications is scheduled. On this schedule, unscheduled outages of equipment are typically of the order of one hour in 20 years (mean probability).

From the above, solar thermal system energy storage can be seen to provide two essential functions. First, it provides for system operation beyond the daylight hours. Secondly, it serves to eliminate unscheduled outages during the daylight hours. Both of these functions are impacted by cloud cover. At Lancaster, California, (the solar data station closest to the JPL Solar Thermal Test Facility) approximately 20% of the days each year can be classified as having significant cloud cover.

Electrical transport with battery energy storage is assumed as a baseline for the dish-Stirling system. Such selection is necessary to meet development time-frame for ADS-1. Large systems for thermal energy storage appear to be much farther into the future. Battery storage will be a separate development from the collector system of ADS-1. However, the power processing interface must be defined to accommodate battery storage. For present purposes, approximately five full-power hours of storage are assumed.

For load profiles such as Burbank, the largest requirements for battery storage are expected during the summer. Winter requirements are perhaps one-half to one-third the summer need, both for storage and for load demand. The battery charge/discharge power ratio will be of the order of 0.5. Battery cycle efficiency is about 0.75. Battery charging for the system may be provided in one of three ways:

(1) Provide battery charging when generated power exceeds load power level

(2) Provide battery charging as a programmed fraction of generated power

(3) Switch individual units to either battery or load as required

## C. SOLAR COLLECTION

The solar collection system includes the solar concentrator, solar receiver and thermal energy storage. Its function is to accept the maximum available direct solar input, convert it into high-temperature thermal energy, provide buffer storage and transport the heat to the working fluid at the conditions specified for operating the Stirling engine.

## 1. Solar Insolation

Cloud-free, direct solar insolation profiles at Lancaster, (1976) are shown in Figure 2-3 for the extremes of summer and winter solstice. Peak insolation in both cases is approximately 1 $kW/m^2$. The average insolation flux level, excluding the first and last half hour of insolation, is about 0.85 $kW/m^2$. Without thermal storage, the solar power system is required to follow the solar input power profile over its entire range. Small amounts of thermal storage will provide variable power operation capability. With a maximum of about one hour of thermal energy storage the solar power system will be able to operate at a fixed power output level over the entire day. The dish-Stirling solar receiver (DSSR) system must collect the designated amount of thermal storage, and must react to the accompanying problems of high-temperature heat transport and control.

The curves of Figure 2-3 are shown foreshortened by half an hour at the beginning and end of the day. During these periods, there is virtually no net value to the solar insolation. In a large field of collectors, the horizon would probably be obscured by shadowing. In addition, even if insolation was available, power input to the receiver would be of the same order as the thermal losses (radiation, conduction, convection). A further advantage of eliminating the low insolation is that heat pipes, if utilized for heat transport, will be able to operate for the entire day with gravity assistance.

Cloud cover is characteristically random and has a significant effect for approximately 20 percent of the days. Short-term cloud cover is more prevalent than long-term cloud cover. The number of cloud passage incidents is almost exactly the inverse of the time for cloud passage. Thus, integrated time of the solar power loss (energy loss) is almost a constant.

## 2. Solar Concentration

The baseline concentrator-receiver systems for ADS-1 is a two-axis, automatic-tracking, point-focusing paraboloid. The reflective surface is made of gores or panels of backsilvered glass mirror on continuously contoured cellular glass substrate. These reflective gores are cantilevered from a circular truss to form a reflective paraboloidal surface with aperture diameter of approximately 10 meters, and with focal length to aperture diameter ratio (F/D) of 0.6. An all-truss structure serves as an intermediate structure between the concentrator surface assembly and the pedestal which provides the azimuth and elevation movements of the concentrator.

Although the concentrator and receiver are considered as individual components, they must operate together. The receiver is attached rigidly to the concentrator by a quadrupod structure. The present design permits a maximum allowable mass, cantilevered at the focal point of 1360 kg (3000 lb), including the Stirling engine-generator. The two-axis concentrator mount requires precise pointing to provide a concentration ratio of 2000.

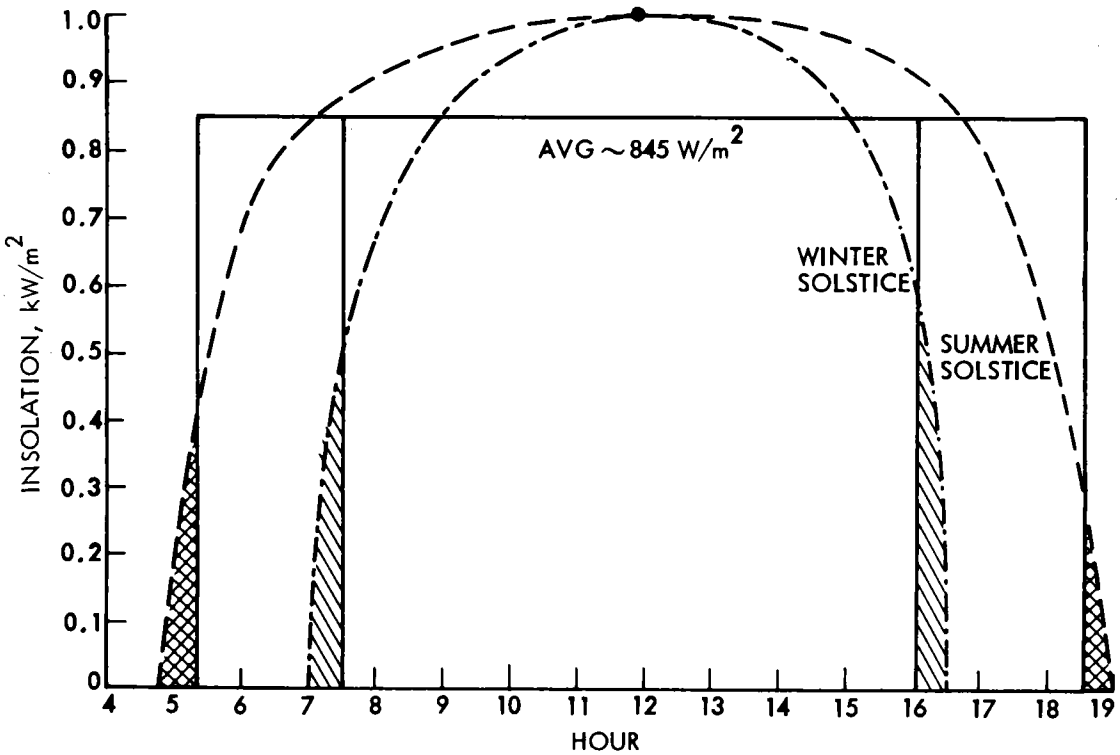


Figure 2-3. Direct Solar Insolation
Lancaster, California 1976
No Cloud Cover

The preliminary collector concept assumes that concentrator efficiency should be ≥0.78 and receiver efficiency should be ≥0.85, for a total efficiency of 0.66. For a 10-m dish, thermal input to the TES/Stirling engine heat exchange tubes will be approximately 52 kWth peak of 44 kWth average.

### 3. Thermal Storage

The single greatest cost element of the solar thermal power system is the concentrator (approx. 45%). For this reason, efficiency of the solar receiver and Stirling engine is very important in order to minimize total system cost. It now appears that thermal energy storage (TES) may be able to make a sizeable contribution to efficiency improvement. Small values or no TES will require that the system operate at variable power output. This in turn causes a decrease of Stirling engine-generator average operating efficiency and an increase of control complexity. Preliminary estimates of efficiency loss are shown in Figure 2-4.

High efficiency is achievable by constant-power operation. For the curves of Figure 2-3, such operation requires a peak (summer) TES storage value of 1.2 full power hours. For the 10-m dish and a collection efficiency of 0.66, the TES storage value required is 53 kWth-hr.

A preliminary survey of TES materials was presented in the previous ASTT Project Semi-Annual Progress Report. Because of the receiver mass limitations, only latent heat storage candidates are allowable for the case of constant power operation. A more detailed study is now in progress.

## D. ENERGY CONVERSION

### 1. Stirling Engine-Generator Alternatives

Both the kinematic Stirling engine and the free-piston Stirling engine (FPSE) are to be evaluated for ADS-1. The kinematic engine utilizes a conventional, rotary generator, while the FPSE takes a linear generator. With fixed-power-level systems, either machine could be used. Selection would be made on the basis of minimum cost of power produced. For the variable-power-level system, the kinematic machine will operate at a variable speed (unless specially controlled), while the FPSE will operate at constant speed (frequency), assuming that constant temperature input is maintained. This difference reflects generator efficiency differences. If a DC link to the public utility is utilized, an induction generator and rectifier will provide power both to battery storage and through an inverter to the load. If an AC link is ultimately utilized for the system, the FPSE may still be able to operate with an induction generator, while the kinematic engine will operate with a special generator. An example would be the Frequency Modulated Alternator having a special speed control, as in the pressure control of the Stirling engine working fluid.

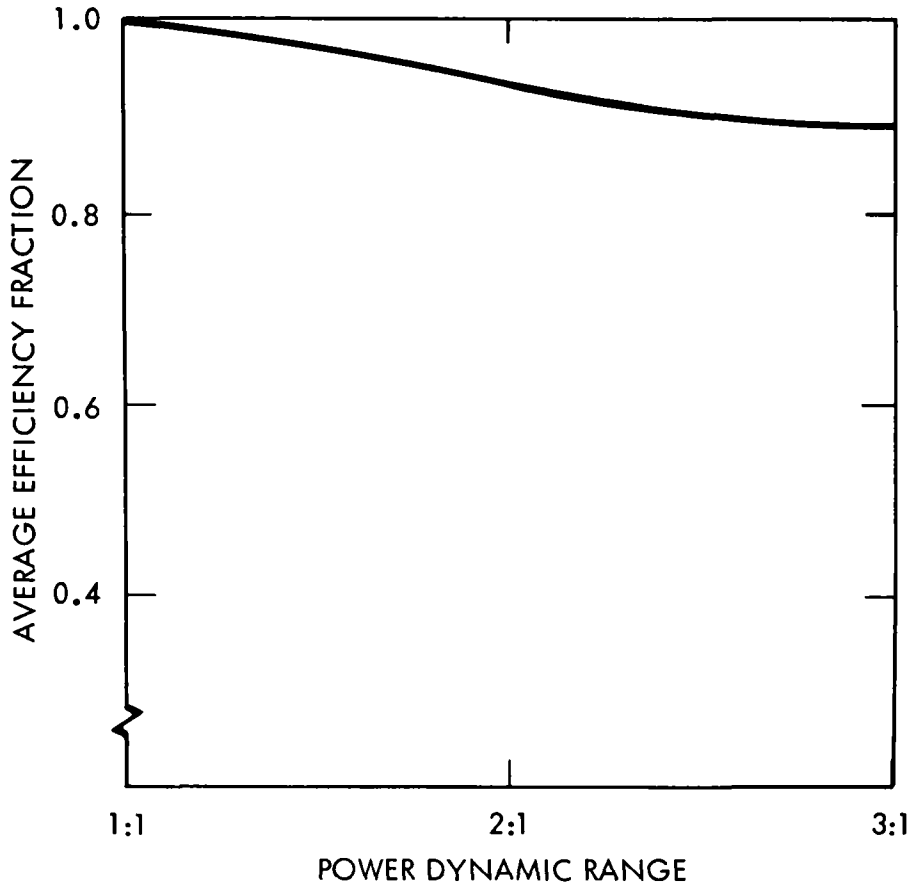


Figure 2-4. Stirling Engine-Generator Operating Efficiency Estimate

## 2. Control Concepts

From the systems viewpoint, a direct current link will be considered for ADS-1. The kinematic options involve either a developmental frequency modulated alternator of unknown efficiency, reliability and cost, or else a pressure-control Stirling engine that is very complex and requires parasitic power for pumping. The FPSE option will require the development of a costly three-phase linear generator option.

a. Fixed Power. With a fixed power input system (1.2-h TES) and a DC link, control is quite simple. The only real concern is that the TES never saturate and allow the receiver to exceed its design temperature. Solar insolation in excess of 0.845 $kW/m^2$ will go into thermal storage. When solar insolation drops below 0.845 $kW/m^2$, the power difference is made up from TES. Scheduling between TES and battery in the event of cloud cover will be the subject of additional study. With a fixed power level operation, a concept of power dispatch and control is suggested in Figure 2-5. A dispatcher will connect load to the inverter output. The difference between load and generator output will then flow into or out of the battery.

In the event of cloud cover, a possible mode of operation is to allow the system to continue operating until TES is depleted. The engine-generator will then shut down and the system will switch to its battery storage. A direct-insolation flux level sensor and integrator are mounted on the collector unit, providing an indication of the status of TES. The sensor and integrator are reset at the time the thermal storage is depleted and the unit is shut down. When energy storage is returned to normal, the engine-generator turns on again and standard operation is restored. If TES is depleted at the end of the day, startup the following day should normally occur a half-hour or less after solar tracking is initiated.

b. Variable Power Input. Small values of TES require the system to operate at variable power input. A suitable concept for control of a variable power system is sketched in Figure 2-6. Load is dispatched through the inverter from the generator, and may be augmented by battery power. A battery storage controller at the battery provides for charging and discharging as a function of (1) load demand, and (2) generator power available. The Stirling engine shaft speed is directly proportional to power output (constant temperature operation) and a tachometer provides a control signal both to the battery controller and to the generator field windings. Inverter output voltage also feeds back to the generator field windings to provide load voltage regulation. Under this scheme, any generated power not required by the load will go into the battery. Also, if load exceeds generator output power, the difference will be made up by the battery. If battery is depleted and generator output drops below load demand, the system will begin to shed load as inverter output voltage begins to drop.

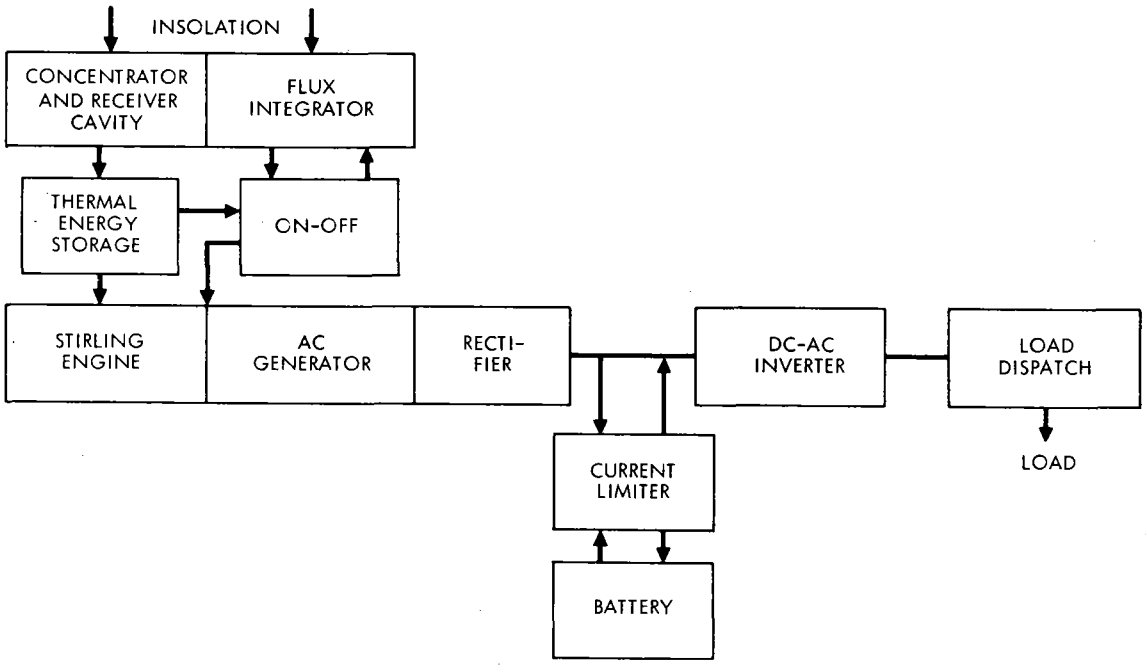


Figure 2-5. Dish-Stirling System Control, Fixed Power Level Operation Concept

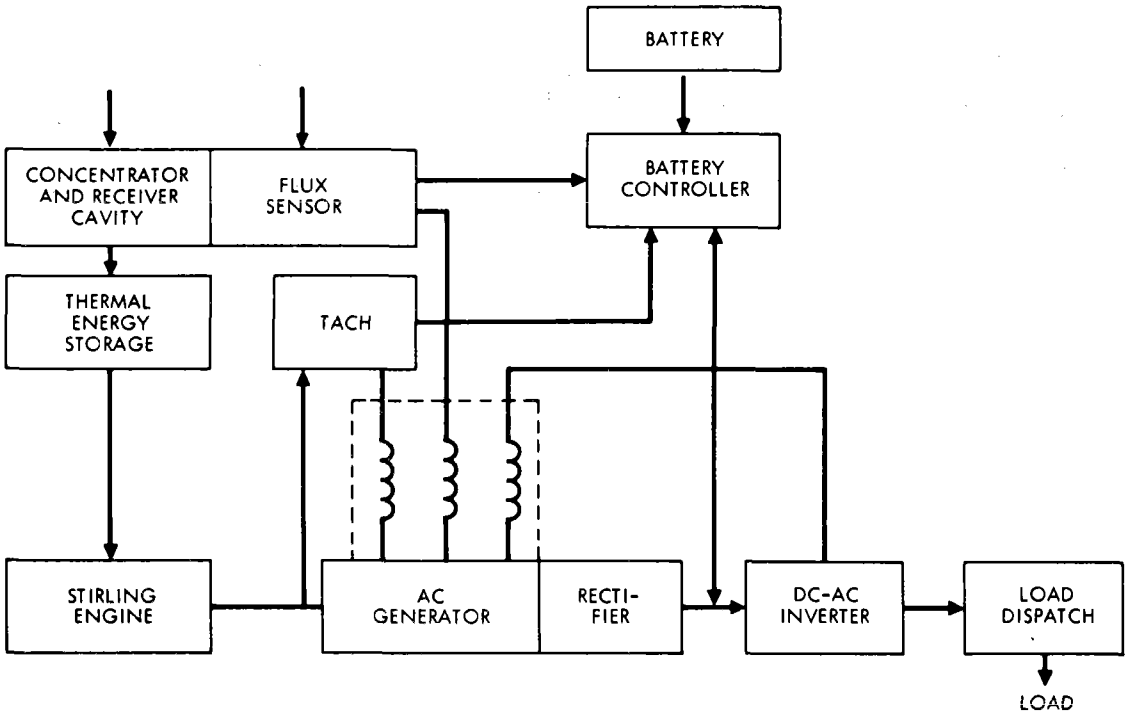


Figure 2-6. Dish-Stirling System Control, Variable Power Level Operation Concept

It is important that the TES not become saturated and allow the receiver to overheat. The solar flux sensor input to the generator field windings and battery controller should eliminate this problem. The assumption here is that, with TES, maximum engine operating power is lower than peak receiver power. A temperature limit signal may also prove desirable that would trigger disorientation of the solar concentrator should saturation occur. A small amount of TES is possibly necessary even if power leveling is not to be considered. Principally, direct exposure of the hairpin heater tubes of the Stirling engine to the concentrated solar insolation of the receiver cavity would produce a risk of hot spots and burnout. A small amount of thermal inertia via buffer storage material around the heater tubes will protect against this type of failure. Secondarily, it may be necessary to provide a small amount of thermal inertia to simplify startup and shutdown procedure in the Stirling power conversion subsystem and for brief cloud-cover transients. But as the amount of thermal storage is increased, temperature drop to the Stirling engine is also increased and some type of augmented heat transport, such as heat pipes, may become important.

# SECTION III

# POWER CONVERSION

## A. THERMAL ENERGY STORAGE AND TRANSPORT

# SECTION III

# POWER CONVERSION

## A. THERMAL ENERGY STORAGE AND TRANSPORT

### 1. Introduction

The objectives of the conceptual design study on the use of liquid metal heat transfer technology in distributed collector solar Stirling power systems are as follows:

(1) Indicate the economic viability of alkali metal heat transport for use in the 1985 time period.

(2) Perform benefit/cost analysis evaluating various promising systems and indicate the relative merit of competing systems.

(3) Define a promising alkali metal heat transport and storage system.

(4) Prepare conceptual designs of one or more of the promising systems with the objective of low capital cost in mind.

(5) Define the necessary developmental effort and design concept demonstrations required to ensure successful implementation of the selected system.

Work undertaken by Advanced Energy Programs, General Electric Company, utilized design guidelines provided by Jet Propulsion Laboratory in assessing the potential for several types of heat transport and thermal storage systems. These systems are intended to integrate the heat receiver with the Stirling engine-generator in various forms and arrangements of thermal transport and storage systems, as discussed in the following paragraphs. Where necessary to develop conceptual designs, a preliminary concept for the heat receiver and the Stirling engine heat exchanger are shown; since the Stirling engine is being developed under a separate program, now getting underway, future specific effort will be necessary to integrate, even more closely, the design of the Stirling engine heat exchanger with the thermal storage and alkali metal heat transport system.

As indicated in Table 3-1, the design guidelines were modified during the course of the program; a slightly larger collector area and larger average solar insolation are specified. These offset lower values specified for first article collector and receiver efficiencies. The power delivered to the Stirling engine remains essentially unchanged at about 52.5 kWth. A reduction in the estimated first article Stirling engine efficiency will result in reduced generator power output and limited availability of excess power for battery storage.

Table 3-1. Design Guidelines

| | 1985 Design | Prototype |
|---|---|---|
| Collector Diameter | 11 m | 11.5 m |
| Collector Area | 95.03 $m^2$ | 104 $m^2$ |
| Concentration Ratio | 2000 | 2000 |
| Receiver Aperture Diameter | 0.246 m | 0.257 m |
| Average Solar Flux | ∿0.76 $kWth/m^2$ | ∿0.845 $kWth/m^2$ |
| Collector Efficiency | 80% | 70% |
| Receiver Efficiency | 90% | 85% |
| Power to TES and to Stirling Engine | 53 kWth | 52.5 kWth |
| Stirling Engine Efficiency | 43% | 40% |
| Stirling Engine Shaft Power | 22.2 kW | 18.3 kW |
| Generator Efficiency | 90% | 90% |
| Generator Design Output | 20 kWe | 16.5 kWe |
| Rectifier Efficiency | 95% | 95% |
| Power to Grid | 15 kWe | 15 kWe |
| Power to Battery Storage (Before Rectification) | <4 kWe | <1.5 kWe |
| Peak Solar Insolation | 1 kWth | 1 kWth |
| Peak Power to TES | 68.4 kWth | 62.1 kWth |
| Focal Point Weight | 1400 kg | 1365 kg |
| Focal Point TES Weight | 550 kg | 600 kg |
| Thermal Storage Duration | 1.7-2.0 hr | 1.7-2.0 hr |
| Sensible Heat Storage Temp. Rise | 100°C (180°F) | 100°C (180°F) |
| Latent Heat Storage Temp. Rise | 55.5°C (100°F) | 55.5°C (100°F) |
| Nominal Stirling Engine Temp., Max. | 827°C (1520°F) | 827°C (1520°F) |

Both latent heat and sensible heat storage were considered. The former was assigned a temperature span of 55.5°C (100°F) to both allow a reasonable $\Delta T$ across the solidifying latent heat material and some superheating or subcooling of the salt. Sensible heat storage systems were assigned a larger temperature range of 100°C (180°F) in order to minimize the mass of sensible heat storage material required for various periods of time. A minimum thermal storage period of 1.7-2.0 hours was required.

The above guidelines were applied in preliminary consideration of the various system alternatives described in this report. A focal-mounted integrated system involving latent heat storage and thermal transport by heat pipes appears to be the most advantageous approach both technically and from the expectation of minimum capital cost.

## 2. System Alternatives

a. Cases to be Studied. As part of the system selection process, a number of potential systems were investigated. Not all met the design guidelines set forth in Table 3-1, but were evaluated for possibly more advanced application. Table 3-2 shows the characteristics of the systems which were considered.

The first nine cases considered included use of battery storage for post-insolation power in either heat pipe or pumped loop systems for heat transport. The tenth and eleventh cases involved the use of thermal storage alone for continuous generation of the basic 15 kWe power beyond the normal insolation period; their development was associated with the need for collector designs which permit large thermal storage at a separately supported focal point. The first nine cases require up to a two-hour period of thermal storage to accommodate variations in solar insolation and to permit efficient continuous operations of the engine-generator at near-design temperature and load conditions without serious off-design operating inefficiencies and with minimized thermal fatigue implications. In these first nine cases, both heat pipes and pumped loops were utilized to transport heat to a single, closely coupled storage system in the heat pipe systems, and to either a local or remotely located thermal storage system in the pumped loops system. Both sensible and latent heat storage were considered for periods of 15 minutes to 2 hours; the brief storage period was for short cloud cover purposes and the longer period ensures much less frequent interruption in the normal operating mode. Cassegranian mounting of the receiver, storage, and engine either to the back surface of the collector or to a fixed mount behind the collector has some potential system advantages which are offset by the additional reflecting mirror losses.

From Table 3-2, and the limits set by the reference collector design, the two key trade-offs are the form of TES (latent or sensible) and the heat transport method (heat pipe or pumped loop). These, as well as several other key items, are discussed in subsequent sections.

Table 3-2. Preliminary Design Options

| PARAMETER | CASE | | | | | | | | | | |
|---|---|---|---|---|---|---|---|---|---|---|---|
| | 1 | 2 | 3 | 4 | 5 | 6 | 7 | 8 | 9 | 10 | 11 |
| Generator Power, Average | 20 $kW_e$ (16.5 $kW_e$)* | | | | | | | | | 15 $kW_e$ | |
| TES Duration, Post Insolation | None | | | | | | | | | 6 Hours | |
| Other Storage | Batteries | | | | | | | | | 6 Hours TES | |
| Heat Transport Method | Heat Pipes | | | | | | Pumped Loop | | | Heat Pipes | |
| Collectors per TES/Engine | 1 | | | | | | 1 | 5 | 10 | 1 | |
| TES Type | Sensible Heat | | Latent Heat | | Sensible Heat | | | | | | Latent Heat |
| TES Duration (during Insolation) | 15 Min. | 2 Hrs. | 15 Min. | 2 Hrs. | 2 Hours | | | | | 6 Hours | |
| Collector/Receiver Type | Focus Mount | | | | Cassegranian Collector Mount | Cassegranian Fixed Mount | Focus Mount | | | Fixed Mount | |

Basic Parameters:*

Generator Efficiency, 0.9
Stirling Engine Efficiency, 0.42 (0.35)
Heat Receiver Efficiency, 0.9 Overall (0.85
Collector Efficiency, 0.8 (Focal Point Collector) (0.70)

*Values in parentheses are for the revised system

Collector Size, 11 m (11.5 m)
Solar Flux, Lancaster, Ca, Data
(1 $kW/m^2$ peak flux, 845 $W_t/m^2$ avg for 11 hour average day)

b. Latent Versus Sensible Heat Storage. In the early part of this study, it was recognized that either latent or sensible heat storage could be used. At that time it appeared that using a mixture of sodium and either Sialon or iron in the sensible heat mode would be an inexpensive way to store heat. It was also apparent that latent heat storage would be smaller and lighter for the same energy storage. Figure 3-1 shows the same data plotted for the 15 kWe cases. With an arbitrary temperature range of 100°C (180°F) allowed for the sensible heat storage, it is clear that latent heat storage materials must be considered for storage times greater than an hour for focus-mounted systems because of the weight limit.

The TES temperature range of 100°C (180°F), assumed for sensible heat storage, requires that the Stirling engine be operated over a similar range. If a true upper limit on Stirling engine heat exchanger temperature exists, then degraded performance over much of the operating time will occur. Although a similar effect also occurs with latent heat storage, the magnitude of the range is less, only about a half, and the duration of the extreme temperatures is relatively short. This comparison is valid irrespective of the exact upper limit placed on the Stirling engine heat temperature, or on the shape of the Stirling engine efficiency versus temperature curve. The operating mode and temperature differences in the latent heat storage heat pipe is discussed more fully later.

Both of the above observations lead to the conclusion that latent heat storage is preferred, if it can be utilized economically and reliably. For focus-mounted systems, which are mass limited, only latent heat storage can provide more than a small fraction of an hour. The situation could be changed if future collector concepts permitted more massive TES units. In this case, the low cost of some sensible heat storage media, such as iron/sodium, may outweigh the compactness of latent heat materials. Clearly, however, latent heat storage is preferred for the present design.

c. Pumped Loop Versus Heat Pipe. Two methods of transporting the liquid metal between the receiver, TES, and Stirling engine have been studied. These are the use of pumps, either electromagnetic or mechanical, and the use of heat pipes.[1] Inherent limits on heat pipes dictated the use of pumps for cases 8 and 9, which require relatively long pipe runs between the receivers and the central TES/Stirling engine module. For focus-mounted systems, case 7, the pump is an alternative to the heat pipe. A case not explicitly listed in Table 3-2 would have the receiver at the focus and would use a pump to circulate liquid metal to a TES/Stirling engine located behind the mirror. In evaluating the use of pumps, three areas of concern were studied: the

[1] Since heat pipe thermal transport was selected for the reference designs, a discussion of heat pipe performance is presented in subsequent sections.

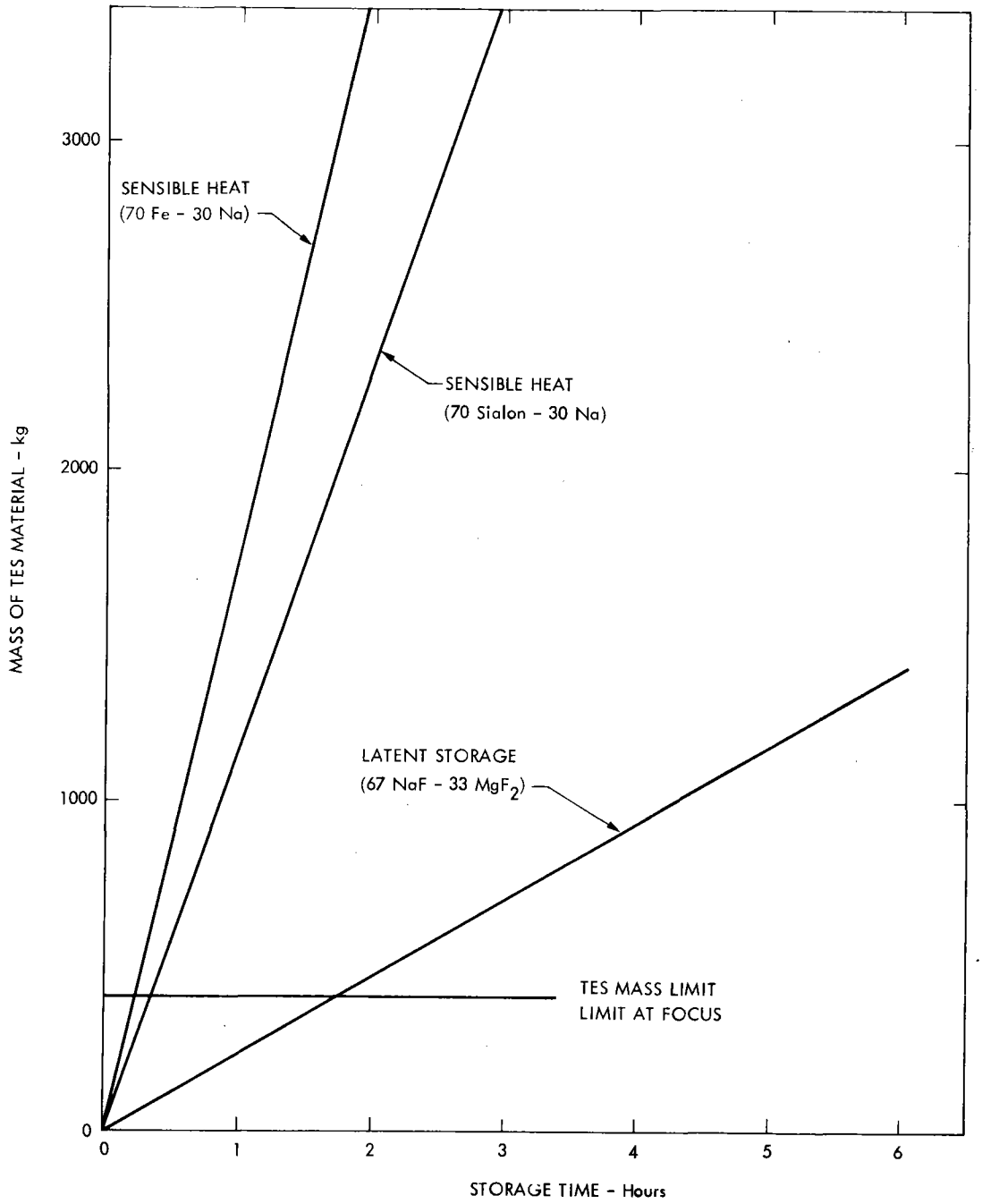


Figure 3-1. TES Mass Required Versus Storage Time

heat loss from long runs of insulated pipe, the power loss due to the pump, and the potential cost, availability, and weight of pumps and valves.

1) Heat Losses. Accounting for heat losses is especially important for some of the pumped loop cases. Table 3-3 shows the estimated heat losses for four different pumped loop configurations, two types of insulation, and two different heat loss rates. The lower heat loss figures represent about 100 W/m (100 Btu/hr-ft) for insulation over pipe, and require either 50 mm (2 inches) of vacuum insulation or 300 mm (12 inches) of a cellular material. Losses from the TES and receiver were not included, being nearly the same for each. Clearly, the losses from the multiple collector units are undesirably great, and would eliminate any potential advantage which might be gained by grouping the TES into a more centralized location. For the focus-mounted and dish-mounted systems, the losses are not necessarily disqualifying.

2) Pump and Valve Considerations. Pumps and valves for liquid metal service at a nominal 1100-1300°K (1500-1900°F) are not currently available, but represent an area of required development. Although liquid metal loops in this temperature range have been operated successfully, the usual practice has been to put the pumps and valves in a relatively cold leg of the loop. In the present system, no such cold leg exists, and both pumps and valves must be designed for at least 1100°K (1500°F) service. This does not imply that such equipment cannot be developed, only that a development program will be required.

Both electromagnetic (EM) and mechanical pumps were considered. EM pumps have the decided advantage of requiring no rotating seals. It is probable that the mass-produced and unattended nature of the overall system will eliminate rotating seals from consideration. Thus, the prime candidate is the EM pump. Estimates of the weight and efficiency of EM pumps were obtained. These showed weights of 50-250 kg (100-600 lb) depending on efficiency and design voltage, and efficiencies between 8 and 12%. System studies showed that approximately 1 kWe would be required for pumping, including the required cooling air flow for the pump winding.

A further complication of the pumped loop is the requirement for control of a pump and up to six valves. While certainly feasible, the added complexity causes concern with long-term operational reliability in an unattended environment.

3) Reasons for Heat Pipe Preference. The major reason for selecting the heat pipe concept as the baseline design over the pumped loop concept is that it will be cheaper, lighter, and more reliable.

Table 3-3. System Losses Through Pipe Insulation

| Cases | Approximate Pipe Length | Heat Losses | | | |
|---|---|---|---|---|---|
| | | 5.08 cm of Vacuum Insulation of Approx. 30.48 cm Cellular | | 10.16 cm of Cellular Insulation of 2.54 cm Super | |
| | | kW | % | kW | % |
| 1 Collector Focal Mt. TES | 6.1 m (20 ft) | 0.6 | ( 1.1) | 1.2 | ( 2.1) |
| 1 Collector Dish Mt. TES | 30.48 m (100 ft) | 3.0 | ( 5.4) | 5.8 | (10.4) |
| 4 Collectors Central TES | 262.13 m (860 ft) | 25.7 | (11.5) | 49.7 | (22.3) |
| 8 Collectors Central TES | 609.6 m (2000 ft) | 59.7 | (13.4) | 116.0 | (25.9) |

The heat pipe concept will be cheaper and lighter because the components of a pumped loop are added to similar ones in a heat pump configuration. For example, the TES cans and outer containment shell are required for both systems. However, in the heat pipe concept, the functions of the pump and valves are performed by the components of the TES and receiver.

The heat pipe concept will be more reliable because there will be no need for a control system pump and remotely operated high-temperature valves. For focus-mounted systems, the pumped loop concept is considered a backup. Additional work will be performed to quantify the above conclusions.

4) Potential Areas for Pumped Loop Use. The one concept where a pumped loop may have an advantage over heat pipes is a configuration in which only the receiver is at the focus and the pump, TES, valves, and Stirling engine are located at the base of the collector. The potential advantage results from being able to put more mass at this location, and hence add to the available heat storage time, or to simplify and lower the cost by using cheaper but more bulky materials. This concept will work only if the collector mount can hold significantly more mass behind the mirror than at the focus. To avoid flexible joints, the entire unit would pivot together. Flexible joints or hoses would be required to place the TES and Stirling engine on the ground, and flexible joints at this temperature level might require development. This concept will also receive more detailed evaluations.

d. TES Without Heat Transport. The direct use of thermal storage material without effective methods of heat transfer from the storage material to the Stirling engine heat exchanger does not appear feasible without significant temperature increases between the heat receiver and the Stirling engine; these temperature increases are a forcing function toward more serious problems in materials selection, operating life, reliability and cost.

Limited thermal analyses were performed to evaluate the $\Delta T$ required to drive the required heat for 15 minutes of operation (39.6 kWth) from the TES material to a Stirling engine heat exchanger. The heat exchanger was comprised of 14 hairpin tubes, each 210 mm in length and having an inside diameter of 3.2 mm. Four cases were examined, with the results shown in Table 3-4.

In these cases somewhat optimistic assumptions have been made which tend to make the calculated temperature rise smaller than might later be achievable. For the latent and sensible heat storage cases involving surrounding the HX tubes with storage material, a straight, continuous length of HX tubing was considered. The necessary use of hairpin type tubes will restrict the ability to locate the storage material.

Table 3-4. 15-Minute Thermal Energy Storage Using No Heat Transport

| Case | Description | ΔT, (Total Over Operational Range) |
|---|---|---|
| 1 | Latent Heat Material Surrounding Stirling Heat Exchanger Tubes | 280°C (504°F) |
| 2 | Latent Heat Material in Cans With Static Liquid Metal Thermal Conductance | 443°C (797°F) |
| 3 | Sodium/Sialon Sensible Heat Material Surrounding Stirling Heat Exchanger Tubes | 260°C (468°F) |
| 4 | Sodium/Iron Sensible Heat Material Surrounding Stirling Heat Exchanger Tubes | 176°C (317°F) |

The Stirling engine heat exchangers provide effective heat transfer in a very small heat transfer surface because of the good heat transfer film coefficients on both the gas side and the liquid metal side (in the case of liquid metal pumped loop or condensing metal vapor heat transfer). The transfer of heat at high rates from a relatively large volume of thermal storage material requires the use of very efficient methods of thermal transfer from relatively small volume increments and large surface areas of the storage medium. Elimination of such effective heat transfer methods forces the necessity of high $\Delta T$'s to move thermal energy by convection or conduction methods.

The above analysis indicates that direct coupling of thermal storage to the Stirling engine is not a readily achievable possibility, although additional study of the problem might reveal some possible alternative method.

e. Advantage of the Focus-Mounted System. The focus-mounted system, using heat pipe thermal transport, will have the following advantages over competing systems:

(1) Low heat losses.

The compact assembly will have a low surface area and will allow the use of efficient insulation. No pipe runs are required.

(2) No possible power losses.

The absence of pumps, valves, and control systems makes more electrical power available for the user.

(3) Maximum TES material within the weight limit.

Considered as a heat transport system, heat pipes are lightweight compared to pumped loops.

(4) Potentially low cost.

The basic simplicity of the system will allow extensive cost-cutting as the design moves from the present concept to the hardware stage.

3. Thermal Design

a. General Description of the Integrated System. As indicated above, the integrated power system mounted at the focal point, providing up to 2 hours of latent heat thermal storage and featuring thermal transport by means of sodium heat pipes, was selected for conceptual design. This required various thermal design analyses to establish the engineering specifications from which the conceptual mechanical design could be prepared. This analysis considered (1) the heat flux impinging

upon the receiver at peak power conditions, (2) the thermal and geometric definition of the TES storage system and its behavior during charging and discharging, (3) the limits on the heat transfer design configurations for the Stirling engine heat exchanger, (4) the methods and engineering limits for transferring heat from the solar heat receiver to the TES and to the Stirling engine, (5) the selection of the fused salt, its dimensional limits and the thermal gradients across it during power extraction, (6) the temperature distribution throughout the system, and some limited considerations for the mode of operation of the system in accepting, storing, and utilizing thermal energy.

Before describing the thermal design effort required for the development of the conceptual design, it is helpful to understand the nature of the integrated focus-mounted system which was eventually developed. The frontispiece shows an isometric cutaway section featuring (1) the primary heat pipe heat receiver, (2) the secondary heat pipe containing the fused salt thermal storage capsules, header plates and wicking, (3) the incorporation of the Stirling engine heat exchanger into the secondary TES heat pipe, (4) the Stirling engine-generator, (5) the thermal insulation, (6) the cold outer casing, and (7) the support structure.

b. Heat Receiver Optical Design. In order to achieve the highest efficiency in a cavity type receiver several objectives must be considered. The design should emulate a black body as nearly as practical. In order to minimize reradiation losses, as much as possible of the internal surfaces should be kept at as low a temperature as possible. It is desirable that the interior of the receiver have a relatively large surface area with respect to the aperture area to ensure that most of the approximately 20% of the incident radiation which is reflected is directed toward another receiver surface and not lost by reflection out of the aperture. Finally, thermal insulation should be effective and low in cost.

The size of the receiver aperture is a significant factor in the design. At a concentration ratio of 2000 and a collector diameter of 11.5 meters the aperture diameter is 0.257 m (10.1 inches). A heat receiver inside diameter larger than this would be advantageous, but it would require more complex heat pipes to cool the area immediately behind the aperture; or it would require that this area be left uncooled, with higher thermal conduction and reradiation losses. Since simple and relatively economic axial heat pipes could be used to cool the cylindrical walls at a chamber ID similar to the aperture, this design approach was utilized.

An analysis was performed to determine the distribution of the thermal flux impinging on the inner cylindrical surface of the heat exchanger using a computer program developed by the General Electric Company specifically for optical thermal analysis of cavity heat receivers located at the focal point of a parabolic collector. As indicated in Figure 3-2, the program integrates the thermal flux impinging on a given increment of a cylindrical wall within the heat

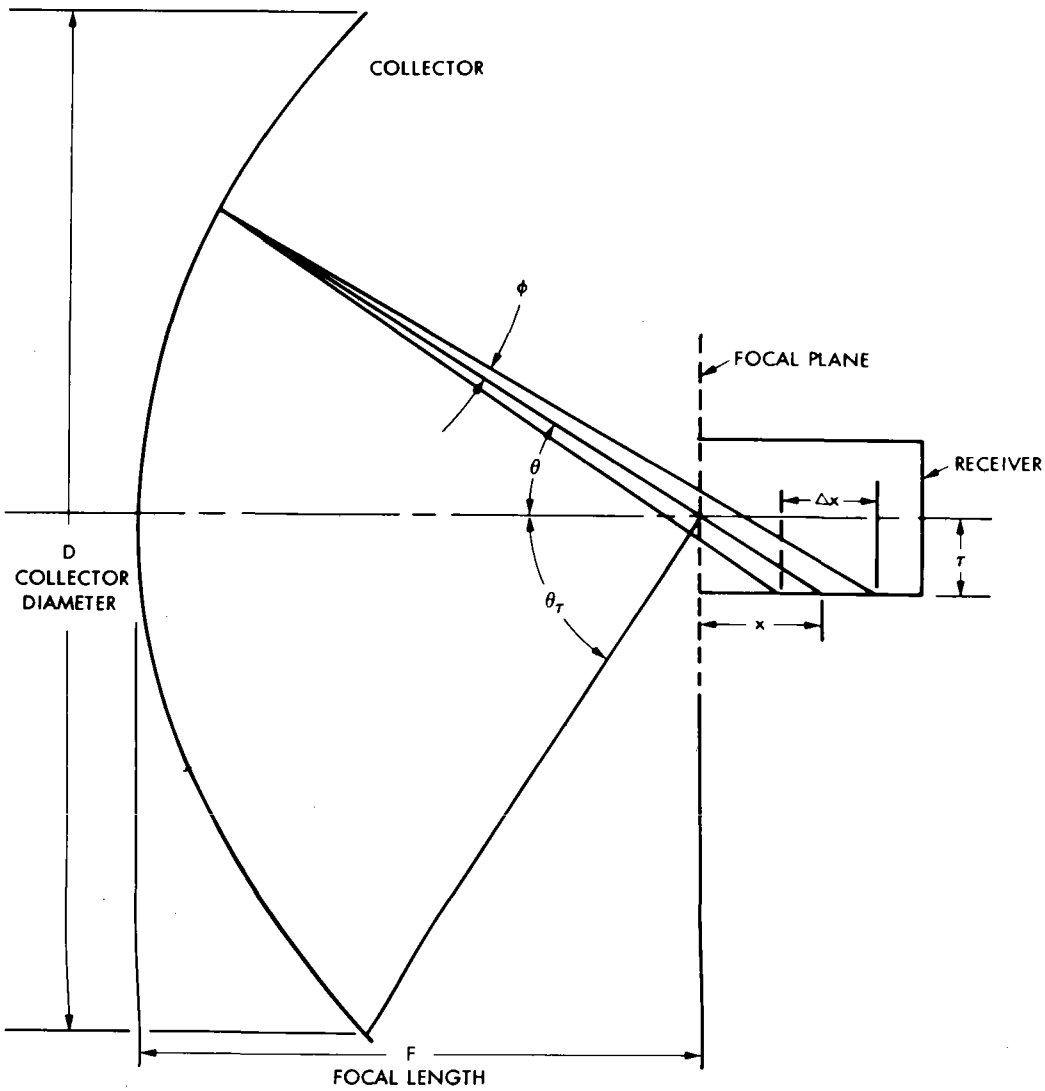


Figure 3-2. Physical Description of Heat Receiver Thermal Flux Analysis Model

receiver from various points on the collector. Light reflected from each band on the collector, at an angle, theta ($\theta$), undergoes some spreading through an average conical dispersion angle, phi ($\phi$). Phi nominally accounts for all the possible errors, but for this analysis the dish was assumed to be geometrically perfect, all errors were accounted for by using an overall collector efficiency of 70%, and phi was limited to half the solar disc angle, or 0.266 degrees.

In this program the receiver wall was divided into a number of points in the x direction. As the angle theta ($\theta$) increased to the rim angle, $\theta_r$, the program calculates each flux increment and sums it to those points which lie within $\Delta x$. The results of this analysis are plotted in Figure 3-3 as thermal flux along the axial length of the heat receiver inside diameter. The peak solar incident thermal insolation is about 500 $kW/m^2$ compared with a liquid metal heat pipe thermal flux capability in excess of 2500 $kW/m^2$; thus, the maximum incident flux is conservative with respect to heat pipe capabilities. The accumulated thermal energy along the length of the heat receiver is shown in Figure 3-4. While only a fraction of the incident radiation is absorbed directly upon contact, reflected energy will distribute the energy more evenly throughout the cavity. Therefore, the maximum flux should be less than indicated.

Based upon the above impinging thermal flux distribution data, a cylindrical heat receiver was selected which featured axial heat pipes in a cylindrical curtain-wall construction with an axial length of 0.508 m (20 inches); this length was sufficient to intercept 88% of the incident energy. The heat receiver ID was equal to the aperture diameter. A single, disk heat pipe was used to cool the rear end of the heat receiver.

The addition of an uncooled light baffle about 0.127 m (5 inches) in axial length and located in front of the heat pipe at the end of the heat receiver was considered to increase the apparent optical length of the heat receiver and to improve black body conditions. If such an uncooled light baffle were used, it would require optimization through a more detailed finite element analysis. It is envisioned that these surfaces would be heated to a temperature about 55-80°C (100-150°F) hotter than the cooled heat pipe surfaces. Because of the relatively poor view of the aperture from these surfaces, the increase in reradiation losses would be less than the reduced absorbtivity of the receiver without the light baffle. Consideration for the possible necessity of such a light baffle is beyond the present conceptual design.

c. <u>TES Thermal Design</u>. A thermal energy storage weight limitation of 550 kg was selected with a goal of providing from 1.7 to 2.0 hours of power at 52.5 kWth.

In order to minimize the temperature drop through the TES material it was essential to provide a thermal path as short as possible through the fused salt to a heat transfer surface. For production

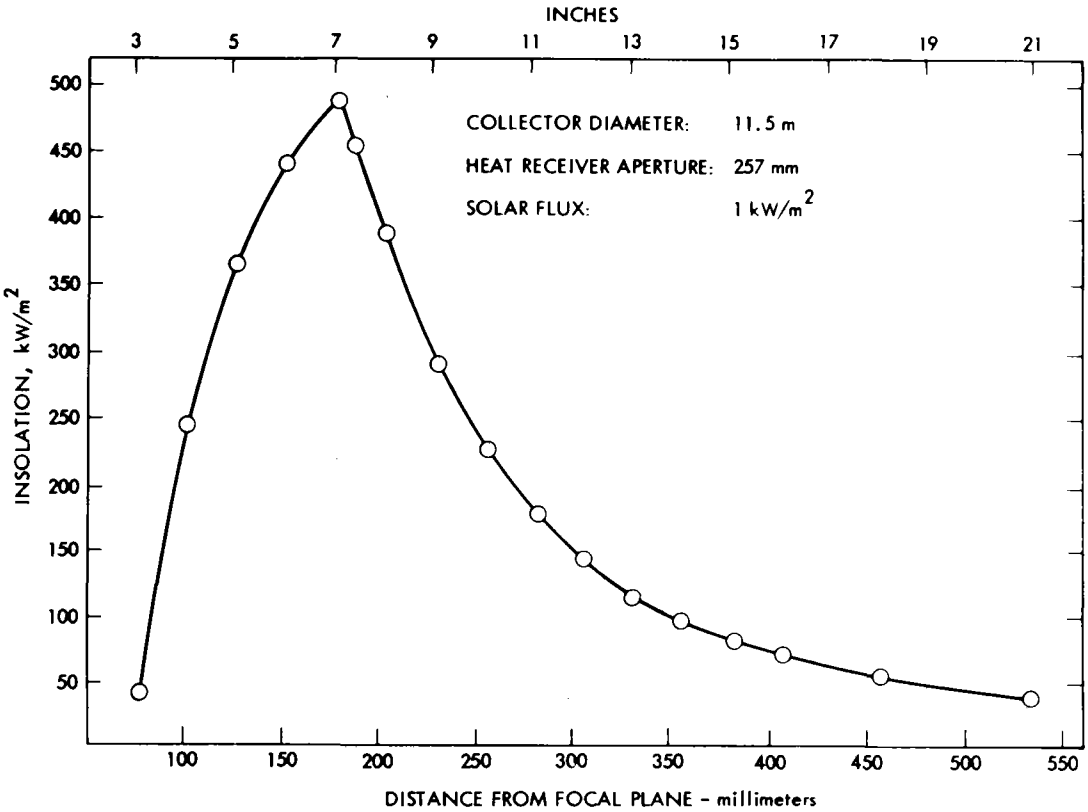


Figure 3-3. Local Impinging Heat Flux along Heat Receiver Cooled Wall

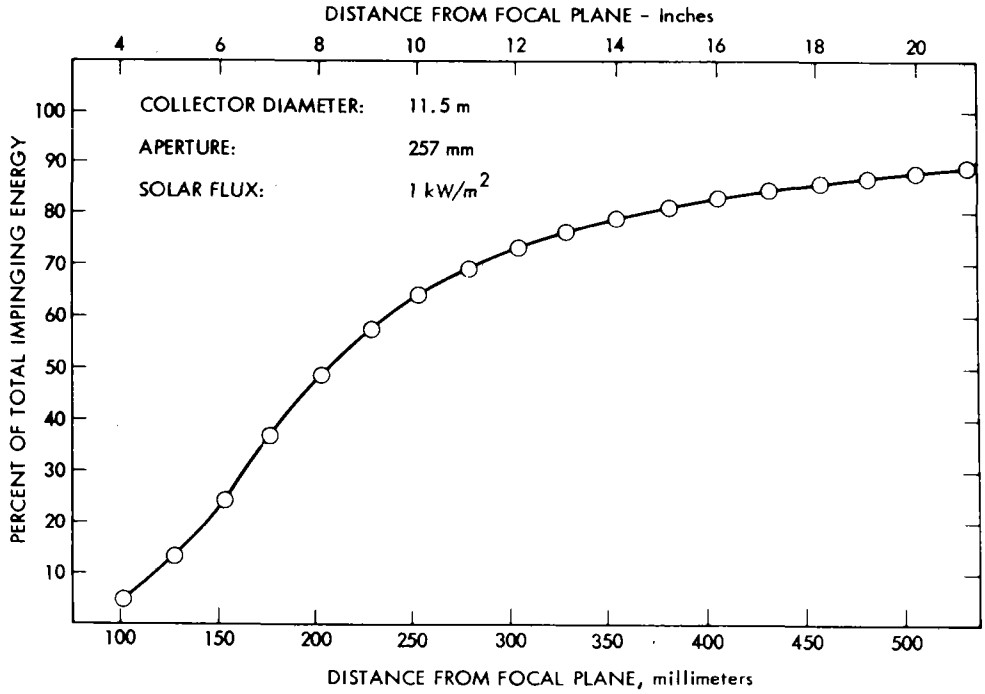


Figure 3-4. Cumulative Impinging Thermal Energy along Heat Receiver Cylindrical Cooled Wall

simplicity and economy and for other heat transfer reasons, it was decided to contain the fused salt in sealed metal cylinders for simple radial heat transfer. These cylinders, in turn, were encased in a cylindrical heat pipe, a L/D ratio of about 1.0 was selected to minimize heat pipe outer surface area for a given required heat pipe volume; this tended to reduce both the materials requirements and manufacturing costs, and the area from which heat losses could occur.

A correlation was made between the expected temperature drop through the fused salt and the number and diameter of TES capsules required for a given power and storage period. Based upon earlier calculations for $NaF-MgF_2$ eutectic salt storage relating the length, diameter and number of TES capsules required for two hours thermal storage at 39.68 kWth, as seen in Figure 3-5, a thermal gradient of 42°C (75°F) was selected. The salt was assumed to operate an additional 8°C (15°F) above its melting point and at the capsule centerline, 5.5°C (10°F) below its melting point. This reduced the number of capsules required at a maximum temperature drop penalty of 55.5°C (100°F), which appeared acceptable in terms of engine performance. (Stirling engine efficiency does not fall off at an unacceptable rate with a 55.5°C (100°F) decrease in operating temperature.)

The actual thermal design was then based upon iterative computer program calculations using the TES properties. The inputs to this program included the number, length and diameter of fused salt capsules and a required power output of 52.5 kW. The program calculated the following:

(1) System weight including that of the TES material, capsule containment, and heat pipe chamber.

(2) Thermal storage time including that involved in a 55.5°C (100°F) sensible heat loss by the TES material, capsules, and heat pipe.

(3) Maximum $\Delta T$ across the TES material.

(4) Heat pipe outer cylinder diameter and length.

By iteration of these calculations, systems meeting the thermal storage objectives were developed for both LiF salt and the $NaF-MgF_2$ eutectic, as shown in Table 3-5.

This thermal design data formed part of the basis for the mechanical design of the thermal energy storage system.

d. Stirling Engine Heat Exchanger Design. The thermal and mechanical interfaces between the thermal transport/thermal storage system and the Stirling engine-generator requires close integration between groups having responsibility for each. A logical point for the thermal interface is a definition of the Stirling engine heat

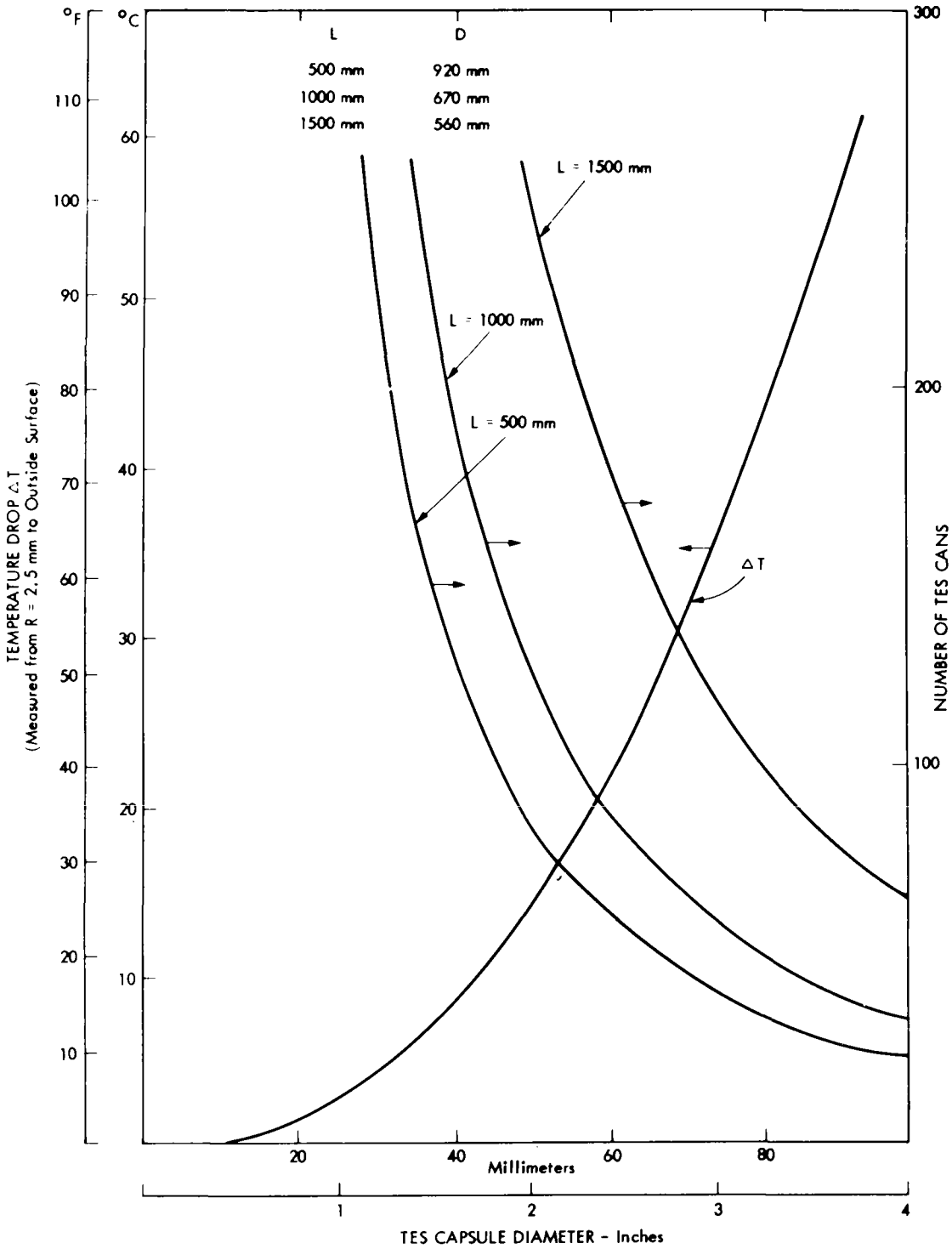


Figure 3-5. Two-Hour Latent Heat TES Requirements at 39.68 $kW_t$ for 67 NaF - 33 $MgF_2$

Table 3-5. Initial TES System Definition

| | $67NaF-33MgF_2$ | LiF |
|---|---|---|
| Weight - Total | 550.0 kg | 550.0 kg |
| TES Material | 346.3 kg | 346.1 kg |
| Cans | 68.3 kg | 75.7 kg |
| Containment Vessel | 114.9 kg | 107.7 kg |
| Wire Mesh and Sodium | 12.4 kg | 13.0 kg |
| Can Support | 8.1 kg | 7.5 kg |
| Dimensions - Containment Vessel | | |
| Length | 653 mm | 653 mm |
| Diameter | 646 mm | 624 mm |
| Thickness | 6.35 mm | 6.35 mm |
| Dimensions - TES Cans | | |
| Length | 622 mm | 605 mm |
| Diameter | 58.4 mm | 48.2 mm |
| Thickness | 0.75 mm | 0.76 mm |
| Number | 97 | 135 |
| Approximate Can Temperature Gradient (Maximum) | 41.6°C | 40.3°C |
| Approximate Storage Time (55.6°C Sensible + Heat of Fusion) | 1.27 hr | 1.88 hr |

exchanger surface area and outer tube surface temperature and the heat flow required to this engine. The mechanical interface requires consideration of accessibility of the heat exchanger tubes to condensing metal vapor, condensate return, location of joints in the leak-tight metal vapor space and methods of mounting, supporting and disassembling the engine-generator from receiver-TES thermal transport system. Since work, under separate contract, on the 15 kWe Stirling engine had not proceeded to a point where interface effort was warranted it was necessary that this alkali metal heat receiver thermal transport and thermal storage program assume a limited responsibility for definition of the Stirling heat exchanger, but only through initial conceptual design. The only formal constraint was that concerning the centerline diameters locating the heat exchanger tubes at the Stirling engine head.

The design of the heat exchanger is an integral part of the design of the Stirling engine. This design must include the heat exchanger itself, the regenerator and the cooler in an integrated manner. For best operating efficiency both the pressure drop in the gas flow system and the dead volume in the heat exchanger must be minimized. The gas flow oscillates through the three heat exchangers at 1800 cycles per minute (1800 rpm); heat transfer and gas flow analysis in the various parts of the system are critical to the design. The engine must receive 52.5 kWth heat input through this heat exchanger during normal operation.

The thermal resistance of the tube wall and the gas side film are controlling factors in heat transfer; the condensing alkali metal coefficient is about 60,000 $W/m^2$-°C whereas the gas side coefficients are only 6000-12000 $W/m^2$-°C. The thermal resistances of the gas side film and of the necessarily thick metal wall are of the same order of magnitude, while the condensing alkali metal thermal resistance is only about 10% of either of the other resistances. Thus, the Stirling engine design itself controls the definition of the heat exchanger, considering such factors as gas flow, pressure drop, dead volume, heat transfer surface area, tube wall thickness (for stress capability and thermal resistance), and system operating temperature.

A limited analysis was made by General Electric Stirling engine development personnel of the design of a 52.5 kWth, $1.76 \times 10^7$ Pascals (2550 psia), helium gas heat exchanger for a Stirling engine with 35% efficiency operating at 1800 rpm. Figure 3-6 indicates the design constraints and the nominal design alternatives for various heat exchanger configurations which could be used. The 24-tube configuration with a 67°C (120°F) temperature drop was selected for the conceptual design as a reasonable balance between the desire for economy and manufacturability on the one hand, and thin-wall, small-tube diameter, on the other hand. The latter aims at low-wall $\Delta T$ and high gas side film coefficient, which are important in minimizing the temperature drop across the heat exchanger.

As the conceptual design is implemented further, heat exchanger optimization by the selected Stirling engine design group will be necessary. Close mechanical design liaison will also be

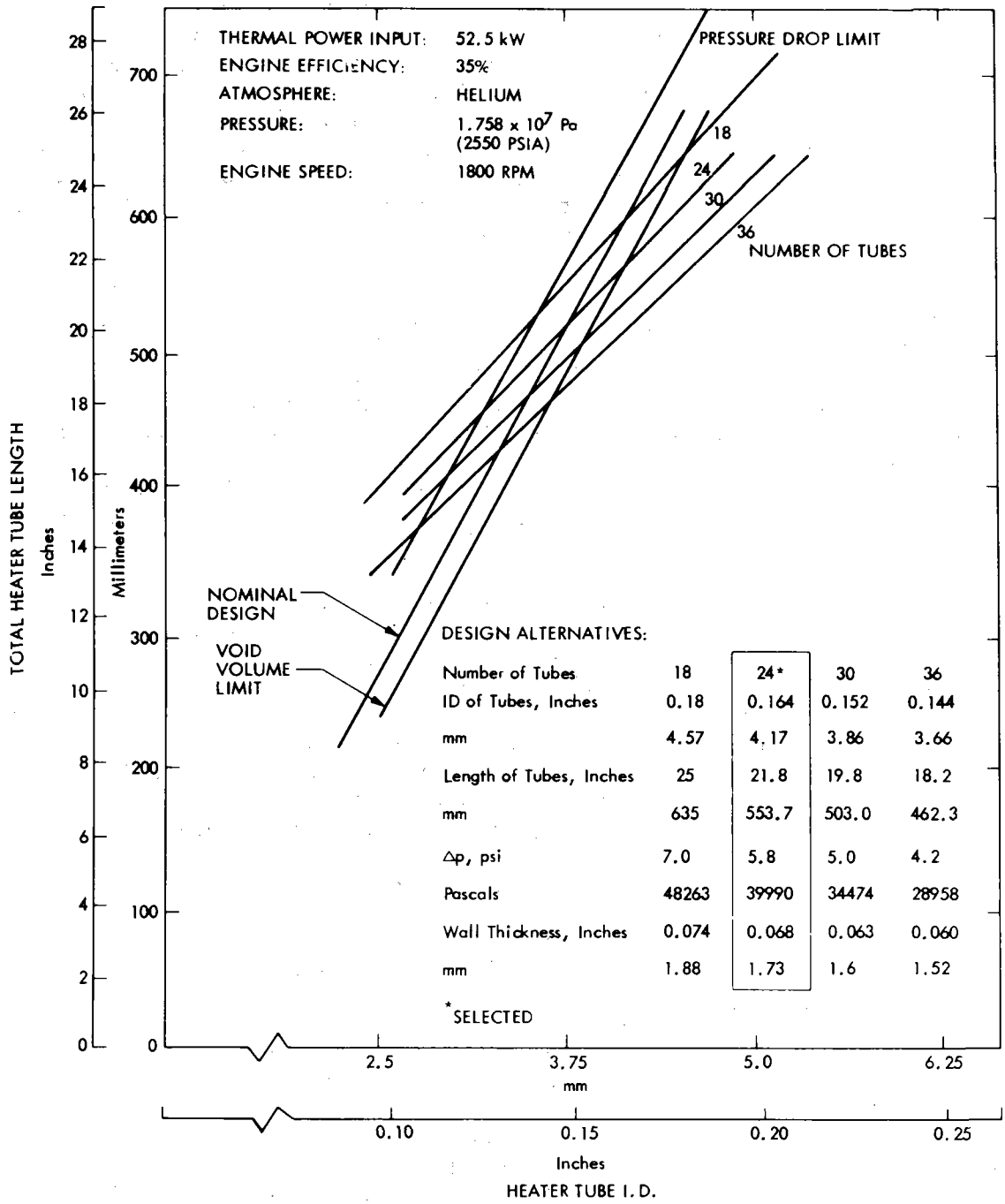


Figure 3-6. Stirling Engine Heat Exchanger Optimization Curves

required to integrate the engine with its thermal transport system. The present 24-tube heat exchanger will suffice for these initial conceptual designs.

e. Heat Pipe Thermal Transport. The two phase heat transfer operations, viz., boiling and condensation, constitute the cycle in the heat pipe to transport heat from the source to the sink. This feature of transporting the latent heat makes the heat pipe a device of very high thermal conductance and with negligible vapor flow pressure drops it becomes a near isothermal device. By proper designs, the thermal resistances can be kept to minimum in the heat pipes and large amounts of heat can be transferred over reasonable distances with minimum temperature gradients.

The liquid metals are the only attractive working fluids in the heat pipes operating above 600°K (1100°R). They have a very high liquid transport factor which is a function of the surface tension, latent heat and the viscosity. Sodium was chosen for the heat transfer fluid because its low vapor pressure, high latent heat, low viscosity and high surface tension are attractive for heat pipe purposes in the 815°C (1500°F) temperature range. Added to its good thermal transport properties, it is inexpensive and is available in abundance. Because the heat transport system operates with the receiver at the lower end of the system and the Stirling engine at the higher portion of the system, gravity works to assist the return of condensing liquid to its heat source in the system; nevertheless, capillary pumping by the use of wicks is necessary to ensure that the condensing liquid is returned to the appropriate heat source, both to ensure heat transfer and to prevent local hot spots from developing.

Sodium heat pipes have been very extensively used over the last ten years and the experimental knowledge is readily available. The basis for these designs is well established in design and performance calculation methods (Ref. 3-7); these design methods were used in the present study. The design took into consideration the low incident angle of the heat pipes in the reference configuration during morning and late afternoon hours (approximately 10° from horizontal), the necessity for wicking, and the effects of cloud cover.

1) Heat Receiver Heat Pipes. The optical design of the heat receiver was described above; the heat pipes in the heat receiver were designed to transport the thermal flux which impinges upon the walls of the heat receiver.

The heat pipe design was based upon transferring a peak power of 62.1 kWth from the receiver to the TES secondary heat pipe at a maximum local flux of 500 $kW/m^2$. The design was predicated upon heat pipe cooling of all the interior walls of the heat receiver. Axially arrayed tubular heat pipes were used to cool the cylindrical surfaces of the receiver on which about 88% of the incident energy impinged and a single, disk heat pipe was used to transfer the remaining thermal energy from the back surface of the heat receiver.

Several sizes and numbers of tubular heat pipes were suitable for use on the cylindrical wall, as indicated in Table 3-6. Thirty-four (34) 25-mm (1-inch) OD heat pipes, each having a length of 508 mm (20 inches) and a wall thickness of 0.86 mm (0.035 inches) (for minimum temperature drop), could be used to transfer heat from the cylindrical wall; nevertheless, mechanical design considerations suggested that 27 such tubes, flattened in the receiver area, should be used to facilitate weld assembly at the TES secondary heat pipe header.

These heat pipes are wicked in the heat receiver area with 60 mesh 304 SS Screen two layers thick. Threaded or knurled inside diameter surfaces have also been considered to distribute condensate return.

All heat pipes have a 127 mm (5 inch) adiabatic length to allow for thermal insulation between the TES secondary heat pipe and this receiver. This insulation is needed since the heat receiver cools during cloud cover or absence of solar insolation. The primary heat pipes will be inoperative and will conduct heat only by thermal conduction from the thermal storage area to the heat receiver during this period.* A total of only 127 mm (5 inches) of condenser section are needed to transfer heat from the primary heat pipes into the secondary heat pipe.

As indicated in Table 3-6, the limiting thermal capacity of of each heat pipe was 11.25 kWth, limited by wicking capacity; the local maximum fluxes of 500 $kW/m^2$ could be readily absorbed. The sodium inventory required is just sufficient to saturate the wick in the primary heat pipes. The single flat plate heat pipe at the end of the receiver was rated at a thermal capacity of 7 kWth, well above anticipated local fluxes which are nominally below 50 $kW/m^2$.

The small number of tubes in the heat receiver and their thin walls promote both economy of manufacture and low temperature loss across the metal wall.

2) Thermal Energy Storage Heat Pipe. The thermal energy storage system, apart from serving the purpose of containing the thermal storage capsules, must transfer heat rapidly to smooth out any temperature gradients in the containment vessel; it must transfer a maximum of 62.1 kWth into the TES chamber and deliver, either directly, or from storage, 52.5 kWth to the Stirling engine while the engine is operational, irrespective of the incoming thermal energy. It provides thermal inertia in that any excess thermal energy input is stored in the form of latent heat in the fused salt. In periods of deficient solar insolation, the thermal storage heat pipe supplies heat to the Stirling engine

*Thus providing a one-way heat transport path, and eliminating the need for active controls.

Table 3-6. Primary Heat Pipe Data

| O.D. | | Wall Thickness | | ΔT | | Capacity per Heat Pipe kWth |
|---|---|---|---|---|---|---|
| inches | mm | inches | mm | °F | °C | |
| 1.0* | 25.4 | 0.035 | 0.864 | 32 | 17.8 | 11.25 |
| 1.5 | 38.1 | 0.065 | 1.651 | 45 | 25.0 | 24.8 |
| 2.0 | 50.8 | 0.095 | 2.413 | 63 | 35.0 | 43.6 |
| 2.5 | 63.5 | 0.146 | 3.759 | 93 | 51.7 | 64.7 |

*Chosen for preliminary design because of minimum temperature gradient.

Heat Pipe Lengths

| | | |
|---|---|---|
| Evaporator | 508 millimeters | 20 inches |
| Adiabatic | 102 millimeters | 4 inches |
| Condenser | 107 millimeters | 5 inches |
| Total | 737 millimeters | 29 inches |

Wicking

In the lower 508 mm (20 in.) of Receiver Heat Pipes

Material 304 SS

Thickness - each layer 0.254 mm

Number of layers - 2

from the TES container. Thermal transport in the TES secondary heat pipe relies upon the use of various kinds of wicking to return the condensate along the cylinder walls and TES capsules toward the heat receiver end. Radial distribution of fluid is accomplished by other wicks.

The outer surfaces of the condenser portions of the primary heat receiver heat pipes protrude into the secondary TES heat pipe and act as the evaporating surfaces for heat input into the secondary heat pipe. The condensing of the sodium vapor in the secondary heat pipe takes place either on the heater tubes of the Stirling engine heat exchanger as power is extracted from the engine, or on the surface of the TES capsules as heat is absorbed into the TES material.

In designing the thickness of the wick or in determining the number of layers of screen wick necessary, the wicking limit is used as the design constraint. The wicking limit $(QL)_{max}$ is given in Btu/ft/hr or kW-m, for the given wick geometry and thickness. The wicking limit is expressed as:

$$(QL)_{max} = \frac{P_c \pm P_g}{F_\ell + F_v}$$

where $P_c$ and $P_g$ are the capillary pressure and gravity force terms and $F_\ell$ and $F_v$ are the liquid and vapor frictional pressure drop factors. The capillary forces increase with the increase in the mesh size for a screen wick and, correspondingly, frictional forces increase. Also the cost/sq. ft. of the wick matrix increases very sharply for the small pore screen structures. The wicking capabilities of wire sceeen and fiber metal type wicks are indicated in Table 3-7. Both from manufacturing and cost considerations, fiber metal wicks have advantages over wire mesh screens. Sintered metals are not economically acceptable as complex wicks. The above factors were considered in selecting the wicking configuration. The specific wick selections are indicated in Table 3-8.

The header plate wicking is designed to transport sodium flow equivalent to 62.1 kWth radially over an effective pumping height of 0.46 m (18 inches) which is the distance between the bottom of the container vessel and the top-most primary heat pipe. The circumferential wicking along the inside of the heat pipe provides the liquid to the rest of the header plate wicking, essentially by gravity flow. The primary heat pipe surfaces in this secondary heat pipe have minimum wicking sufficient to keep the evaporator wick saturated.

The additional radial wicking at the front and aft of the secondary TES heat pipe is designed to distribute the condensate return to the fore and aft ends of the TES capsules. The TES capsule wicking collects and distributes the liquid along the TES capsules as it is pumped radially inward in the radial wick; for this reason the wicking provided on the TES capsules is very minimal. The space available

Table 3-7. Radial Wicking Capabilities of Wire Screen and Fiber Metal Wicks for 0.46 m (18 in.) Effective Pumping Length

| Wick Type | Porosity | Permeability $m^2 \times 10^{-10}$ | Capillary Radius (μm) | Thickness (m) | Max. Wicking Capability (kW) |
|---|---|---|---|---|---|
| Wire Screens: | | | | | |
| 200 Mesh | 0.604 | 0.427 | 64.00 | 0.0127 | 32.4 |
| 250 Mesh | 0.670 | 0.3716 | 50.90 | 0.0127 | 64.7 |
| 300 Mesh | 0.629 | 0.2136 | 42.67 | 0.0127 | 58.0 |
| 400 Mesh | 0.670 | 0.1459 | 30.48 | 0.0127 | 67.9 |
| Fiber Metals: | | | | | |
| FM1101 | 0.9 | 0.56 | 26.5 | 0.0038 | 64.65 |
| FM1102 | 0.8 | 0.087 | 13.5 | 0.0038 | 25.33 |
| FM1103 | 0.7 | 0.028 | 7.5 | 0.0038 | 16.02 |
| | | | | 0.0127 | 74.17 |
| | | | | 0.01016 | 59.33 |
| FM1104 | 0.6 | 0.013 | 5.0 | 0.0038 | 11.55 |
| FM1105 | 0.5 | 0.0009 | 2.3 | 0.0038 | 18.00 |

Table 3-8. TES Secondary Heat Pipe Wicking

| Wicking Location | Capillary Radius ($m \times 10^{-6}$) | Wick Thickness (mm) | Type |
|---|---|---|---|
| Primary Heat Pipes | 2.12 | 0.254 | 60 Mesh SS Screen |
| TES Capsules | 2.12 | 0.4572 | 60 Mesh SS Screen |
| Container (Circumferential) | 2.12 | 0.9144 | 60 Mesh SS Screen |
| Header Plate (Radial) | 26.5 | 10.16 | FM1103 Stainless Steel |
| Front End (Radial) | 7.5 | 3.81 | FM1101 Stainless Steel |
| Aft End (Radial) | 7.5 | 3.81 | FM1101 Stainless Steel |

between the TES capsules provides the area for vapor flow either from the primary tube heat source or from the TES capsules to the condenser tubes. Sufficient amounts of sodium are provided in the TES system to saturate all the wicks.

f. System Thermal Loss. System thermal losses were calculated for two different cases; the first when the sun is shining and the receiver is in operation, and the second when the sun is not shining and the Stirling engine is running off the TES alone.

A one-dimensional analysis has been performed for the second case which indicated that the system thermal loss would be on the order of 2 kWth. The same analysis also indicated that the surface temperature of the system would be on the order of 38°C (100°F) on a 21°C (70°F) day. The greatest single loss occurred through the vacuum insulation followed by conduction through the cellular insulation at the rear (Stirling engine end) of the receiver/TES unit.

The problem of thermal loss while receiving energy from the sun is complicated by losses from the receiver. While in operation, in addition to the roughly 2 kWth lost through the insulation, a further 5 kWth or so would be lost by radiation from the receiver. These additional losses are accounted for by the estimated efficiency of the receiver.

g. System Thermal Performance. The thermal energy storage and heat transport system is designed to be able to provide sufficient energy for approximately 1.7-2.0 hours of Stirling engine operation at 52.5 kW. The TES is designed to act as a thermal flywheel, slowing down the rate of temperature changes at the Stirling engine in response to fluctuations in the quantity of energy impinging on the receiver. It also is designed to minimize the energy that would be lost by reradiation when cloud shadowing reduces the incoming radiation to near zero; this is accomplished by use of primary heat pipes in the heat receiver which will permit heat flow only from the receiver to the TES and not in the reverse direction.

The temperature profile is basically controlled in the TES system by the melting point of the thermal storage material, the power demanded from the TES capsules, and the thickness of the solidified salt on the capsule walls. The temperature at which power will be supplied to the Stirling engine will drop approximately 41°C (75°F) only when the last liquid salt is solidifying in the core of the TES capsules and, simultaneously, full power is being demanded from the TES. For moderate thermal power demands on the TES, or when a major part of the TES mterial is molten, only a very minor drop in Stirling engine temperature will occur. The effect of the thickness of the solidified layer on the temperature gradient required to extract given power is illustrated in Figure 3-7.

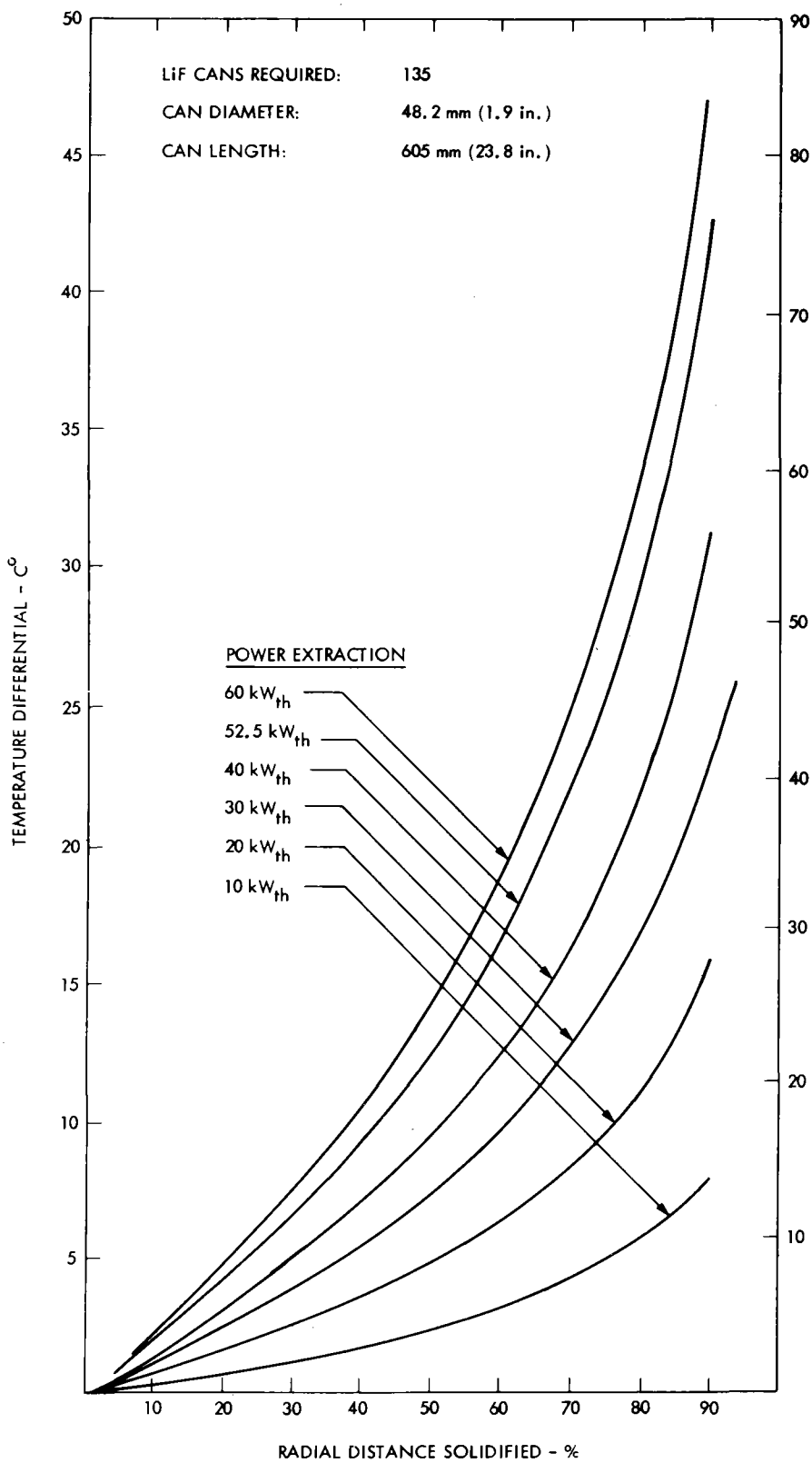


Figure 3-7. Temperature Drop Across the Solidified Salt Layer at Various Power Extraction Levels

Because of thermal resistance of the solidifying salt, the cooling curve expressed by the surface temperature of the container (and of the Stirling engine heat exchanger) will be represented by a modified rather than a classical solidification curve, as shown in Figure 3-8.

As an example of system operation, consider first the case where heat is supplied to the TES system when the salt is all in the solid state. As energy arrives on the surface of the TES can, the can reaches the melting temperature of the TES material and is briefly held there as the material immediately under the surface melts. The temperature then rises slightly since some temperature gradient is needed to drive heat through the liquid TES material to reach the liquid-solid interface.

Consider next the case where heat is extracted from the TES cans. As power is extracted from the TES cans, the can temperature drops progressively with time as the salt solidifies on a front along the inner circumference of the can. At a maximum power of 52.5 kW this temperature drop can be as much as 41°C (75°F); allowing another 5.5°C (10°F) of sensible heat in subcooling below complete solidification, this $\Delta T$ can be as high as 47°C (85°F). At lower power extraction rates a longer time is required to completely deplete the thermal storage latent heat and the $\Delta T$'s are relatively lower. For brief periods of cloud cover the liquid solidification front will be close to the can surface and the $\Delta T$'s under low or high power will be relatively minor. The system temperature profiles at the two extremes of power levels are given in Table 3-9 for the two salts under consideration.

In summary, the TES system will require some temperature gradient to thermally charge or discharge the system. However, the magnitude of the temperature gradient is dependent upon the energy transfer rate and the thickness of the solidified salt inside the TES can. Only during the final stages of TES thermal discharge at maximum power levels will the TES can temperature (and the Stirling engine temperature) drop as much as 41-47°C (75-85°F). This does not impose any significant efficiency loss on the Stirling engine. In most other modes of operation the TES can surface will operate at the TES temperature (or slightly above it, depending upon the heat flow into the TES material). Brief variations in heat receiver power will make only relatively minor changes in the TES can temperature and in the Stirling engine operating temperature.

## 4. Mechanical Design Description

a. Introduction. In order to develop a more promising initial conceptual design for the focus mounted system, layout drawings of various configurations and concepts were prepared. These drawings were then studied from the standpoint of operating performance, cost and weight. The most attractive design was then selected and called the basic design. As heat pipe and TES analytical studies progressed,

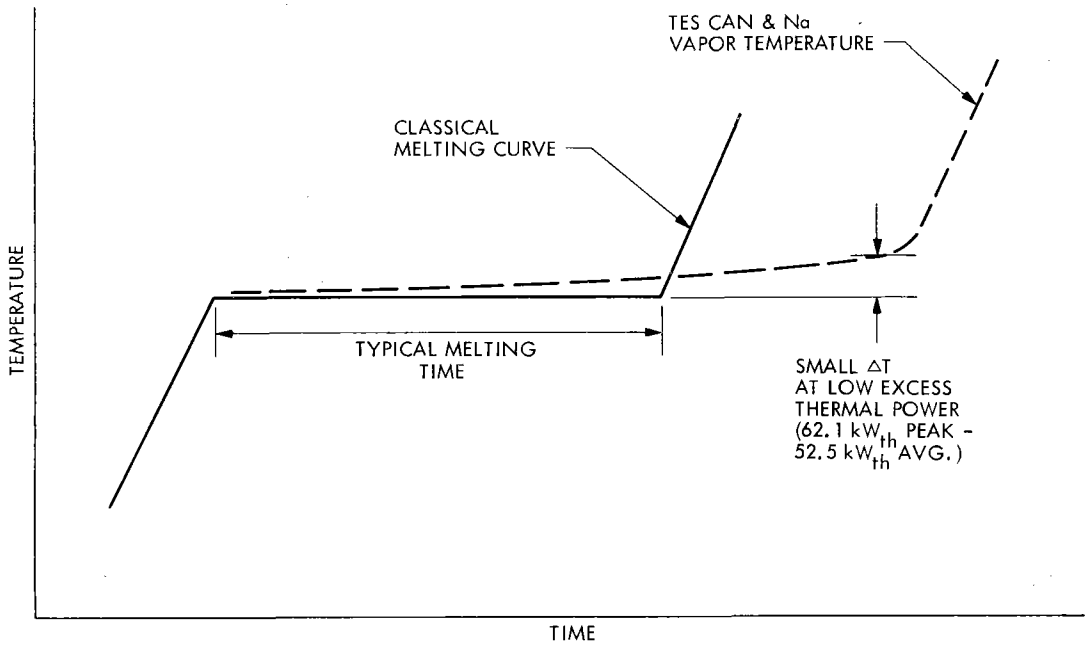


a) CHARGING TES SYSTEM

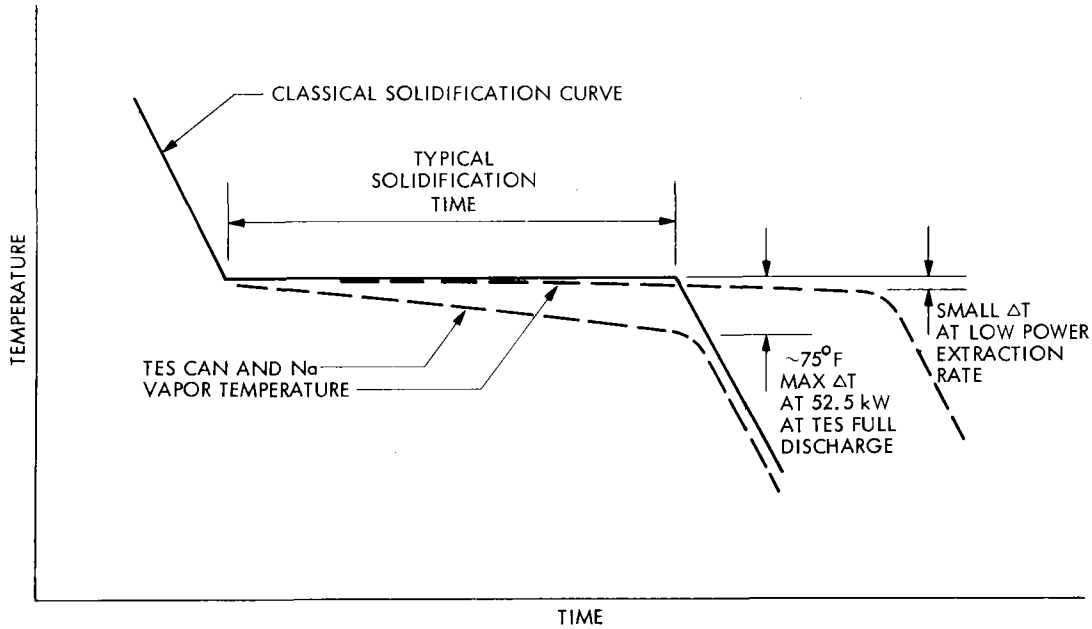


b) DISCHARGING TES SYSTEM

Figure 3-8. Suggested Temperatures in the Thermal Energy Storage Sodium Vapor Space (and at the Stirling Engine) During Charging and Discharging of the TES.

Table 3-9. Heat Storage and System Temperature Profiles

| Characteristic | Heat Storage Material | | | |
|---|---|---|---|---|
| | $NaF-MgF_2$ | | LiF | |
| Melting Point | 827°C (1520°F) | | 857°C (1575°F) | |
| TES Container Surface Temperature: | | | | |
| Maximum | 835°C (1535°F) | | 866°C (1590°F) | |
| Minimum | 779°C (1435°F) | | 810°C (1490°F) | |
| TES Weight | 550 kg (1212 lb) | | 550 kg (1212 lb) | |
| Can Size/Number | 5.84 cm (2.3 in.) D/97 | | 4.85 cm (1.9 in.) D/135 | |
| Can $\Delta t$, Maximum | 41.6°C (74.9°F) | | 40.3°C (72.5°F) | |
| Storage Time | 1.27 Hr | | 1.88 Hr | |
| | 55.5°C (100°F Range) | | 55.5°C (100°F Range) | |
| | Maximum | Minimum | Maximum | Minimum |
| Temperature Range, °C (°F) | | | | |
| Receiver Tube, OD | 852°C (1567°F) | 847°C (1557°F) | 883°C (1622°F) | 878°C (1612°F) |
| Condenser Tube, OD | 835°C (1535°F) | 779°C (1525°F) | 866°C (1590°F) | 860°C (1580°F) |
| TES Vapor Space | 835°C (1535°F) | 779°C (1435°F) | 860°C (1590°F) | 810°C (1490°F) |
| Stirling Engine HX Tube, OD | 835°C (1535°F) | 779°C (1435°F) | 860°C (1590°F) | 810°C (1490°F) |
| Stirling Working Fluid | 768°C (1415°F) | 713°C (1315°F) | 799°C (1470°F) | 743°C (1370°F) |

details of these components were added to the basic design drawing. An isometric drawing was prepared from the mechanical drawing and is shown as the Frontispiece to this report.

The basic design configuration places the heat receiver, thermal energy storage system and Stirling engine all on the same axis and is the most compact of the various concepts studied. Since the Stirling engine/generator is an integral part of the design, assumptions were made with regard to the type engine which might be utilized and primarily a method of attachment to the TES unit. If the Stirling engine cannot be designed in a configuration approximately as shown, major disadvantages in the basic design may result.

The major uncertainty in any of the designs studied is the ability of wicking to transport adequate sodium liquid to the condenser section of the heat pipes and outer surfaces of the heat storage containment capsules. At low sun elevations (the worst condition), the wicking must be capable of pumping sodium approximately 0.61 m (24 inches) high against the force of gravity. Before proceeding with more extensive design effort, experimental demonstration of the wicking concept in a configuration similar to the Basic Design would be highly desirable.

b. Basic Design. The basic design for the focus-mounted system will be broken down into four subsystems as follows:

(1) Primary Heat Exchanger or Heat Receiver.

(2) Thermal Energy Storage System or TES.

(3) Stirling Engine/Generator.

(4) System Mounting or Collector Mounting Ring.

A parts list for the entire focus-mounted system is shown in Table 3-10. The parts list provides a brief description, indicates the number required, specifies the presently selected material, and lists the material configuration and approximate dimensions.

c. Primary Heat Exchanger. The Primary Heat Exchanger consists of twenty-seven 25-mm (1-inch) diameter heat pipes located on a diameter slightly greater than the 0.26 -m (10.1-inch) diameter aperture. The tubes are flattened for approximately 0.51 m (20 in.) over their overall 0.74-m (29-in.) length. Prior to flattening, a 60-mesh tubular stainless steel wire screen would be inserted inside the tube and expanded along the entire length of the evaporator section. A manufacturing process for producing the tubular screen and expanding the screen inside

Table 3-10. Parts List for the Focal-Mounted System Basic Design

| Part No. | Description | No. Req'd | Material | Configuration | Size |
|---|---|---|---|---|---|
| 1 | Primary Heat Pipes | 27 | 310 s/s | Tube | 0.035" wall |
| 2 | Flat Plate Heat Pipe | | 310 s/s | Tube & Plate | 0.035" wall<br>1/8" plate |
| 3 | Wicking, Primary HP Evap. End | | 304 SS | 60 mesh<br>0.239 lb/ft$^2$ | 124 ft$^2$ |
| 4 | Wicking, Primary HP Cond. End | | 304 SS<br>0.0025" wire dia. | 60 mesh | 9.2 ft$^2$ |
| 5 | Flat Heat (Front of containment vessel) | | HA 188 | Forging | 1/4 to 1/2" thick |
| 6 | MIN-K Insulation | | MIN-K | Block | 0.0116 lb/in.$^3$ |
| 7 | Receiver Internal Wall | | 310 s/s | Sheet | 0.030" thick |
| 8 | Cordierite Front Ring | | Cordierite | Cast | 2" thick |
| 9 | Convection Shield | | 310 s/s | Sheet | 0.030" thick |
| 10 | Front Inner Vacuum Casing | | Inco 617 | Sheet | 1/8" thick |
| 11 | Front Outer Vacuum Casing | | C Steel | Plate | 3/16" thick |
| 12 | Bellows Guide Ring | | C Steel | Sheet | 3/16" thick |
| 13 | Bellows | | C Steel | Sheet | -- |
| 14 | Bellows Shroud | | C Steel | Sheet | 0.030" thick |
| 15 | Aft Outer Vacuum Casing | | C Steel | Sheet | 3/16" thick |
| 16 | TES Containment Cylinder | | Inco 617 | Sheet | 1/8" thick |
| 17 | Mounting Ring | | C Steel | Angle | 1/2" thick |
| 18 | Aft Inner Vacuum Casing | | Inco 617 | Sheet | 1/8" thick |
| 19 | Multifoil Radiation Insulation | | 304 SS | Foil | 0.0015" thick |
| 20 | Aft Flat Head | | HA-188 | Forging | 3/8" thick |
| 21 | Stirling Engine Support Cone | | C Steel | Plate | 1/4" thick |
| 22 | Stirling Engine | | -- | | -- |
| 23 | Sodium Fill Port | | 321 s/s | Tube | 0.035" thick wall |
| 24 | Expansion Bellows | | HA-188 | Sheet | -- |
| 25 | Stirling Engine Heat Ex. | | -- | Multiply | -- |

Table 3-10. Parts List for the Focal-Mounted System Basic Design (Continuation 1)

| Part No. | Description | No. Req'd | Material | Configuration | Size |
|---|---|---|---|---|---|
| 26 | Rear Capsule Support Plate | | HA-188 | Sheet | 1/8" thick |
| 27 | TES Capsule | 104 | 316 SS | Tube | 1.9" dia., 24" ln. 0.030" wall |
| 28 | TES Capsule | 36 | 316 SS | Tube | 1.9" dia., 15" ln. 0.030" wall |
| 29 | Aft Capsule Support Wicking | | 304 SS | 400 Mesh | 140 $ft^2$m 0.25" thick |
| 30 | Wick Containment Washers | | 304 SS | Sheet | N/I |
| 31 | Forward Capsule Support Wicking | | 304 SS | 400 Mesh | 399 $ft^2$, 0.25" thick |
| 33 | Forward Flat Heat Wicking | | 304 SS | 250 Mesh | 1102 $ft^2$ |
| 34 | TES Capsule Wicking | | 304 SS | 60 Mesh | 275 $ft^2$ |
| 35 | Front Capsule Support Mount | | Inco 617 | Bar | -- |
| 36 | Rear Capsule Support Mount | | Inco 617 | Bar | -- |
| 37 | Front Capsule Support Plate | | HA-188 | Plate | 1/4" thick |
| 38 | Lifting Eye | | C Steel | | |
| 39 | Capsule Assy. Tie Bolt and Sleeve | 4 | C Steel | Assembly Tools | |
| 40 | Lithium Fluoride | | LiF | Bulk | In TES Tubes |
| 41 | Insulation | | Fiberglas | Blanket | 12 $lb/ft^3$ |
| 42 | Wind Shield | | 310 s/s | Sheet | 0.030 |
| -- | Sodium, Primary HP | 0.675 lbs | Sodium | Liquid Metal | -- |
| -- | Sodium, Secondary HP | 12.5 lbs | Sodium | Liquid Metal | -- |

of the heat pipe must be developed. This wicking will ensure a uniform distribution of liquid sodium along the 0.51-m (20-inch) long evaporator section. The forward end of the heat pipe would then be welded closed. The aft end of the heat pipe would contain a small evacuation and fill tube (not indicated on the drawing). After cleaning the inside of the tube it would be evacuated and back-filled with a measured amount of sodium. The fill tube would then be pinched and seal-welded closed. The evacuation and filling process would be automated in a manner similar to that used in the mass production of fluroescent tubes or mercury vapor lamps.

The pressure inside the heat pipe will range from a vacuum at ambient conditions to approximately $1.03 \times 10^5$ Pascals (15 psia) at operating temperature, (see sodium vapor pressure vs. temperature curve in Figure 3- 9 ). At the operating temperature circumferential and longitudinal stress due to internal pressure will be nil. Stresses due to the long cantilever length of the pipes are approximately $2.76 \times 10^6$ Pascals (400 psi). Fatigue stresses due to vibration which might be improved by the Stirling engine cannot be analyzed at this time. The low stresses imposed on the heat pipes, therefore, allow considerable latitude in the selection of a material. Oxidation and sodium corrosion resistance will be the primary factors in material selection. A stainless steel, such as AISI Type 310 (or Type 321) has been indicated in the parts list.

The rear face of the cavity type heat receiver contains a single flat plate type heat pipe. Wicking will be attached to the internal faces via tack or spot welds. A 25-mm (1-inch) diameter tube is used for the condensing section. This unit would also be fabricated from AISI 310 or other stainless steel. A complete stress analysis of this heat pipe from the standpoint of bending moments applied to the 25-mm (1-inch) tube has not been performed. The flat-plate surfaces have been indicated as approximately 3-mm (0.125-inch) thick on the drawing. The thickness can probably be reduced.

The heat pipe cluster is surrounded by a can-type cavity inner-wall liner. This liner is supported at the rear by the heat pipes and at the front by the Cordierite* ring. It is free to expand thermally along its axis. AISI Type 310 stainless steel approximately 0.8-mm (0.030-inch) thick has been selected for the material because of its oxidation resistance.

The annulus between the cavity liner and the front inner vacuum casing is filled with low thermal conductivity insulation. The drawing indicates MIN-K 2000 insulation at a density of 320 $kg/m^3$ (20 $lbs/ft^3$). This material is a mixture of inorganic oxides with silica and titania being the most prevalent compounds. It can be provided in block or powdered form. Its thermal conductivity at a

*A low thermal expansion, thermal shock-resistant ceramic.

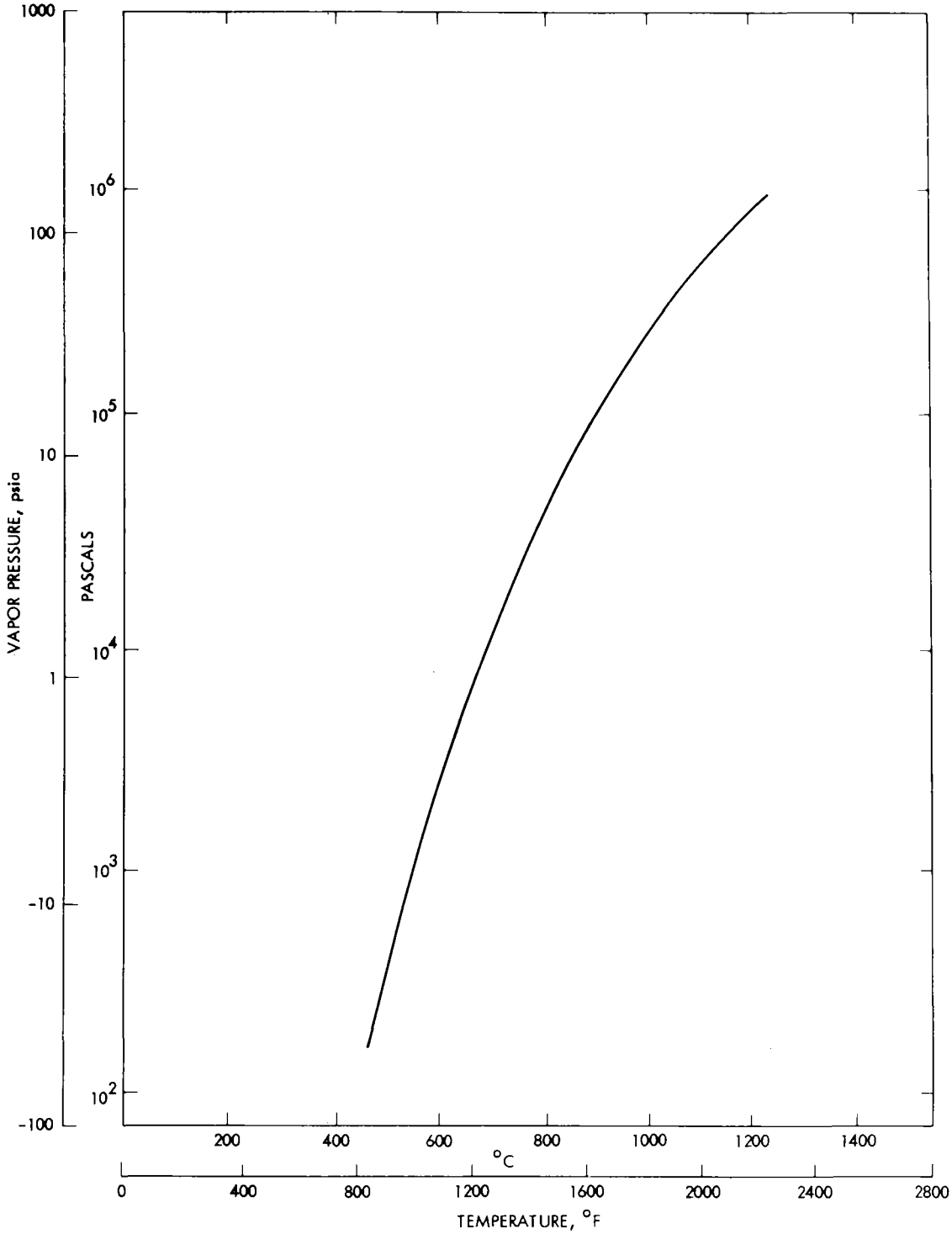


Figure 3-9. Sodium Vapor Pressure versus Temperature
(WADD TR 61-96)

mean temperature of 538°C (1000°F) in air is approximately 0.036-W/m°C (0.021 Btu/hr-ft°F). This material is very expensive compared to insulations such as Fiberfrax or Thermoflex; the latter, however, are not as good insulators. Since the outer vacuum insulation jacket extends the entire length of the cavity receiver, the need for MIN-K insulation is questionable and it is more likely that Fiberfrax or some cheaper material would actually be used. To prevent excessive heat losses from the TES containment vessel, MIN-K insulation in block form would be employed behind the flat plate heat pipe.

The front inner vacuum casing (PN 10) supports the Cordierite aperture ring and contains the heat receiver cavity insulation. The parts list indicates this material as INCO 617; however, as this shell extends further from the TES containment front head its temperature decreases. On the basis of design analyses, it appears stainless steel AISI Type 321 could be utilized at a point where this shell extends approximately 0.2 m (8 inches) forward of the TES front head. This would require a weld joint and the economics of a weld joint vs. extending the INCO 617 all the way forward to the front outer vacuum casing would be the determining factor.

The front outer vacuum jacket casing (PN 11) carries the heat receiver and a portion of the TES weight back to the mounting ring. An expansion bellows with guide ring compensates for thermal expansion between the inner and outer shells. Multifoil radiation insulation in the vacuum jacket reduces heat losses from the heat receiver and TES system to a minimal amount. It further provides a method of supporting the entire focus mounted system without allowing direct heat conduction paths from the TES system or other hot parts to the mounting ring. It also provides a secondary containment for a portion of the TES containment vessel (i.e., shell only).

d. Thermal Energy Storage System (TES). The TES system consists of a cylindrical containment vessel with flat front and rear heads. The heat-receiver heat pipes are welded in the forward head and the Stirling heat exchanger protrudes through the rear head. The Stirling engine cylinder is sealed to the rear head with an expansion bellows. One-hundred-and-forty LiF-filled tubular capsules supported by front and rear support plates are located in a hexagonal pattern inside the cylindrical shell. Capsules are approximately 51 mm (2.0 inches) in diameter, 30 of which are 0.38 m (15 inches) long and 104 of which are 0.61 m (24 inches) long. All surfaces are wicked as described previously. The front and rear capsule support plates contain holes into which the capsule support pins are inserted during assembly and holes for vapor passage. The interstitial spaces between capsules provides an axial path for sodium vapor to travel throughout the TES system.

The TES capsules and their front and rear support plates, along with wicking, would be assembled as a packaged core and then inserted into the containment vessel. Temporary tie-bolts would contain the capsule core during assembly. The capsule assembly is

supported from mounts welded to the inside of the containment cylindrical shell. Rotating the capsule assembly locks this unit into the containment cylindrical vessel. Thermal expansion of capsules relative to the containment shell is taken up by the rear capsule pins sliding in the rear support plate. The rear wicking is held in contact with the aft end of the capcules by washers welded to the rear capsule pins.

The TES front head sees little if any pressure differential at operating temperatures, and at ambient temperatures is subjected to a differential pressure of $1.0 \times 10^5$ Pascals (14.7 psi). Since the vapor pressure of sodium rises at a very slow rate with increasing temperature, and material allowable stress decreases with temperature at a faster rate, a plot of head wall thickness vs. temperature for INCO 617 and HA 188 was prepared (see Figure 3-10). These curves indicate the need, at at this point in the design study, for HA 188 if reasonable wall thicknesses are to be utilized in head construction. Pressure differentials were obtained from data on sodium-vapor pressure and material allowable stresses from Figure 3-11. Wall thickness calculations were based on formulas for Unstayed Flat Heads as found in Section VIII of the ASME Code. No effort was made to calculate ligament strengths (i.e., area between heat pipes); however, additional metal thicknes in this area will be necessary to keep stresses within the allowable value. A much more rigorous stress and thermal analysis of the head would be conducted in a detailed design phase. Oxidation and corrosion allowances would also be factored into calculations at this time. Although the design does not require ASME Code approval, due to the low operating pressure, Code design, fabrication and test procedures would be utilized wherever possible.

The cylindrical shell of the TES containment vessel sees no differential pressure at ambient conditions since it is surrounded by a vacuum jacket and a differential pressure of approximately $0.8 \times 10^5$ Pascals (12 psi) at maximum operating temperature. Using formulas for circumferential and longitudinal stress from Section VIII of the ASME Code and assuming a joint efficiency of 1.0, a wall thickness of approximately 2.5 mm (0.10 inch), utilizing INCO 617, is indicated. This does not include loads imposed by the TES capsule supports, bending mounts or vibrational loads imposed by the Stirling engine.

The rear head is exposed to the same pressures as the front head. The large opening for the Stirling engine heat exchanger will require adequate reinforcement as shown on the drawing. Like the front head and cylindrical shell, this structure will require a detailed thermal and stress analysis. The forward and rear heads are both depicted as welded assemblies on the drawing; however, a forging might actually be utilized in mass production.

The TES tubular capsules containing LiF are made of 0.76 mm (0.030 inch) thick Type 316 stainless steel. Similar size capsules have been manufactured from Cb-1Zr and tested for over 5000 thermal cycles for low earth orbit space power applications. The capability of using more economic materials must be established.

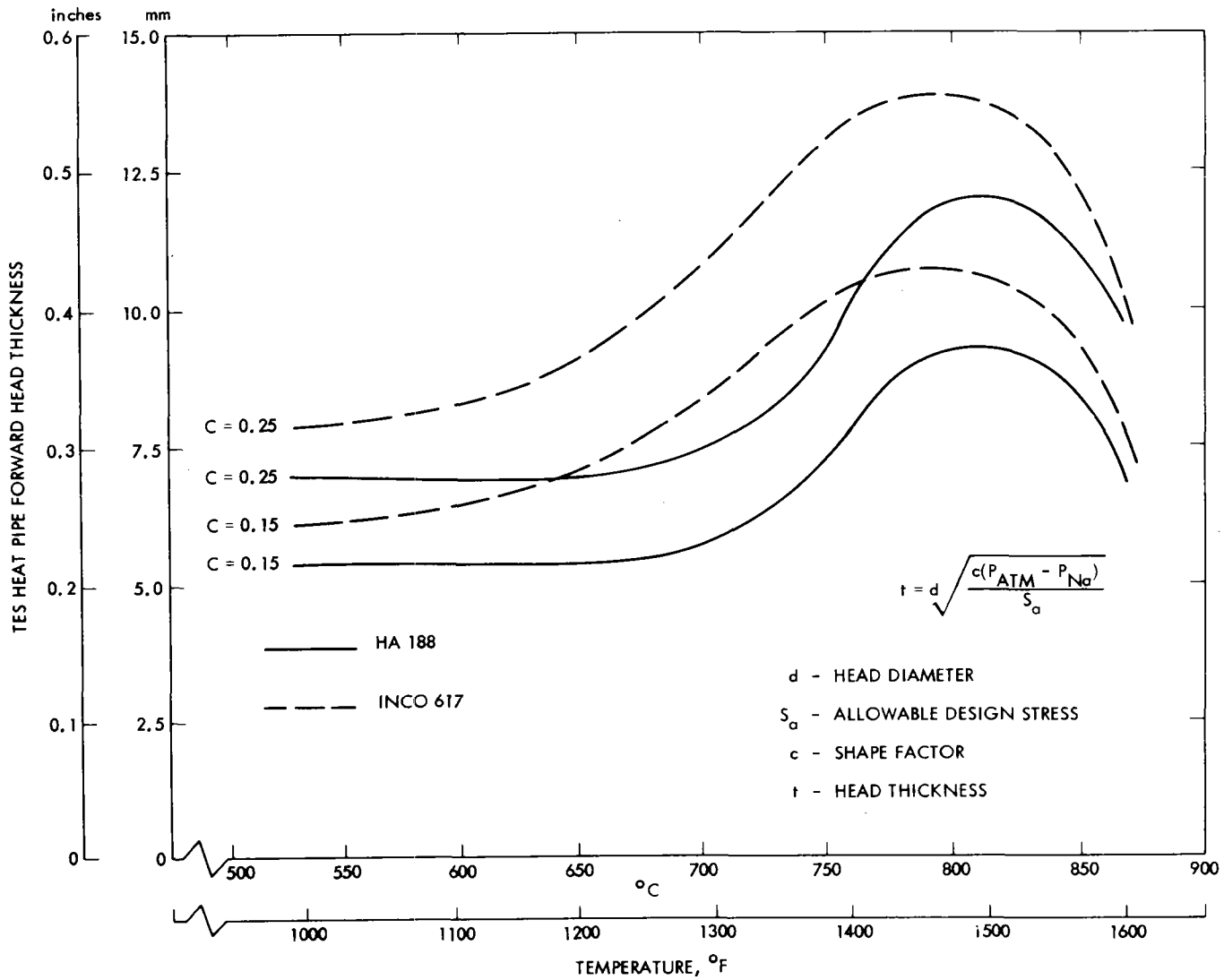


Figure 3-10. Thickness Required for TES Heat Pipe Forward Head vs Operating Temperature

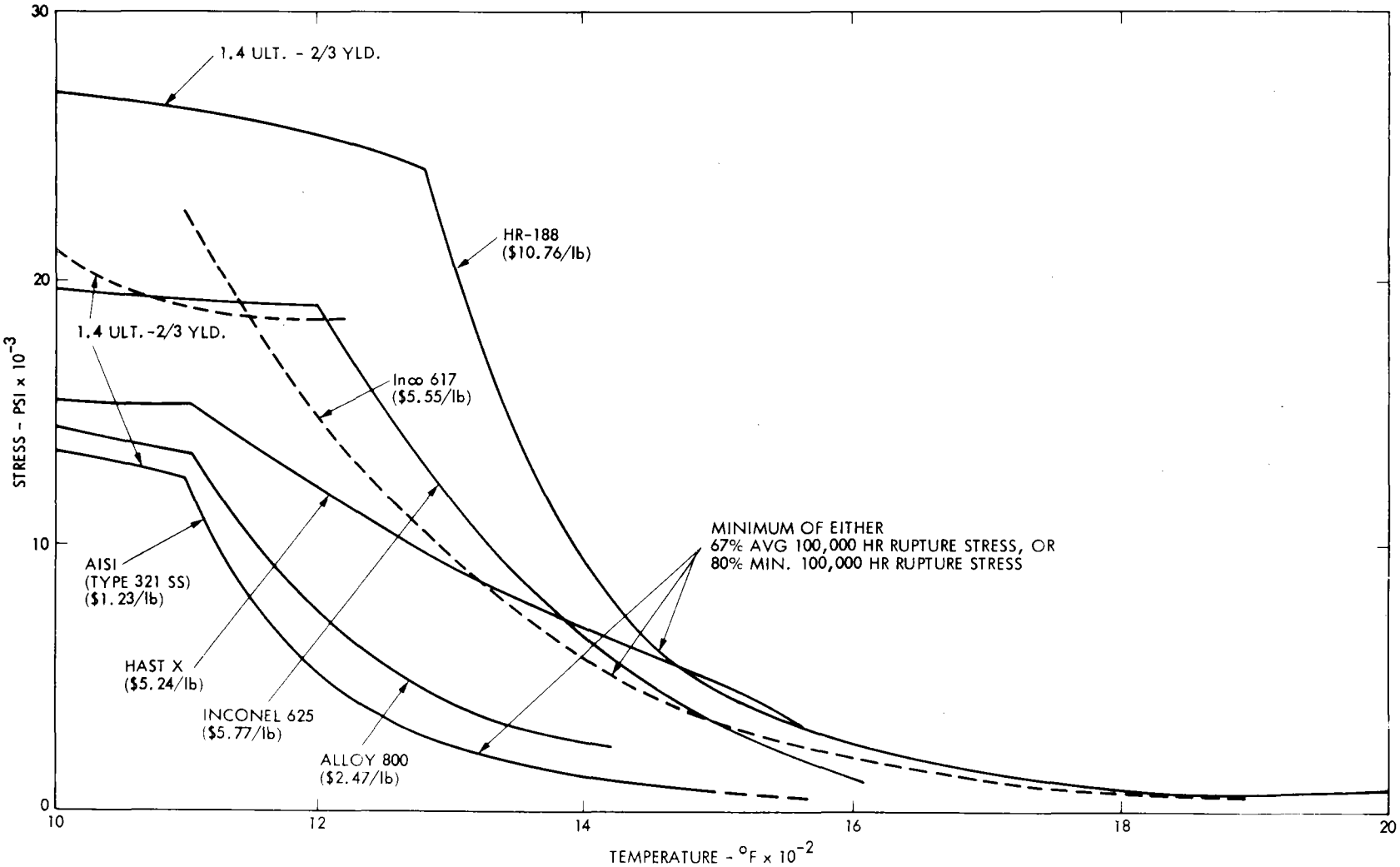


Figure 3-11. Allowable Design Stresses (ASME Design Criteria)

The front capsule support plate carries the entire TES capsule load of about 454 kg (1000 lbs) at high sun angles. This load is transferred to the TES system containment shell through the locking supports. Its thickness is indicated as 6.4 mm (0.25 inch). A simple, flat, circular plate uniformly loaded with edge supports was assumed in calculating the plate thickness. HA 188 material was selected to keep weight to a minimum. Capsule front support pines are welded to this plate so that thermal expansion is in the aft direction. When the collector is in the stored position the TES capsule weight is also taken by the front support plate.

5. Mass and Cost Analysis

a. Weight and Cost Analysis Objectives. A preliminary mass and cost analysis was made of the reference designs described above. There were several reasons for going into great detail at this stage of what is really only a first-cut conceptual design.

First, it was necessary to find out how close to the focal mount mass limit this design was so that revised designs would meet technical objectives.

Second, it is recognized that this component must be a very low cost part in production quantities. Thus, it was of the greatest importance to see what this early design might cost so that expensive features and materials could be eliminated or reduced in future design iterations.

Third, by identifying parts by material, mass, function, and cost, it becomes easier to assess the practicality of the design concept.

b. Mass Summary. Table 3-11 shows a summary of the detailed mass breakdown. The TES material represents 28% of the total weight, the largest single item. However, it is clear that any weight restrictions will have to take place in the areas of the structure and the insulation.

c. Cost Analysis. Preliminary cost analysis was performed on the reference designs. The goal was to identify those areas which would require design effort in order to reach a minimum cost in quantity production. For 16.5 kWe, a first cut goal of $6600 was set for the unit. The first cost calculations showed $15000 for materials alone.

This unit made extensive use of HA-188 alloy which costs approximately $24/kg, used LiF as the TES material, at about $7/kg, and

Table 3-11. Summary Mass Table

| Item | Mass - kg | % of Total Weight |
|---|---|---|
| Receiver | 210 | 16 |
| TES Area Structured | 181 | 14 |
| TES Salt | 359 | 28 |
| TES Cans | 79 | 6 |
| TES Area Wicking and Sodium | 86 | 7 |
| Multifoil Insulation | 201 | 16 |
| Outside Steel Shell | 157 | 12 |
| TOTAL | 1273 | |
| Stirling Engine (Estimate) | 147 | |
| Generator (Estimate) | 68 | |
| TOTAL | 1488 | |

high-cost insulation systems. A calculation was made of the following three substitutions:

(1) Substituting stainless steel for HA-188 saves $4500. This could be done either by derating the system or by innovative design changes.

(2) Substituting cheaper insulation for the rather expensive MIN-K would save $2300 with little change in performance. A redesign of the outer multi-layer vacuum insulation would save even more.

(3) The use of $NaF-MgF_2$ eutectic in place of LiF could save $2000 and may be the preferred TES material in any case.

The net effect of these three changes alone brings the cost of materials down to $6200. It is anticipated that additional improvement will be made during future design phases.

When mass production quantities are built, say over 100,000 units per year (equivalent to only two large coal-fired plants), the labor costs are a very low fraction of the total cost. Hence, it is reasonable to believe that costs of well under $400/kWe are attainable.

## REFERENCES


3-1. Chi, S.W., Heat Pipe Theory and Practice: A Source Book, McGraw-Hill Book Company, 1976.

3-2. Dunn, P.D., and Reay, D.A., Heat Pipes, 2nd Edition, Pergann Press, 1976.

3-3. Skrabek, E.A., and Bienert, W.B., "Heat Pipe Design Handbook," Vol. I and II, Contract No. NAS9-11927, August 1972.

3-4. Corman, J.C., "Engineering Design of Heat Pipes," GE Technical Information Series No. 71-C-271, December 1971.

3-5. Harbaugh, W.E., "Applying Heat Pipes to Thermal Problems," Heating, Piping, and Air-Conditioning, October 1970.

3-6. Harbaugh, W.E., "Liquid Metal Heat Pipes," lecture notes for presentation at weekend workshop in Thermal Contact Resistance and Heat Pipes, University of Tennessee Space Institute, Tullahane, Tennessee, April 24-25, 1971.

3-7. Winter, E.R.F., and Barsh, W.O., "The Heat Pipe," Advances in Heat Transfer, Vol. 7, 1971, Academic Press, New York.

# SECTION III

# POWER CONVERSION

## B. STIRLING SOLAR ENGINE

## B. POWER CONVERSION - STIRLING SOLAR ENGINE

A key task of the Advanced Systems Development Project is the design of solar-specific engines with >40% efficiency in both an advanced technology version (1985 and beyond), and a near-term test-bed version The development of the solar Stirling engine will benefit from Stirling engine development in other areas -- most notably, the automotive one.

Both kinematic and free-piston Stirling are candidates for solar energy conversion systems. The kinematic Stirling engine transmits power through connecting rods or other linkages to a rotating alternator. In the free piston engine, the power piston connects directly to a linear alternator. But the heat input components would be almost identical for both types of engines. The kinematic Stirling engine has a much longer and more extensive development history than the free piston engine whose conception is of recent origin. After thousands of hours of engine operating in laboratories in the U.S., Holland and Sweden, the kinematic Stirling has well defined problem areas: shaft seal life is limited; improvements in heat transfer and fluid flow are required for the achievement of the engine's efficiency potential; and more cost effective materials and production methods must be identified.

The free piston Stirling presents a difficult design problem because of the oscillation of 2 separate masses actuated by interdependent spring systems. However, because there are no mechanical losses between the piston and the alternator a 20% gain in efficiency over the kinematic Stirling might be achievable. No shaft seals are required because the alternator is housed within the engine. The free piston Stirling represents a high development risk. Also, linear alternators are only in the early stages of development, and potential problems are not fully known.

### 1. Development Plan

The development plan calls for identical 6-7 month conceptual programs for both the free piston and the kinematic Stirling engine. Each program is divided into three main tasks: (1) the generation of several advanced technology engine concepts; (2) a fabrication and economic assessment of one of those concepts; and (3) the conceptual design of a test bed engine. Under a fourth task which will be active throughout the program, the engine system interface will be addressed. More detailed task descriptions are given below. The schedule of work is shown in Figure 3-12.

a. <u>Task I - Advanced Configuration Definition and Parametric Analysis</u>. Under Task I, advanced engine concepts will be generated. The meaning of 'advanced' is that the concepts will include technology which is not ready to incorporate in an engine prototype today -- but which can reasonably be expected to become mature by mid-1980. Heat input concepts for remote, as well as closely coupled engine-receiver systems, are being considered. After an initial screening exercise a

parametric performance analysis will be carried out for three of the most attractive configurations - looking at a heat and coolant temperature range and part load operation. The basis for the analysis is the energy input derived from daily profiles of the West Associates Lancaster, CA, Insolation Study. A single most promising engine configuration and heat input concept will emerge from this task effort.

b. Task II - Implementation Assessment. Under this task, an assessment of the selected advanced engine concepts will be made with respect to the technology status of critical components, the producibility and cost, in various quantities up to 500,000 units, durability and failure modes; service requirements and power growth potential.

c. Task III - Conceptual Design of a Test Bed Engine. Under this task, the advanced engine configuration concept selected under Task I will be translated into a conceptual design of a near term (1981) test bed engine with ≥40% efficiency. This, of course, means that advanced technology components will have to be replaced with components which can be installed with confidence in a 1981 Stirling engine. Design layouts, engineering specifications based on the exercise of the appropriate engine optimization codes will result from this task. Because this design will serve as the basis for the detail 15 kW Solar Stirling engine to be executed in the follow-on program, the design will include an auxiliary heat input source for engine checkout prior to its mating with the solar receiver/heat pipe.

d. Task IV - Engine-System Interface Requirements. The designs of engine and the solar receiver are significantly interdependent. In close coupled systems, the engine heater tubes may be buried in the receiver. Other areas of interdependence are the insolation profile and the control modes. This task was specifically set aside for all work requirements which require close liaison and two way feed back between the engine and the system designs. All interface requirements are being channeled through the NASA project manager.

It is anticipated that at the end of this program phase, a reasonably clear choice will be available with respect to a single configuration Stirling engine development - either kinematic or free piston.

e. Current Technical Status. In response to the request for proposals issued in March 1978, proposals were received from three companies.

As a result of the technical and business evaluation, MTI was selected as the contractor for the combined free piston - kinematic Stirling engine study program. For the conceptual design phase, MTI has several subcontractors: United Stirling, Sunpower, Minneapolis

Honeywell, Dynatherm and Masco. United Stirling will be working on kinematic engine concepts; Sunpower will assist in the free piston computer programs; Honeywell will contribute heat receiver concepts; Dynatherm will bring in heat transport concepts and MASCO will perform production and economic studies.

The contract was initiated on August 29, 1978 and is now in its first task: Conceptual design of a 15 kW engine which incorporates technology which can be predicted to be mature (available for a pre-prototype production engine) by 1985.

A detailed schedule for the program is shown in Figure 3-12.

The initial work consisted of generation and screening of engine configurations concepts and heat input concepts. The latter include receiver and heat transport configurations, since the engine heater must be designed to receive a uniform flux density on its external surfaces so as to provide uniform heating to all internal flow passages.

In September the decision was made to consider only heat input to the engine via a heat pipe. This was believed to be the best solution for most uniform heating, and also provides more freedom to the cavity designer for accepting small flux dual distributions in the receiver.

The free piston engine configurations are being generated by MTI and will be subjected to parametric analysis. The kinematic engine configurations are being generated by United Stirling.

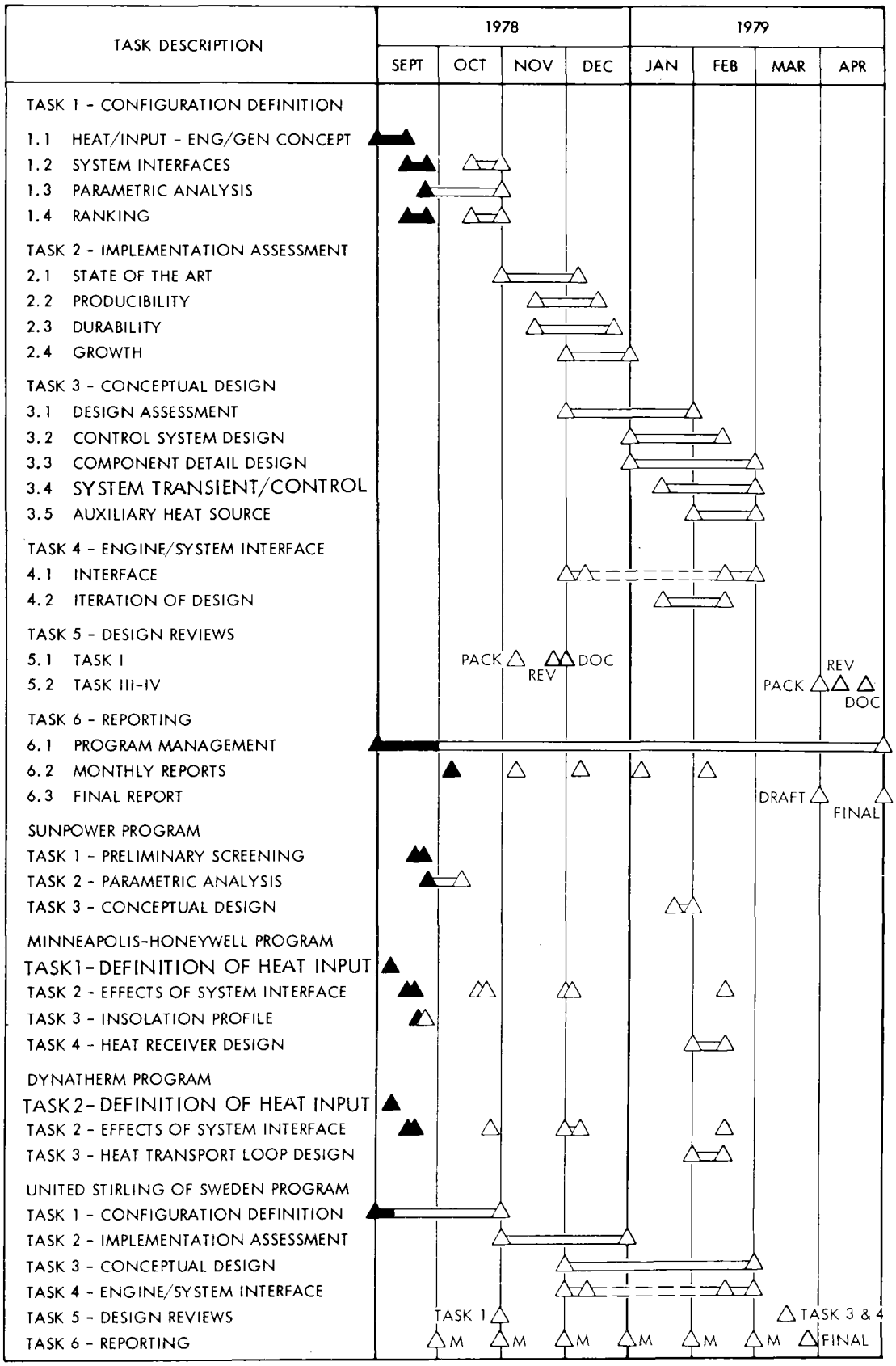


Figure 3-12. 15kW Combined Solar Stirling Engine Program

# SECTION IV

# POWER PROCESSING, POWER MANAGEMENT AND UTILITY INTERFACE

## SECTION IV

## POWER PROCESSING, POWER MANAGEMENT, AND UTILITY INTERFACE

### A. INTRODUCTION

There are many methods of solar thermal generation system implementation. Various system concepts and implementations were considered and the results of two attractive candidate systems with proven technology and performance history are discussed and analyzed here. Each system has a collector-receiver, short-time thermal storage and a Stirling engine.

This study defines a system for interfacing a dispersed solar thermal electric power generating plant with a public utility, evaluates the impact of a reasonable site plant on its basic units and defines and analyses various aspects of the following:

(1) power processing

(2) power management

(3) utility interface

The continuous variation of radiant solar energy during a day or a season places demands on solar electric generation processes which are unique when compared to conventional electric generating systems where available input energy is essentially constant. Fortunately, there is a good degree of coincidence and direct correlation between the daily solar energy profile and the electric system load curve. However, in order to be an available source of electric power, a solar generation system must possess energy storage systems capable of transmitting power to the utility grid or the load center during periods of little or no available solar energy.

In this study, three important assumptions are made about maximizing the efficiency and reliability of solar electric generation. These are as follows:

(1) All the solar energy that is collected is utilized in generating electrical power. The utility grid is an infinitely large sink capable of accepting any power generated. No dumping of energy is allowed.

(2) The solar electric generating system will have a back-up battery system. During periods of high insolation, the battery system will be charged and only generators will supply power to the grid. During period of low insolation, both generators and the battery system will supply power

to the grid. During periods of no insolation, only the battery system will supply power, at a reduced level, to the grid.

(3) The battery system will be charged with energy from the solar insolation input and not from the utility-line power. This assumption is made in order to compare plants with significant thermal storage (Ref. 4-1) and those with significant battery storage (Refs. 4-2, 4-3). In the future, and during actual plant operation, it may be desirable to charge the battery from the utility during off-peak hours.

## B. SYSTEM DEFINITION

The collection and distribution of electrical power from many dispersed electrical generation units is a complicated and challenging undertaking composed of the following three distinct areas:

(1) Power Processing

(2) Power Management

(3) Utility Interface

The first area involves the collection, inversion and conversion, routing, protection, synchronization, efficiencies, power distribution and losses, and various topics related to establishing a mechanism to transfer electric power.

The second area is analogous to a supervisory control system, where someone, or some automatic system, at the utility dispatch center, decides which element of the system (e.g., a certain generator) should be used to generate, transmit, and distribute power, based on the load demands and the available power at that particular time. It is within this area that the stability of the system is considered, and efficient and economical operation of the system is ensured. This area also includes the control and management of power.

The third area relates to the control, protection, synchronization equipment, and the operating procedure necessary for the transfer or isolation of power flow from the generator or the storage system to the utility.

### 1. Objectives

Generating a significant amount of power suitable for transmission over utility grids or for feeding reasonable size load centers requires

parallel operation of a large number of 15 kWe basic solar electric generation units (Refs. 4-4, 4-5). Such a large number of units operating in parallel imposes unique constraints on instrumentation, and control. The extent of these constraints, in general, depends on the size of the plant. Therefore, the impact of a generation concept for a basic input unit on a larger size plant must be evaluated completely before the generation concept is finally selected for basic units. A preferred plant design will determine the preferred generation concept for its units.

The overall control objective of the plant is achieved through a digital control system. The control system can be envisioned as a block which has connections and interfaces with all the other blocks of the solar generation unit. This system is capable of receiving commands from and sending status information to a control center (i.e., it enables the operation of the system as a part of a much larger system). The main purposes of the controller are to:

(1) receive monitoring information from the various system elements (i.e., blocks)

(2) implement the various control functions (e.g., voltage regulation, current limiting, parallel operation, operating strategies, start and stop procedures, etc.)

(3) send control commands to appropriate blocks

It is envisioned that the controller will be a micro-processor based digital controller with appropriate input/output, memory, and processing capabilities. Software development will be needed, but due to the similarities between a large number of units, the per unit cost of software development can be minimized.

Besides studying generation concepts and associated control requirements, plant efficiency and reliability of alternative systems will also be considered. The efficiency of a system with stored energy is defined by the ratio of total energy output of the system to the total energy input of the system. The total energy output takes into account the energy supplied from the energy storage system. The system efficiency, therefore, is the energy efficiency.

The effective load carrying capability is a direct measure of a generating unit's ability to contribute to overall system reliability. In general, the effective load carrying capability of the system is dependent on several factors. These are:

(1) Plant design and tracking capability

(2) Plant location and solar insolation conditions

(3) Utility load profile

(4) Forced outage rate of the equipment

(5) Storage

A solar electric generating system to be integrated into a utility system should have the same degree of reliability as other types of generating systems feeding the grid. Under normal operating conditions, non-solar generating systems have the capability of supplying a required amount of power at all times under any weather condition. A solar generating system will not inherently have this capability because of varying nature of solar energy input during a day or a season. In order to increase the availability factor of solar plants, an energy storage system (Ref. 4-6) should be incorporated. A battery system, energized with solar energy during periods of higher insolation, will be able to feed utility systems at a reduced power level during periods of low or no insolation.

## 2. Problem Definition

This section defines the problems addressed in this study. The input-output specification for a 15 kWe unit is detailed for a power requirement of 15 kWe for power factors from 0.8 to unity and a storage requirement of five hours for power supply at a load factor of 0.55. The problems discussed are the following:

(1) Configuration and analysis of a 15 kWe generating unit and a 10 MWe plant with conventional AC generation and AC link.

(2) Configuration and analysis of a 15 kWe generating unit and a 10 MWe plant with conventional AC generation and DC link.

(3) Determination of technical and economic impacts of a 10 MWe plant on its basic unit and vice versa, by analyzing the following aspects of both generation schemes:

   (a) Efficiency

   (b) Plant Layout

   (c) Advantages and Disadvantages

   (d) Cost

(4) Determination of storage power requirements for basic units and 10 MWe plants.

3. Assumptions

The concentrator and receiver block collects all the sun energy that is available to the system. A thermal storage and transport system is used to provide a partially smoothed heat input to the heat engine (Ref. 4-1). The engine converts the heat input into mechanical action. The heat engine powers a generator. Waveform harmonic content reduction, system and line protection, as well as synchronization blocks are also provided. Various assumptions are made with respect to the above. These are as follows:

(1) An average solar insolation of 845 $W/m^2$ is incident on each concentrator.

(2) This average insolation encompasses both summer and winter months.

(3) All the solar energy that is collected is utilized, i.e., no dumping of energy is permitted. The grid is an infinitely large sink capable of accepting any power generated.

(4) The Stirling engine temperature is kept constant.

(5) The battery is charged by generators and not by the utility line.

(6) The battery storage system will be able to supply power to the load for a period of $t_2$ = 5 hours.

(7) Six percent of power generated is allowed for auxiliary power losses for operation of pumps in thermal storage system, control electronics, and instrumentation. Two percent of plant generated power is allowed for distribution losses.

A graphic interpretation of summer solstice presented previously in Figure 2-3 gives an average time of 13.7 hours over which insolation of 845 $W/m^2$ is available for six summer months. A similar figure for winter solstice is found to be 9.0 hours. Over the year this average time, $t_1$ is found to be 11.4 hours for an average insolation of 845 $W/m^2$ throughout the year without cloud cover.*

Several operational control modes are possible with Stirling engines (Ref. 4-7). These relate to operational speed, temperature, and pressure. All these various operational modes have distinctive applicability to the system studied.

*However cloud cover reduces this value to 9.17 hrs at 845 $W/m^2$ for a yearly average.

4. System Output Specifications[1]

(1) Power Output Capacity: The solar generation unit shall have an output capacity of 15 kWe with a power factor of 0.8 to 1.0. The unit shall be able to deliver 8.25 kWe (55% of 15 kWe) whenever the unit is operated on the battery-inverter system.

(2) Storage: Storage shall be at a level to allow five hours of operation at an output of 8.25 kWe (55% of 15 kWe).

(3) Output Voltage: Output voltage shall be either 208 VAC or 460 VAC 3Ø.

(4) Output Waveform: Output waveform shall be sine wave at nominal 60 Hz, and distortion not exceeding 6%.

(5) Output Frequency: The output frequency shall be:

(a) 60 ± 0.5 Hz for stand-alone operation.

(b) Capable of locking with the utility grid frequency, when the system is connected to the utility grid. Output frequency stability will be equal to the utility grid frequency stability.

(6) Protection: The unit shall be short-circuit proof. The unit to be protected for excessive reverse power flow, for over-current and over-voltage, as well as under-voltage. Also, the utility grid shall be protected from adverse effects whenever appropriate.

(7) Overload Operation: The system shall be capable of operating at:

(a) 125% capacity for 15 minutes

(b) 150% capacity for 10 seconds

(c) 200% capacity for 0.1 second.

(8) Stable Operation: The system shall have stable operation over the normal operating range, as well as emergency conditions (TBD, e.g., sudden loss of load).

(9) Integration Potential: The generation unit shall be capable of integrating with a large number of similar units to form a much larger generation system. The integration capability shall include, but not necessarily be limited to, synchronizing functions.

---

1. For a 10 MWe system, output performance characteristics will differ.

(10) Accessories: Appropriate accessories for system status, monitoring and recording shall be provided.

## C. POWER PROCESSING (15 kWe)

### 1. Introduction

A 15 kWe solar generation unit consists of the following elements: a concentrator and receiver, a thermal storage system, a heat engine, an electric generator, battery storage, power processing and protection and synchronization system, as well as a control system that oversees the operation of the unit. Each element can be viewed as a block.

There are several ways of interconnecting these blocks to form an operating system. There are two basic generating approaches: AC generation and DC generation. In addition, there are variations of these generating approaches. In this section, attention is focused on five possibilities that are attractive. These are as follows:

(1) DC Generation/DC Link

(2) Conventional AC Generation/DC Link

(3) Conventional AC Generation/AC Link

(4) Special AC Generation/AC Link (Field-Modulated Generators)

(5) Regenerative Battery Charger

In the development of all these cases, it has been assumed that it is desirable to collect and utilize all the sun energy possible through the selected collector. Thus, the energy input to the system is not actively controlled.

Furthermore, based on how the system is configured and how the received energy is managed, there may be certain impact on the selection of batteries, generators, inverters, system control, etc. This section will also address these considerations.

### 2. Various Generation Unit Concepts

Several alternative conceptual block diagrams are developed here. Each of these has its own advantages and disadvantages. Before viable concepts can be selected, a detailed investigation into each concept may be appropriate.

a. Case 1: DC Generation/DC Link. In this case, a DC generator is used to generate DC power directly, which in turn is used for charging the battery system, as well as feeding into a DC/AC inverter to generate AC. The block diagram for this case is shown in Figure 4-1.

to generate AC. The block diagram for this case is shown in Figure 4-1. The charging of the battery is controlled by regulating the voltage output of the DC generator. The latter, in turn, is controlled by adjusting the generator field current. The level of AC output voltage is varied by controlling the DC/AC inverter unit. Depending on whether the output shaft speed of the heat engine can be kept constant or not, two operational modes of the DC generator are possible. If the output shaft speed of the engine is kept constant (e.g., at 1800 $\pm$ 0.5% RMP), the DC generator will be operated at essentially constant speed. If the engine output shaft speed is allowed to vary, the generator will not be operated at a constant speed. This will have impacts on generator size and makes the voltage regulation more complicated. Furthermore, the efficiency of the generator will be lower.

Regulation of the frequency and the voltage to the line is achieved through control actions in the DC/AC inverter.

The power stored in the battery may be transferred to the line by passing it through the DC/AC inverter.

b. Case 2: Conventional AC Generation/DC Link. This case is similar to Case 1 except rather than a DC generator, a conventional

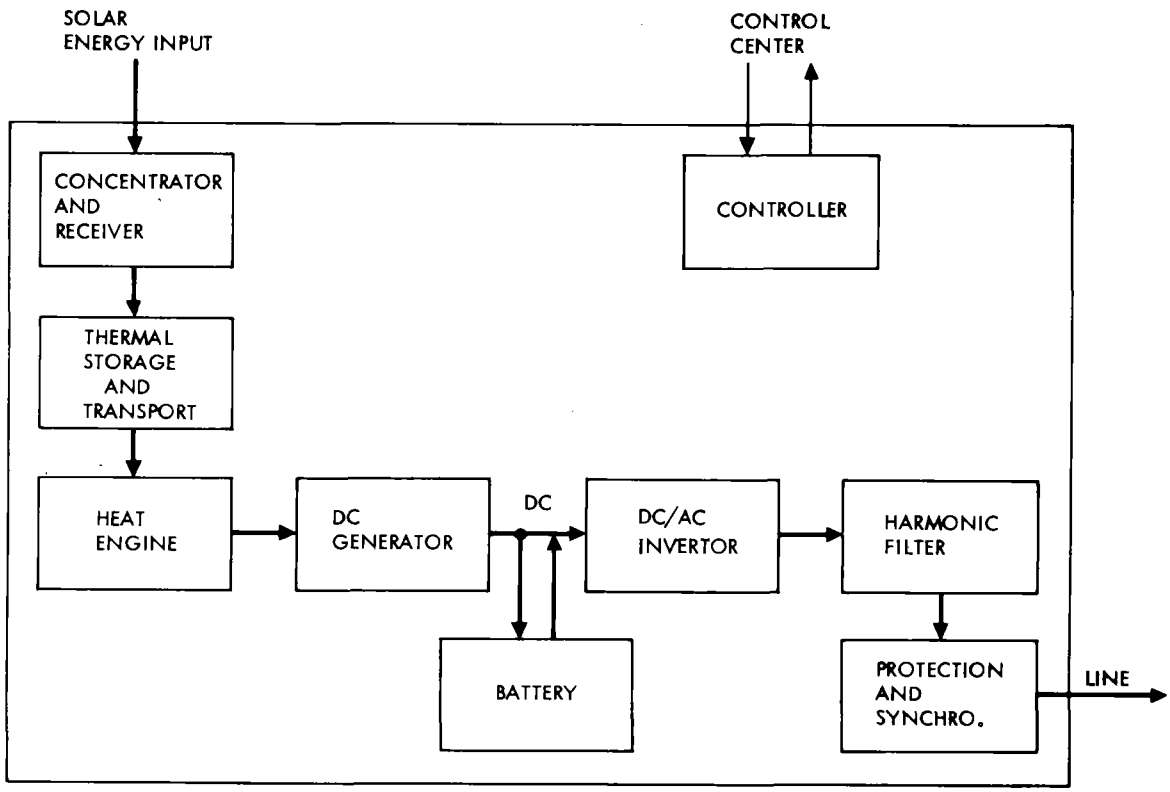


Figure 4-1. Conceptual Block Diagram for a Solar Generation Unit
Case 1: DC Generation/DC Link

AC generator and rectifiers are used. Thus, the undesirable aspects of the brushes in DC generators are avoided, yet DC voltage is developed. The block diagram for this case is shown in Figure 4-2.

c. Case 3: Conventional AC Generation/AC Link. In this case the generator selected is a conventional AC generator. The generator is run at constant speed (e.g., 1800 ± 0.5% RPM), and a portion of the output of the generator, after being filtered for undesirable harmonics, is fed into the AC line. The remaining portion of the output power of the generator is rectified and controlled in the inverter/converter unit to generate DC voltage to charge the battery. Conversely, when the power stored in the battery is needed, it can be transferred to the line by passing it through the inverter/converter unit.

The required frequency regulation must be achieved by regulating the shaft input speed to the generator, i.e., by regulating the output shaft speed of the heat engine. An alternate possibility is to use a squirrel cage generator and allow the generator to frequency lock to the utility. This system will allow paralleling of multiple systems.

The block diagram for this case is shown in Figure 4-3.

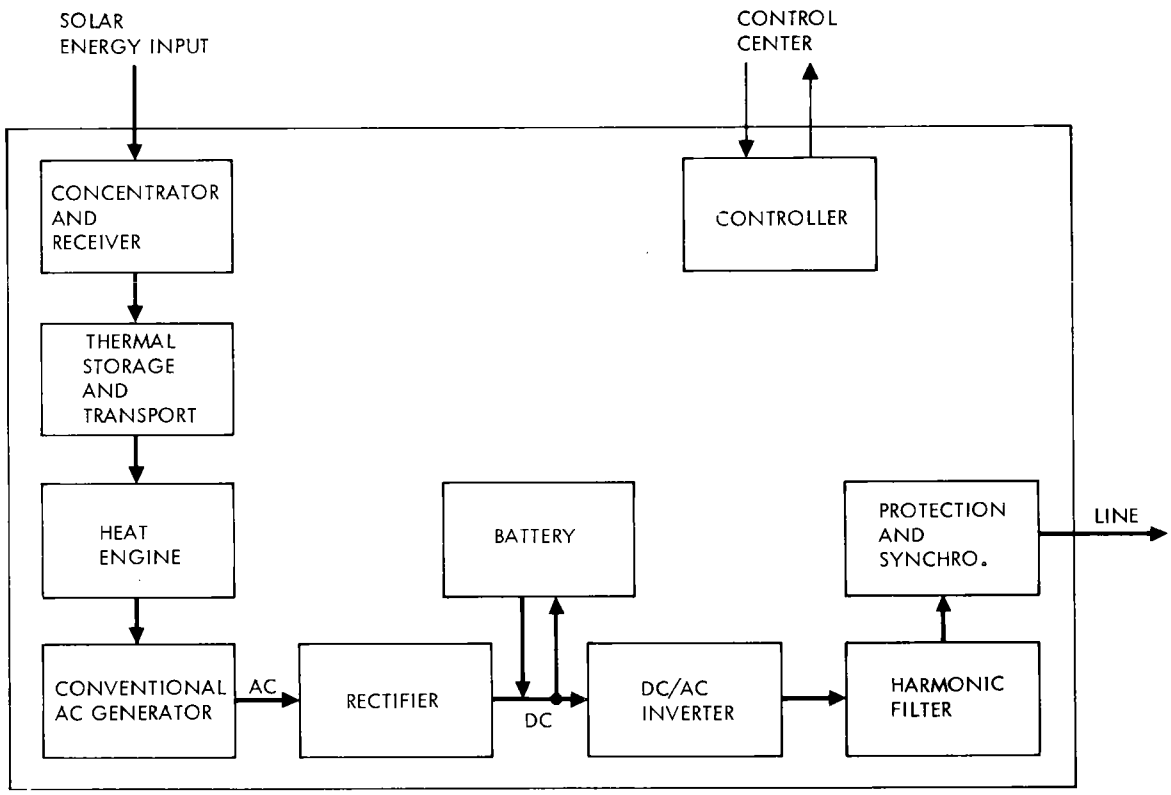


Figure 4-2. Conceptual Block Diagram for a Solar Generation Unit
Case 2: Conventional AC Generation/DC Link

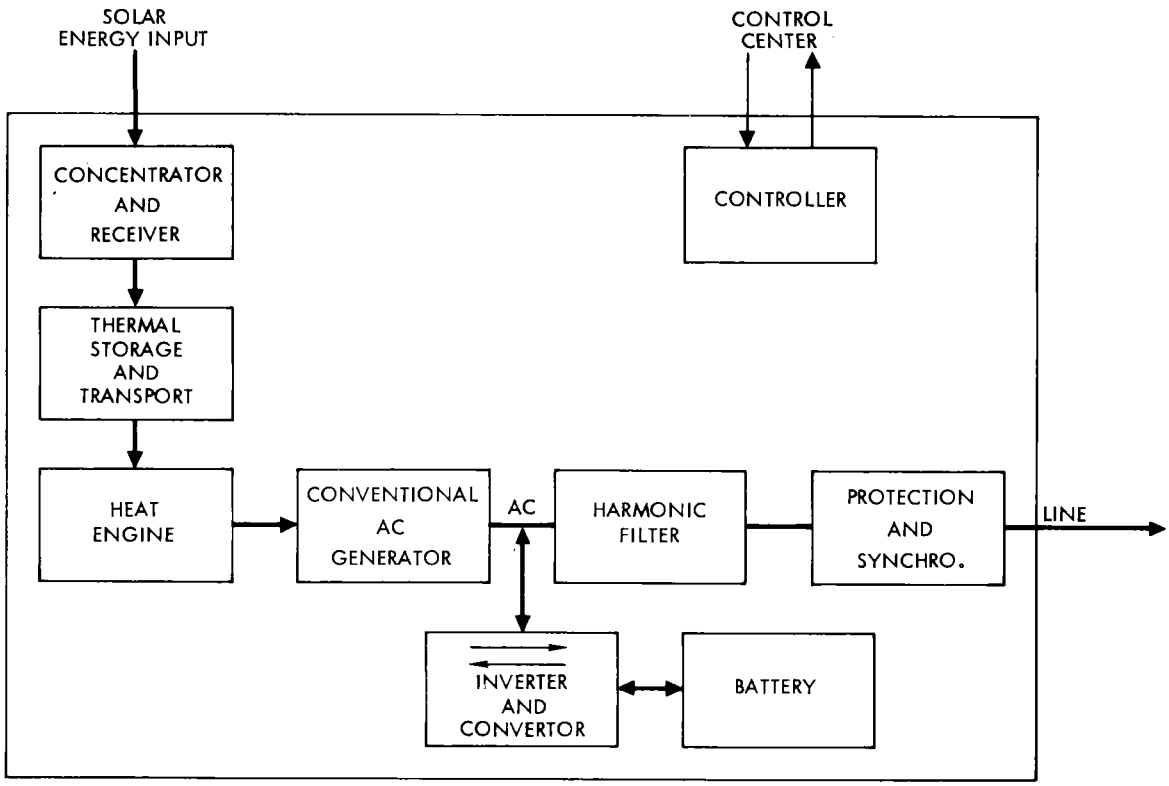


Figure 4-3. Conceptual Block Diagram for a Solar Generation Unit Case 3: Conventional AC Generation/AC Link

d. Case 4: Special AC Generation/AC Link. In this case, a special AC generator is used.* A field modulated generator is an excellent example of special AC generator (Ref. 4-8, 4-9). The field modulated generator is basically a power amplifier with a reference signal coming from the utility line. The generator is mechanically tied to the heat engine. Since the device is basically a power amplifier, its output frequency is that of the reference signal. Thus for a large variation of the input shaft speed, the output frequency is slaved to the line. In this case the speed of the heat engine shaft does not need to stay constant, because it is not the shaft speed that regulates the frequency, but it is the utility reference input.

The charging and discharging of the battery is similar to Case 3. The block diagram for this system is shown in Figure 4-4.

e. Case 5: Regenerative Battery Charger. In Cases 1 and 2, the charging of the battery was controlled by regulating the output voltage of the generator unit, and the output voltage to the line was

*Another special AC generator is of the cycloconverter type which provides fixed output frequency with a variable speed shaft.

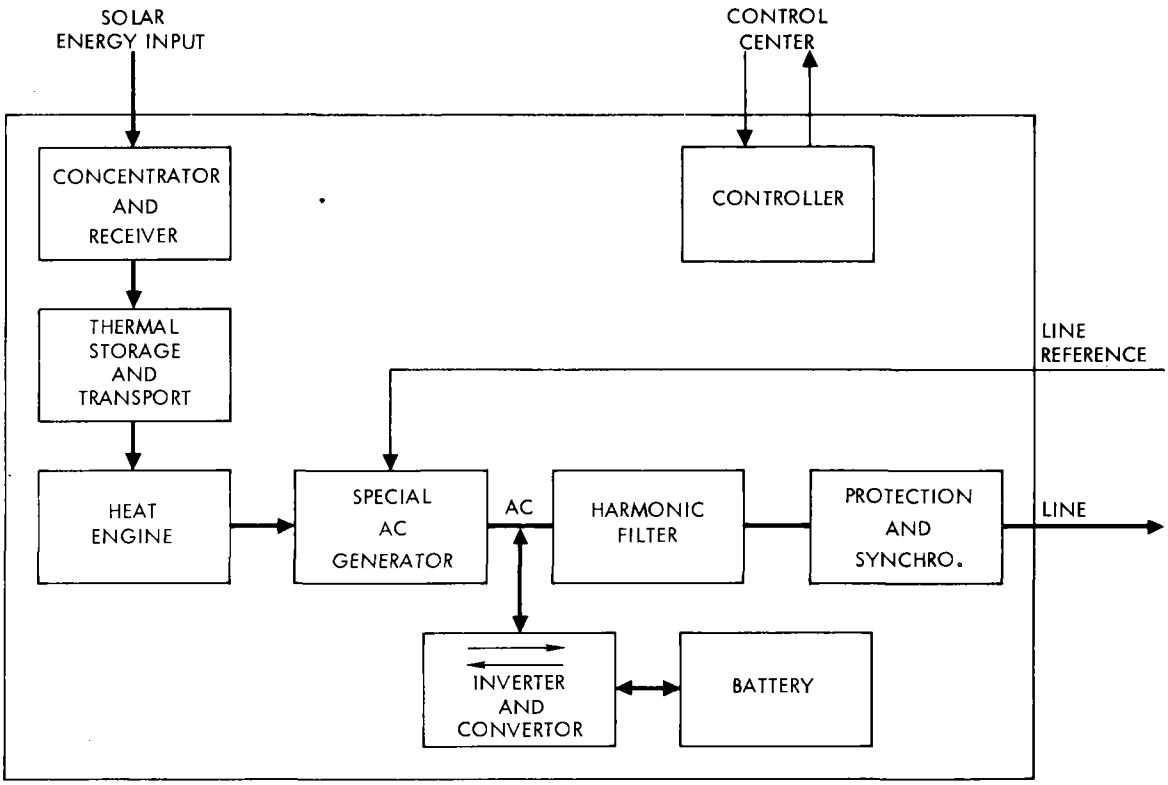


Figure 4-4. Conceptual Block Diagram for a Solar Generation Unit
Case 4: Special AC Generation/AC Link

regulated by DC/AC inverter. However, in this case (Case 5), the charging of the battery is controlled by regulating the output voltage level of the generator unit. The block diagram for this system is shown in Figure 4-5. As in Cases 1 and 2, the speed of the shaft output of the heat engine may be allowed to vary. When the system is operating from batteries, the DC/DC converter in a reverse operating mode provides power to the DC/AC inverter.

3. Component Characterization

Various components for power processing are required. The components selected should be viable from the standpoint of operational characteristics, reliability and cost. The following is a discussion of various components and building blocks for power processing.

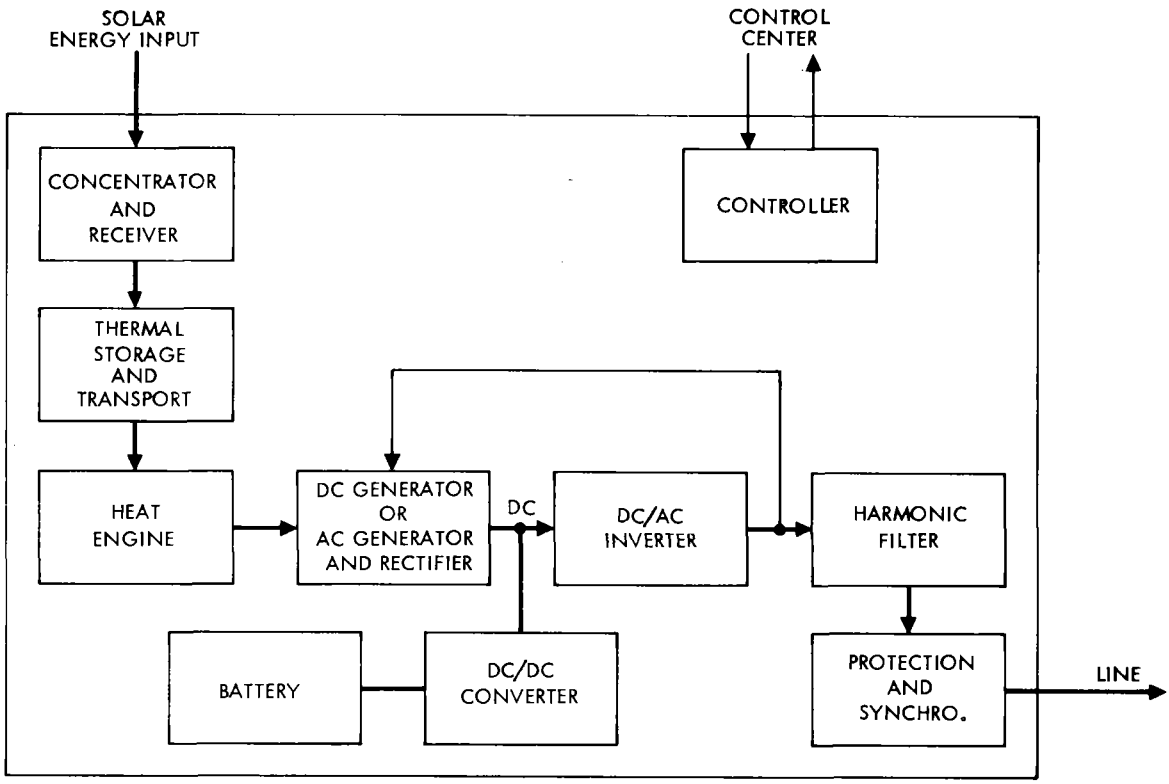


Figure 4-5. Conceptual Block Diagram for a Solar Generation Unit Case 5: Regenerative Battery Charger

a. Batteries (Refs. 4-7, 4-10). Two types of batteries are suggested for the application involved. The batteries are the Redox type and the lead calcium types described below. Redox batteries are suggested for application in future systems design whereas lead calcium would be used for the near-term. Other advanced battery types are being considered.

(1) Redox Batteries (Ref. 4-10). The redox battery utilizes two large tanks with $F_e^{+2} \rightleftarrows F_e^{+3}$ and $Cr^{+2} \rightleftarrows Cr^{+3}$ for Redox reaction. The materials are kept separate in the Redox cell by a charged ion-exchange membrane. Chloride ions transfer through the membrane, but other ions are excluded for hydrogen ions. Presently membrane life is limited and substantial development is in progress to increase membrane conductivity and life.

(2) Lead Calcium Batteries (Ref. 4-11). Lead calcium batteries are lead acid batteries with approximately 0.1% calcium as an alloying element to the lead. This results in a long life and relatively maintenance-free battery. These batteries are currently available and are suggested for near-term systems development. Energy efficiency of lead calcium batteries is approximately 80%.

b. Alternators/Generators. Two classes of alternators may be used for this application. The alternator speeds are determined by the Stirling engine shaft maximum speed requirements. Alternators can be run at speed substantially in excess of the prescribed speed of the Stirling engine. Moderate-speed alternators are more economical than low-speed alternators. Interfacing gearing may be used between the Stirling engine and the alternator shaft. This interface should be analyzed to determine if there are cost and efficiency advantages. The two classes of alternators are as follows:

(1) Special AC Alternators: The special AC alternator type is the field modulated frequency down converter (Refs. 4-2, 4-9). The principle of operation of this device is as follows:

A conventional 3Ø synchronous machine of basic frequency will have induced voltages of frequencies ($f_R + f_M$) and ($f_R - f_M$) when excited with an alternating current of frequency $f_M$ (60 HZ). When such three-phase voltages are full-wave rectified and their outputs tied in parallel, an output voltage containing a full-wave rectified sine wave at frequency $f_M$ results. The resulting full-wave rectified sine wave can be converted to a single phase sine-wave voltage at the modulation frequency $f_M$ (this is 60 HZ and is derived from the utility) by using a suitable switching circuit employing controlled rectifiers. To provide three-phase output would require three separate alternators.

Efficiency of this system is essentially constant from half load to full load. The efficiency is in excess of 80%. This type of alternator is in the development phase but could be available for near term programs.

(2) Conventional Alternators/Generators: These can be broken down into AC alternator and DC generators. For the former case several types of AC alternators may be considered for generating the electrical power at each solar generation unit. These types include induction, synchronous, and

high-speed solid rotor (RICE) machines. The induction machine is more versatile since it is a readily available commercial machine with a high efficiency rating.

DC generators are available in the power and speed ranges desirable for this application. Efficiencies of DC generators are approximately comparable to those of AC alternators. DC generators have a number of distinct disadvantages, namely:

(a) Commutator and attendant maintenance.

(b) Brushes and attendant maintenance.

(c) Cost: The initial capital cost is greater than that of a comparable AC alternator.

c. Inverters/Convertors (Ref. 4-12). Inverters are devices which transform DC power to AC power. They are generally referred to as DC-link inverters. The output of the inverter is stepwave DC power. This stepwave AC power is coupled to the utility through a harmonic reduction filter in order to keep harmonic currents to a low level. There are various inverter techniques and these are categorized into two classes. These are as follows:

(1) Line Commutated Inverters (Ref. 4-13). The simple 12-pulse current-fed line-commuted inverter is shown in Figure 4-6. Silicon-controlled rectifiers are commutated off by the 60 Hz, three-phase system to which the inverter is tied. The attraction of this system; it is simple, cheap and efficient. Its major disadvantages, which make it a low level contender for this application, are as follows:

(a) It is quite prone to commutation faults resulting from transient AC system disturbances.

(b) Requires large amounts of controllable passive power factor correction.

(2) Switching Inverter. These consist of two types. The first is transistor type and the other is SCR forced commutated type. The SCR type require commutation componentry to turn off (commutate) the silicon controlled rectifiers. A phase shift modulation inverter is shown in Figure 4-9. This type is one of several available switching inverters.

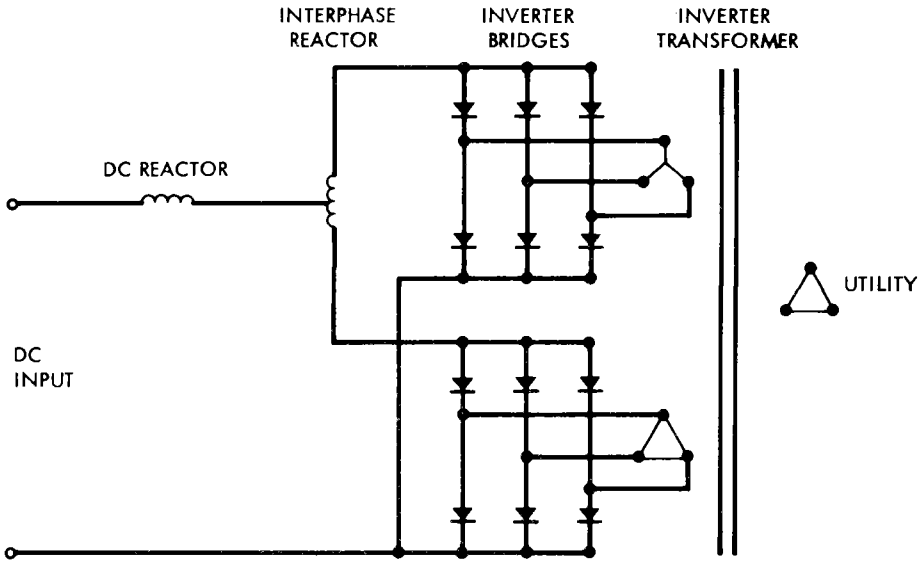


Figure 4-6. Basic 12 Pulse Current-Fed Line Commutated Inverter

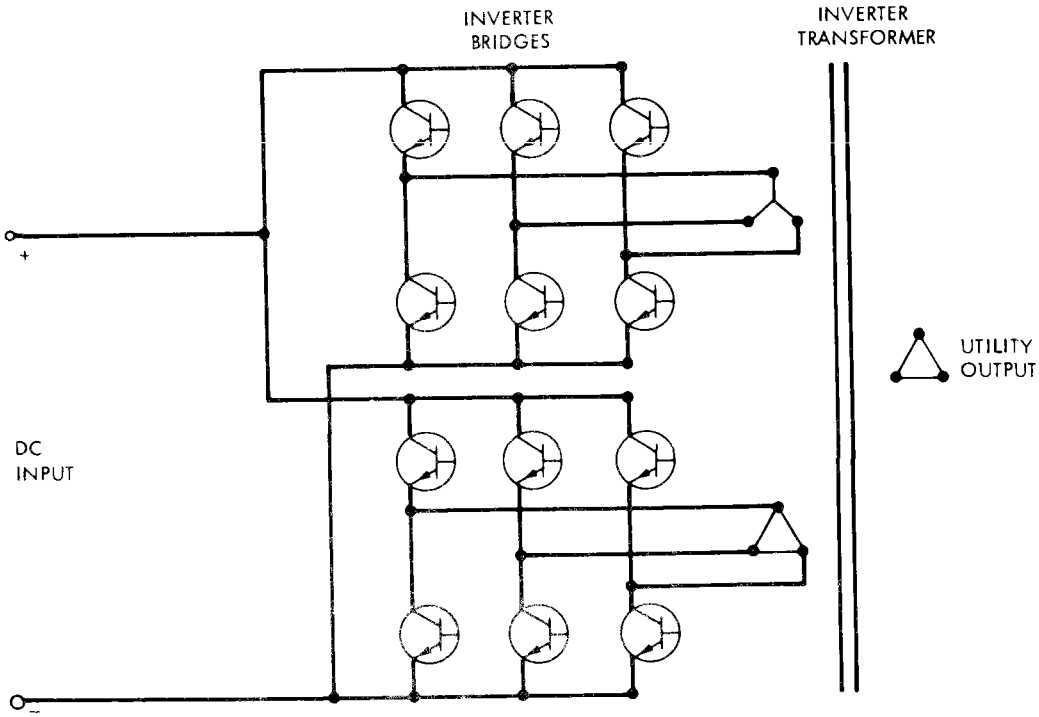


Figure 4-7. Phase Shift Modulation Inverter

4. Selection of Two Viable Options

Two attractive generation approaches out of five discussed earlier are: conventional AC generation with AC link and conventional AC generation with DC link. These two alternatives use proven technology and have known performance history (Other alternatives are not presently common but may find future applications.) These two generation concepts have been analyzed in the following paragraphs.

In analyzing generation concepts to evaluate performance parameters, the following definitions have been assumed:

$P_b$ = Battery power input

$P_b'$ = Battery power input

$P_g$ = Generator power output

$_I$ = Receiver power input

$P_{inv}$ = Converter power input

$P_{inv}'$ = Inverter power output

$P_o$ = Power output + auxiliary losses before the transformer

$P_o'$ = Power output

$t_1, t_2$ = Charge, discharge time of battery

$\eta_e$ = Engine power efficiency

$\eta_b$ = Battery energy efficiency

$\eta_g$ = Generator power efficiency

$\eta_r$ = Receiver power efficiency

$\eta_{inv}$ = Inverter/converter power efficiency

$\eta_R$ = Rectifier power efficiency

$\eta_t$ = Output transformer power efficiency

a. <u>AC-Link Units (Figure 4-8)</u>. Mathematical relationships among various equipment power and efficiency are as follows:

$$P_g = \eta_r \eta_e \eta_g P_I, \quad P_{inv}' = 0.55 P_o, \quad P_b = \eta_{inv} P_{inv},$$

$$P_b' t_2 = \eta_b P_b t_1, \quad P_{inv}' = \eta_{inv} P_b' \quad \text{and} \quad P_o = P_g - P_{inv}$$

It can be shown that:

$$P_o = P_g / \left(1 + 0.55 t_2 / \eta_{inv}^2 \eta_b t_1\right), \text{ kWe}$$

$$P_b' = 0.55 P_o / \eta_{inv}, \text{ kWe}$$

$$P_o' = 0.94 \, P_o \eta_t$$

Solar generating unit (SGU) energy efficiency = $(P_o' t_1 + 0.55 P_o' t_2)/P_I t_1$

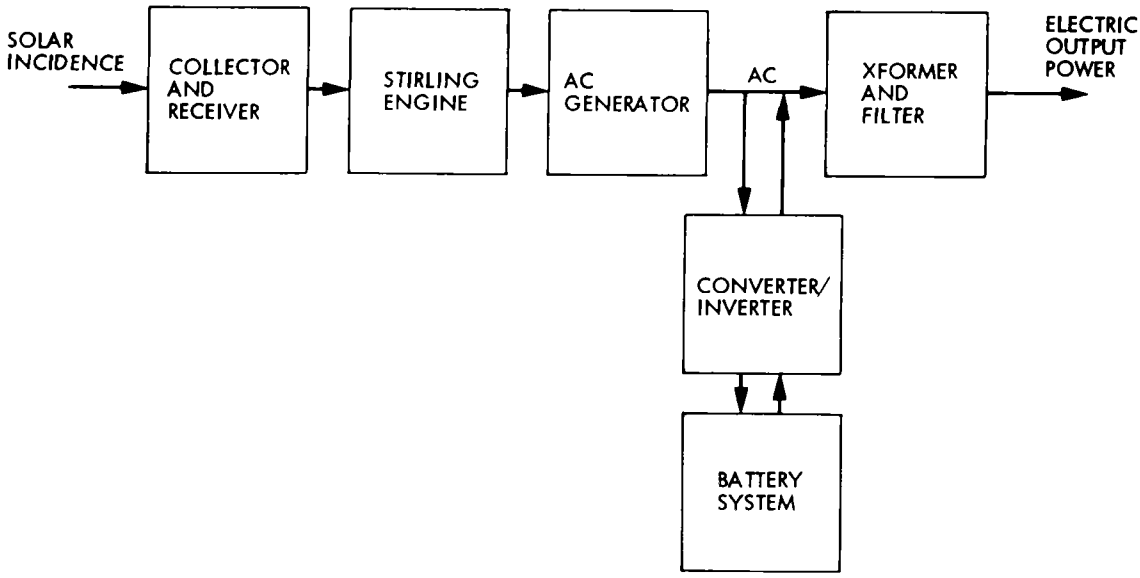


Figure 4-8. Block Diagram of a Solar Generation Unit (SGU) for the AC-Link Approach Using a Conventional AC Generator

b. DC-Link Units (Figure 4-9). Mathematical relationships among various equipment power and efficiency are as follows:

$$P_g = \eta_r \eta_e \eta_g P_I, \quad P_b' = 0.55 P_o/\eta_{inv}, \quad P_b' t_2 = \eta_b P_b t_1,$$

$$P_{inv}' = P_o, \quad P_o/\eta_{inv} = P_g \eta_R - P_b$$

Then:

$$P_o = \eta_{inv} P_g \eta_R/(1 + 0.55 t_2/\eta_b t_1), \text{ kWe}$$

$$P_o' = 0.94 P_o \eta_t$$

$$\text{SGU energy efficiency} = (P_o' t_1 + 0.55 P_o' t_2)/P_I t_1$$

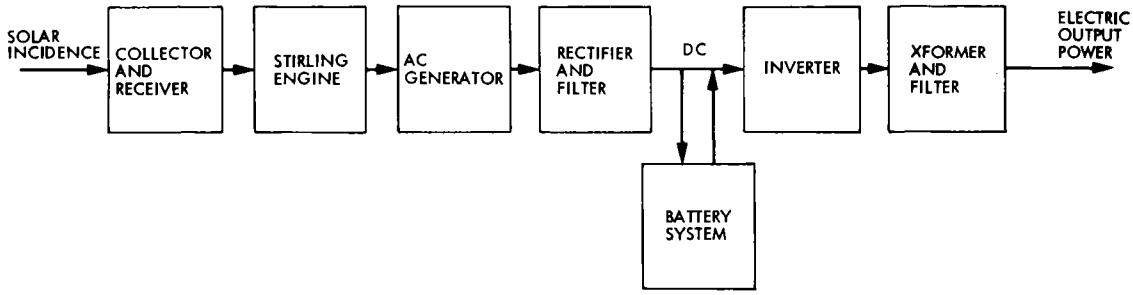


Figure 4-9. Block Diagram of a Solar Generation Unit for the DC-Link Approach Using a Conventional AC Generator

c. Unit Performance. Utilizing the analytical expressions, the sizes of the electrical equipment, as well as system efficiencies, are calculated for the AC-link system with a conventional AC generator and the DC-link system with a conventional AC generator and rectifier. The results are summarized in Table 4-1.

## D. POWER COLLECTION

### 1. Selection of Viable Options (Refs. 4-14, 4-15, 4-16)

The power from many solar units is collected to provide power for stand-alone operation or feeding into an electric utility bus. Means for protection and isolation of equipment is provided.

a. AC-Link Plant (10 MWe). A preliminary conceptual design for the AC-link plant was developed and is shown in Figure 4-10. The plant is broken down into various building blocks determined by commercial cost and availability constraints and by reliability

Table 4-1. Component Sizes and Expected Performance of 15 kWe Solar Generation Unit

| Items | AC Link | | DC Link | |
|---|---|---|---|---|
| | Power Output kW | Energy Efficiency | Power Output kW | Energy Efficiency |
| Collector and Receiver | 57.8 | 0.72 | 57.8 | 0.72 |
| Stirling Engine | 24.3 | 0.42 | 24.3 | 0.42 |
| Generator | 22.3 | 0.92 | 22.3 | 0.92 |
| Battery | 9.8 | 0.80 | 9.3 | 0.80 |
| Inverter/Converter | 9.1 | 0.92 | 15.6 | 0.92 |
| Rectifier | N/A | N/A | 22.1 | 0.99 |
| Output Transformer | 15.2 | 0.98 | 14.4 | 0.98 |
| Overall System | 15.2 | 0.235 | 14.4 | 0.223 |

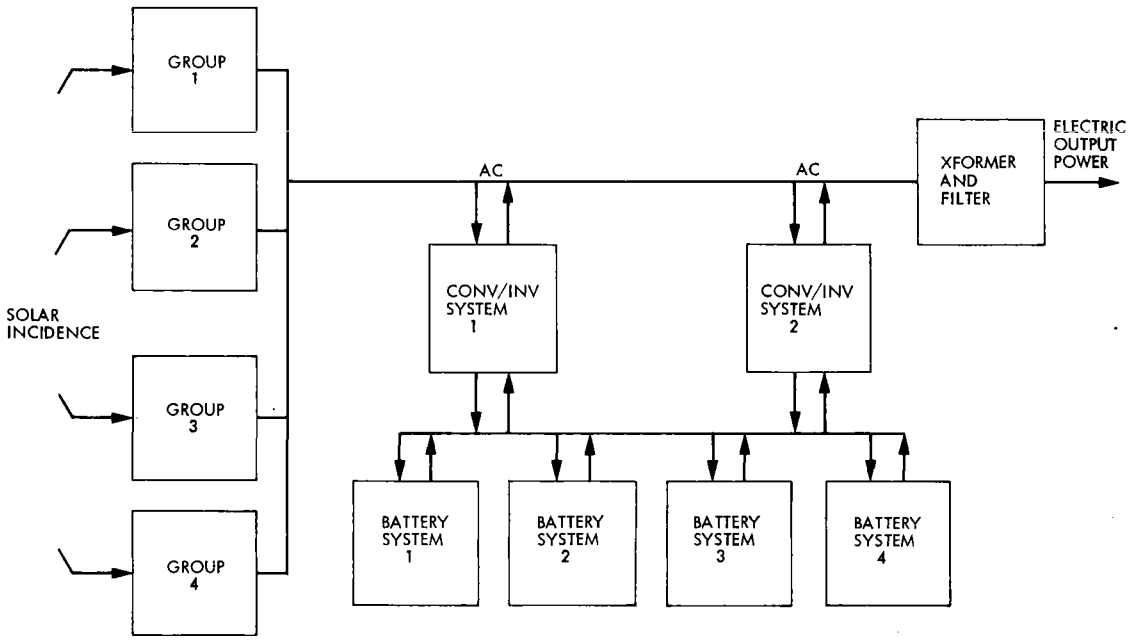


Figure 4-10. Conceptual Block Diagram for an AC-Link Plant

considerations. In the AC-link plant 165 solar units are used to form a group. There are four groups in total leading to 660 solar units for the plant. A part of the AC power generated is passed through the inverter/converter system to charge the battery system. The remaining generated power and the power from the battery system form the electric output of the plant. In order to enhance the reliability of the plant, redundancy in the battery and inverter systems has been provided. A single line diagram for the plant is shown in Figure 4-11.

b. DC-Link Plant (10 MWe). A preliminary conceptual design for the DC-link plant has been developed and is shown in Figure 4-12. In the DC-link plant 174 solar units are used to form a group. There are four groups in total leading to 696 solar units for the plant. A portion of all the DC power collected from all the solar units is used to charge the battery system. The remaining portion of the DC power collected and the power from the battery system is fed to two inverter systems and subsequently to the plant output bus. In order to enhance the reliability of the plant redundance in the battery and the inverter systems has been introduced in the plant design. A single line diagram for the plant is shown in Figure 4-13.

2. Analyses of Options

a. AC-Link Plant (Figure 4-11). Mathematical relationships among various equipment power and efficiency are as follows:

$$P_o = P_g / \left(1 + 0.55 t_2 / \eta_{inv}^2 \eta_b t_1\right)$$

$$P_b' = P_{inv} / \eta_{inv} \quad \text{and} \quad P_{inv}' = 0.55\ P_o$$

$$P_o' = 0.98\ P_o \eta_t$$

$$\text{Plant energy efficiency} = (P_o' t_1 + 0.55 P_o' t_2)/660 P_I t_1$$

b. DC-Link Plant (Figure 4-12).

$$P_o = \eta_{inv} P_g \eta_R / (1 + 0.55 t_2 / \eta_b t_1)$$

$$P_b' = 0.55\ P_o / \eta_{inv} \quad \text{and} \quad P_{inv}' = P_o$$

$$P_o' = 0.98\ P_o \eta_t$$

$$\text{Plant energy efficiency} = (P_o' t_1 + 0.55 P_o' t_2)/696 P_I t_1$$

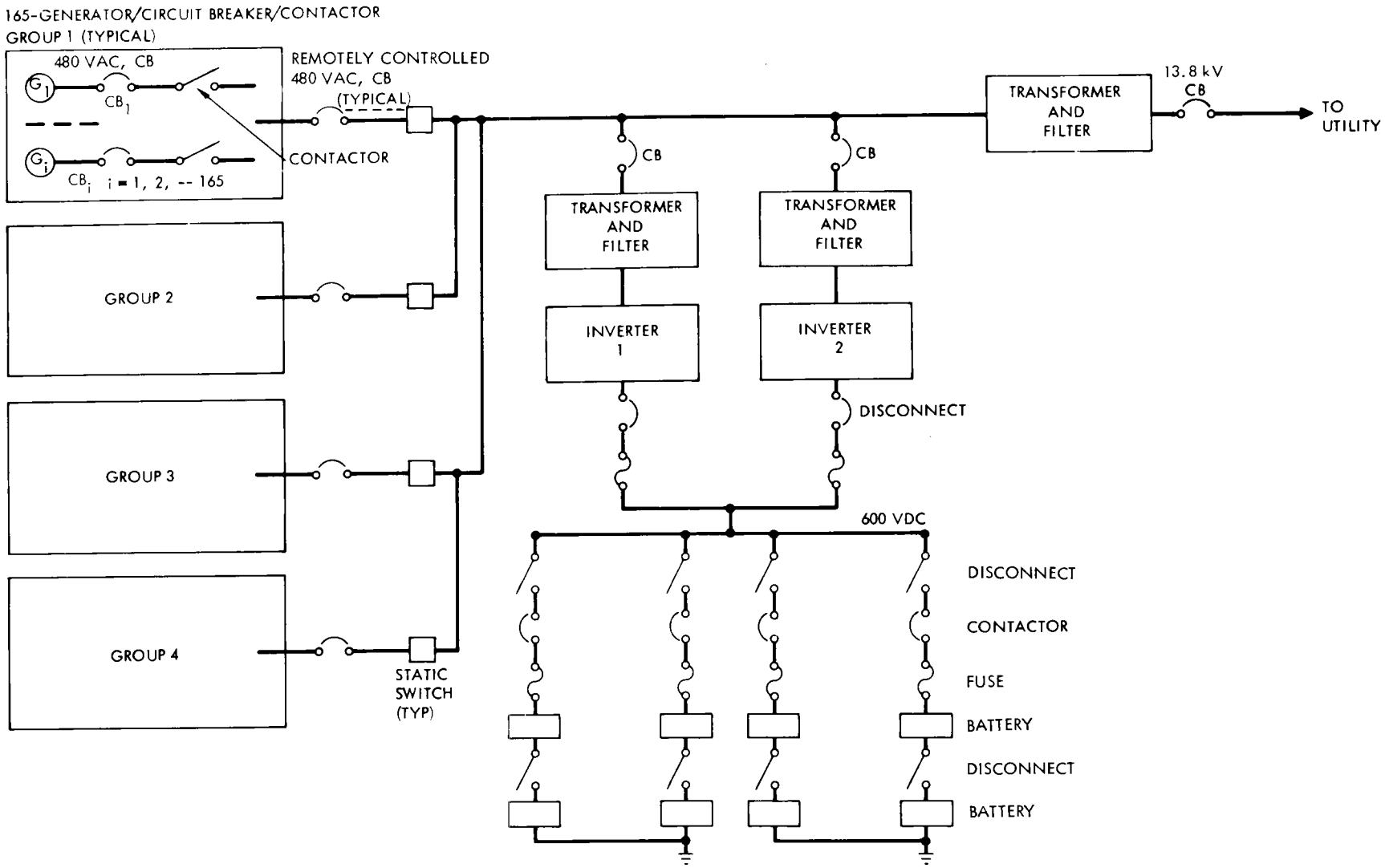


Figure 4-11. A Single Line Diagram for a Four-Group 10 MWe Plant Using AC Link

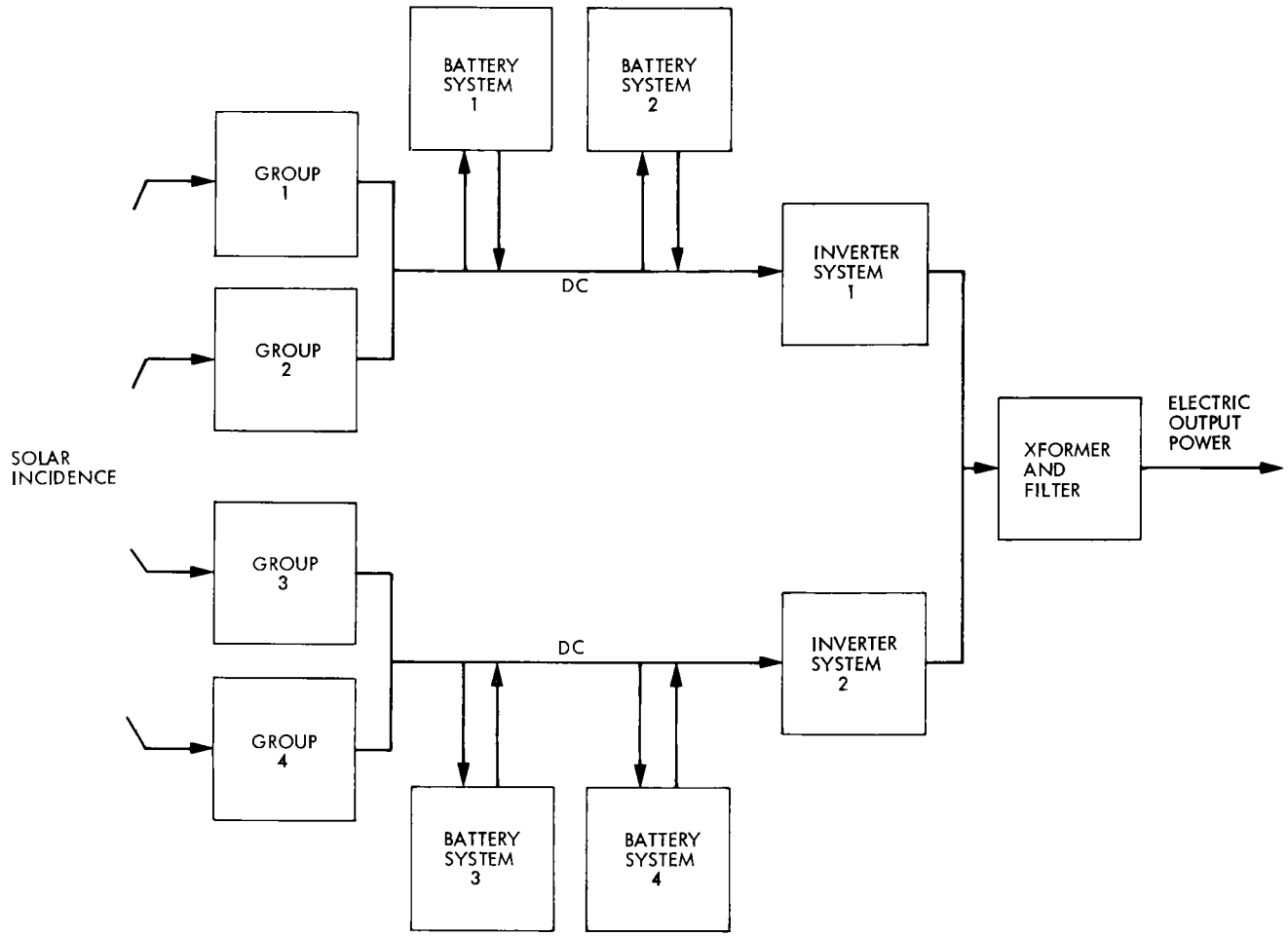


Figure 4-12. Conceptual Block Diagram for a DC-Link Plant

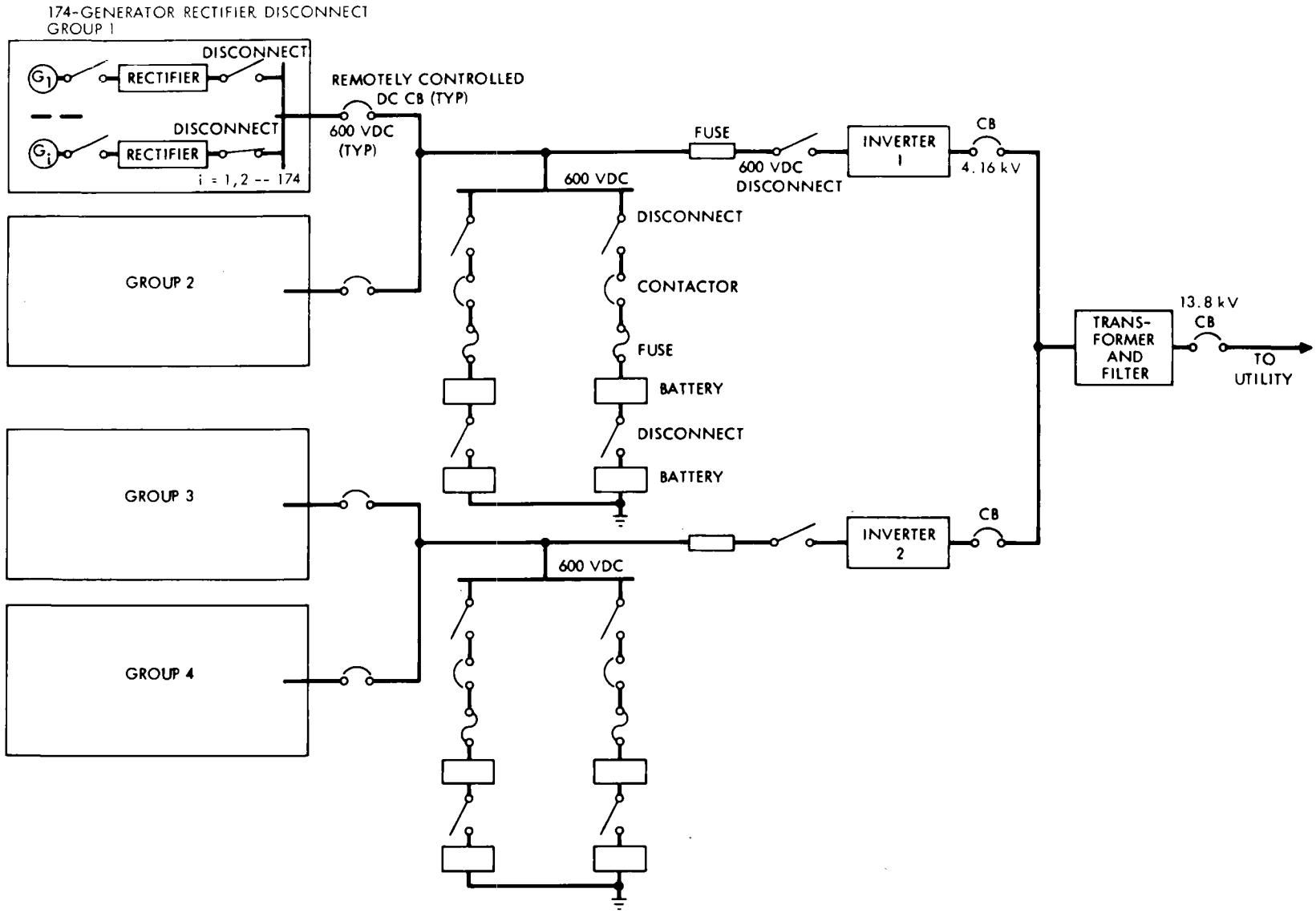


Figure 4-13. A Single Line Diagram for a Four-Group 10 MWe Plant Using DC Link

c. Plant Performance. Utilizing the analytical expressions, the sizes of electrical equipment and the plant efficiency are calculated for both AC-linked and DC-linked plants. The results are summarized in Table 4-2.

Table 4-2. Electrical Component Size and Expected Performance for 10 MWe Plants

| Items | AC Link (660 Generating Units) | | DC Link (696 Generating Units) | |
|---|---|---|---|---|
| | Power Output MWe | Energy Efficiency | Power Output MWe | Energy Efficiency |
| Generators | 0.021 x 660 | 0.92 | 0.021 x 696 | 0.92 |
| Battery | 6.1 | 0.80 | 6.1 | 0.80 |
| Inverter | 5.7 | 0.93 | 10.4 | 0.93 |
| Rectifiers | N/A | N/A | 0.0208 x 696 | 0.99 |
| Output Transformer | 10.0 | 0.99 | 10.0 | 0.99 |
| Overall System | 10.0 | 0.235 | 10.0 | 0.223 |

3. Performance and Cost Comparison

Performance parameters and cost are two dominant factors considered in the final selection of a generation concept.

a. Performance Analysis. Table 4-1 indicates that the performance parameters for AC-link units are in some respects superior to those for DC-link units. The power rating of inverters of DC-link units is substantially larger than the power rating of inverters in AC-link units. Table 4-2 shows similar results except on a larger scale. The combined output of both inverters is 5.7 MWe in an AC-link plant, whereas the combined output of two inverters is 10.4 MWe in a DC-link plant.

A DC link plant requires 696 rectifiers not needed in an AC plant. The output transformer feeding the utility grid receives power from the inverter. Therefore the inverter handles the entire forward power flow under normal conditions and only a fraction of the power under other condition. An inverter malfunction will affect the supply of power under all conditions.

b. Cost Analysis. In order to make a numerical cost comparison for the two generation alternatives, cost figures for inverters, rectifiers, synchronizing gears, etc., must be available. Requests were directed to appropriate manufacturers for these figures, and replies are expected in the near future. However, price information for many items is difficult to obtain since some of the items are still in the R&D stages. In addition, instrumentation and control requirements of the battery-inverter system are not defined.

## 4. Equipment Selection

Lists of required equipment for both AC-link plant and DC-link plant are provided in Tables 4-3 and 4-4. These tables will help in the evaluation of costs associated with each plant.

Table 4-3. Parts List for a 10 MWe Plant with AC Link

| Equipment | Output Rating | Quantity |
|---|---|---|
| Receivers | 57.8 kW | 660 |
| Stirling Engines | 24.3 kW | 660 |
| Conventional AC Generators | 22.3 kW | 660 |
| 480V Generator Circuit Breakers (CB) | 30 A | 660 |
| 480V Remotely Controlled CB | 3160 A | 4 |
| Inverter/Converter-Transformer System | 3 MW | 2 |
| Battery Systems | 1.6 MW | 4 |
| Storage System CB | 4000 A | 2 |
| Output Transformer | 11 MW | 1 |
| Synchronizing Gear | | 1 |
| 13.8 kV Output CB | 440 A | 1 |
| Static Switches to Prevent Reverse Power Flow | 3160 A | 4 |

Table 4-4. Parts List for a 10 MWe Plant with DC Link

| Equipment | Output Rating | Quantity |
|---|---|---|
| Receivers | 57.8 kW | 696 |
| Stirling Engines | 24.3 kW | 696 |
| Conventional AC Generators | 22.3 kW | 696 |
| 480V Rectifier & Filter System | 21.0 kW | 696 |
| 480V DC Disconnects | 50 A | 696 |
| 480V AC Circuit Breakers | 30 A | 696 |
| 600V DC Remotely Controlled CB | 4500 A | 4 |
| Battery Systems | MW | 4 |
| 600V DC Disconnects | 2500 A | 4 |
| Inverter Systems | 5.5 MW | 2 |
| 4.16 kV Circuit Breakers | 900 A | 2 |
| Output Transformer | 11 MW | 1 |
| 13.8 kV Output CB | 440 A | 1 |

5. Layout Considerations

a. Plant Layout. The final selection of a plant layout (Ref. 4-17) will depend on constraints imposed by standards, code and regulatory requirements, amount of available land, environmental considerations, technical requirements and feasibility, operating procedures, and economics. In the absence of complete knowledge about these constraints, only general arrangements were studied and presented as examples. Further studies and detailed guidelines in this direction are needed before a final decision can be made.

b. Group Layout. Two of the several possible group layouts are shown in Figure 4-14 and 4-15. A circle represents a complete unit consisting of a concentrator, a receiver, a Stirling engine, a conventional AC generator, and a rectifier if DC link is used. Each generator (G) has its own provision for isolation, all generator buses (GB) have separate circuit breakers (CB), and each group has its own circuit breaker (B). Figure 4-14 shows 44 units connected to each of four generator buses while Figure 4-16 shows 24 units connected to each of seven generator buses. Depending on values of d, $D_1$, $D_2$ and $D_3$, group layout may be determined completely. Figure 4-14 may be suitable for a DC-link plant while Figure 4-15 may be suitable for an AC-link plant.

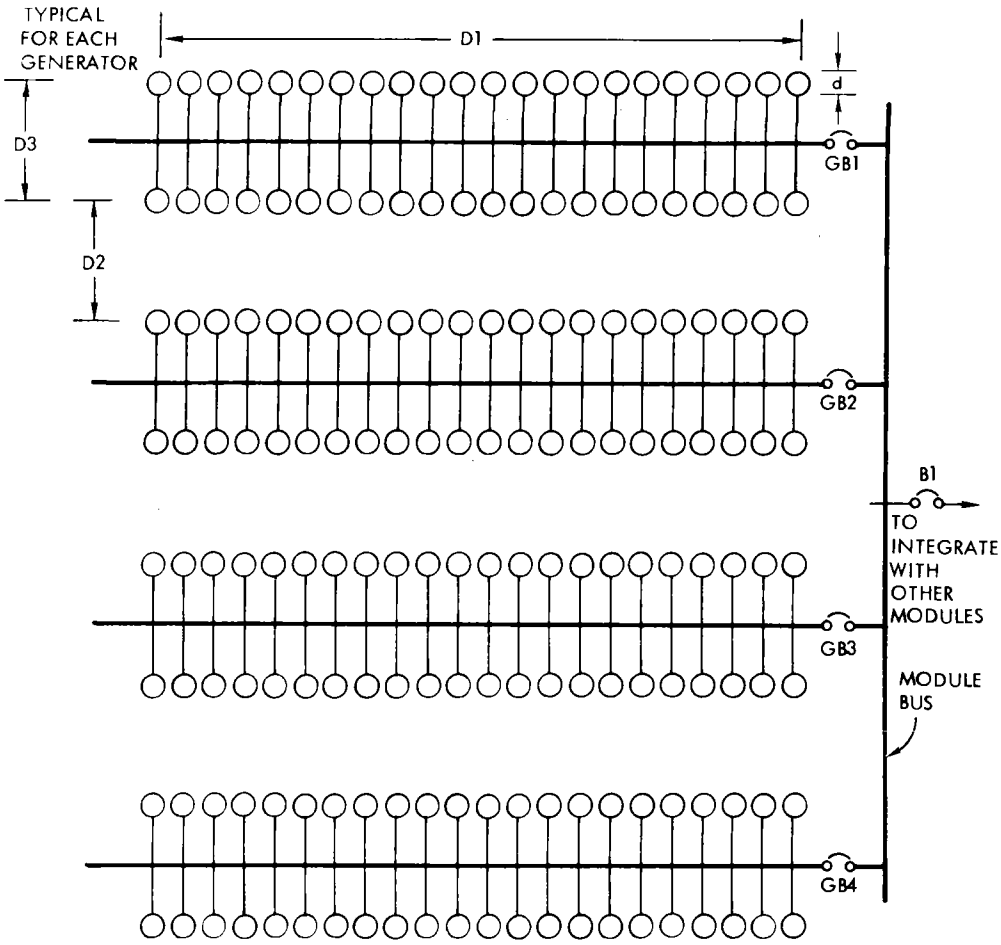


Figure 4-14. A Group Layout for a 10 MWe Plant with DC Link

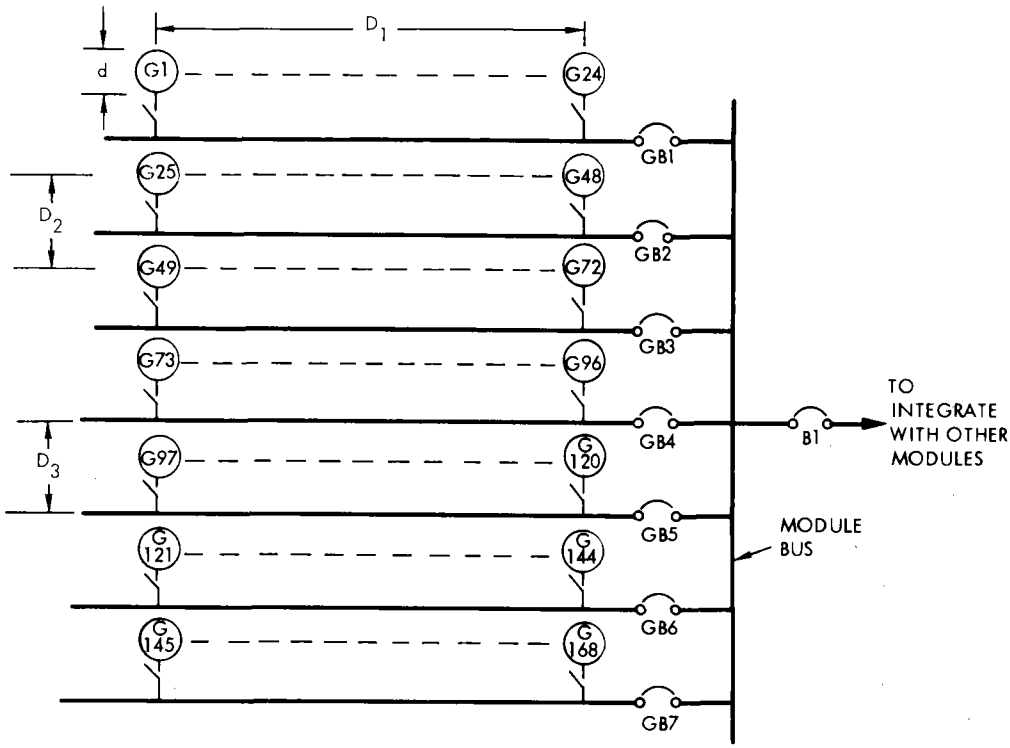


Figure 4-15. A Group Layout for a 10 MWe Plant with AC Link

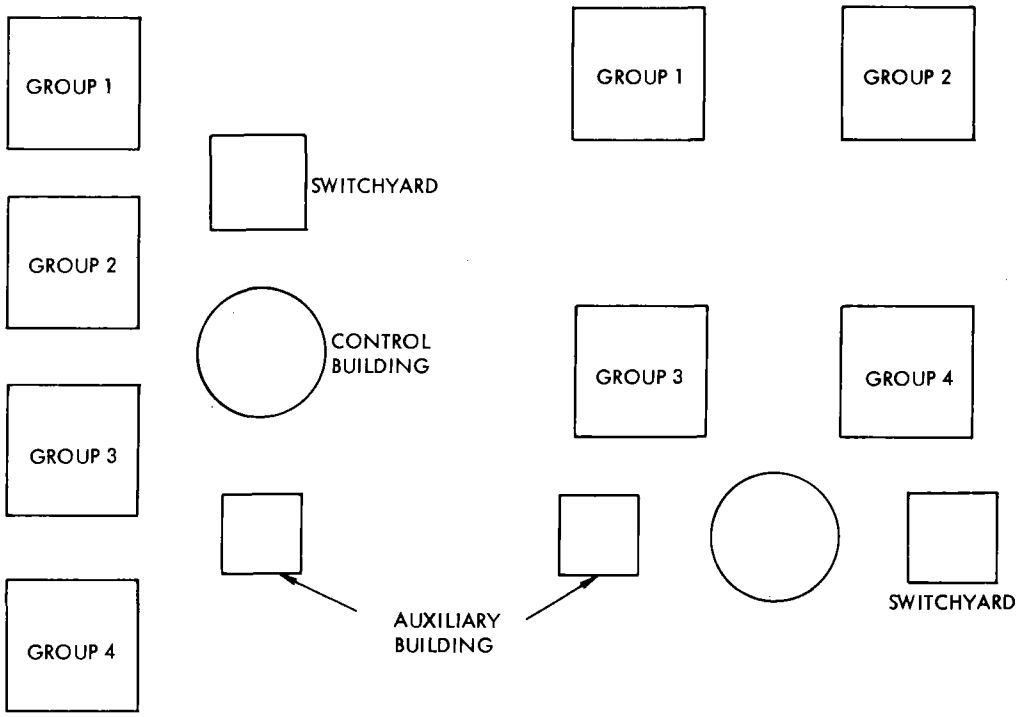


Figure 4-16. Plant Layouts

Isolation devices provide flexibility of control and ease of maintenance and will have to be coordinated for control and protection.

Other group layouts may be the following:

(1) 14G x (12 GB) for 168 generators (AC link)

(2) 15G x (11 GB) for 165 generators (AC link)

(3) 16G x (11 GB) for 176 generators (DC link)

(4) 29G x (6 GB) for 174 generators (DC link)

c. Plant Layouts. The selection of a plant layout will include detailed considerations regarding size and location of three important component parts of a power plant. These are as follows:

(1) Control room or building

(2) Auxiliary building

(3) Switchyard, as shown in Figure 4-16.

Control buildings will house control panels with meters, monitors, annunciators, alarms, synchronizing gears, engine control systems, excitation control systems, data loggers, battery control systems, performance charts, etc. Scope, size and location of the control building will help determine the plant layout completely.

Auxiliary buildings may house equipment such as battery, inverter and rectifier systems, and other miscellaneous items not interfacing directly with the control room operator and not installed in the field. Auxiliary building and control room may be separate or connected together. Switchyards will include high voltage transformers, lightning arrestors, utility/plant interface switchgears, etc.

## 6. Stability, Paralleling and Load Sharing

The controller in each unit is responsible for operating the unit efficiently and to specification, meanwhile allowing adequate stability margin. It must allow starting and stopping of the system, as well as synchronization with the line.

Prior to the development of control schemes, a control and power management philosophy needs to be developed. This philosophy must ensure balanced power flow in the system at all times. In other words, the power received through the concentrator must go to the load and storage system, so that a power flow balance is maintained at all times. The power management philosophy selected here is that, given a selected size for components of the unit, it is desirable to use all the energy available to the system, whenever possible. When the solar energy available exceeds the load demand, then the excess energy will be used to charge the battery (if not fully charged already). When solar energy available

is less than that demanded by the load, then it will be necessary to provide battery energy (if possible) to meet the demand, or leave part of the load demand unmet.

Based on these assumptions, the control strategies may be determined. Depending on the status of the batteries, the load demand, the energy available at the collector, and a host of other variables related to system states and security, the controller exercises appropriate strategies to route the available power to the load and to and from storage.

The development of the controller for a single generation unit is straight forward once the operational philosophy is agreed on, and if each element of the solar generation unit satisfies some controllability and observatility requirements.

It is envisioned that the development of the control strategies may be based on the well-known linear state regulator problem, where first the dynamics of the system are determined, namely:

$$\dot{\underline{X}} = A\underline{X} + B\underline{u}$$

where $\underline{X}$ is the system state vector and $\underline{u}$ is the control vector. Using the usual quadratic performance criterion, will lead to:

$$\underline{u}(t) = K(t)\ \underline{X}(t)$$

where

$$K(t) = -R^{-1}(t)\ B^{T}(t)\ P(t)$$

where K(t) is the matrix of feedback gain and P is the solution to the Raccati equation solved in backward time. It is quite possible that since the parameters of the system may be time-invarient, then the feedback gain matrix may become constant and there may be no need to solve the Raccati equation in real time.

The operational system will have the capability and viability of operating a large number of generator systems and inverters in parallel and provide stable operational modes under dynamic conditions, such as load application or removal, radical change in insolation availability, transitional modes from battery charging to battery discharging and fault clearing.

## E. POWER MANAGEMENT

In order to assure stable, economical, and efficient operation of the plant, a power management system will be implemented. It will be similar to the electric utility power management system, where someone, and/or some automatic system, at the utility dispatch center, usually decides on which element of the system (e.g., a certain generator) should be used to generate, transmit, and distribute power, based on the load demands and the available power at that particular

time. It is within this area that the operational stability of the system is considered, and efficient and economical operation of the system is ensured.

Power management involves certain issues which include the following:

(1) Plant supervisory control system configuration

(2) Stability of many interconnected generators

(3) Power management philosophy within the plant

(4) Normal operational strategies

(5) Emergency operational strategies

(6) Starting and stopping procedures

(7) Economic dispatch within the plant

(8) Monitoring and control requirements within the plant

(9) Digital computing system requirements for the plant

It is envisioned that a control system consisting of a control center, controllers at the group level, and controllers at each SGU will be used to implement the power management system. The control center will be in charge of the overall plant operation, the group controller oversees the operation within each group and the controller at each SGU will be in charge of the operation of that unit. The SGU controller can be envisioned as a block which has connections and interfaces with all the other blocks of the SGU. It is capable of receiveing commands from and sending status information to the plant control center, i.e., it provides the capability for the unit of allowing it to be operated as part of a much larger plant. The main functions of the controller are 1) to receive monitoring information from the various SGU elements (i.e., blocks), 2) to implement the various control functions (e.g., various regulation, operating strategies, start and stop procedures), and 3) to send control commands to appropriate blocks.

A block diagram of a control system hierarchy is shown in Figure 4-19. Individual subsystem strategies will be detailed and then integrated with the higher level block controller for proper remote dispatch and interface.

## F. UTILITY INTERFACE

### 1. Equipment Description (Refs. 4-18, 4-19)

The problem of utility interface differs from a conventional utility interface because solar electric plants may be required to have a battery

storage system capable of bidirectional power flow. Power from the battery is used to provide energy through the inverter to the utility. In addition, the battery system may be able to receive energy from the utility. It should be noted that there are several choices of utility interface voltages. Generally, the system will tie to the distribution networks at voltages in the range of 4kV to 34.5 kV. The optimum choice will provide an economical solution with an attendant high reliability. The inverter system or AC generator requires transformer coupling to the utility due to the relatively low DC voltage at which the source is expected to operate. An interface voltage of 13.8 kV was selected in order to provide an economical interfacing switchgear cost.

2. Additional Utility Interface Issues

Some additional issues considered in determining utility interface for a solar electric plant with battery storage are the following:

(1) Output transformer and voltage level: the output transformer is rated at the output power level. In the case of a 10 MWe plant, a 10 MVA, 3-Ø, 60 HZ 13.8 kV transformer is selected.

(2) Harmonic reduction transformer: a high level of harmonic content present in the inverter output is filtered by this transformer. The output of the harmonic reduction transformers is combined and stepped up to the level of the utility-line voltage.

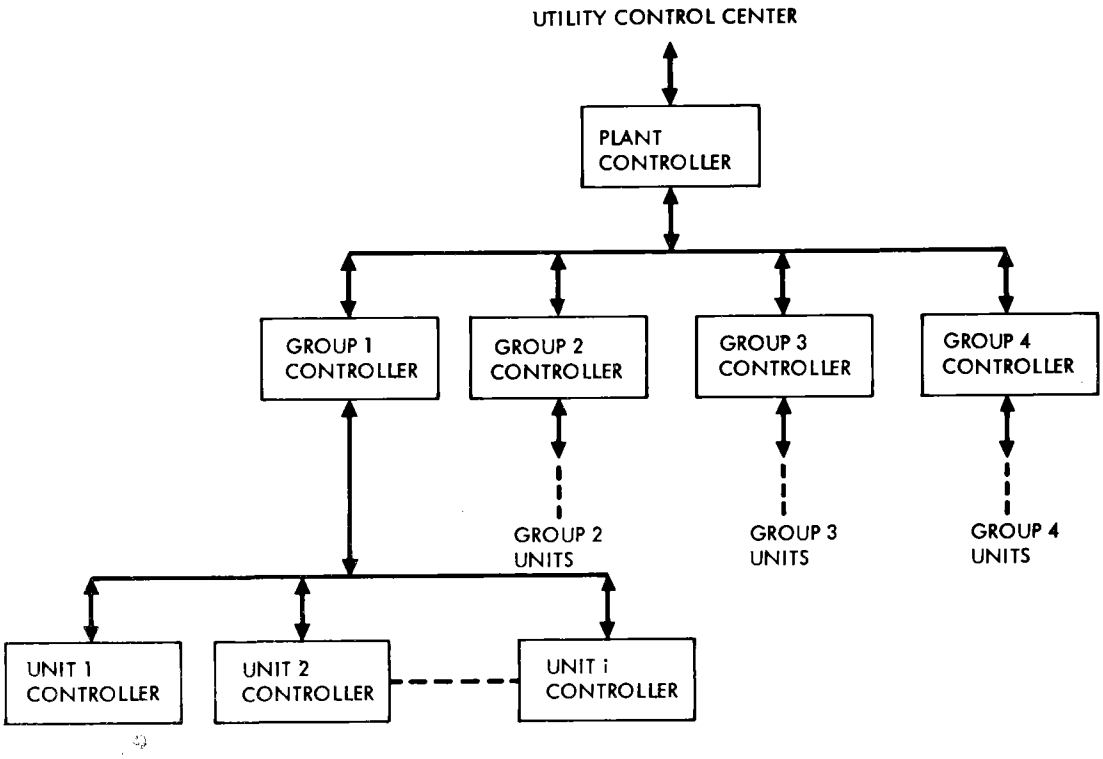


Figure 4-17. Control Hierarchy

(3) Reactors. Reactors are connected between the harmonic reduction transformers and the output transformer to provide an inductive impedance to the utility line for control and proper fault coordination.

(4) Lightning arrestors: to protect interface equipment from lightning, lightning arrestors are provided on the high-voltage side of the output transformer.

## G. CONCLUSION

There are several viable approaches for the design of each solar generation unit. There are also two viable approaches (AC-link and DC-link) to plant design. Each of these approaches has advantages and disadvantages.

From the electrical point of view, the AC-link plant is an attractive approach. Yet, the final selection of a design concept for the plant must go beyond electrical considerations and must include trade-offs in other parts of the system. For example, in the case of the Stirling engine, which is an important part of the system and constitutes a major developmental effort, the selection of AC-link approach or DC-link approach may impact the engine design. Thus, it is necessary to include a detailed model of the Stirling engine in any future analysis. Such an effort is in process.

## REFERENCES


4-1. Stearns, J.W., "Dispersed Solar Thermal Power System Operation and Control with Thermal Storage Applied to Power Leveling," JPL RFP #EL-2-3816-263 for Design and Fabrication of a Dish-Stirling Solar Receiver, Exhibit 1, Part A.1, Attachment A, October 6, 1978.

4-2. Sheldon, E.L., "The Potential and Applications for Energy Storage," Conference at School of Engineering, Oklahoma State University, Stillwater, Oklahoma, October 27 and 28, 1976.

4-3. Smith, J.C., "The Lead-Acid Battery: What is the Future?" Electrochemical Society, October 9-14, 1977.

4-4. Bahrami, K.A., and Krauthamer, S., "Solar Thermal Distributed System/A Preliminary Look at the Design of a 15 kVA Dish-Electric Concept Solar Generation Unit," IOM #342-78-B-354, June 3, 1978.

4-5. Das, R.L., Krauthamer, S., and Bahrami, K.A., "Solar Thermal Distributed System/Technical Evaluation of AC- and DC-Link 15 kWe Dish-Electric Solar Generation Units," JPL IOM #342-355, October 6, 1978.

4-6. "An Assessment of Energy Storage Systems Suitable for Use by Electric Utilities," EPRI EM-264, Project 225, ERDA E(11-1)-2501.

4-7. Pons, R.L., "Stirling Engine Performance Model," SPS-001, Ford Aerospace and Communications Corporation, Aeronutronic Division, Newport Beach, California.

4-8. Ramakumar, R., "Development and Addition of Field Modulated Generator System for Wind Energy Application," School of EE, Oklahoma State University, Stillwater, Oklahoma.

4-9. Ramakumar, R., and Tsung, C.C., "An Approach to Model Field Modulated Generator Systems," Midwest Power Symposium, October 1975.

4-10. Lewis, P.A., and Zemkoski, J., "Prospects for Applying Electrochemical Energy Storage in Future Electric Power Systems," 1973 IEEE Intercom Technical papers, Session 13, International Convention and Exposition, 74-CHO 898-7-IEEE, March 26-30, 1973.

4-11. "Lead Calcium Batteries for Switchgear, Control, Uninterrupted Power Supply, and Other Standby Applications," Section 12-212B-1 (company brochure), C&D Batteries Division, Electra Co., April 1977.

4-12. Phillips, G.A., Vogt, J.M., and Walton, J.W., "Inverters for Commercial Fuel Cell Power Application," IEEE Transactions on Power Apparatus and Systems, May/June 1976 (PAS 95 No. 3).

4-13. Bedford, B.D., and Noft, R.G., Principles of Inverter C/CTs, John Wiley & Sons, 1964.

4-14. Bechtel Corporation, Final Report on "A Conceptual Design of a Photovoltaic Control Station Power Plant," prepared for Spectralab, Inc., under Subcontract No. 66725, July 1976.

4-15. Wood, P., "DC-AC Inversion for Utility Power Systems," Westinghouse Electric, Pittsburgh, International Semiconductor Power Converter Conference.

4-16. "Solar Total Energy - Large Scale Experiment #2," Final Report, Document #78SDS4200, General Electric, Space Division.

4-17. Handley, L.M., et. al., "4.8 Megawatt Fuel Cell Module Demonstrator," 12th IECEC, 77-9057.

4-18. Eksstrom, Ake, et. al., "Parallel Connection of Converters for HVDC Transmission," IEEE Transactions on Power Apparatus and Systems, Vol. 97, pp. 714-724, May/June 1978.

4-19. Glasgow, J.C., and Birchenough, A.G., "Design and Operating Experience on the U.S. DOE Experimental MOD-O, 100 kW Wind Turbine," DOE/NASA/1028-78/18.

# SECTION V

# ADVANCED CONCENTRATOR SUBSYSTEM

# SECTION V

# ADVANCED CONCENTRATOR SUBSYSTEM

## A. INTRODUCTION

Conceptual studies were presented in the previous Semi-Annual Progress Report, evaluating a range of two-axis tracking, point focusing concepts for advanced dispersed solar concentrators. The objective was to establish a conceptual design having promise of meeting the cost and performance goals of the solar thermal electric program. As a result of these studies, a point-focusing paraboloidal concentrator, with dish-mounted Stirling engine-alternator power conversion module was selected as the most cost-competitive candidate system concept for application in the 1985 time frame.

## B. CONCEPT DESCRIPTION

The primary concept selected is the deep dish configuration, as shown in Figure 5-1. This advanced concentrator conceptual design consists of mirrored glass gores installed in a cantilever configuration on a truss type support ring of triangular cross-section to form a complete but physically discontinuous reflective surface. Two groups of independent, optical-quality reflective gores form a paraboloidal concentrator surface with aperture diameter between 5 and 15 meters. The focal length to aperture diameter ratios (F/D) are in the range of 0.5 to 0.7. Each reflective gore is to be fabricated of thin, backsilvered glass mirror bonded continuously over a contoured substrate of structural, cellular glass. An all-truss structure serves as an intermediate structure between the concentrator surface assembly and the pedestal which provides the azimuth and elevation movements of the concentrator. Tracking sensors, drive elements and control are discussed in sections to follow.

A second concept, the concave bubble Fresnel lens configuration shown in Figure 5-2, is expected to receive additional attention during FY 1979. This concept appears to have a potential for very low cost which may offset its lower efficiency and lower power-conversion temperatures.

## C. PROTOTYPE ADVANCED CONCENTRATOR

A prototype advanced concentrator of the deep-dish paraboloidal configuration is to be procured and tested in a system technology demonstration. The technology demonstration will provide empirical concentrator performance data and integration of the concentrator with the receiver and power conversion subsystems that are being developed in parallel. An aperture diameter of about 10 meters with F/D ratio of 0.6 was chosen for the prototype concentrator. Selection criteria for making this choice were as follows:

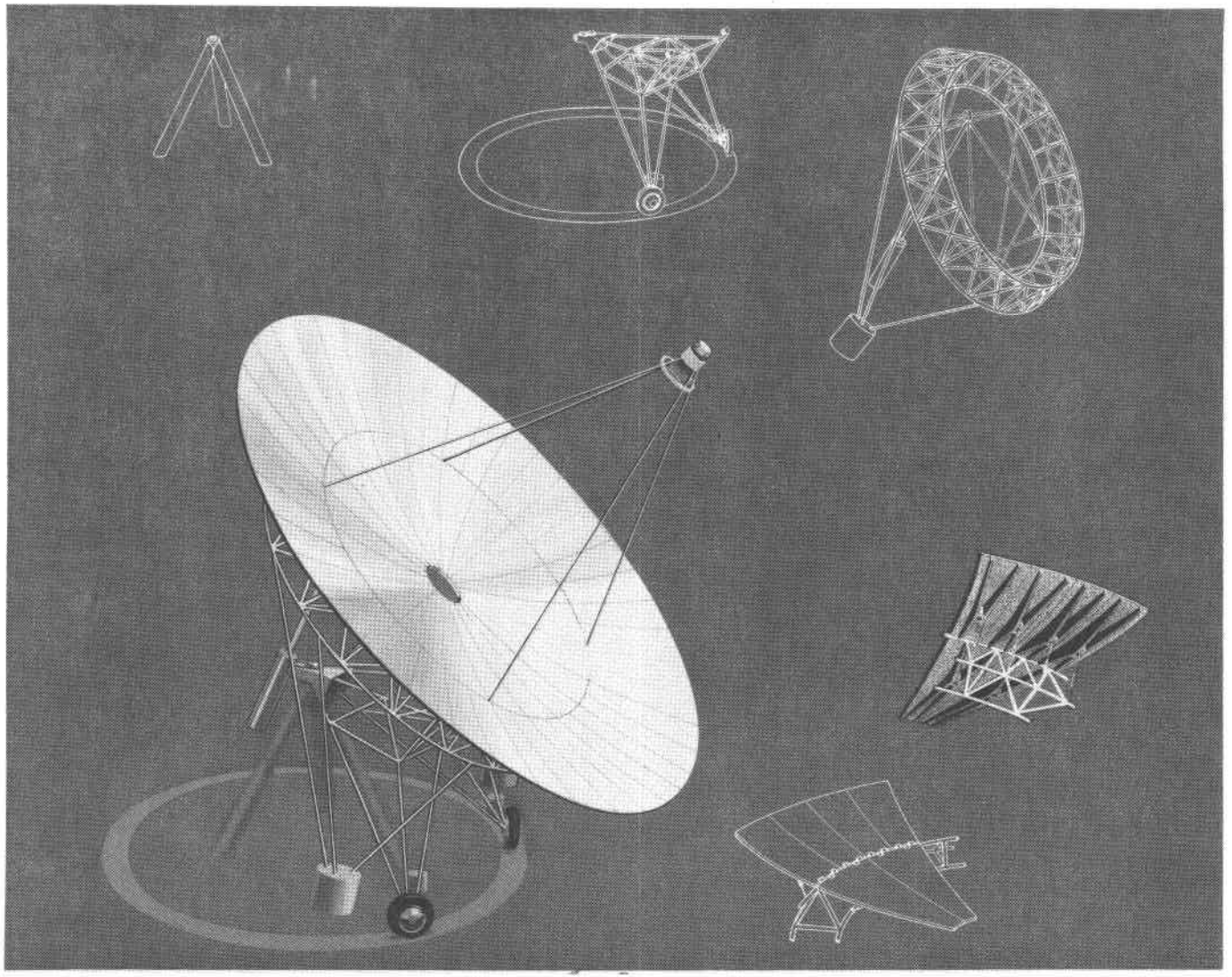

Figure 5-1. Deep-Dish, Point-Focusing Concentrator

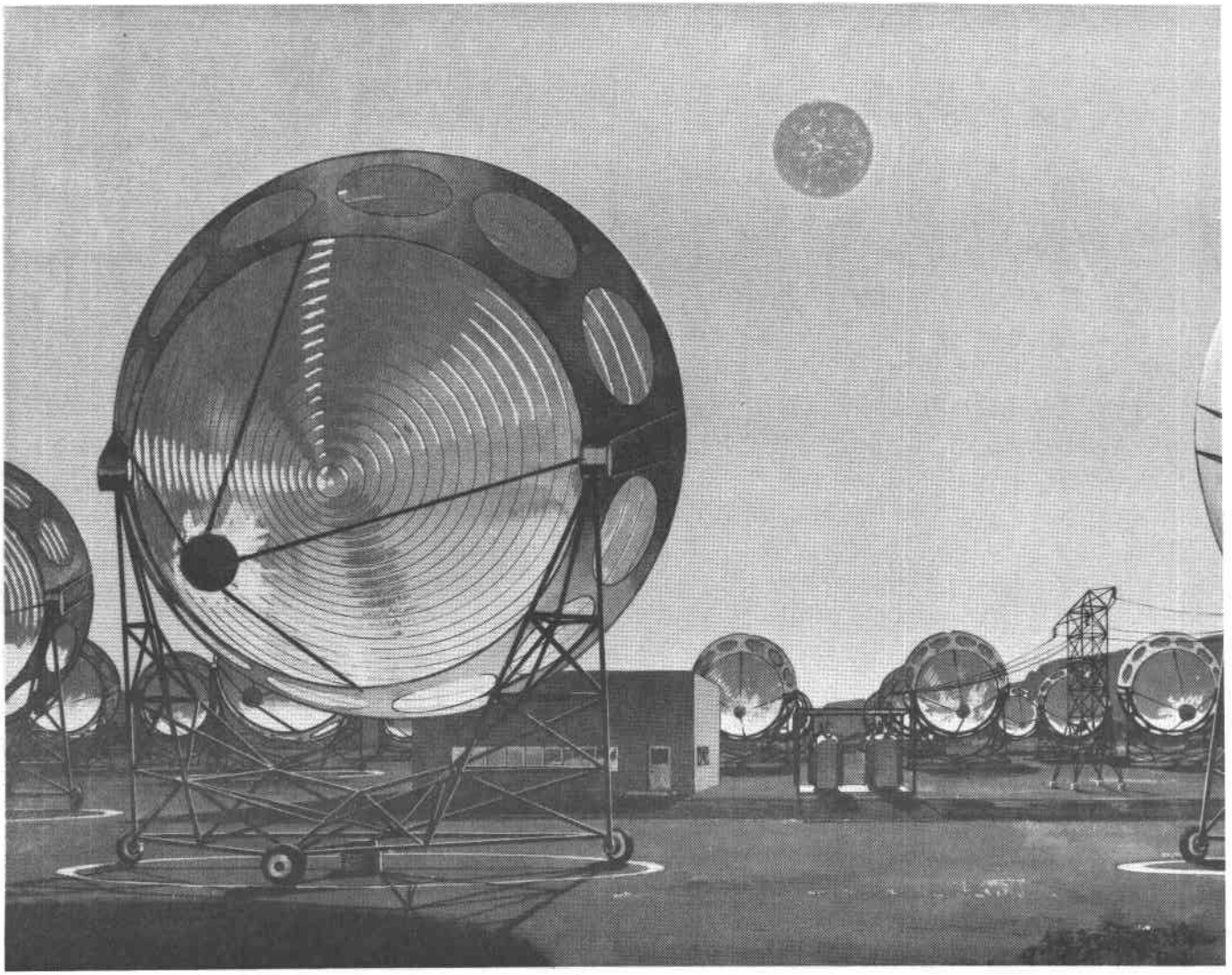

Figure 5-2. Concave Bubble Fresnel Lens Configuration

(1) Represent mid-range technology for dispersed solar thermal systems

(2) Be compatible with selected Stirling engine generators

(3) Be within the limits of existing fabrication capability

It is expected that a development contract will be let in mid FY 1979, with delivery of a prototype concentrator for test before the end of FY 1981.

## D. STRUCTURAL DEFORMATION ANALYSIS

Structural deformation in the concentrator contributes to beam divergence and displacement at the receiver aperture, and therefore, influences aperture sizing. First-order displacement effects can probably be eliminated. Divergence contributions, however, must be accommodated in the receiver optical design.

A preliminary analysis of structural deformation effects at the receiver focal plane was accomplished. The structural deformation effect on the concentration of rays reflected by a representative concentrator with aperture diameter of 12 meters was evaluated by determining the displacement of ray intercepts associated with 100 equal area (Figure 5-3) regions of the dish relative to the displaced focus. The impinging rays were parallel with the undistorted optical axis (Figure 5-4). The effects of displacements and rotations of the reflective surface support structure (other than the mirrored glass gores), the feed support quadripod, the azimuth axis pedestal, the structure between the azimuth and elevation axis, including the elevation drive linear actuator, were included. While the mirrored glass gores were treated as rigid, the effect of their distortion is expected to be small. The resulting ray intercepts are shown in Figures 5-5, 5-6, and 5-7 for three separate loading conditions.

The envelope of intercepts for the cases considered was no larger than a 9.0-cm diameter circle. It can be located within the aperture for static and slowly changing conditions such as wind loads, but not gust loads. Though not all of the available data has been analyzed and plotted, preliminary conclusions can be drawn that with a properly designed concentrator of this type, the dispersion of intercepts (e.g. circular envelope diameter of 9.0 cm) due to structural deformation under the operational design loads at the focal point will contribute no more than 6 percent growth of receiver aperture (e.g., 1.6 cm above current aperture diameter of 25 cm).

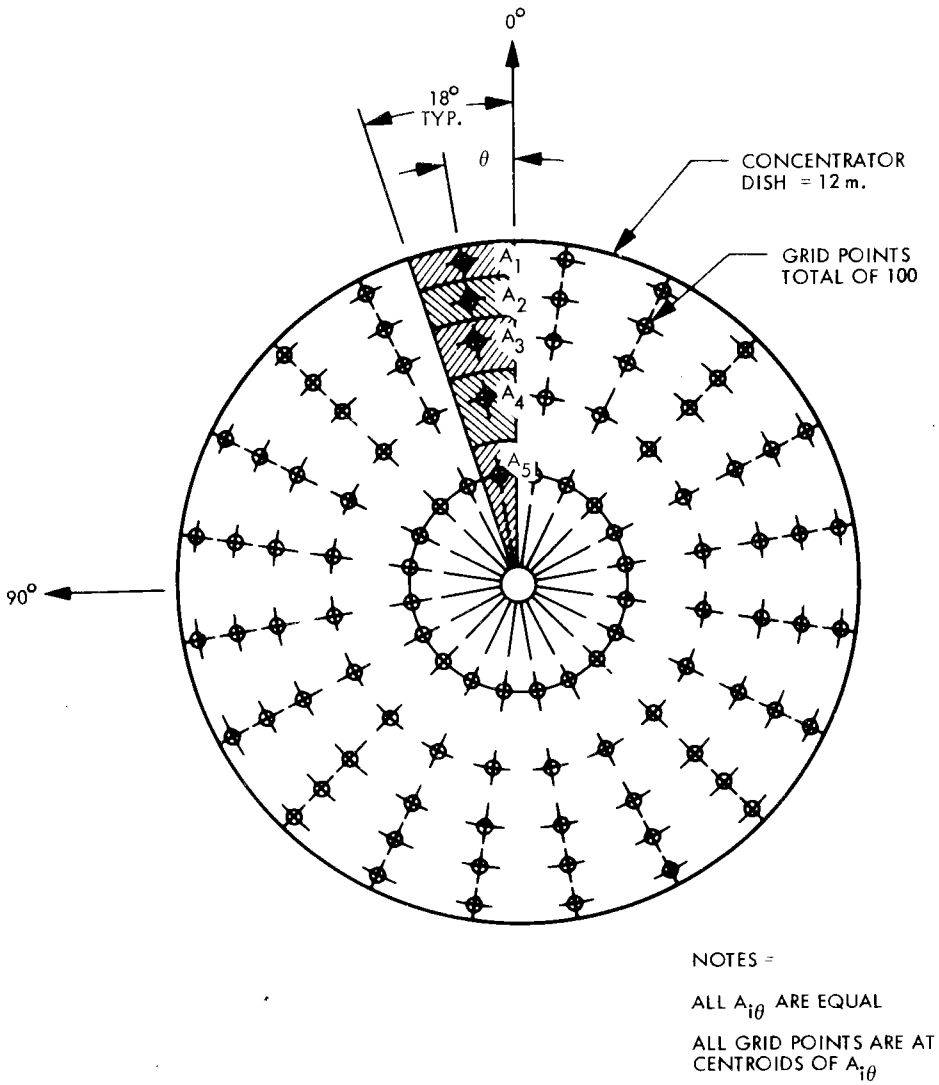


Figure 5-3. Surface Grid Point Geometry for Structural Deformation Analysis

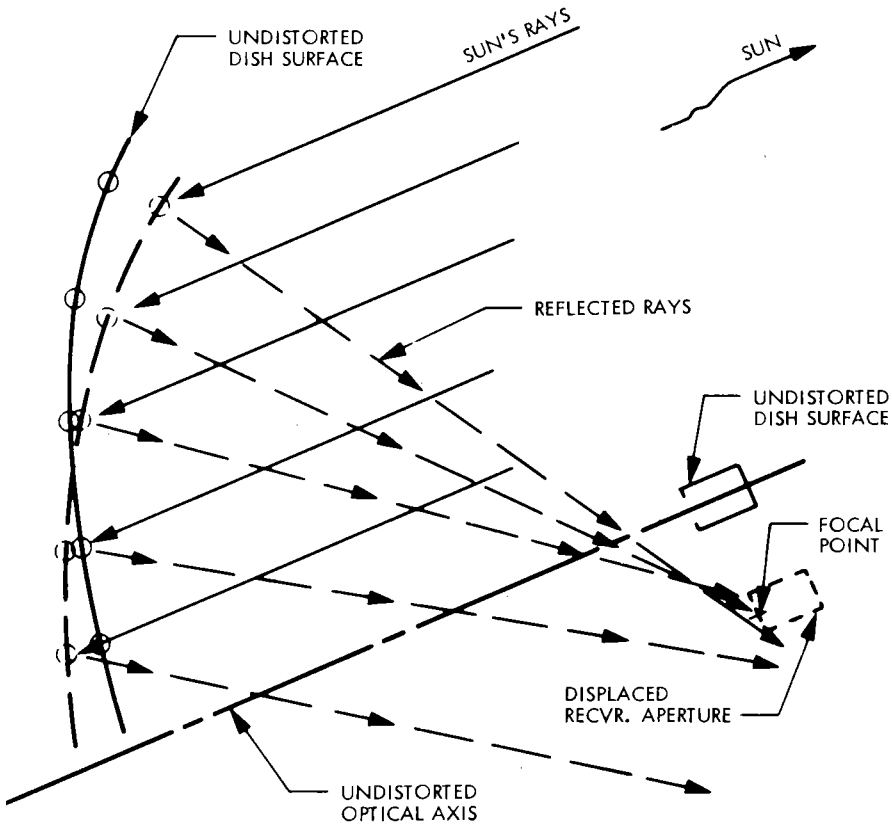


Figure 5-4. Displacement of Reflected Rays Due to Structural Deformation

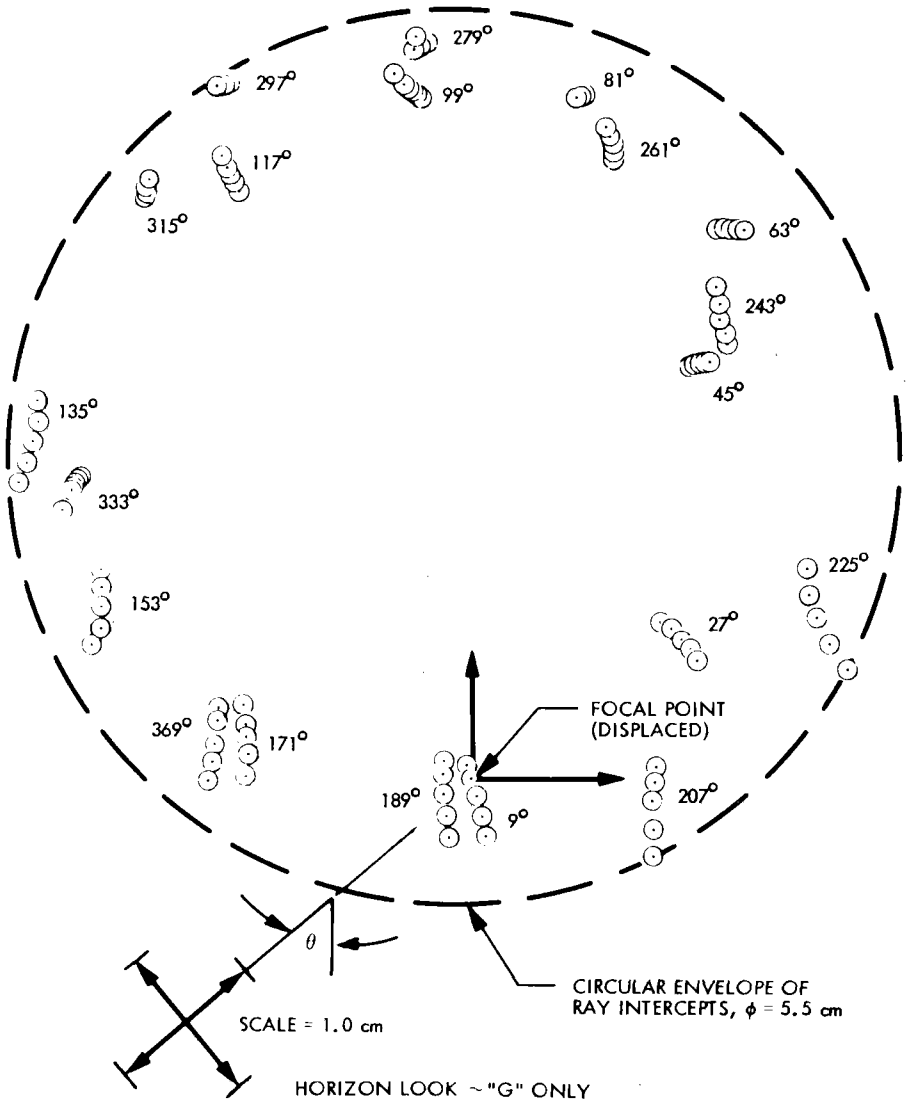


Figure 5-5. Ray Intercepts at Displaced Focal Point

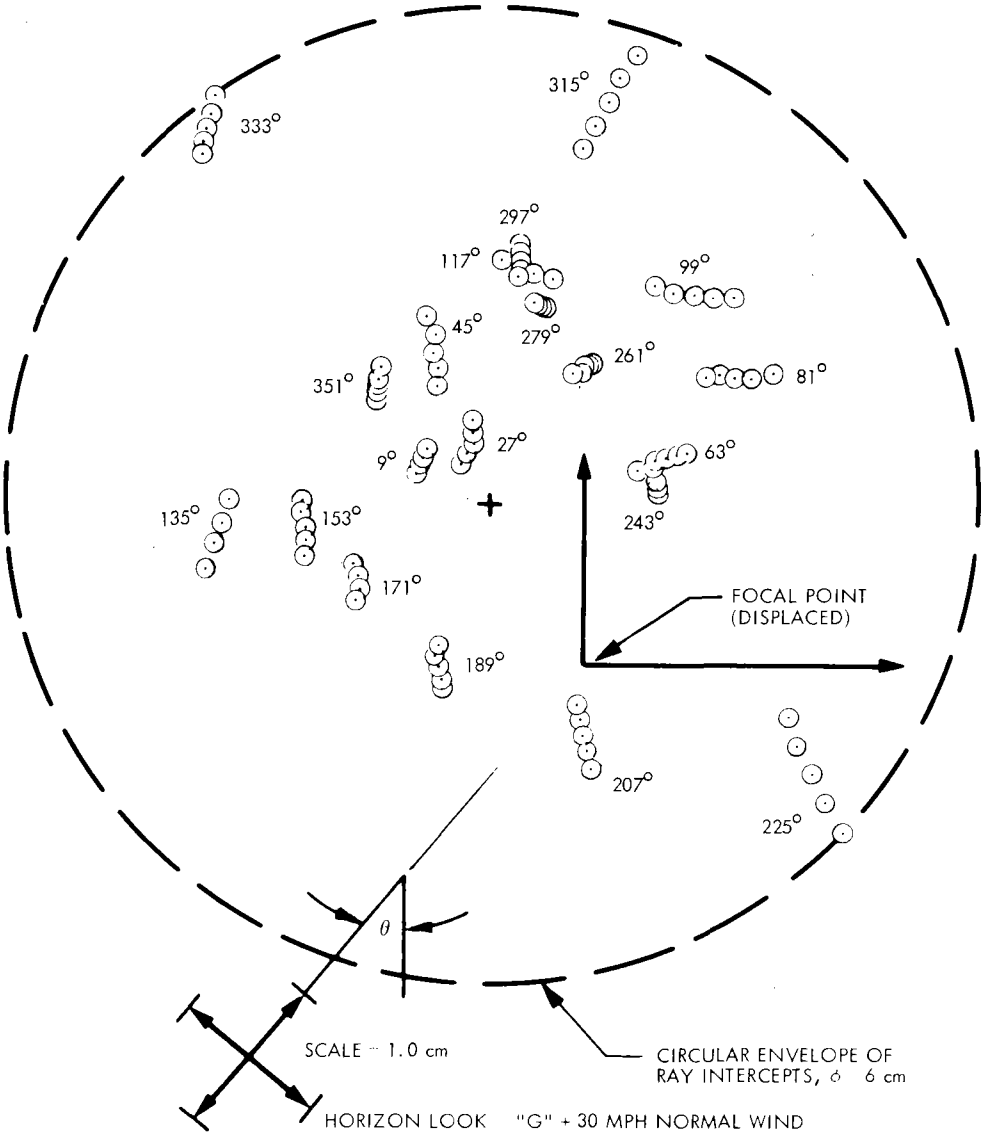


Figure 5-6. Ray Intercepts at Displaced Focal Point

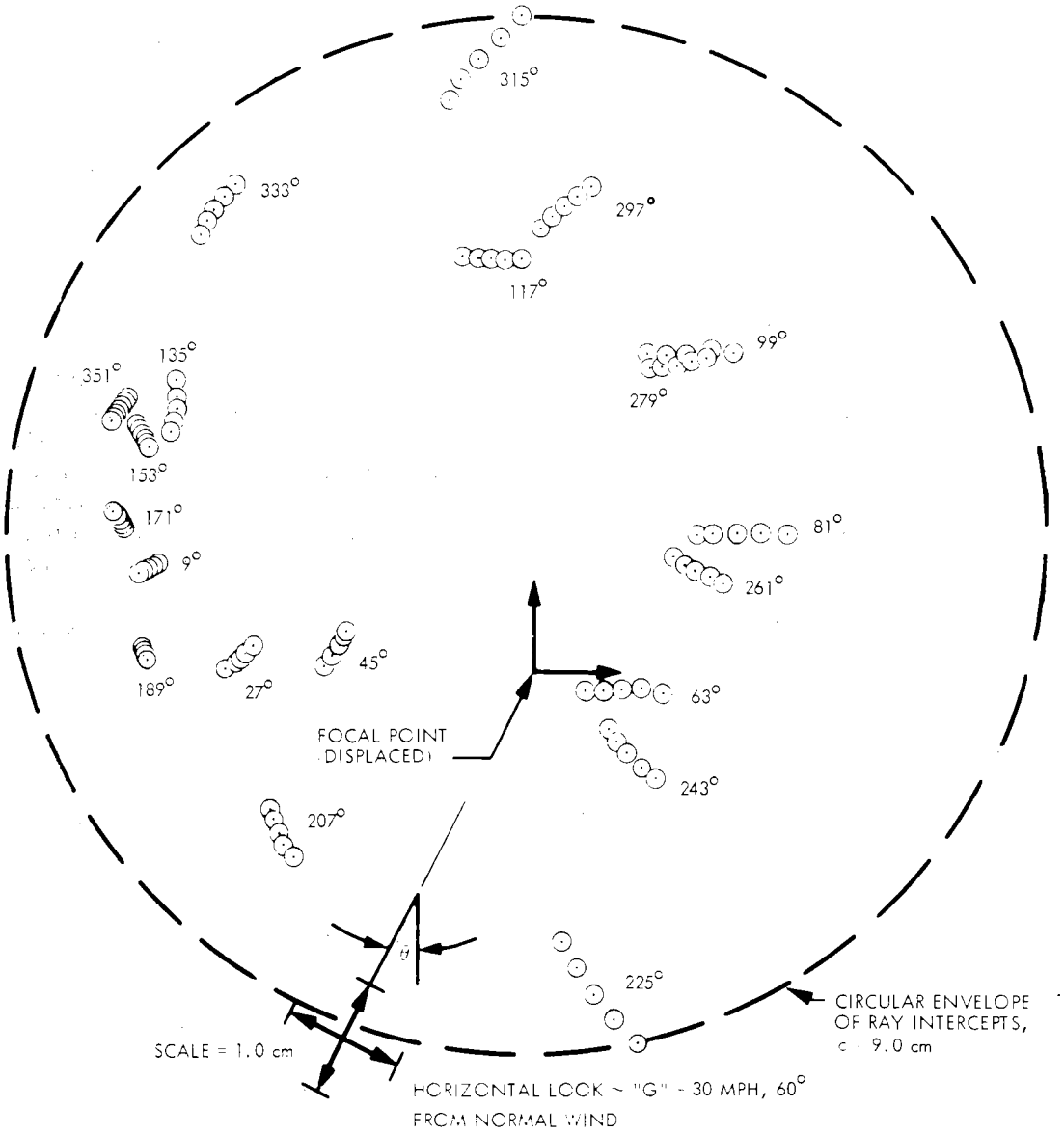


Figure 5-7. Ray Intercepts at Displaced Focal Point

## E. PERFORMANCE OF REFLECTIVE SURFACES

### 1. Introduction

During this reporting period, the investigations of the light reflective surfaces for solar concentrators were continued. Primary consideration was given to high reflectivity glass mirrors with a secondary emphasis on coated metal reflectors. The approach was to survey the most promising candidates from a historical data base, present status and future capability. The aspects treated include efficiency of solar reflectances, effect of dust and contamination accumulation, stability of reflective metallization, environmental effects, cleaning effects and price structure. This subsection summarizes the results of the work performed. A more detailed presentation of data can be found in Appendix A.

### 2. Efficiency of Solar Concentrator Reflective Surfaces

Investigations of the efficiency of solar concentrator mirrors continued during this period. The data from new glass and aluminum mirrors in the absence of environmental degradation effects were reviewed. Data sources included in-house JPL measurements, Sandia Corporation data and McDonnell Douglas Astronautics data, as well as vendor information. (See Tables 5-1 and 5-2.) In general, these data have been organized by experimental sources so that measurements on different batches are kept separate. For example, the Corning glass transmission data (samples 8-11) represent entirely different data sources, glass batches and measurements from the hemispherical reflectance data (samples 27-29).

High reflectance of the mirror is of extreme importance in the successful development of solar concentrators because a relatively small reduction in reflecting efficiency can translate into non-negligible cost penalties. These cost penalties can be due to a number of phenomena such as: (a) larger mirror area required to project a given heat flux into the thermal receiver, (b) higher cleaning costs, and (c) increased mirror operating temperature with resulting decrease in performance life.

This evaluation study shows that second-surface high-quality glass mirrors have the highest potential. Corning Code 0317 fusion glass has solar reflectances in the 90 - 94% range. Some samples of rolled and float glass show high reflectance in the ~85 - 90% range. Front-surface aluminized mirrors also show high reflectivity ~85 - 90% but further evaluation is required to solve the glass versus aluminum question.

### 3. Effect of Dust and Contamination Accumulation

The effect of environmental degradation on mirror reflectance was examined. Atmospheric dust and other contamination were determined to exhibit the single largest concentrator reflectance factor ~20% loss within one month (without cleaning). The environmental factors were found to be complex and, in general, site and season dependent. Various

Table 5-1. Summary of Reflective Surfaces for Solar Concentrator

| No. | Producer/ Supplier | Material Type | Glass Thickness mm (in) | Hemispherical Solar Reflectance | Glass Thickness mm (in) | Solar Transmittance | Reflectance at 500 nm* $R_1$ | $\sigma_1$ (m rad) | $R_2$ | $\sigma_2$ (m rad) | Coef. Thermal Expansion -cm/cm°C | Cost† $/Mft$^2$ | Remarks |
|---|---|---|---|---|---|---|---|---|---|---|---|---|---|
| 1 | Alcoa | Alzak | 0 | 0.85 | 0 | 0 | 0.56 (505) | 0.42 | 0.33 | 10.1 | NA | NA | Aluminum |
| 2 | Alcoa | S460666 | 0 | 0.32 | 0 | 0 | -- | -- | -- | -- | NA | NA | Aluminum |
| 3 | Alcoa | S460667 | 0 | 0.92 | 0 | 0 | -- | -- | -- | -- | NA | NA | Aluminum |
| 4 | ISC | 90-10 | 0 | 0.90 | 0 | 0 | 0.86 | -- | -- | -- | -- | 1.50 | Silver plated brass |
| 5 | ISC | 80-20 | 0 | 0.88 | 0 | 0 | 0.80 | -- | -- | -- | -- | 1.50 | Requires overcoat Cu-Zn 80% Cu, 20% Zn |
| 6 | ISC | 70-30 | 0 | 0.91 | 0 | 0 | 0.81 | -- | -- | -- | -- | 1.50 | |
| 7 | 3M | Scotchcal 5400 | 0 | 0.85 | 0 | 0 | 0.86 | 1.9 | -- | -- | -- | 0.5 (E) | Estimated cost |
| 8 | Corning | Code 7806 (fusion) | | | 1.14 (0.045) | 0.88 | -- | -- | -- | -- | 70 (-7) (0-300°C) | 1.40 | >10 Mft$^2$, $0.45 |
| 9 | Corning | Code 0317 (fusion) | -- | -- | 2.29 (0.090) | 0.910 | -- | -- | -- | -- | 88 (-7) (0-300°C) | 0.65-0.80 1.10-1.80 | Without metallization With metallization |
| 10 | Corning | Code 0317 (fusion) | -- | -- | 1.52 (0.060) | 0.909 | -- | -- | -- | -- | 88 (-7) (0-300°C) | | |
| 11 | Corning | Code 0317 (fusion) | -- | -- | 2.8 (0.110) | 0.903 | -- | -- | -- | -- | 88 (-7) (0-300°C) | | |
| 12 | Schott B270 | B270 (Rolled) | -- | -- | 3 (0.120) | 0.913 | -- | -- | -- | -- | NA | 0.5-0.8 | Without metallization |
| 13 | PPG Works | #6 (Float) | -- | -- | 3.17 (0.125) | 0.881 | -- | -- | -- | -- | 86 (-,) (25-300°C) | 2.15 | >10$^7$ft$^2$, $0.60-0.65 |
| 14 | ASG | (Float) | -- | -- | 3.17 (0.125) | 0.847 | -- | -- | -- | -- | 85 (-7) (0-300°C) | 0.30 | |
| 15 | Sheldahl | Aluminized Teflon | NA | 0.87 | -- | -- | 0.80 | 1.3 | 0.07 | 30.9 | NA | NA | |
| 16 | Kingston Ind. | Kingflux (Al) | 0 | < 0.85 | 0 | 0 | 0.65 (498) | 0.37 | 0.23 | 16.1 | NA | 2.00 | Similar to Alzak; JPL measurements, 85.4% small quantities |
| 17 | Corning | Microsheet Al | -- | 0.95 | 0 | 0 | 0.77 (550) | 1.1 | 0.18 | 6.2 | NA | NA | |
| 18 | Carolina Mirror Co. | 2nd Surface Ag Glass | -- | 0.83 | 0 | 0 | 0.92 | 0.15 | -- | -- | NA | NA | |
| 19 | Payne Co. | Microglass | 0.15 (0.006) | 0.94 | -- | -- | -- | -- | -- | -- | NA | NA | |
| 20 | Payne Co. | Microglass | 0.30 (0.012) | 0.93 | -- | -- | -- | -- | -- | -- | NA | NA | |

* Measurements at other wavelengths are shown in parentheses. Data from R. B. Pettit.

† These costs are preliminary and are being updated.

Table 5-2. Summary of Additional Data on Solar Concentrator Mirrors

| No. | Producer/ Supplier | Material Type | Glass Thickness mm (in) | Hemispherical Solar Reflectance | Glass Thickness mm (in) | Solar Transmittance | Reflectance at 500 nm* $R_1$ | $\sigma_1$ (m rad) | $R_2$ | $\sigma_2$ (m rad) | Coef. Thermal Expansion -cm/cm°C | Cost† $/Mft$^2$ | Remarks |
|---|---|---|---|---|---|---|---|---|---|---|---|---|---|
| 21 | CE | Glass (float) (Soda lime) | -- -- | -- -- | 3.17 (0.125) | 0.838 | -- | -- | -- | -- | 85 (-7) (0-300°C) | 0.50 | |
| 22 | Ford | Glass (float) (soda lime) | -- | -- | 3.17 (0.125) | 0.844 | -- | -- | -- | -- | 85 (-7) (0-300°C) | 0.40 | |
| 23 | Fourco | Glass (float) (Soda lime) | -- | -- | 3.17 (0.125) | 0.891 | -- | -- | -- | -- | -- | NA | |
| 24 | Liberty Mirrors | Cr coated front surface glass | 3.17 (0.125) | 0.65 | -- | -- | -- | -- | -- | -- | 32-93(-7) (20-300°C) | NA | Special measurements |
| 25 | | Lead-sulfide front surface glass | 3.17 (0.125) | 0.25 | -- | -- | -- | -- | -- | -- | 32(-7) (20-300°C) | NA | Auto side mirrors applications only |
| 26 | Schott-Jena | Tempax (sheet) | -- | -- | -- | -- | -- | -- | -- | -- | 32 (-7) (20-300°C) | NA | |
| 27 | Corning | Code 0317 (fusion low Fe) | 1.47 (0.058) | 0.95 ± 1 | -- | -- | -- | -- | -- | -- | 88 (-7) (0-300°C) | + | Sandia data + see item #9 vacuum deposited silver |
| 28 | Corning | Code 0317 (fusion low Fe) | 1.47 (0.058) | 0.94 ± 1 | -- | -- | -- | -- | -- | -- | 88 (-7) (0-300°C) | + | Sandia data + see item #9 chemically deposited silver |
| 29 | Corning | Code 0317 (fusion low Fe) | 1.47 (0.058) | 0.926 | -- | -- | -- | -- | -- | -- | 88 (-7) (0-300°C) | + | JPL measurements old glass. 12/1/78 |
| 30 | 3M | Metallized Polyester | 0.07 (0.0028) | 0.86 | -- | -- | 0.86 (E) | 1.9 (E) | -- | -- | -- | 0.50 | Measurements @AM2 20% degradation/7 yrs. |
| 31 | Flabeg Corp. | Crown Glass (float) | 3.17 (0.125) | TBD | -- | -- | -- | -- | -- | -- | 70 (-7) (0-300°C) | -- | Resin and/or Mylar reverse side sealant |
| 32 | Corning | 7806 (modified) (fusion) | 0.050(E) | 0.95 (E) | -- | -- | -- | -- | -- | -- | 70 (-7) (0-300°C) | -- | |

* Measurements at other wavelengths are shown in parentheses. Data from R. B. Pettit.

† These costs are preliminary and are being updated.

E Estimated

types of atmospheric contamination were identified and typical particle sizes lie in the 1 - 80 micron diameter range. Approaches to minimize these effects include surface treatment (such as antistatic coatings), cleaning solution compatibility, and cleaning frequency optimization.

## 4. Stability of Reflective Coatings

A review of the various types of reflective coatings for both first surface aluminum and second surface glass mirrors was undertaken. Basically two practical methods are in current use (a) chemical vapor deposition and (b) vacuum deposition. Both types of coatings have been used successfully within the mirror industry. This evaluation shows that both methods are comparable, with the vacuum deposition method being superior initially. Coating stability with time, however, depends on the type and quality of sealants used to protect the coating from the environment. Further research in this area is needed.

## 5. Environmental Effects

Deployment of solar concentrator mirrors in the natural environment will subject it to a variety of phenomena. Temperature and humidity are the primary phenomena of concern with hail, ozone, dew, snow and other hazards being secondary. Proper design is important for temperature control and high performance sealants are needed to prevent environmental attack of the metallization.

## 6. Cleaning of Reflective Surfaces

Mirrors exposed to the natural environment will undergo degradation effect due to dust/contamination on the surface and, therefore, will require periodic cleaning. Various cleaning methods are under consideration but further research is required to identify the type of cleaning agent that will do minimum damage to the mirror surface. At the present time, frequent cleaning with de-ionized water and soft wiping cloth appears most desirable. Experimental confirmation is needed.

## 7. Price Estimates

Some price information on glass and aluminum reflective surfaces has been accumulated. Initial estimates show glass to be cheaper than front surface aluminum. Glass in relatively large batches, the order of one million square feet, may be obtained in the near future for 0.65 - 0.80 dollars per square foot. The silver metallization in mass production may be obtainable in the range of 0.5 - 1.00 dollars per square foot. Although the front surface mirrors are more expensive at the present time, this situation could change rapidly as the solar concentrator technology matures.

## F. CELLULAR GLASS GORE ENGINEERING TEST UNIT DEVELOPMENT

### 1. Introduction

The reflecting paraboloidal surface of the advanced concentrator conceptual design is constructed from mirrored, cellular glass gores cantilevered from a truss-type support ring. During this reporting period, progress was made in the cellular glass gore development procurement.

### 2. Preliminary Cellular Glass Gore Design

The previous conceptual cellular glass gore design was modified in an attempt to simplify fabrication of the gore. Figure 5-8 presents the preliminary design for the outer gores of the dish concentrator.

### 3. Fabrication Concepts

Fabrication concepts for the cellular glass gore were conceptualized during this reporting period. The preliminary gore design will require cellular glass pieces laminated together using some form of bonding. Lamination studies will be required in FY79 to perfect this technology. A back-silvered glass mirror must be continuously bonded to the machined cellular glass surface. Figure 5-9 shows a proposed concept for achieving an accurate paraboloidal mirror surface. The back-silvered glass sheet is deformed over a precision mold surface and held in place by vacuum. Adhesive material is spread over this surface and the cellular glass gore is then positioned onto this material. The adhesive is allowed to set. The bond material then takes up the irregularity in the cellular glass surface.

### 4. Prototype Hardware

A contract shall be issued early in FY79 for procurement of three cellular glass gores.

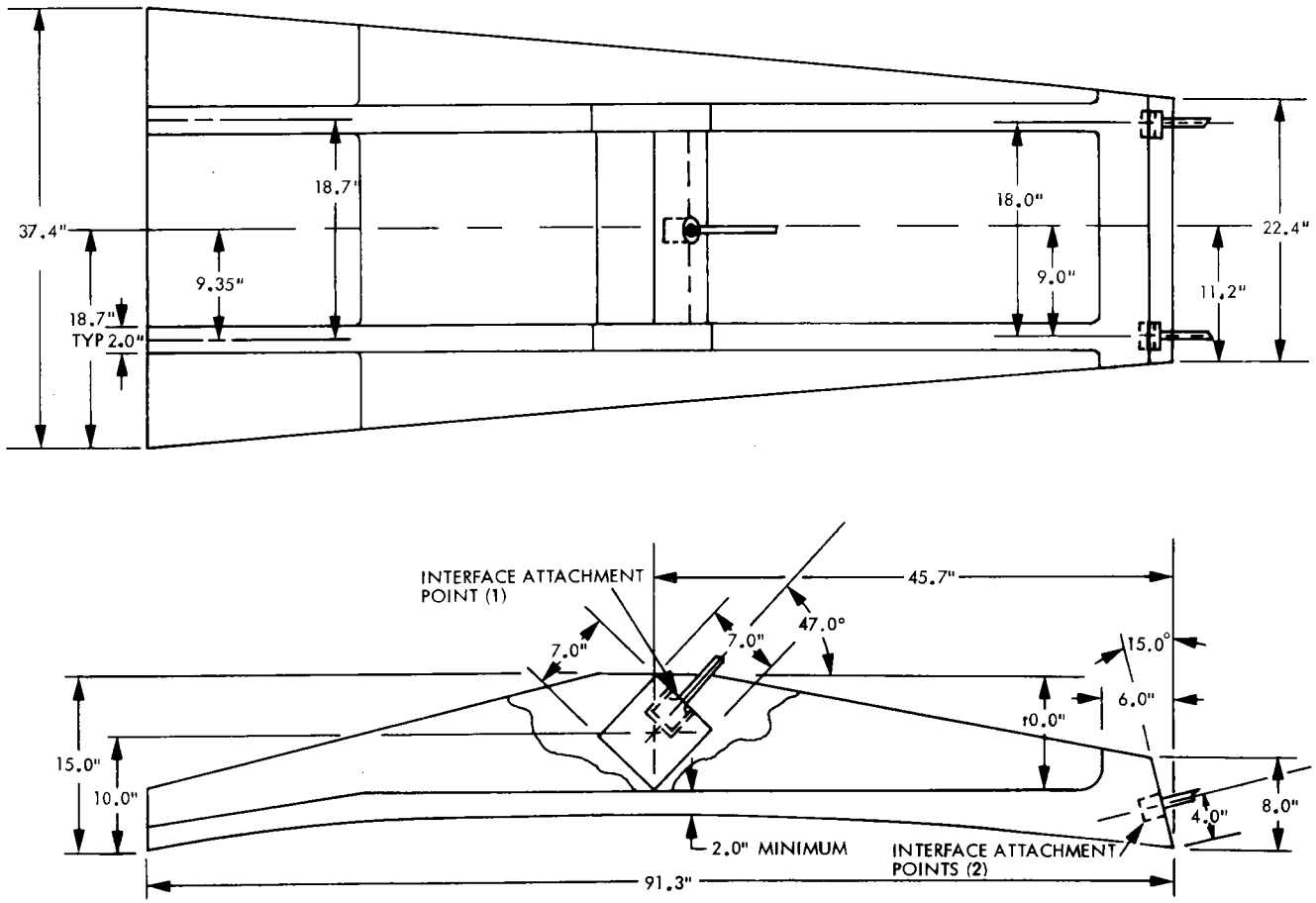


Figure 5-8. Preliminary Design of Cellular Glass Gore

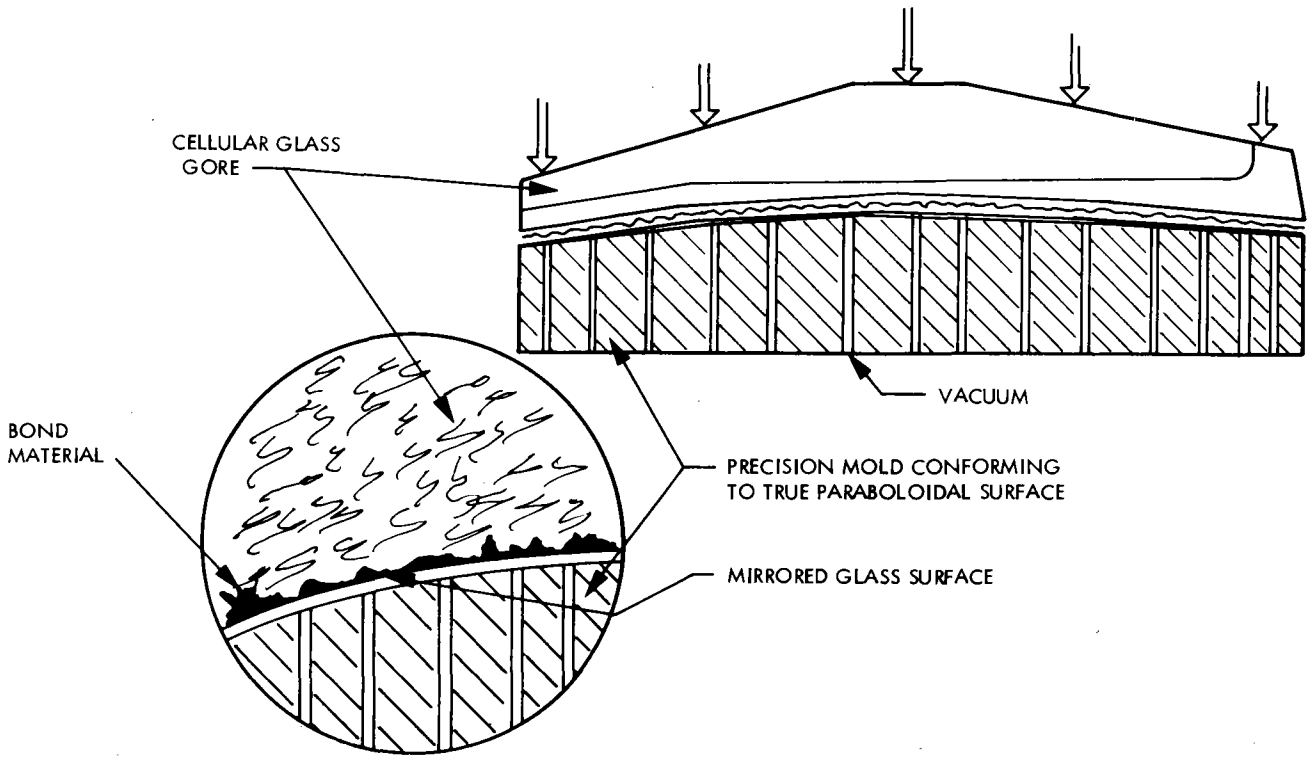


Figure 5-9. Cellular Glass Gore Mirror Fabrication

# SECTION VI

# ADVANCED RECEIVERS

# SECTION VI

# ADVANCED RECEIVER

## A. INTRODUCTION

The main thrust in the advanced receiver efforts in the first six months was on exploration of advanced concepts potentially leading to the development of low-cost, high-efficiency, reliable, long-life solar receivers. This receiver will be part of a distributed receiver solar power system using a Stirling engine power conversion subsystem known as Advanced Development System No.1 (ADS #1). In the first six-month period, this work, along with some preliminary system and component definition and requirement work, was essentially conducted in-house. These efforts are continuing in the current period.

In the current report period, conceptual designs were developed for receiver concepts generated in the first report period. These designs are being modelled and will be analyzed by the use of a developed computer program to assess their relative performances for the selection of a best design for further development and to provide fundamental receiver performance information.

Both the heat pipe receiver design and the non-heat pipe design will be evaluated to provide alternate approaches to the dish-Stirling system. To secure the best concepts possible from all sources, solicitation of alternate receiver concepts from industry sources was also initiated. An RFP procurement package for the Design and Fabrication of a non-heat pipe Dish-Stirling Solar Receiver was prepared and the RFP was released in October, 1978. Also, an RFP for a heat pipe receiver will be issued in November.

## B. TECHNICAL APPROACH

The current activities were a continuation of work from the last report period, and were in the following areas: receiver computer program development, preliminary heat exchanger design for receiver concepts generated in the first report period, and preliminary cavity and insulation designs. More details are given in the following discussion.

### 1. Receiver Computer Program Development

In order to provide an effective tool for the analysis of receiver performances of various configurations and to provide a receiver design tool the development of a receiver computer program was initiated. The development work continued into this report period. The program has been

evaluated by using it on a receiver for which test data were available. The agreement between predicted and actual test data was quite good so the program is now in the operational condition. It will be used for the future performance analysis of receiver concepts and designs, and can be used in the fine tuning of any receiver design. The program, called HEAP, is now available for use with the release and publication of a report describing the code.

## 2. Preliminary Heat Exchanger Design

In the first report period, all the receiver concepts generated were classified into five categories, i.e., receiver using simple directly exposed heat exchanger tubes, receiver using buried heat exchanger tubes, receiver with porous structure heat exchanger, heat-pipe receiver, and receiver with liquid metal transport loop.

A simple tube, (non-heatpipe), heat exchanger was designed to establish a base-line design for comparison with future receiver designs. An important aspect of this task was to formulate a method of determining the necessary heat transfer area for different tube configurations.

The receiver was designed to meet the requirements of a proposed Stirling engine operating at a mean pressure of 2500 psia, and at an average bulk gas temperature in the heater region of 1500°F. The heater was required to supply the engine with 53 kW of thermal energy. The two major constraints on the selection of the heater tube configuration were void volume and peak pressure drop. The void volume was not to exceed 1.5 in.$^3$ with a maximum allowable pressure drop of 10 psi.

A computer program was developed to model the receiver tubes in various configurations. The average heat transfer coefficient and peak pressure drop for a given number of tubes of a certain internal diameter were determined through the use of the computer program. The program was written to use this information to determine the tube length (and resulting void volume) required to transfer 53 kW of thermal energy. A large number of possible tube configurations were evaluated. Calculated results showing the interrelationship of heat transfer coefficient, pressure drop, void volume, tube I.D., and number of tubes are available.

The results were used to determine which of the configurations met the design requirements. The combinations which met the requirements consisted of a large number (>80) of a small diameter (ID < 0.04") tubes. One of the acceptable combinations was used in the baseline receiver design. Essential parameters of this design are given in Table 6-1.

This simple tube receiver design was selected to minimize the possibility of local hot spots by providing the receiver with a uniform heat flux. The area per tube exposed to the insolation was increased by approximately 700% when compared to the receiver tested at Table Mountain. The ceramic cavity was designed to reflect the insolation onto the tubes, while minimizing the amount of insolation back-reflected out of the aperture.

Table 6-1. Preliminary Receiver Design Parameters

| | |
|---|---|
| No. of Tubes | 141 |
| Tube Diameter (ID) | 0.0028 ft (0.0336 in) |
| Tube Length | 1.0 ft |
| Average Heat Transfer Coefficient | 1080 Btu/hr-ft$^2$-°F |
| Heat Transfer Area | 1.23 ft$^2$ |
| Peak Pressure Drop | 10.8 psi |
| Void Volume | 1.49 in$^3$ |

In order to reduce the manufacturing cost and improve reliability, the receiver constraints have recently been changed. The void volume has a maximum limit of 10 in$^3$ and the peak pressure drop is 18 psi. These changes will have a large effect on the design. It is now possible for the receiver to be made from a small number (≈25) of large diameter (≈0.25") tubes. The receiver will be redesigned on the basis of the new constraints.

After the completion of the simple tube receiver, the concept of tubes embedded in a thermal storage media will be investigated. Several eutectic salts are being considered as the storage media. In addition to thermal storage, the constant temperature of a melting/freezing salt will provide uniform tube temperatures, thus minimizing thermal stresses.

## 3. Cavity and Insulation Design

Heat losses from a solar receiver are by radiation (and reflection), convection, and conduction. Proper design of receiver cavity and cavity insulation can minimize these losses and thus improve the performance of a solar receiver. For this reason cavity and its insulation design are also an important portion of the receiver development work. In this report period a preliminary study was made in these two areas.

For the type of application under consideration, a cavity type of receiver is more efficient than an external receiver, therefore, only a cavity receiver was considered in the present development work. In a cavity receiver the aperture and the cavity geometries are the two major factors affecting performance and were carefully studied in the design process.

For an isothermal diffuse-surface receiver, the whole interior surface is treated as one single surface, and the geometric (or view) factor between the cavity wall ($A_W$) and the opening area ($A_O$) can be

simply defined in terms of the area ratio of the aperture to cavity wall ($A_o/A_w$). The radiation loss, regardless of the cavity shape, can be estimated using $A_o/A_w$ as parameter. In practice, the receiver is not isothermal but rather a non-uniform temperature cavity, and the energy exchange between individual surfaces at different temperatures and orientations would have to be taken into consideration. Accordingly, receivers with different internal shapes will have different efficiencies. It is, therefore, important to optimize the cavity shape to achieve a high receiver efficiency.

Three regular geometries, a sphere, a cylinder, and a frustum of cone, were used to evaluate the geometric effect on receiver performance. The relationship between the receiver efficiency and the area ratio of the cavity size to the aperture size ($A_w/A_o$) was obtained. The frustum receiver has the highest efficiency compared to the cylindrical receiver and the spherical receiver. The simple tube receiver efficiency changed from 74 percent to 77 percent depending on the cavity shape and size.

One of the requirements for the receiver design is to deliver the working fluid to the engine at a temperature in the neighborhood of 800°C (1500°F), this implies an average cavity temperature of 850°C (1600°F) will have to be maintained. As the cavity temperature increases, the temperature gradiant also increases, which means a higher conduction loss for the receiver. Thus, it is essential to use an insulation with low thermal conductivity at high temperature gradient. However, for most materials, the thermal conductivities tend to increase at higher temperature. Several high temperature insulation materials and their thermal conductivities at various temperatures are shown in Table 6-2. Materials operating in the high temperature range must possess chemical and thermal stabilitiy so that the material will not undergo physical or crystallographic phase change. For instance, Table 6-2 shows calcium silicate which is used for experimental receiver, has a maximum temperature 650°C (1200°F), as a result, for a temperature of 850°C, it is necessary to utilize other insulation materials or alternate approaches.

Two approaches can be taken to provide the insulation for a receiver at 850°C, either by using different materials having lower conductivities and at the same time physically and chemically stable at high temperatures, or using different techniques to meet this purpose.

At high temperatures, insulation materials usually can be classified in either one of the following forms: powders, foams, fiber and dense material. For any mixture, the property of the mixture depends on the property of each component that comprises the mixture. It is, therefore, advisable to use low thermal conductivity material for each component. Since gases have lower thermal conductivities than solid, high temperature insulation materials often use gases as one component of the mixture. The thermal conductivity depends on the areas occupied by gases and solid. Thus, loosely filled, powder insulation has the lowest thermal conductivity but requires a container. Fiberous

Table 6-2. Thermal Conductivities of Insulation Material for High Temperature (W/cm°C)

| Material | Max Temp. °C (°F) | 260°C (500°F) | 537.7°C (1000°F) | 815.5°C (1500°F) |
|---|---|---|---|---|
| Diatomaceous earth, silicon powder | 815.5 (1500) | $9.17 \times 10^{-4}$ | $1.28 \times 10^{-3}$ | N/A |
| Fiberglass, metal mesh blanket, #900 | 537.7 (1000) | $6.92 \times 10^{-4}$ | N/A | N/A |
| Glass block | 871.1 (1600) | $9.17 \times 10^{-4}$ | $1.28 \times 10^{-3}$ | N/A |
| Hydrono Calcium Silicate | 648.8 (1200) | $7.78 \times 10^{-4}$ | N/A | N/A |
| Micro-quartz fiber, blanket | 1649.0 (3000) | $7.27 \times 10^{-4}$ | $1.29 \times 10^{-3}$ | $1.87 \times 10^{-3}$ |
| Zirconia grain | 1659.0 (3000) | $1.87 \times 10^{-3}$ | $2.23 \times 10^{-3}$ | $2.82 \times 10^{-3}$ |

materials are very common at high temperatures. Asbestos fibers, fiberous potassium titanate, aluminum silica fibers, carbon and graphite fibers and zirconide fibers are commercially available insulation.

Among them, zirconide fibers have been extensively used in the metallurgical industry and are found to have a melting point of 2600°C. It is chemically stable at high temperatures since it is a fully oxidized ceramic composition.

These were only the results of a preliminary survey. Other insulation materials and techniques will be explored during the next reporting period.

## C. FUTURE PLANS

The work of the advanced receiver subsystem for ADS #1 has progressed from the concept generation stage to the preliminary design stage and will very soon proceed to the detailed design and prototype fabrication and finally to prototype testing. The efforts planned for the next reporting period are described in the following paragraphs.

1. Receiver Performance Analysis

With the HEAP program ready and the preliminary design on hand receiver performance analysis will be conducted on continuous basis to achieve the following purposes:

(1) To ascertain the potential performance of each design configuration.

(2) To understand the receiver general characteristics and the transient behavior of each design.

(3) To provide information for the fine-tuning of improved design.

(4) To double check the contractor's analysis and design.

(5) To provide information for a better formulation of prototype test program.

2. Final Establishment of Interface Requirements with the Concentrator and the Power Conversion Subsystem

This again is a continuous effort due to the fact that both the concentrator and the power conversion subsystems are being developed at the same time. In the design phase the effort will be intensified to work out practical interface problems to meet the design purposes.

3. Formulation of Prototype Test Plan

A good test plan is absolutely necessary for the collection of the maximum amount of useful test data with minimum of expenditures. For this reason a prototype test plan will be worked out thoroughly in the near future and the following will be carefully taken into consideration.

(1) Identification of essential test parameters.

(2) Formulation of test ranges.

(3) Establishment of instrumentation requirements.

(4) Establishment of minimum test facility requirements.

(5) Formulation of test procedures.

(6) Establishment of test criteria.

(7) Establishment of safety requirements and procedures.

4. Development of a Terminal Concentrator for the Enhancement of Receiver Efficiency.

As found in Ref. 6-2, an 80% efficiency can be expected for a receiver that will meet the ADS #1 operation requirements. In order to increase this efficiency to a higher level, either a very high quality concentrator or a well designed terminal concentrator is required. A high quality concentrator may be very costly; therefore, the pursuit of an effective terminal concentrator appears to be a worthwhile effort for the enhancement of receiver efficiency.

5. Development of Support Technology Program

Many factors affect the performance, the lifetime and the cost of a receiver. An understanding of the effects of these factors is a prerequisite to achieving the development goal of the advanced receiver subsystem. For this reason, the program for the investigation of the important factors will be formulated and undertaken to support the main receiver development effort. The following are a few of the important areas in which research work is necessary:

(1) Temperature gradient - material interrelation.

(2) Material compatibility with working fluid.

(3) Heat transfer problems peculiar to specific configuration.

## REFERENCES


6-1. "Thermal Power Systems, Research and Development Project, Advanced Technology Development Semi-Annual Progress Report," JPL Publication 78-3, Jet Propulsion Laboratory, Pasadena, California, June 1978.

6-2. "Solar Receiver Performance in the Temperature Range of 300° to 1300°C," JPL Internal Document No. 5102-82, Jet Propulsion Laboratory, Pasadena, California, May 1978.

6-3. "Evaluation of Sanders Associates Solar Receiver Concept," JPL Internal Document No. 5102-87, Jet Propulsion Laboratory, Pasadena, California, August 1978.

# SECTION VII

# TRACKING AND CONTROL ANALYSIS

## SECTION VII

## TRACKING AND CONTROL ANALYSIS

The major work emphasis during this reporting period was directed toward the important areas of intercept factor analysis and an optimal control formulation of the sun tracking problem. Previously, an intercept factor function was derived and it was assumed that a Gaussian flux distribution was generated at the focal plane. This was expressed as follows:

$$\Phi(R,\delta) = \int_0^R \frac{z}{\sigma^2} e^{-(z^2+\delta^2/2\sigma^2)} I_o\left(\frac{z\delta}{\sigma^2}\right) dz \qquad (1)$$

where R was aperture radius, z was radial dimension, S was pointing error, $\sigma$ was the standard derivation of the flux distribution, and $I_o(\cdot)$ was a Bessel function.

As a natural consequence, the intercept factor function for a radially symmetric flux distribution at the focal plane was derived which more closely modeled expected distributions that are to be found in actual systems. Then, the expected value of the intercept factor for typical control schemes was derived to give a measure of energy loss due to the control employed. The control method class analyzed was the on-off deadband type which is often found in solar collector systems. The expression for the expected value is:

$$E\{\Phi(A)\} = \int_0^{\sqrt{2}\,A} f_z(z)\ \Phi(z)\ dz \qquad (2)$$

where A is the deadband size, $f_z(z)$ is the pointing error density function, and $\Phi$ is the intercept factor function. Detailed analysis, results, and examples are given in Appendix B-1.

The other major area of accomplishment was the optimal control formulation of the sun tracking control problem. Because the varied methods for control (on-off, proportional, et al.,) have different performance characteristics, it was desired to develop a bench mark algorithm that could be used as a comparison technique.

It was shown that the disciplines of Modern Control Theory and Optimal Control Theory, which are generally reserved for aerospace and large scale systems applications, can be straightforwardly applied to the sun tracking performance of solar concentrators. With the conversion

from a standard tracking problem to a regulator problem using the trim rate technique, and with the optimal control formulation, it was shown that an almost zero steady state tracking error could be achieved (even with wind disturbances). This implies less energy will be lost and the entire system will be more cost effective.

The optimal control techniques described in detail in Appendix B-2 offer a straightforward, albeit time consuming, methodology for deriving control algorithms. A very important ramification of these techniques is that they can serve as comparison standards for other types of control algorithms and aid in their development.

# SECTION VIII

# OPTICAL ANALYSIS

# SECTION VIII

# OPTICAL ANALYSIS

## A. INTRODUCTION

A central problem inherent in the development of a solar-thermal power system is the optical analysis of the solar concentrators. A fundamental point of optical analysis is that the solar source is not a point source. Rather, the light from the small, but finite solar source arriving at any small element of the reflector, is a cone. Consequently, cone optics is employed instead of the classical ray tracing optics. An optical performance analysis of various solar concentrators was made using Schrenk's simulation procedures (Refs. 8-1 and 8-2 which are based on cone optics. The basic assumptions include treating the solar disk either as a uniform source or one with limb darkening (i.e., decreasing brightness from the center of the disk toward the limb), neglecting the circumsolar radiation. The pointing or tracking error is taken to be deterministic while the surface errors, as well as specular spreading, are assumed to be uniform distributions. The above simplified assumptions are made in order to provide quick, first-cut analysis of a variety of concentrator concepts. Other error distributions, such as normal distributions, will be employed in future as needed, with a great increase in computing time.

Progress has been made in the past reporting period in the optical performance analysis of the following areas:

(1) Paraboloidal reflector

(2) Offset paraboloidal reflector

(3) CPC - Fresnel and CPC - paraboloid systems

(4) Cassegrainian system

(5) Cavity flux computations

Analyses of (1) and (5) are presented in this section, and (2), (3), and (4) are presented in Appendix C.

## B. PARABOLOIDAL REFLECTOR

Some results for the simple paraboloidal reflector (F/D=1) were reported previously in References 8-3 and 8-4 as a basis of comparison for a Fresnel-type concentrator with truncated paraboloidal facets. Further results were obtained in terms of the normalized concentration ratio for F/D=0.6, where F and D represent the focal length and the diameter of the reflector respectively, and the normalized concentration ratio refers to the quantity: concentration ratio/reflectivity of the reflector. The distribution of the normalized concentration ratio is

given as a function of R/D, where R denotes the radial distance from the optical axis in the focal plane of the paraboloid. The effect of limb darkening on the flux distributions is to replace the "flat top" by a smooth-varying dome-shaped curve. The intercept factor, which is defined as the ratio of the energy entering the receiver aperture to the total solar energy arriving at the focal plane, plays a key role in determining the optimal receiver aperture size for the collection of maximum net thermal energy. The computed flux distributions at the focal plane for the paraboloidal reflector of F/D=0.6 are presented in Figures 8-1 to 8-5, which correspond to the following cases:

| | | |
|---|---|---|
| (1) | Flux distribution for ideal case (no slope error no specular spreading and no tracking error) | (Fig. 8-1) |
| (2) | Intercept factor for ideal case | (Fig. 8-2) |
| (3) | Flux distributions for various slope errors (0.0°, 0.1°, 0.2° and 0.3°) | (Fig. 8-3) |
| (4) | Intercept factor for the above slope errors | (Fig. 8-4) |
| (5) | Flux distributions for various tracking errors (0.0°, 0.1°, 0.2° and 0.3°) | (Fig. 8-5) |

If the diameter of the concentrator is taken to be 10 m, then from Figure 8-1 the extent of the solar image is determined to be about 4.5 cm in radius and the intercept factor for a given radius of the cavity opening can be determined from Figure 8-2. The degradation of the concentration ratio is very severe as the slope error increases, as shown in Figure 8-3. The intercept factor as a function of R/D for the various slope errors is given in Figure 8-4 from which one may compare the sizes of various cavity openings for various slope errors for a given value of the intercept factor. For example, if the intercept factor is 90%, the radius of the cavity opening has to be increased by approximately 2.3 cm when the slope error is increased by 0.1°. Figure 8-5 shows that the net effect of the tracking errors on the flux distribution is a displacement with very little distortion of the shape except for a slight bending near the "tails" of the distribution.

## C. CAVITY FLUX COMPUTATIONS

The importance of the computed flux distributions at the focal plane is that it serves as a preliminary baseline for sizing the receiver aperture opening. It is very tempting to use the incident fluxes at the focal plane to calculate the reradiation from the cavity opening by treating the latter as a grey body. However, this usually leads to underestimation of the reradiation losses which play an important role in the system optimization of the receiver. The next iteration is to compute the fluxes incident on the walls of the receiver cavity which serve as direct inputs to a heat transfer program. For the purpose of providing parametric inputs for the optical-thermal interface, flux

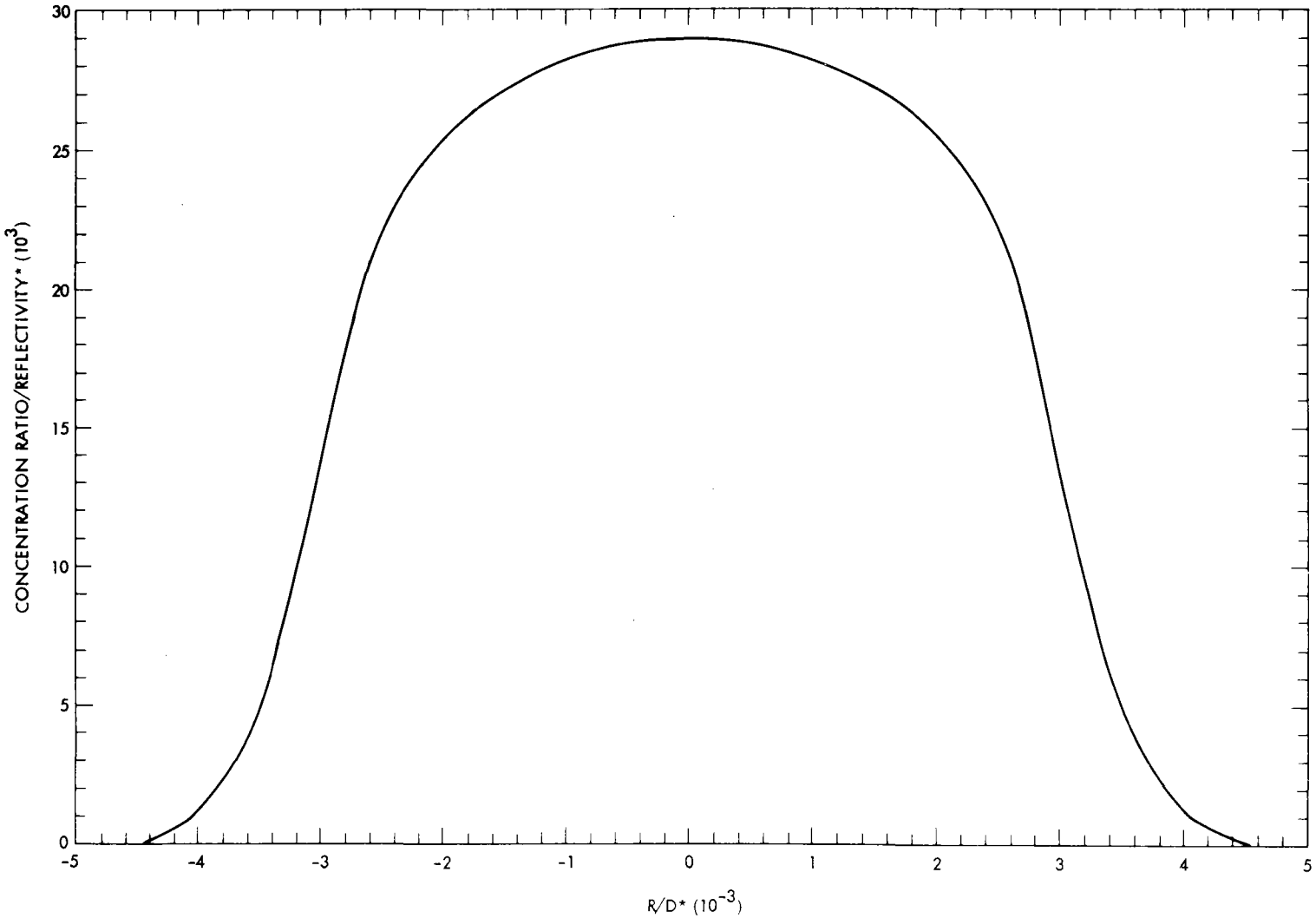


Figure 8-1. Distribution of Normalized Concentration Ratio, F/D = 0.6
(For a Perfect Paraboloidal Reflector)

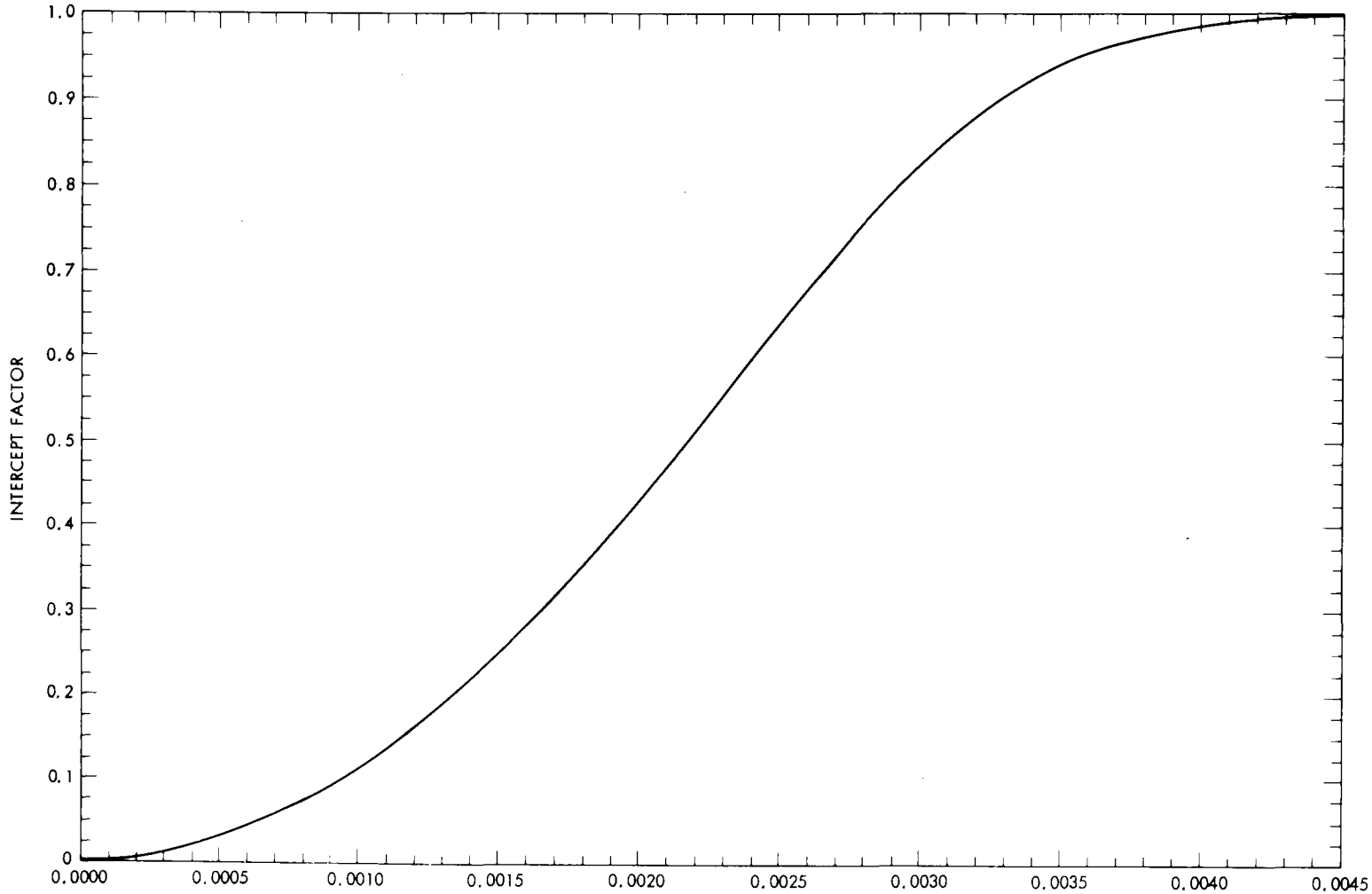


Figure 8-2. Intercept Factor as a Function of R/D, F/D = 0.6
(For a Perfect Paraboloidal Reflector)

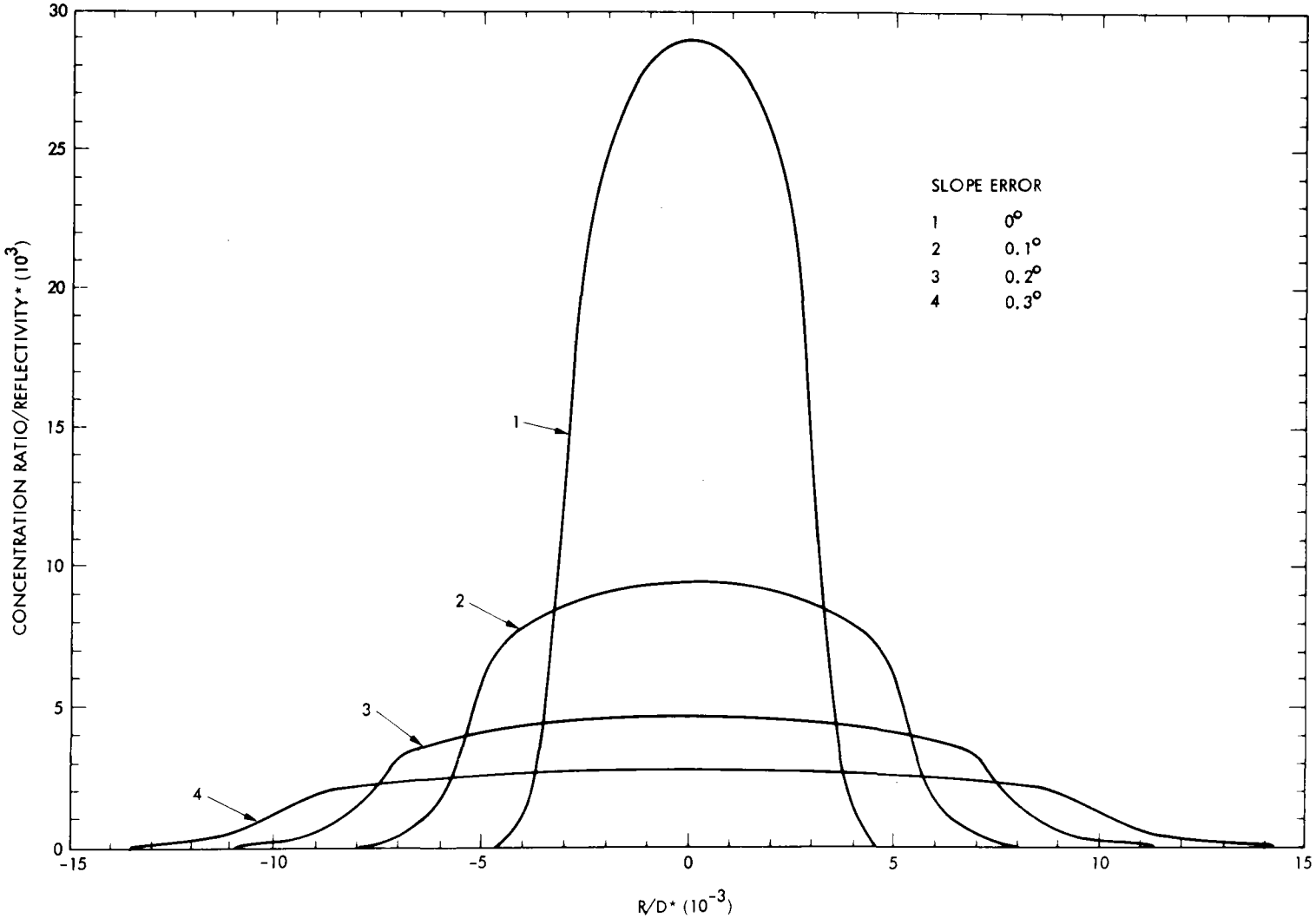


Figure 8-3. Distribution of Normalized Concentration Ratio, F/D = 0.6
(For a Paraboloid with Different Slope Errors)

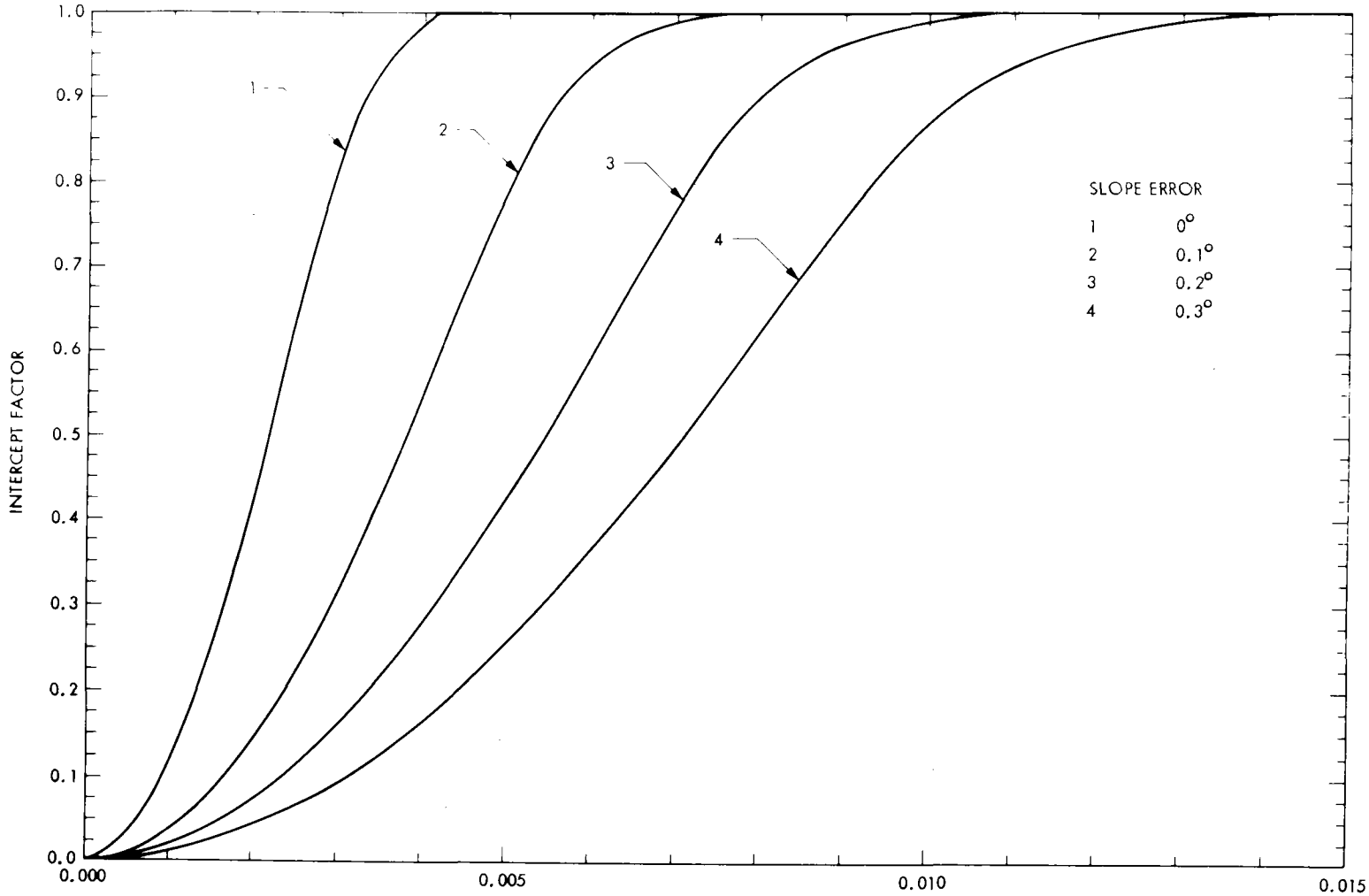


Figure 8-4. Intercept Factor as a Function of R/D F/D = 0.6
(For a Paraboloid for Different Slope Errors)

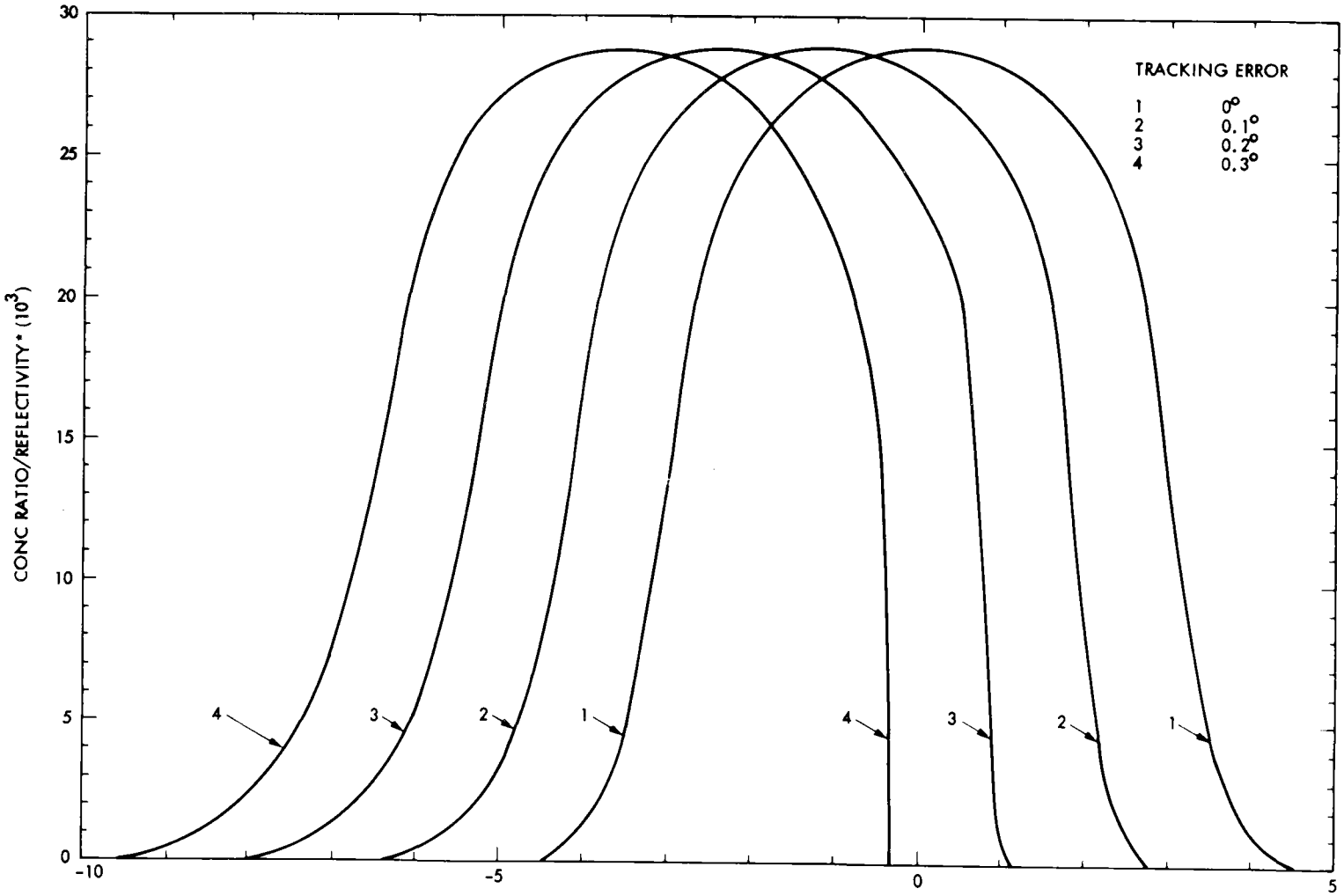


Figure 8-5. Distribution of Normalized Concentration Ratio F/D = 0.6
(For a Paraboloid for Different Tracking Errors)

distributions have been computed for a cylindrical receiver cavity with the following assumptions: F/D = 0.6, Focal length = 6.6m, diameter of paraboloidal reflector=11m, specular spreading angle = 0.5mrad, slope error = 3mrad, radius of center of hole of reflector = 0.914m, and limb darkening parameter = 1.15. The computed results are presented in Figures 8-6 and 8-7 for the following cases:

(1) For planes perpendicular to the optical axis for various locations at and beyond the focus (distances measured behind focal plane):

(a) Focal Plane

(b) 6" (0.1524m)

(c) 12" (0.3048m)

(d) 18" (0.4572m)

(e) 24" (0.6096m)

(f) 30" (0.7820m)

(g) 36" (0.9144m)

(2) For cylindrical surfaces of the following radii:

(a) 3" (0.0762m)

(b) 6" (0.1524m)

(c) 9" (0.2286m)

(d) 12" (0.3048m)

(e) 15" (0.3810m)

(f) 18" (0.4572m)

From the results presented above, the normalized concentration ratio decreases rapidly for planes situated farther and farther away from the focal plane. For example, the normalized concentration ratio for a plane situated at 12 inches beyond the focal plane is at least an order of magnitude lower than that computed at the focal plane. It is accompanied by a spread of the flux distribution along the radial distance from the optical axis. The normalized concentration ratio along the cylindrical surface also decreases rapidly with increasing radius. For each cylindrical surface the flux distribution possesses a maximum which becomes shifted away from the focal plane and broadens as the radius increases.

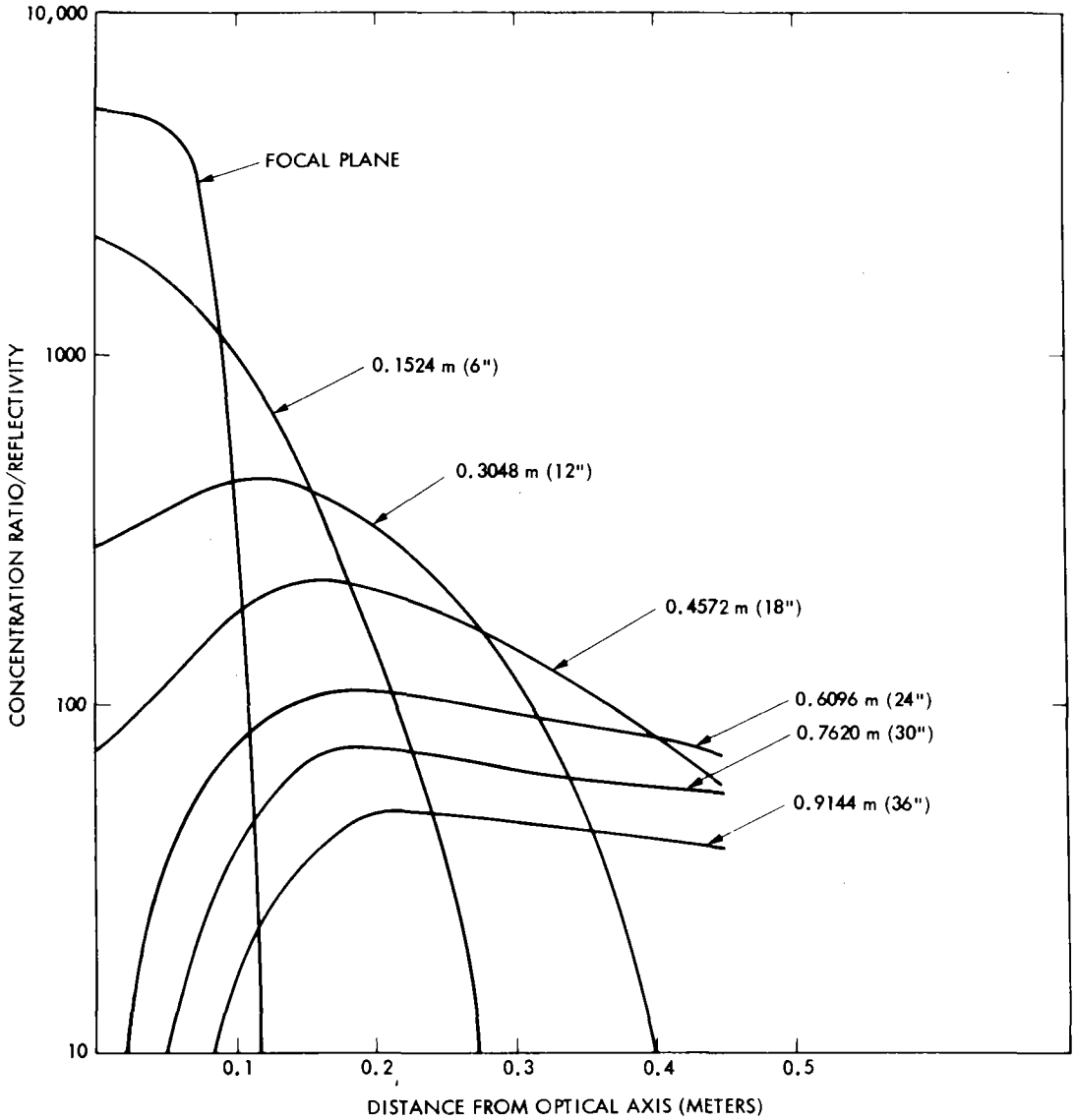


Figure 8-6. Distribution of Normalized Concentration Ratio Along Planes Perpendicular to the Optical Axis as a Function of Distance from Optical Axis

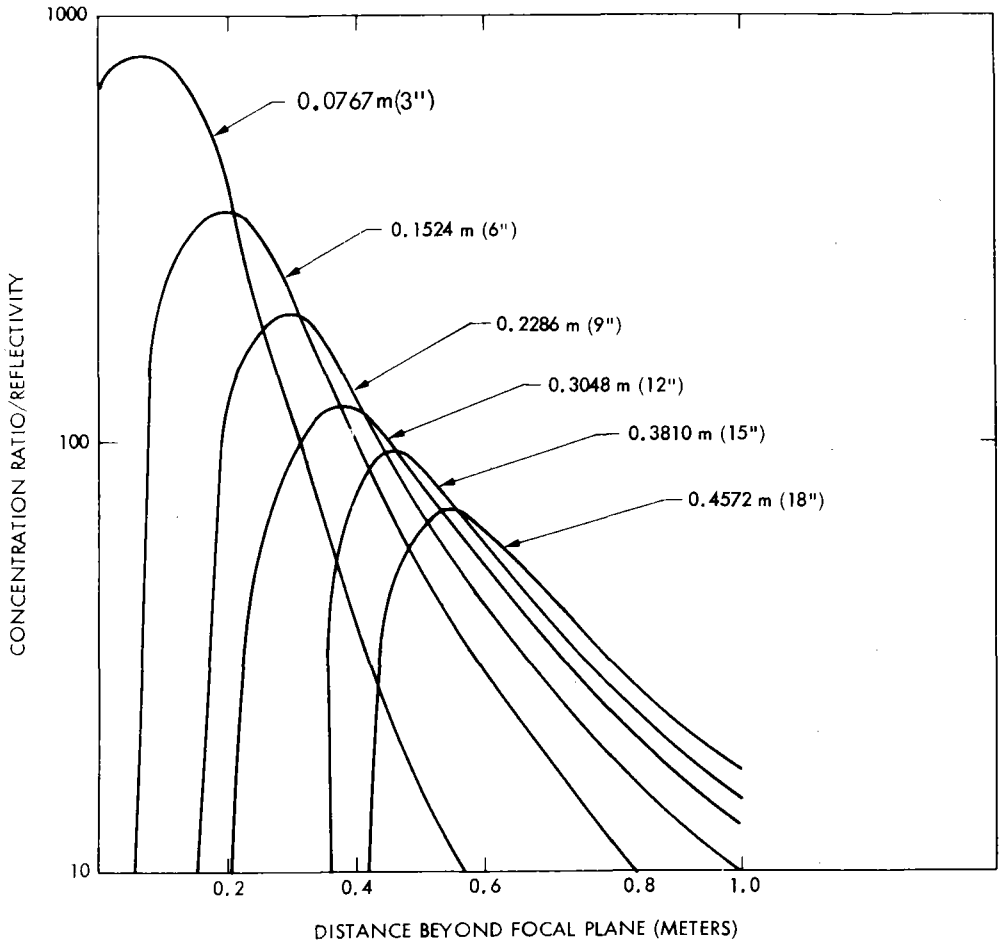


Figure 8-7. Distribution of Normalized Concentration Ratio Along Cylindrical Surfaces for Various Radii as a Function of Distance Beyond Focal Plane

Another approach which will also aid in the design of a receiver cavity is to generate isoflux surfaces in the vicinity of the focus. These isoflux surfaces are surfaces such that at each point the flux directed normal to the tangential surface assumes a constant value. Preliminary results for the isoflux surfaces are presented in Figure 8-8 with the following assumptions inherent in the calculation: F/D = 0.6 with F (focal length) = 6m and D (diameter of concentrator) = 10m. The other parameters - specular spreading angle, slope error and limb darkening parameter - remain the same as before. The isoflux curves are generated by an interpolation process and by variation of two sets of parameters: (1) coordinates specifying the location, and (2) the direction cosines of the surface normal for a surface element passing through the location. The two sets of parameters are adjusted such that the computed flux from the parabolic constant along the curves with the flux directed normal to the tangential surface. By rotating the isoflux curves about the optical axis, we can generate isoflux surfaces, assuming there are no pointing errors. A receiver cavity with the shape given by the isoflux surfaces would ideally have flux uniformly distributed on its surface under the assumed conditions. However, it must be noted that the flux can be very sensitive to the orientation of the surface normal. The constant values presented in the graph are for normalized concentration ratio (concentration/reflectivity) of 600, 300 and 150. The value of the flux can be obtained by multiplying the above quantity by the reflectivity of the mirror and the incident solar insolation. For example, if the insolation = 800 $W/m^2$ and the reflectivity = 0.9, the constant values in the isoflux curves corresponding to 432 $kW/m^2$, 216 $kW/m^2$ and 108 $kW/m^2$ respectively.

## D. FUTURE PLANS

The results of a preliminary optical analysis on the paraboloid reflector were presented in the preceding discussion. (The results of the optical analyses on the offset paraboloidal reflector, CPC-Fresnel, CPC-paraboloid and the Cassegrainian system are discussed in Appendix C.) First-cut computations of fluxes on the cavity walls, as well as the generation of isoflux surfaces, were performed and discussed separately for each solar concentrator system. Since the optical performance is greatly influenced by the errors associated with the surface characteristics of the reflector, future effort will be directed toward the proper characterization of the surface in terms of different error distributions. Specifically, there will be investigation on how the choice of error distributions influence the computed concentration ratio distributions. There will also be different levels of refinement: for example: if a normal distribution is selected, a single parameter - the standard deviation - may be used to characterize the error distribution; a higher level of refinement may require two parameters - the circumferential and radial standard deviations. It will also be important to relate the analytic parameters to the manufacturer's specifications and error tolerances. Investigation of advanced concentrator concepts will also continue. Preliminary results on the Cassegrainian system have just been generated -

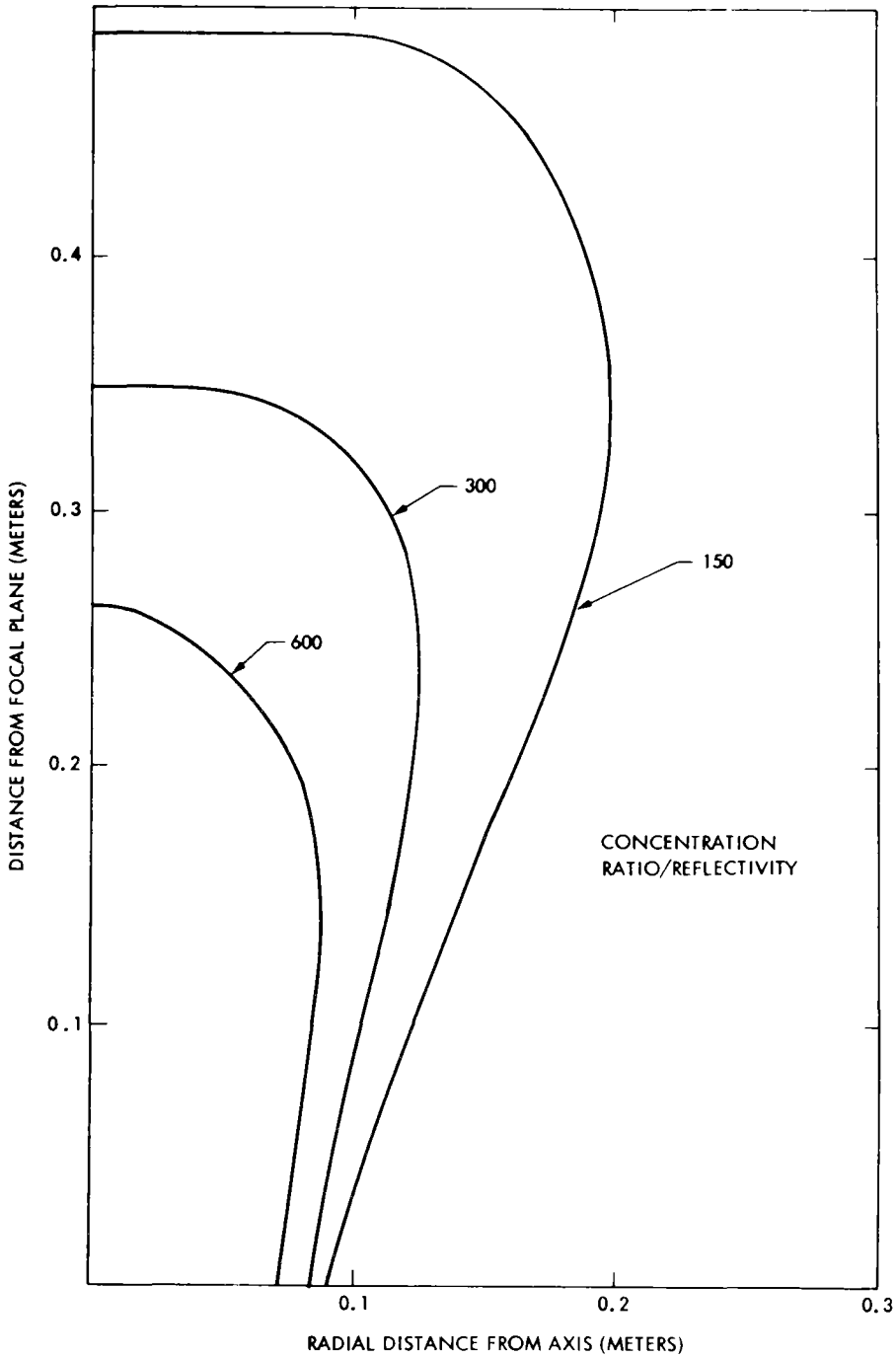


Figure 8-8. Solar Receiver Isoflux Surfaces

## REFERENCES


8-1. Schrenk, G.L., "Final Report — Analysis of Solar Reflectors — Mathematical Theory and Methodology for Simulation of Real Reflectors," Allison Division, G.M.C., EDR3693, 1963.

8-2. Schrenk, G.L., "The Role of Simulation in Development of Solar Thermal Energy Conversion Systems," Proceedings of the 11th IECEC, Vol. II, pp. 1256-1263.

8-3. Poon, P.T., and Higgins, S.N., "Optical Performance of Fresnel-type Concentrator with Truncated Paraboloidal Facets," presented at the Second Annual Helioscience Institute Conference and Exhibit on Alternate Energy Sources, April 1978.

8-4. "Thermal Power Systems, Research and Development Project, Advanced Technology Development Semi-Annual Progress Report," JPL Publication 78-3, Jet Propulsion Laboratory, Pasadena, California, June 1978.

8-5. Rabl, A., "Optical and Thermal Properties of Compound Parabolic Concentrators," Solar Energy Group, Argonne National Laboratory, Argonne, Illinois, AN/SOL-75-01.

# SECTION IX

# HEAT TRANSFER ANALYSIS

# SECTION IX

# HEAT TRANSFER ANALYSIS

This section reports briefly on the progress and results achieved during the second half of the program in the areas of receiver simulation models, and the receiver-engine optimization.

## A. HEAT ENERGY ANALYSIS PROGRAM (HEAP)

The documentation and the User's Manual of this computer code were completed and published. Part of the program's technical description was reported previously in the first semi-annual progress report. However, a complete and updated description is currently being prepared for publication. This documentation will include all the information needed to perform a detailed analysis of almost any solar receiver or collector. A list of the program, a detailed sequence of logical and analytical statements, a set of input data tables for user's convenience and an explanation of the output results will be given. Also to be included is a solved example using the JPL-Table Mountain solar receiver.

The input data necessary to apply (HEAP) to a given solar receiver includes:

(1) Surface optical properties such as emissivity (or absorptivity) both in the solar band and in the infrared region of the radiation spectrum

(2) Physical properties such as density, specific heat and thermal conductivity

(3) Solar flux distribution on the receiver interior or exterior surfaces

(4) Geometry and receiver dimensions to determine surface areas, volume and conduction paths

(5) Ambient and other source/sink temperatures

(6) Fluid flow rate

The program computes the radiation view factors if the receiver is an axisymmetric type with axisymmetric solar flux, otherwise, the user may have to input externally the radiation view factors.

The program structure uses the forward finite-difference scheme in solving the heat transfer rate equations together with the first law of thermodynamics applied to a receiver represented in space by nodes and in time by increments.

The program can handle steady state and transient problems. Timely variations of solar flux distribution and ambient temperature are included to enable a complete 24-hour simulation of receivers under either a quasi steady-state or a transient condition. The program output includes a list of radiation view factors, check on summation and reciprocity rules, accumulated solar irradiation, accumulated energy extracted by fluid, receiver efficiency and the nodal temperature distribution at the end of a particular time interval.

The JPL-Table Mountain solar receiver, shown in Figure 9-1, was used as an example to test and debug the program. This receiver was built at JPL in 1977 as part of a separate energy program aimed also at studying solar-thermal electric power plants. The actual receiver performance was previously tested experimentally and the results provided an excellent means of testing the accuracy of the simulated program HEAP shown in Figure 9-2. The results of the comparison between the experimental test results and the simulated ones showed:

(1) The simulation process gives a complete map of the nodal temperature profile with any needed level of refinement. In comparison, temperatures can be measured by high temperature thermocouples in only a few accessible locations.

(2) The simulated temperature map profile was not biased in either direction of the experimental values. It formed a mixed bias in both directions.

(3) With all the uncertainties in the actual surface physical and optical properties, their variations with temperature, and the actual flux distribution compared to the simulated one, the deviation was under 5%.

The program (HEAP) was further tested under the transient conditions using again the example Table-Mountain receiver. Individual nodes respond differently to solar flux and ambient temperature variations due to their varying heat capacities. The outlet fluid temperature response is the most important since it interfaces with the engine. The time taken to reach 90% or 99% of the steady state value can be simply found with a special run using step changes. Again, simulating the transient performance was very informative and matched the experimental evidences.

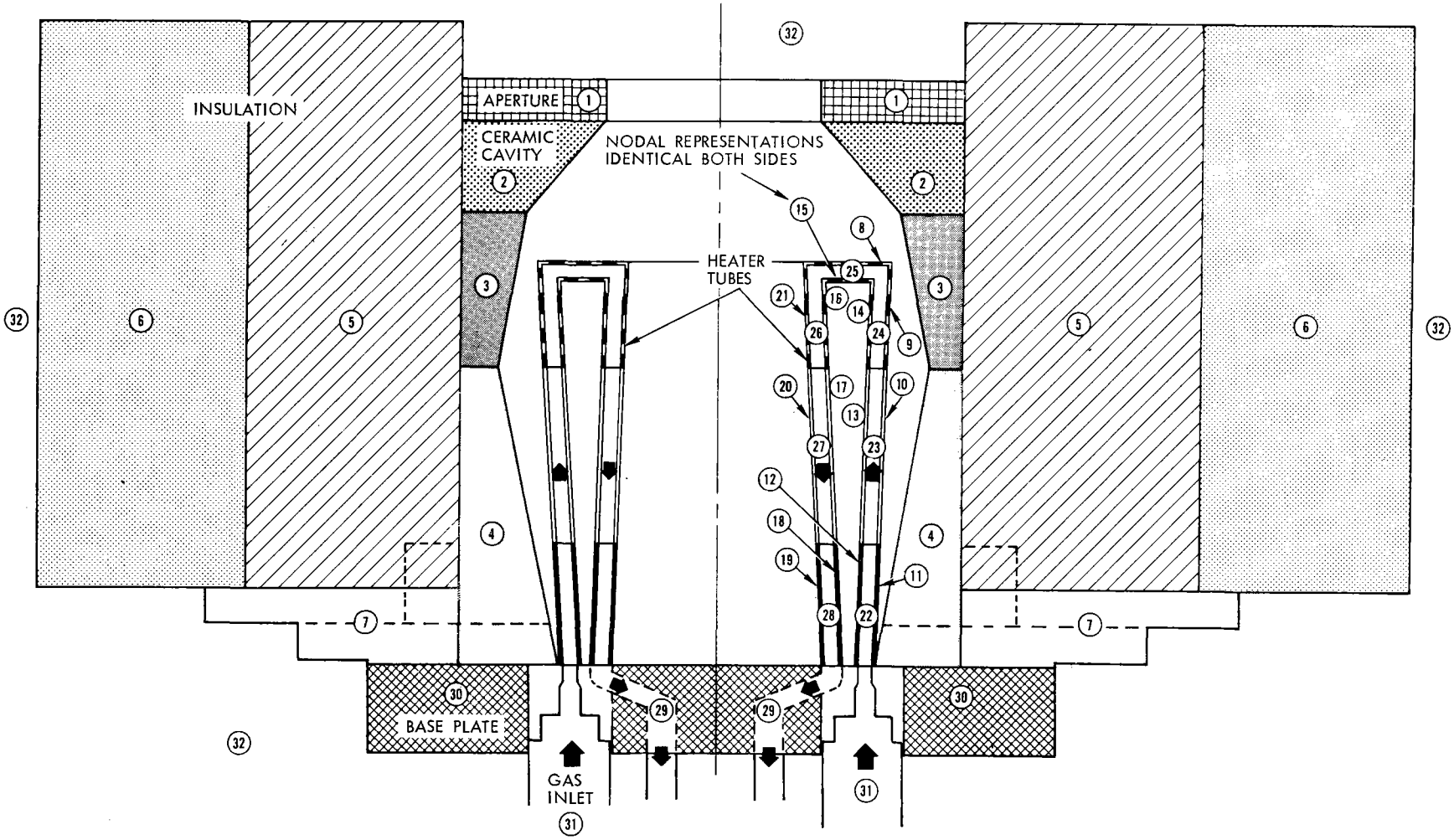


Figure 9-1. Node Representation of a Receiver

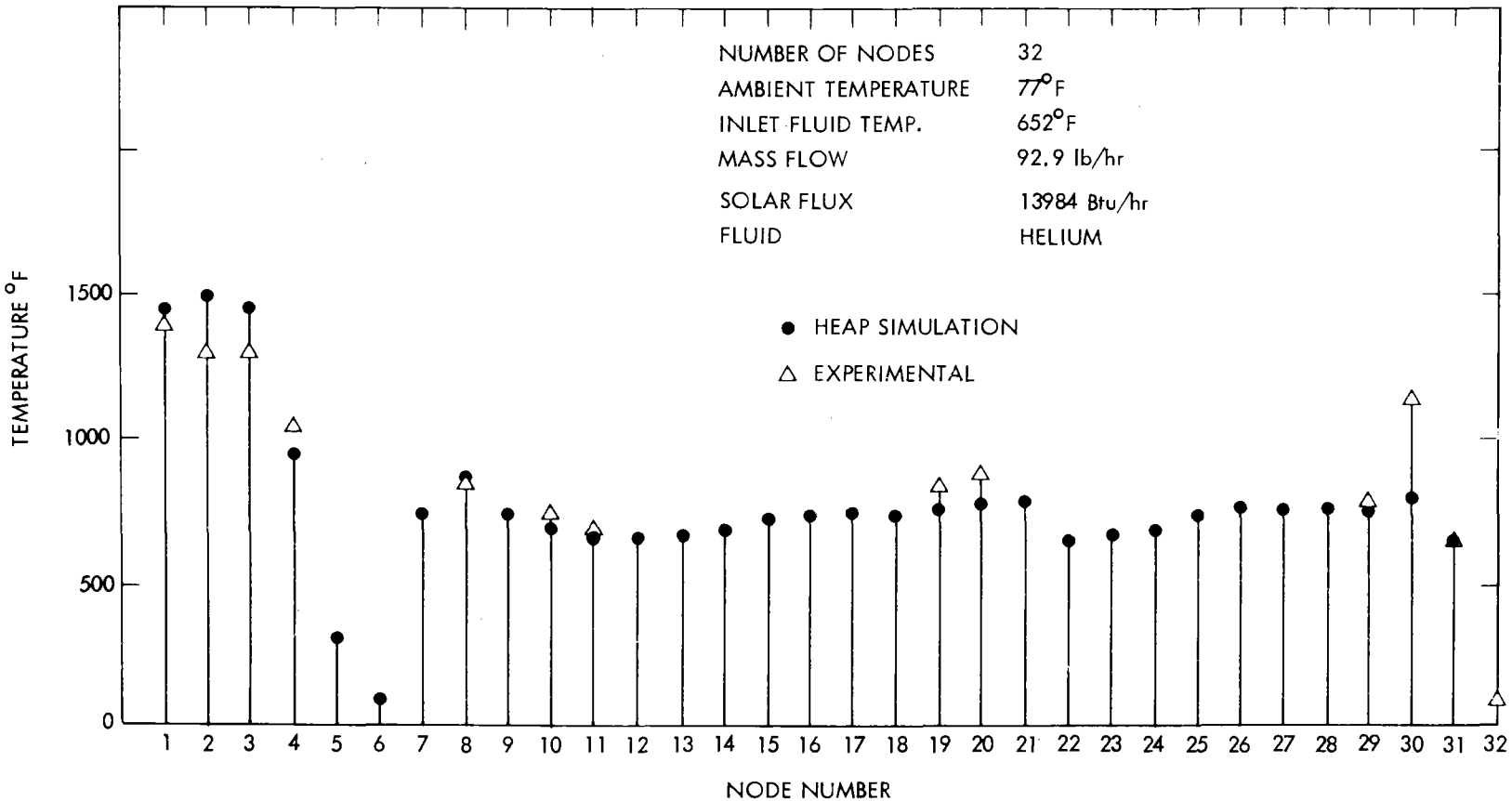


Figure 9-2. HEAP Simulation Results

# APPENDIXES

# A THROUGH D

# APPENDIX A

# EVALUATION OF RECENT DATA ON SOLAR CONCENTRATOR REFLECTIVE SURFACES

## SECTION I

## SUMMARY

Recent data on reflective surfaces show that the solar reflectance from mirrors, when covered with dust, varies with wavelength. Other measurements have indicated it to be relatively constant, with measurements at 500 nm being sufficient to characterize the reflectance loss. Additional data on glass transmission, reflectance, cleaning procedures, abrasion of surfaces and silver coatings are included in this appendix.

One approach to investigating aging effects on the silvered mirrors exposed to the external environment is suggested in the following discussion.

## SECTION II

## BACKGROUND AND RESULTS

The basic geometry of mirror light reflection is shown in Figure A-1 and the reflectance as a function of wavelength in Figure A-2. The dramatic decrease in reflectance due to dust in the 0.6 micron range is noted. Figures A-3 through A-5 and Tables A-1, A-2, and A-3 show the reflectance efficiencies and the relationships between transmission and reflectance for glass.

The effects of iron content and thickness are shown (Figure A-7) for various types of glasses.

For three dimensional curved surfaces, the glass flatness is important. The flatness is found to have wider variations in roughness in the direction perpendicular to the draw.

Although 0.060 to 0.125-inch thick glass sheets have been sagged successfully with RMS slope errors of 3-4 milliradians, the three-dimensional case is more difficult due, among other phenomena, to spring-back or some residual memory effects.

## SECTION III

## ABRASION TESTS

Abrasion tests were performed by blowing silica flour (∿105-125 μm) onto reflective surfaces at normal incidence (Figure A-6). This graph indicates two major conclusions. First, it can be seen that some

functional relationship exists between transmission loss and total kinetic energy of the impacting particles. Second, it is clear that no acrylic-coated or bulk acrylic reflector is as resistant to abrasion damage as is glass.

Scanning electron micrographs were taken of damaged surfaces from both the abrasion test specimens and witness specimens taken from the desert with known exposure history. The abrasion specimens revealed several order of magnitude greater damage than did the witness specimens. In addition, the damage morphology was quite different. The desert specimens had few widely separated crater type damages whereas the abrasion specimens had, in addition to the crater type damages, numerous closely spaced fine scratches measuring approximately $10^{-6}$ to $10^{-7}$ mm in length.

## SECTION IV

## DUST EFFECTS ON REFLECTANCE DEGRADATION

The general effects of reflectance degradation for desert soiled mirrors are summarized in Table A-4, and Figure A-7 shows the dust-rain effects in the Sandia program. A drop in reflectance of 12% due to dust is noted in the latter figure.

At the present time, upside-down stowage appears to be best in spite of the fact that overnight dew or frost may sometimes run off and clean the mirrors during morning deployment.

## SECTION V

## DUST CLEANING PROCEDURES

The effect of various cleaning procedures on the reflectance is shown in Tables A-5 and A-6. A summary of previous glass cleaning effects are shown in Figure A-8. Alumino silicate and borosilicate glasses are found to be superior.

## SECTION VI

## EFFICIENCY OF SILVER COATINGS

The present data on solar efficiency of silver coatings for various glasses and parameters are summarized in Tables A-7 through A-13. Failures of the vapor deposited silver coatings after relatively short exposures, 165 to 184 days (Table A-10) are noted. Reflectances of vapor or chemically deposited silver caotings are quite similar (Table A-13).

## SECTION VII

## AGING EFFECTS ON SILVER MIRROR SURFACES

Recent information reveals that it is possible to study aging effects on silvered surfaces using old automobile side mirrors. Although the majority of the auto mirrors were chromium front surface or lead-sulphide second surface, some mirrors were consistently made with silver in the 700-900 angstrom range (G.M., Buick). These mirrors should be available in used auto companies as far back as 30-50 years. It is recommended that this type of study be undertaken as time and budget permits.

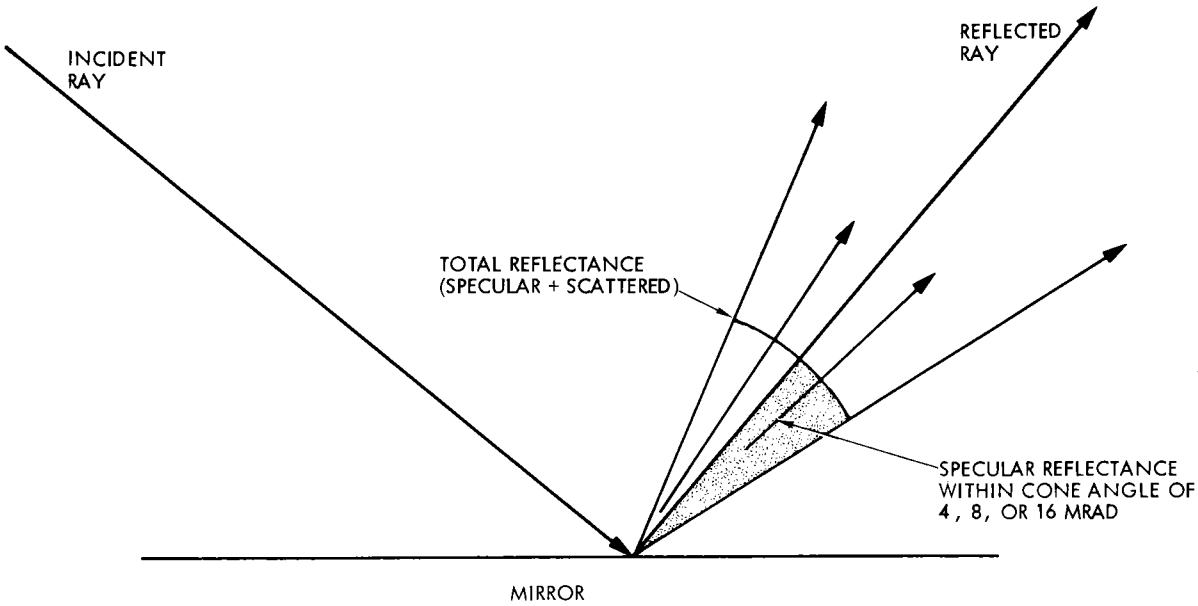


Figure A-1. Reflectance Geometry

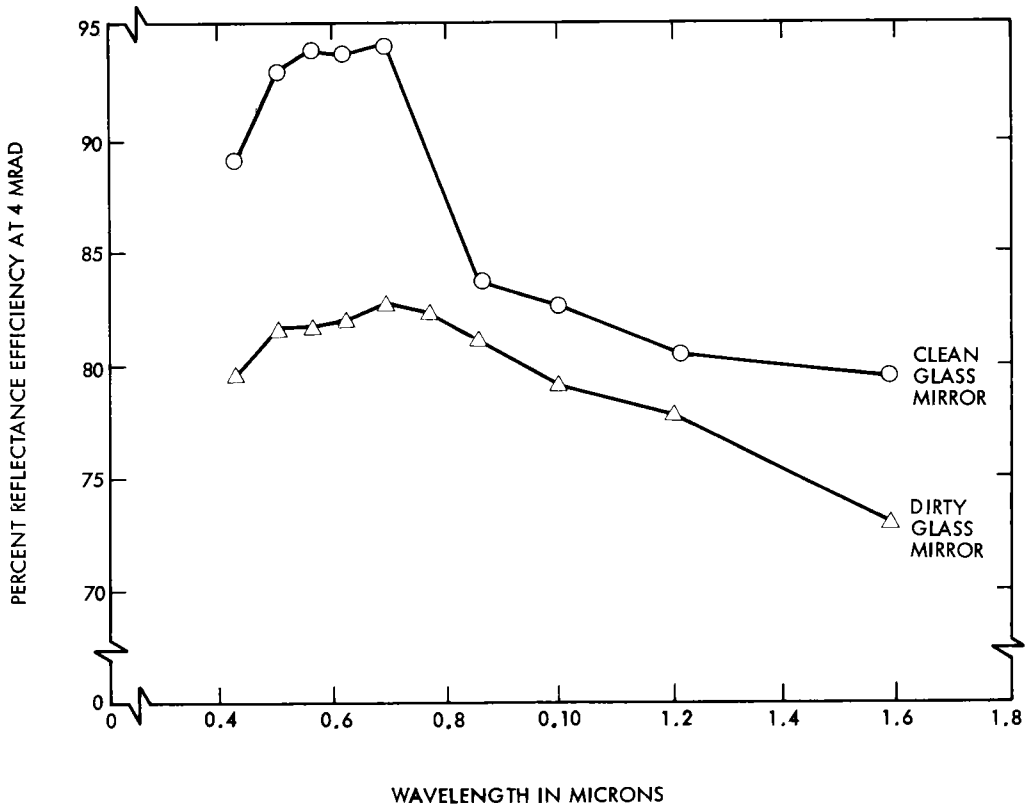


Figure A-2. Reflectance vs Wavelength

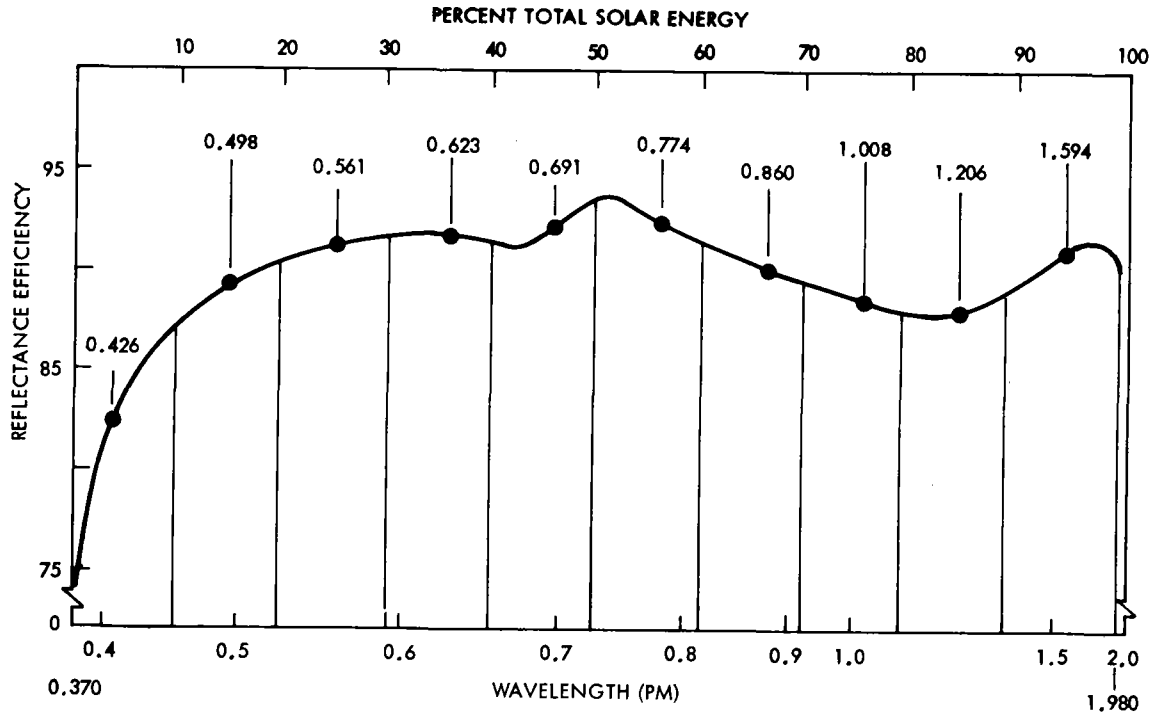


Figure A-3. Reflection Efficiency versus Wavelength

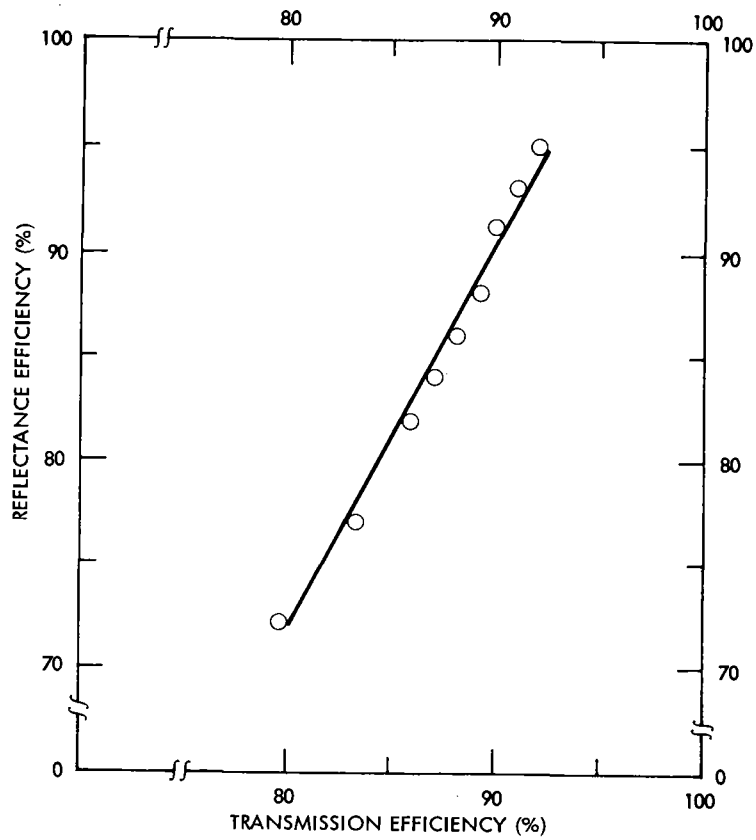


Figure A-4. Expected Reflectance Efficiency from Glasses with Varying Transmission Efficiency

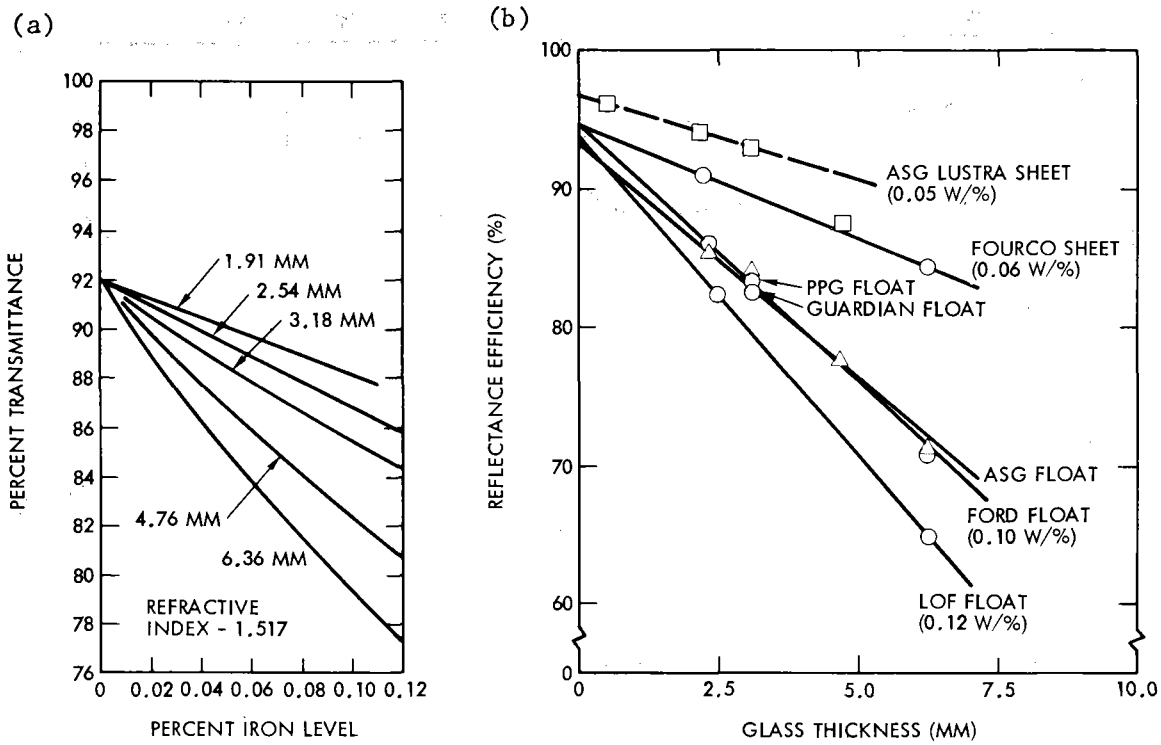


Figure A-5. Reflectance Properties

Table A-1. Glass Transmission

| Total Transmission Efficiency (T) | Transmission Efficiency in the Glass (G) | Expected Reflectance Efficiency of Mirror (R) |
|---|---|---|
| 0.75 | 0.81 | 0.63 |
| 0.80 | 0.87 | 0.72 |
| 0.83 | 0.90 | 0.77 |
| 0.86 | 0.93 | 0.82 |
| 0.87 | 0.94 | 0.84 |
| 0.88 | 0.95 | 0.86 |
| 0.89 | 0.96 | 0.88 |
| 0.90 | 0.98 | 0.91 |
| 0.91 | 0.99 | 0.93 |
| 0.92 | 1.00 | 0.95 |

Table A-2. Reflectance Efficiency of Glass Mirrors at AM2

| Glass (Wt Percent Iron Oxide) | | Mirror Manufacturing and Silvering Process | Thickness in mm (In.) | Specimen No. | Over Solar Spectrum using Beckman 125 mrad | At Wavelength of 560 nm using Specular Photometer | | | Over Solar Spectrum using Specular Spectro Photometer | | |
|---|---|---|---|---|---|---|---|---|---|---|---|
| | | | | | | 16 mrad | 8 mrad | 4 mrad | 16 mrad | 8 mrad | 4 mrad |
| ASG Ind Lustra Sheet (0.05 - 0.06) | | Buchmin Industries Mirrorlab Process | 0.7 (0.028) | 134.1 | 96.0 | | | | 94.0 | 94.0 | |
| | | | 2.4 (0.093) | 110.1<br>110.2 | 94.0<br>94.0 | | | | 93.0<br>92.0 | 92.0<br>92.0 | 86.0<br>88.0 |
| | | Gardner Mirror and Process | 3.2 (0.125) | 65.3<br>65.13<br>65.15<br>65.16<br>67.3 | 91.4<br>93.5<br>93.5<br>94.3<br>91.9 | 95.5<br>94.5<br>94.5<br>95.0<br>95.5 | 95.0<br>94.0<br>94.5<br>95.0<br>94.5 | 93.5<br>93.5<br>93.5<br>94.0<br>94.0 | 92.0 | 93.0 | 87.0 |
| | | Binswanger Mirror Co. Mirrorlab Process | 4.7 (0.187) | 114.1 | 88.0 | | | | 86.0 | 86.0 | |
| Fourco Sheet (0.06) | | Tyre Bros. Two Part London Laboratory Process | 2.3 (0.090) | 32.3<br>50.2<br>50.3<br>50.4<br>50.5 | 93.1<br>90.4<br>90.3<br>90.7<br>90.3 | 95.0<br>96.0<br>97.0<br>96.5<br>95.0 | 94.0<br>96.0<br>96.0<br>96.5<br>95.0 | 90.0<br>94.0<br>96.0<br>96.0<br>92.0 | | | |
| | | | 6.4 (0.250) | 33.3<br>51.2<br>51.3<br>51.4<br>51.5 | 86.8<br>83.9<br>84.4<br>84.5<br>84.3 | 89.0<br>94.0<br>93.0<br>93.0<br>91.0 | 89.0<br>94.0<br>92.0<br>93.0<br>90.0 | 88.0<br>88.0<br>88.0<br>91.0<br>88.5 | | | |
| PPG Industries Float | (0.05) | Buchmin Industries Mirror Lab Process | 3.2 (0.125) | 1<br>2<br>3 | 92.0<br>92.0<br>92.0 | 95.0<br>95.0<br>95.0 | 95.0<br>95.0<br>96.0 | 95.0<br>95.0<br>95.0 | 90.0<br>89.0<br>90.0 | 89.0<br>88.0<br>89.0 | 81.0<br>81.0<br>84.0 |
| | (0.07) | | 2.4 (0.093) | 111.1<br>111.2 | 88.0<br>88.0 | | 95.0 | | 87.0<br>87.0 | 86.0<br>86.0 | 82.0<br>81.0 |
| | (0.10) | | 3.2 (0.125) | 86.1 | 83.5 | | | | 83.3 | 82.8 | 77.1 |

Continued next page

Table A-2. Reflectance Efficiency of Glass Mirrors at AM2 - (Continuation 1)

| Glass (Wt Percent Iron Oxide) | Mirror Manufacturer and Silvering Process | Thickness in mm (In.) | Specimen No. | Over Solar Spectrum using Beckman 125 mrad | At Wavelength of 560 nm using Specular Photometer | | | Over Solar Spectrum using Specular Spectro Photometer | | |
|---|---|---|---|---|---|---|---|---|---|---|
| | | | | | 16 mrad | 8 mrad | 4 mrad | 16 mrad | 8 mrad | 4 mrad |
| Ford Motor Float (0.09 - 0.10) | Buchmin Industries Mirrorlab Process | 2.4 (0.093) | 52.2 | 85.7 | 96.5 | 96.0 | 96.0 | | | |
| | | | 52.3 | 85.7 | 94.5 | 94.5 | 94.0 | | | |
| | | | 52.4 | 85.9 | 94.0 | 93.5 | 93.0 | | | |
| | | | 52.5 | 86.0 | 96.0 | 95.0 | 95.0 | | | |
| | | | 52.6 | 86.1 | 93.0 | 93.0 | 93.0 | | | |
| | | 3.2 (0.125) | 65.x | 83.3 | 91.0 | 91.0 | 86.0 | 81.9 | 81.9 | 78.0 |
| | | | 65.22 | 83.2 | 91.0 | 91.0 | 88.0 | 81.0 | 81.0 | 76.0 |
| | | 6.4 (0.250) | 6.001 | 70.7 | 89.0 | 88.5 | 88.5 | | | |
| | | | 6.002 | 70.7 | 89.0 | 89.5 | 88.5 | | | |
| Guardian Ind Float (0.10) | Buchmin Ind Mirrorlab Process | 3.2 (0.125) | 66.3 | 82.5 | 93.5 | 92.5 | 92.0 | | | |
| ASG Industries Float (0.10 - 0.13) | Binswanger Mirror Co. Mirrolab Process | 2.4 (0.093) | | | | | | | | |
| | | 3.2 (0.125) | Lot No. 2 | 83.7 | 92.0 | 91.0 | 90.5 | 81.6 | 82.1 | 78.5 |
| | | | B-1 | 84.2 | 92.0 | 92.0 | 86.0 | 83.1 | 83.1 | 78.8 |
| | | | B-2 | 83.7 | 92.0 | 92.0 | 89.5 | 82.3 | 82.3 | 75.9 |
| | | | B-3 | 84.8 | 92.5 | 92.0 | 87.5 | 84.8 | 84.8 | 80.9 |
| | | 4.8 (0.188) | Lot No. 1 | 77.9 | 88.0 | 88.0 | 81.5 | 76.0 | 76.0 | 71.8 |
| | Buchmin Ind. Mirrorlab Process | 6.4 (0.250) | 64.22 | 71.1 | 88.0 | 88.0 | 88.0 | 71.0 | 71.0 | 66.0 |
| LOF Float (0.12) | Tyre Bros. 2-Part London Lab Process | 2.5 (0.100) | 29.3 | 82.4 | 93.0 | 92.0 | 92.0 | | | |
| | | 6.4 (0.250) | 30.1 | 64.7 | 81.0 | 79.0 | 75.0 | | | |

Table A-3. Glass Survey Summary

| Manufacturer | Process | Composition | Thickness | | Solar Transmittance | | Optical Flatness % Power Outside | | Approximate Cost | |
|---|---|---|---|---|---|---|---|---|---|---|
| | | | Tested | Possible | Measured | Possible | 1 mrad | 2 mrad | 1M, $ft^2$ | >10M, $ft^2$ |
| ASG | Lo-Iron Float | Soda Lime | 0.125 | | 0.847 | | | | 0.30 | |
| | Sunadex-Twin Ground | Soda Lime | | >4mm | | >0.91 | 0* | 0* | 1.30 | |
| CE | Float | Soda Lime | 0.125 | | 0.838 | | 18 | 1 | 0.50 | |
| | Heliolite-Twin Ground | Soda Lime | | | | 0.91 | 0* | 0* | 1.30 | |
| Corning | 0317 Fusion | Aluminosilicate | 0.110 | >0.020 | 0.903 | | 15 | 0 | 0.65 - 0.80 | |
| | 0317 Fusion | Aluminosilicate | 0.090 | | 0.910 | | 19 | 0 | 0.65 - 0.80 | |
| | 7806 Fusion | Lime Borosilicate | 0.045 | | 0.876** | >0.91 | | | 1.40 | 0.45 |
| Fourco | Rolled | Soda Lime | 0.125 | | 0.891 | | 90 | 57 | | |
| Ford | Float | Soda Lime | 0.125 | >0.105 | 0.844 | >0.88 | 5 | 0 | 0.40 | |
| Guardian | Float | Soda Lime | | >0.085 | | >0.88 | | | 1.00 | |
| LOF | Float | Soda Lime | 0.125 | | 0.831 | | 7 | 0 | | |
| PPG | Mid-Iron Float | Soda Lime | 0.125 | | 0.866 | | 8 | 0 | | |
| | Lo-Iron Float | Soda Lime | 0.125 | >0.060 | 0.881 | >0.89 | 20 | 4 | 2.15 | 0.60 - 0.65 |

* Based on Measurements of ASG Tinted Twin Ground Glass
** Measured by R. Pettit, SLA, Total Hemispherical Solar Transmittance

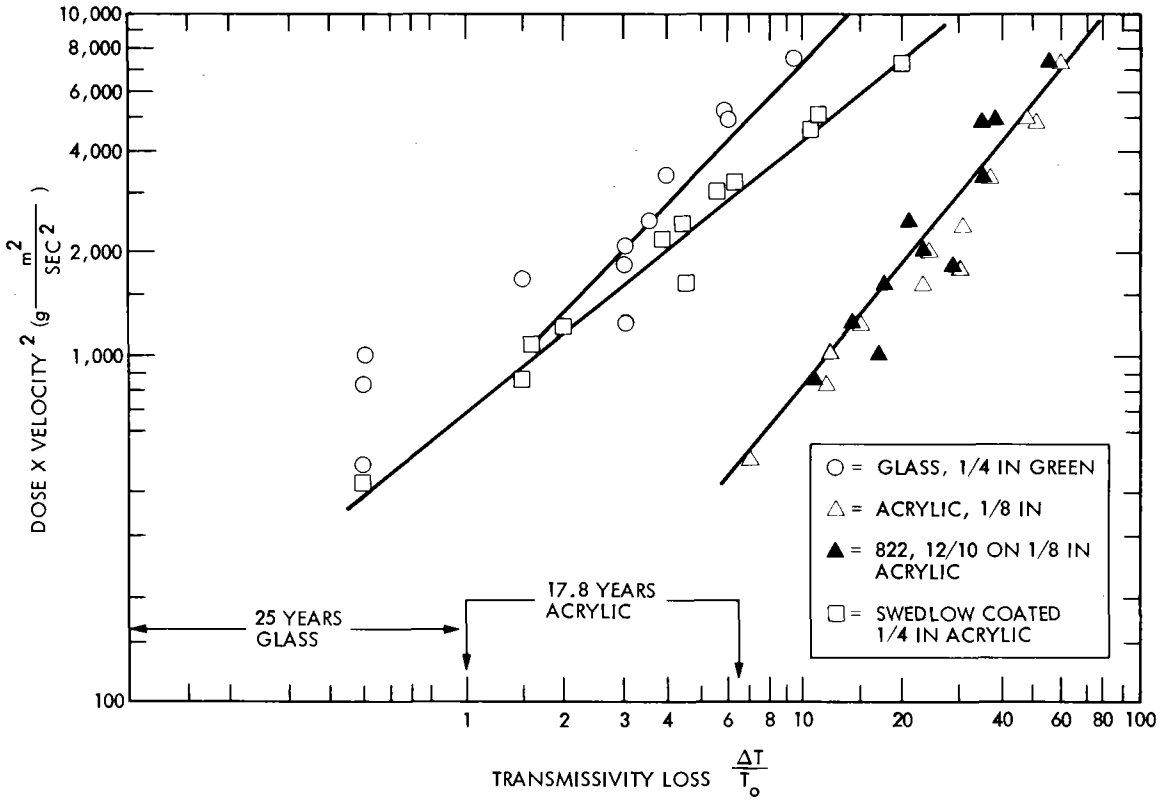


Figure A-6. Glass Abrasion

Table A-4. Reflectance Degradation as a Function of Wavelength for Desert Soiled Mirrors

| Specimen Number | Mirror Glass | Mirror Condition | Instrument | Specularity | Solar Reflectance Efficiency at the Following Wavelengths in Nanometers | | | | | | | | | | Average Value Over Solar Spectrum |
|---|---|---|---|---|---|---|---|---|---|---|---|---|---|---|---|
| | | | | | 426 | 498 | 561 | 623 | 691 | 774 | 860 | 1008 | 1208 | 1594 | |
| 65.16 | ASG Ind Lustra Sheet 3.2 mm (0.125) | Dirty | Beckman | 125 | 92.5 | 95.5 | 96.5 | 96.0 | 94.5 | 92.0 | 90.5 | 89.5 | 89.5 | 92.0 | 92.9 |
| | | | Specular Spectro Photometer | 16 | 83.6 | 87.7 | 89.4 | 88.5 | 92.2 | 86.8 | 85.4 | 83.9 | 84.7 | 89.9 | 87.0 |
| | | | | 8 | 83.6 | 87.7 | 89.4 | 88.5 | 90.1 | 86.8 | 85.4 | 83.9 | 84.7 | 89.2 | 87.0 |
| | | | | 4 | 79.6 | 81.7 | 81.7 | 82.1 | 82.8 | 82.4 | 81.2 | 79.2 | 77.9 | 73.0 | 80.0 |
| | | | Specular Photometer | 16 | | | 96.5 | | | | | | | | |
| | | | | 8 | | | 96.0 | | | | | | | | |
| | | | | 4 | | | 95.5 | | | | | | | | |
| | | Clean | Beckman | 125 | 94.0 | 96.5 | 98.0 | 97.0 | 96.5 | 94.5 | 92.0 | 90.5 | 90.5 | 93.5 | 94.3 |
| | | | Specular Spectro Photometer | 16 | 90.9 | 93.7 | 94.5 | 93.7 | 95.2 | 91.7 | 90.5 | 89.8 | 89.5 | 94.6 | 92.0 |
| | | | | 8 | 91.1 | 93.7 | 95.6 | 94.4 | 92.5 | 90.0 | 89.4 | 80.2 | 89.5 | 93.8 | 93.0 |
| | | | | 4 | 89.1 | 93.1 | 94.0 | 93.8 | 94.3 | 80.0 | 83.8 | 82.6 | 80.5 | 79.6 | 87.0 |
| | | | Specular Photometer | 16 | | | 95.0 | | | | | | | | |
| | | | | 8 | | | 95.0 | | | | | | | | |
| | | | | 4 | | | 94.0 | | | | | | | | |

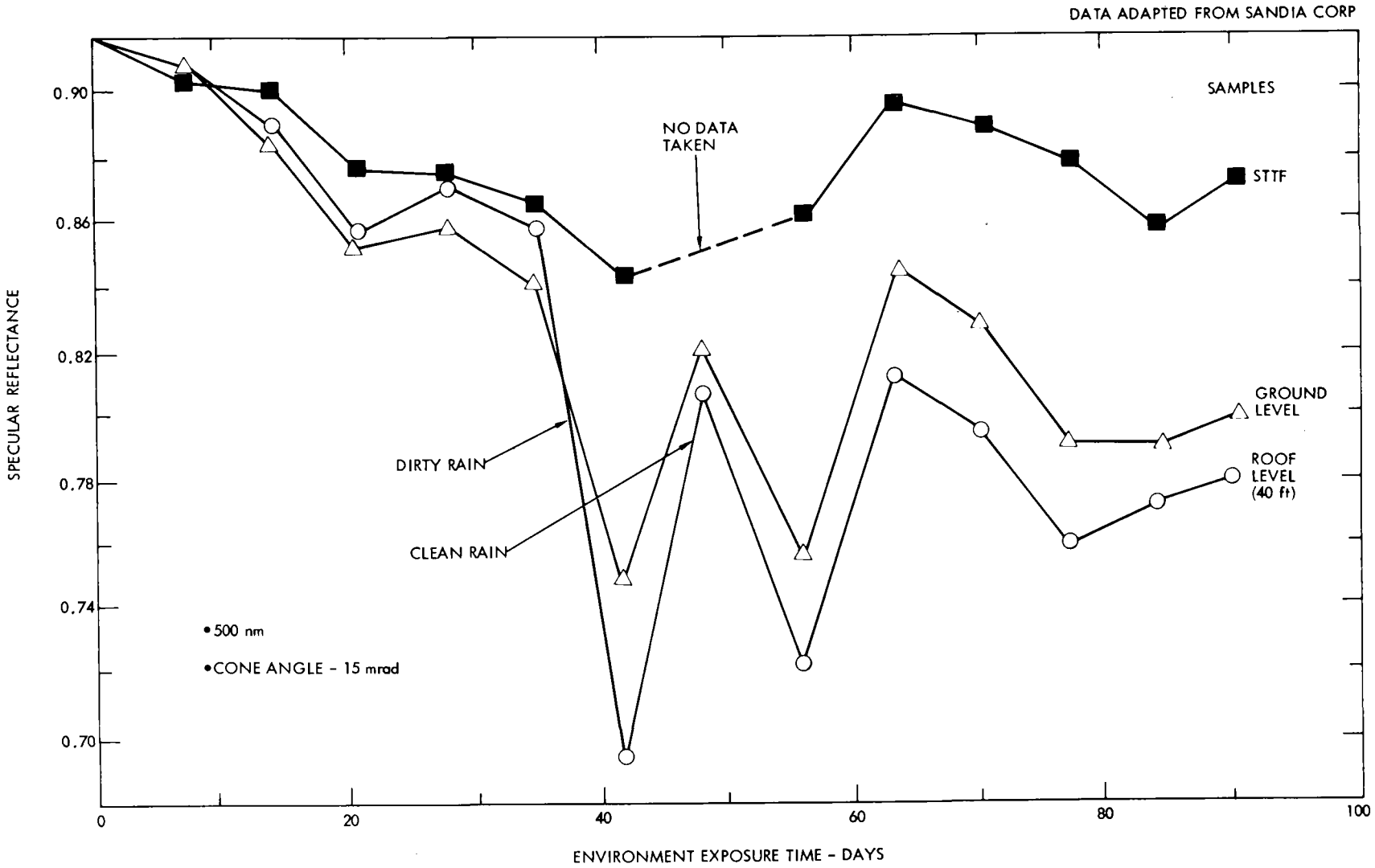


Figure A-7. Glass Mirrors: Specular Reflectance vs Environmental Exposure Time
Location - Albuquerque, N.M. - 1978

Table A-5. Washing of Model Heliostat using Different Washing Solutions

| Company | Exposure Time (days) | Reflectance Efficiency (%) | | Washing Solution Application | | | | | Rinse Solution Application | | | | Drying Time (min) |
|---|---|---|---|---|---|---|---|---|---|---|---|---|---|
| | | Dirty | Clean | Pressure (psi) | Time | Quantity (gal.) | Nozzle | Dwell Time (sec) | Pressure (psi) | Time (sec) | Quantity (gal.) | Nozzle | |
| McGean | 20 | 59.1 | 64.75 | 80 | 35 sec | 0.83 | 80.10 | 30 | 80 | 90 | 3.2 | 65.16 | 20 |
| Turco | 20 | 66.62 | 63.54 | 40 | 3 min | 2 | 80.04 | 60 | 50 | 105 | 4.0 | 90.20 | 20 |
| TEC | 30 | N/A | N/A | 150 | 80 sec | 4 | Graco Gun | 60 | 150 | 145 | 5.0 | Graco Gun | 30 |

Table A-6. Washing of SRE Heliostats using McGean Chemical's Washing Solution

| Heliostat No. (1) | Prewash Reflectance Efficiency (percent) | Postwash Reflectance Efficiency (percent) | Application Time | | Solution Quantity | | Solution Type | | Nozzle Size | |
|---|---|---|---|---|---|---|---|---|---|---|
| | | | Wash (min) | Rinse (min) | Wash (gal.) | Rinse (gal.) | Wash | Rinse | Wash (gpm) | Rinse (gpm) |
| $H_1$ | 65.9 | 78.2 | 1.0 | 5.0 | 1.50 | 14.0 | A69M | Deionized Water | 1 | 5 |
| $H_2$ | 56.1 | 76.5 | 1.0 | 3.7 | 1.25 | 8.75 | A69M | Deionized Water | 1 | 5 |
| $H_3$ | 69.2 | 87.5 | 1.0 | 3.0 | 0.75 | 8.0 | A69M | Deionized Water | 1 | 5 |
| $H_4$ | 73.3 | 84.0 | 1.0 | 2.0 | 1.25 | 5.75 | CB120 | Deionized Water | 1 | 5 |
| IH1 | 76.8 / 72.2 | 85.1 / 86.6 | 1.4 | 2.8 | 1.60 | 7.75 | CB120 | Deionized Water | 1 | 5 |

NOTES:

(1) $H_1$, $H_2$, $H_3$ = Acrylic first surface mirrors, $H_4$ = Laminated mirror, IH1 = 3/32 mirror bonded to foam core / Laminated mirror

## Visual Appearance

Visual evaluations were made under artificial daylight (MacBeth Examolite type TC-440) and with an intense concentrated beam light source (Burton Lamp). The specimens were examined in both reflected and transmitted light and were evaluated as follows:

A. (excellent) - No spots and/or haze are visible when examined with the concentrated beam light source less than 6 in. from the specimen.

B. (good) - A few spots and/or a slight haze are visible only with lighting conditions as for A.

C. (fair) - Many spots and/or much haze are visible only with lighting conditions as for A.

D. (poor) - Some spots and/or haze are visible without the concentrated beam light source, but with artificial daylight.

E. (very poor) - An excessive accumulation of weathering products is readily visible with artificial daylight.

Any appearance degradation which could not be removed by scrubbing with a cloth and water is considered to be permanent damage.

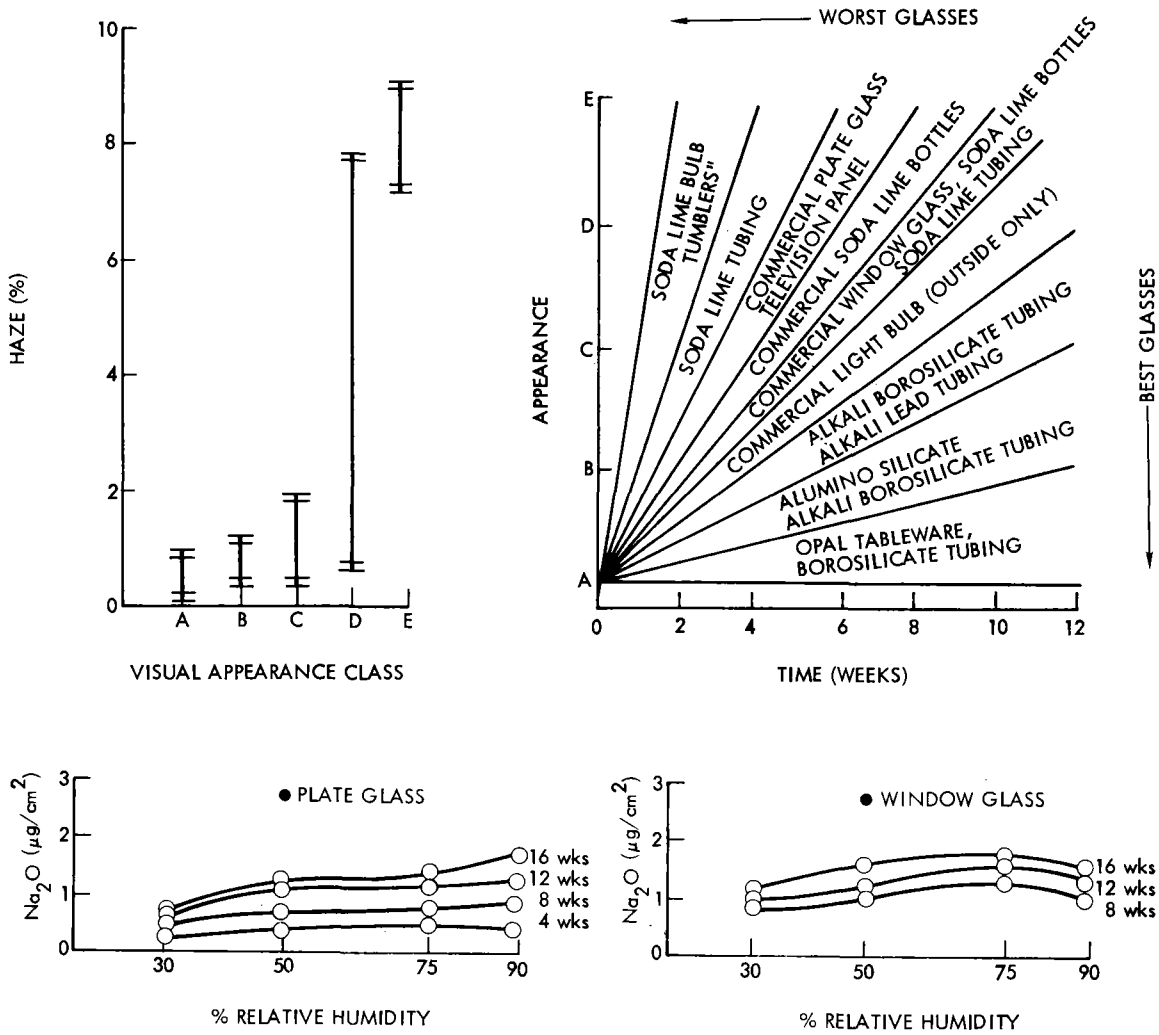


Figure A-8. Cleaning Effects

Table A-7. Solar Efficiency of Silvering Processes[1]

| Silvering Process | | Silver Thickness $gm/m^2$ | Over Solar Spectrum using Beckman | At $\lambda$ of 550 nm using Specular Photometer | | |
|---|---|---|---|---|---|---|
| | | | 125 mrad | 16 mrad | 8 mrad | 4 mrad |
| Peacock Laboratory | | 1.35 (125 $mg/ft^2$) | 85.0 | 93.5 | 91.0 | 62.0 |
| London Laboratory | 2 Part | 0.86 (80 $mg/ft^2$) | 84.3 | 91.0 | 90.0 | 88.5 |
| | 3 Part | 0.84 (78 $mg/ft^2$) | 84.5 | 93.0 | 92.5 | 85.0 |
| Hilemn | | 0.82 (76 $mg/ft^2$) | 84.1 | 92.5 | 91.5 | 79.0 |
| Mirrolab | | 1.01 (94 $mg/ft^2$) | 85.3 | 92.5 | 90.0 | 59.5 |

Note (1): 6.4 mm (1/4 inch) thick Fourco sheet glass was used.

Table A-8. Solar Efficiency versus Silver Thickness

| Type Glass and Thickness in millimeters (inches) | Specimen No. | Silver Deposition in grams per square meter | Beckman Spectro Photometer (Over Solar Spectrum) | Specular Photometer (550 nm) | | | Specular Spectrophotometer (Over Solar Spectrum) | | |
|---|---|---|---|---|---|---|---|---|---|
| | | | 125 mrad | 16 mrad | 8 mrad | 4 mrad | 16 mrad | 8 mrad | 4 mrad |
| Fourco Sheet Glass 6.4 mm (1/4-inch) | 58.4 | 0.65 (60 mg/ft$^2$) | 83.7 | 91.5 | 90.0 | 81.0 | | | |
| | 59.3 | 0.86 (80 mg/ft$^2$) | 84.1 | 91.5 | 91.0 | 89.0 | | | |
| | 60.1 | 1.01 (94 mg/ft$^2$) | 86.3 | 92.5 | 90.0 | 59.5 | | | |
| | 61.3 | 1.08 (100 mg/ft$^2$) | 83.1 | 90.0 | 88.0 | 82.0 | | | |
| | 62.1 | 1.29 (120 mg/ft$^2$) | 84.7 | 92.0 | 90.5 | 85.5 | | | |

Continued next page

Table A-8. Solar Efficiency versus Silver Thickness - (Continuation 1)

| Type Glass and Thickness in millimeters (inches) | Specimen No. | Silver Deposition in grams per square meter | Beckman Spectro Photometer (Over Solar Spectrum) | Specular Photometer (550 nm) | | | Specular Spectrophotometer (Over Solar Spectrum) | | |
|---|---|---|---|---|---|---|---|---|---|
| | | | 125 mrad | 16 mrad | 8 mrad | 4 mrad | 16 mrad | 8 mrad | 4 mrad |
| ASG Industries Float Glass 2.4 mm (3/32-inch) | 87.1 | 0.65 (60 mg/ft$^2$) | 85.0 | 92.0 | 92.0 | 91.0 | | | |
| | 88.1 | 0.86 (80 mg/ft$^2$) | 85.0 | 93.0 | 92.0 | 92.0 | | | |
| | 89.1 | 1.01 (94 mg/ft$^2$) | 86.0 | 93.0 | 92.0 | 88.0 | 83.6 | 83.2 | 77.2 |
| | 90.1 | 1.08 (100 mg/ft$^2$) | 85.0 | 93.0 | 93.0 | 93.0 | | | |
| | 91.1 | 1.29 (120 mg/ft$^2$) | 85.0 | 92.0 | 92.0 | 92.0 | | | |

Table A-9. Film Integrity Test Results on Some Selected First Surface Coatings

| Company | Coating | Silver | | Reflectance Efficiency at 560 nm and 4 mrad | | | |
|---|---|---|---|---|---|---|---|
| | | | | Before Exposure | After Exposure | | |
| | | Compatibility | Adhesion | | $(NH_4)_2S$ (3 hr) | HF-Detergent (12 hr) | Salt Spray (450 hr) |
| Textar Plastics | CR-212 | Poor | Poor | 0.79 | 0.49 | - | 0.44 |
| | C-254 | Good | Good | 0.82 | 0.62 | 0.50 | 0.59 |
| DuPont | 500 IMRON | Good | Good | 0.83 | 0.79 | 0.81 | 0.63 |
| | 326L | Good | Good | 0.83 | 0.71 | 0.77 | 0.60 |
| | RK 3637 | Good | Good | 0.84 | 0.81 | 0.79 | 0.32 |
| Sierracin | FX-103 | Good | Good | 0.82 | 0.41 | 0.37 | 0.46 |
| Owens Illinois | 650 | Good | Good | 0.84 | 0.50 | 0.66 | 0.19 |
| | 650 M | Good | Good | 0.59 | 0.30 | 0.54 | 0.08 |

Table A-10. Properties of Coated Vapor Deposited Silver Mirrors

| Supplier | Coating Identification | Initial Values at Various Acceptance Angles in Milliradians (mrad) | | | | Exposure at Fort Irwin in Mojave Desert | |
|---|---|---|---|---|---|---|---|
| | | Over Solar Spectrum using Beckman | At Wavelength of 550 nanometer using Specular Photometer | | | | |
| | | 125 mrad | 16 mrad | 8 mrad | 4 mrad | Exposure (days) | Results |
| ROHM and HAAS Co. | 70-2 (R&H No. 1) | 93.5 | 87.0 | 83.5 | 75.0 | 165 | Coating Failed |
| | 71-2 (R&H No. 2) | 96.8 | 95.5 | 95.0 | 94.0 | 166 | Coating Failed |
| | 72-2 (R&H No. 3) | 97.3 | 96.5 | 95.5 | 92.6 | 184 | Corrosion Starting |
| | 73-1 (R&H No. 4) | 97.2 | 96.5 | 95.0 | 92.0 | 184 | Corrosion Starting |
| | 74-2 (R&H No. 5) | 97.6 | 94.0 | 90.5 | 82.0 | 184 | Slight Crazing |
| | 76-1 (R&H No. 6) | 97.1 | 96.0 | 96.5 | 94.0 | 184 | Extensive Crazing |
| | 76-1 (R&H No. 7) | 97.1 | 95.0 | 94.5 | 92.5 | 184 | Slight Crazing |
| | 77-2 (R&H No. 8) | 96.8 | 93.0 | 90,5 | 82.5 | 184 | Extensive Crazing |
| | 78-1 (R&H No. 9) | 97.6 | 95.0 | 94.5 | 92.0 | 184 | Extensive Crazing |
| | 79-2 (R&H No. 10) | 97.9 | 94.0 | 92.5 | 84.5 | 185 | Coating Failed |
| | 80-1 (R&H No. 11) | 97.6 | 95.5 | 95.0 | 87.0 | 184 | Severe Corrosion |
| | 81-1 (R&H No. 12) | 95.4 | 90.0 | 89.0 | 85.0 | 184 | Moderate Crazing |
| O'Brien Corp. | 69-1 (6-73C) | 95.4 | 93.0 | 90.5 | 82.5 | 165 | Coating Failed |
| | 68-1 (874-C-200) | 96.3 | 90.5 | 87.0 | 71.0 | 184 | Coating Failed |

Table A-11. Solar Transmission Efficiency of Some Coatings

| Supplier | Specimen Identification | Over Solar Spectrum using Beckman | At Wavelength of 550 nanometer using Specular Photometer | | |
|---|---|---|---|---|---|
| | | 125 mrad | 16 mrad | 8 mrad | 4 mrad |
| De Soto Inc. | 1091-3-51 Fluorocarbon Acrylate | 99.9 | 100 | 99.5 | 99.0 |
| | 1091-6-51 Polyurethane | 99.9 | 99.5 | 98.5 | 98.5 |
| | 1091-10-51 Thermosetting Silicone | 99.7 | 98.5 | 98.5 | 98.0 |
| Rohm and Haas Co. | R&H No. 5 | 99.6 | 99.5 | 100 | 99.5 |
| | R&H No. 7 | 99.7 | 99.0 | 99.0 | 98.0 |
| | R&H No. 12 | 99.3 | 99.0 | 98.5 | 97.0 |
| PPG Industries | PPG No. 2 | 99.5 | 100 | 99.5 | 99.5 |
| | PPG No. 5 | 99.5 | 99.0 | 98.5 | 99.0 |
| DuPont Co. | 500 S IMRON | 99.5 | 100 | 100 | 100 |
| | 326 L Acrylic | 98.5 | 99.5 | 99.5 | 99.0 |
| | RK-63654 | 99.3 | 99.0 | 99.0 | 97.0 |
| O'Brien Corp. | 874-C-200 | 99.5 | 100 | 99.0 | 99.5 |
| | 5-73C | 99.4 | 99.0 | 99.0 | 98.0 |

Table A-12. Properties of Coated Chemically Deposited Silver Mirrors

| Specimen No. | Company | Coating | Measuring Instrument | Specularity | Efficiency at the following Wavelengths in Nanometers | | | | | | | | | | Avg Over Solar Spectrum |
|---|---|---|---|---|---|---|---|---|---|---|---|---|---|---|---|
| | | | | | 426 | 498 | 561 | 623 | 691 | 774 | 860 | 1008 | 1208 | 1594 | |
| 99-2 | DuPont | 500 IMRON | Specular Spectro Photometer | 16 | 60 | 79 | 85 | 86 | 90 | 90 | 91 | 93 | 93 | 83 | 85 |
| | | | | 8 | 58 | 77 | 83 | 85 | 86 | 89 | 89 | 91 | 91 | 82 | 83 |
| | | | | 4 | 55 | 73 | 79 | 83 | 83 | 85 | 86 | 88 | 88 | 81 | 80 |
| | | | Specular Photometer | 4 | | | 83 | | | | | | | | |
| 102-2 | Sierracin | FX-103 | Specular Spectro Photometer | 16 | 60 | 80 | 88 | 90 | 93 | 94 | 95 | 98 | 97 | 75 | 87 |
| | | | | 8 | 59 | 80 | 87 | 90 | 92 | 93 | 95 | 96 | 95 | 75 | 86 |
| | | | | 4 | 59 | 80 | 87 | 89 | 90 | 92 | 95 | 96 | 94 | 71 | 85 |
| | | | Specular Photometer | 4 | | | 82 | | | | | | | | |
| 104-1 | Textar Plastics | C-254 | Specular Spectro Photometer | 16 | 58 | 76 | 84 | 90 | 90 | 92 | 93 | 96 | 96 | 87 | 86 |
| | | | | 8 | 58 | 75 | 83 | 88 | 89 | 92 | 93 | 95 | 96 | 87 | 86 |
| | | | | 4 | 57 | 75 | 82 | 87 | 88 | 90 | 93 | 94 | 96 | 80 | 84 |
| | | | Specular Photometer | 4 | | | 82 | | | | | | | | |
| 101-2 | DuPont | RK3637 | Specular Spectro Photometer | 16 | 57 | 79 | 86 | 90 | 90 | 92 | 93 | 95 | 96 | 90 | 87 |
| | | | | 8 | 56 | 77 | 85 | 88 | 90 | 91 | 91 | 94 | 94 | 88 | 85 |
| | | | | 4 | 56 | 77 | 83 | 88 | 90 | 90 | 90 | 92 | 94 | 83 | 84 |
| | | | Specular Photometer | 4 | | | 84 | | | | | | | | |

Table A-13. Solar Reflectance Efficiency of Silver at Air Mass Two

| Mirror Manufacturer or Process | Silver Deposition | Exposure (days) | Acceptable Angle (milliradians) | Solar Reflectance Efficiency at the following Wavelengths in Nanometers | | | | | | | | | | Average Value Over Solar Spectrum |
|---|---|---|---|---|---|---|---|---|---|---|---|---|---|---|
| | | | | 426 | 498 | 561 | 623 | 691 | 774 | 860 | 1008 | 1208 | 1594 | |
| Theoretical | Vapor | | $\pi \times 10^3$ | 96.3 | 97.9 | 98.4 | 98.7 | 98.9 | 99.1 | 99.2 | 99.4 | 99.4 | 99.4 | 98.7 |
| Liberty Mirror | Vapor | Protected by Top Coat | 125 | 93.0 | 95.5 | 95.5 | 96.0 | 96.5 | 97.5 | 97.5 | 98.0 | 98.0 | 98.5 | 96.6 |
| | | | | 98.0 | 97.5 | 96.5 | 97.0 | 97.0 | 97.0 | 96.5 | 97.0 | 97.5 | 97.0 | 97.1 |
| | | | | 90.0 | 94.0 | 96.0 | 97.0 | 96.0 | 98.0 | 97.0 | 97.0 | 97.0 | 96.0 | 96.0 |
| | | | 16 | 87.0 | 93.0 | 94.0 | 94.0 | 95.0 | 97.0 | 97.0 | 97.0 | 97.0 | 96.0 | 95.0 |
| | | | 8 | 87.0 | 93.0 | 94.0 | 94.0 | 95.0 | 97.0 | 97.0 | 96.0 | 96.0 | 96.0 | 95.0 |
| | | | 4 | 87.0 | 93.0 | 94.0 | 94.0 | 95.0 | 96.0 | 95.0 | 95.0 | 95.0 | | 94.0 |
| Mirrolab | Chemical | 1* | 125 | 97.0 | 98.0 | 98.5 | 98.5 | 99.0 | 99.0 | 98.0 | 98.5 | 98.0 | 98.0 | 98.3 |
| | | | 16 | 89.1 | 93.7 | 94.5 | 96.2 | 95.5 | 92.6 | 93.3 | 95.7 | 96.7 | | 94.1 |
| | | | 8 | 88.2 | 92.9 | 93.8 | 95.5 | 94.8 | 92.0 | 93.3 | 95.7 | 95.6 | | 93.5 |
| | | | 4 | 87.2 | 91.4 | 93.0 | 93.8 | 94.4 | 91.5 | 93.3 | 95.7 | 94.6 | | 92.8 |
| London Laboratory | Chemical | 7 | 125 | 80.0 | 92.0 | 96.5 | 98.0 | 99.0 | 99.0 | 99.0 | 99.0 | 98.5 | 99.0 | 96.0 |
| PPG Industries | Chemical | 42 | 125 | 89.0 | 93.8 | 96.0 | 96.5 | 97.0 | 97.0 | 96.8 | 97.0 | 96.7 | 97.1 | 95.7 |
| | | | 125 | 87.5 | 92.5 | 94.0 | 95.2 | 96.4 | 96.5 | 96.0 | 96.8 | 96.5 | 97.0 | 94.8 |

*Stored in nitrogen 88 days prior to testing.

# APPENDIX B

# TRACKING AND CONTROL STUDIES

## PART I

## EFFICIENCY DEGRADATION DUE TO TRACKING ERRORS FOR POINT-FOCUSING SOLAR COLLECTORS

## PART II

## OPTIMAL CONTROL OF SUN-TRACKING SOLAR COLLECTORS

PART I

# Efficiency Degradation Due to Tracking Errors for Point Focusing Solar Collectors

**R. O. HUGHES**

ABSTRACT

An important parameter in the design of point focusing solar collectors is the intercept factor which is a measure of efficiency and of energy available for use in the receiver. Using statistical methods, an expression of the expected value of the intercept factor is derived for various configurations and control law implementations. The analysis assumes that a radially symmetric flux distribution (not necessarily Gaussian) is generated at the focal plane due to the sun's finite image and various reflector errors. The time-varying tracking errors are assumed to be uniformly distributed within the threshold limits and allows the expected value calculation.

INTRODUCTION

A point focusing solar concentrator** or parabolic dish is one of the devices that can effectively concentrate terrestrial sunlight to produce high quality thermal energy. Some other concepts are the central receiver, parabolic troughs, and fixed spherical reflector with movable focus. All of these techniques require some form of sun tracking to produce the desired level of solar concentration.

A point focusing solar concentrator forms a flux distribution in two spatial dimensions at its focal plane (not its focal point because the sun is not a point source) and if the aperture of the receiver (the device that collects the concentrated sunlight) is very large, then virtually all the energy will be received. If the aperture is small or the flux is not centered in the aperture (due to pointing errors), then the total received energy will be noticeably less than 100 percent. This percentage of energy is termed intercept factor.

The intercept factor is an important concept in the design of solar thermal systems as can be seen in the following general expression for the net power, Q, collected by a receiver,

$$Q = \rho I_o A G \Phi \alpha - q_r \qquad (1)$$

where $\rho$ is a specular reflectance constant, $I_o$ is the nominal direct isolation, A is effective collector area, G is shading factor, $\alpha$ is receiver absorptance, $q_r$ is heat loss, and $\Phi$ is the intercept factor. The intercept factor, $\Phi$, is the most dynamic quantity in the above equation as the others are either constant or slowly time varying. The size of the receiver aperture fixes the upper bound on the value of the intercept factor and is determined by the flux distribution generated by the reflective surface. The lower bound of the intercept factor is virtually zero and occurs when the pointing error is very large.

*This paper presents the results of one phase of research carried out at the Jet Propulsion Laboratory, California Institute of Technology. The work was jointly sponsored by the Department of Energy and the National Aeronautics and Space Administration under interagency Agreement and Contract No. NAS 7-100.

**Accepted nomenclature is that a solar collector consists of a concentrator and a receiver.

Optical errors, resulting from imperfect reflector surfaces, are the primary drivers in the generation of the focal plane flux distribution. These errors include slope errors (small local surface deviations in slope), contour errors (larger deviations due to inaccurate structural support or dynamic deflection), and specular errors (spreading of light beams resulting from the reflective material used). The major effect of these errors is the enlargement of the flux distribution at the focal plane -- hence, a larger receiver aperture is required and the effective concentration ratio (concentrator area/receiver aperture area) is reduced. See Reference 1 for a succinct discussion on the optical and thermal properties of point focusing solar collectors.

Another error mechanism is the pointing error which is defined as the angular difference between the aperture center and the flux distribution center. Contained within this class of errors are constant or slowly time varying errors such as misalignments, receiver sag, and atmospheric refraction. Others are more transient in nature and are caused by wind loads and/or the control scheme employed (References 2 and 3). A major emphasis of this study is to analyze the effects of these transient pointing errors on solar thermal systems for various flux distributions.

In Reference 4, a derivation of an intercept factor function was presented which assumed a two dimensional normalized Gaussian flux distribution, *i.e.*

$$f(x,y) = \frac{1}{2\pi\sigma^2} e^{-(x^2+y^2)/2\sigma^2} \qquad (2)$$

was present at the focal plane and where $\sigma$ was the standard deviation. It was shown that the intercept factor as a function of pointing error ($\delta$), the receiver aperture radius (R), and the flux distribution ($\sigma$) could be expressed as

$$\Phi(\delta,R,\sigma) = \int_0^R \frac{z}{2} e^{-(z^2+\delta^2)/2\sigma^2} \cdot B_o\left(\frac{z\delta}{\sigma^2}\right) dz \qquad (3)$$

where $B_o(\cdot)$ was a modified Bessel Function of order zero. The equation was solved numerically for various parameter values and results are plotted in Figures 1 and 2. The results prove useful heuristically for preliminary analysis, but a more general method using arbitrary flux distributions is indicated.

RADIALLY SYMMETRIC FLUX DISTRIBUTIONS

Let a "radially symmetric" distribution be defined as one that depends only on the radial distance from its center and not on the angular displacement; and therefore, any slice through the center will be identical with any other slice. Hence, Gaussian distributions, ones shaped like cones, and many others are radially symmetric. Now assume that the solar flux distribution generated by the reflec-

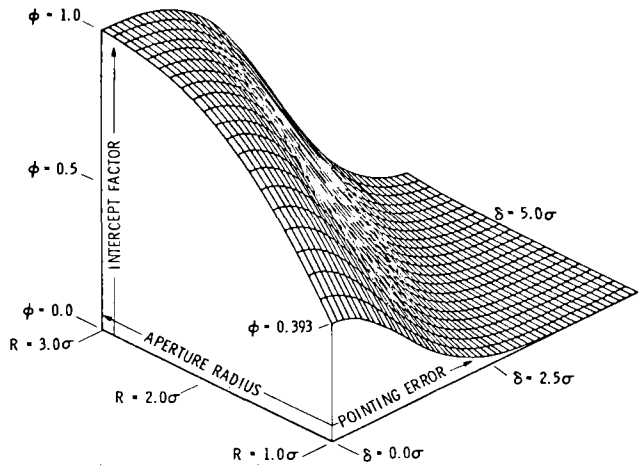


Fig. 1 Intercept Factor Function

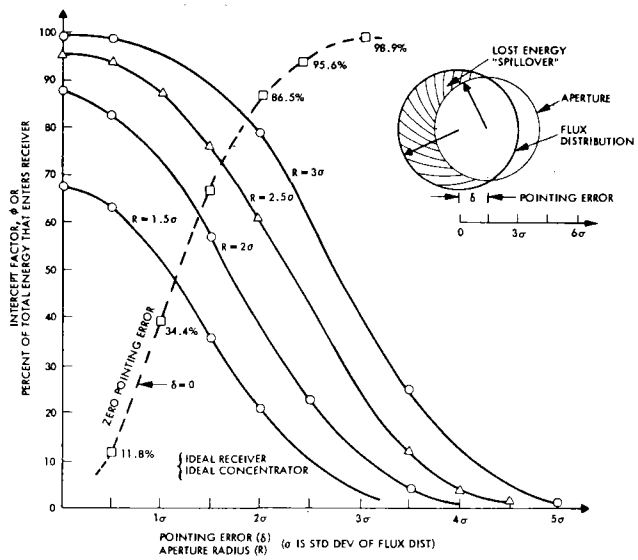


Fig. 2 Intercept Factor Function

tive surface at the focal plane is radially symmetric - and call it f(z) where z is the radial distance from the center. Let the receiver aperture at the focal plane have radius R and be offset from the distribution's center by an amount $\delta$ (the pointing error). A graphical representation is shown in Figure 3, where $\theta$ and $\beta$ are angular measures. The problem becomes that of finding the amount of "mass" or "volume" of the distribution contained within the aperture circle. The expression for the incremental area, dA, is

$$dA = 2\beta z dz = (2\pi - 2\theta) z dz. \qquad (4)$$

As the amount of flux within dA is constant, namely f(z), the incremental amount of energy or volume within dA is

$$dV = (2\pi - 2\theta)\, z\, f(z)\, dz, \qquad (5)$$

and the total volume within the aperture would be

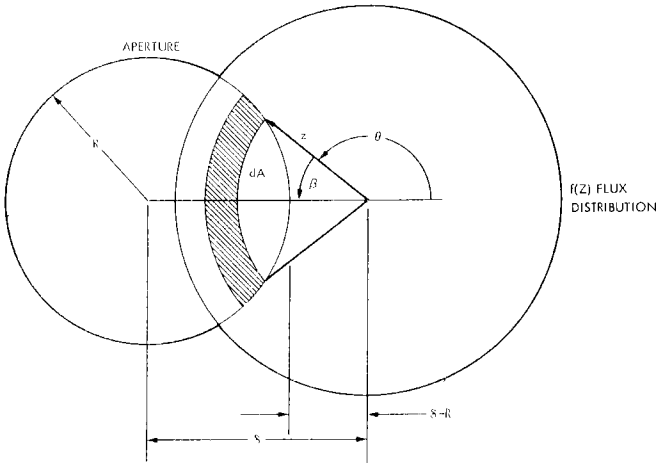


Fig. 3 Radially Symmetric Flux Distribution

$$V = \int_{z=\delta-R}^{z=\delta+R} (2\pi - 2\theta)\ z\ f(z)\ dz. \tag{6}$$

An expression for $\theta$ in terms of z is required to perform the above integration. Using the law of cosines, *i.e.*

$$R^2 = \delta^2 + z^2 - 2\ \delta\ z \cos\beta \tag{7}$$

and using

$$\cos(180^\circ - \theta) = -\cos\theta, \tag{8}$$

an expression for $\theta$ is

$$\theta = \pi - \cos^{-1}\left(\frac{z^2 + \delta^2 - R^2}{2\delta z}\right). \tag{9}$$

Hence, the desired expression is

$$V = \int_{\delta-R}^{\delta+R} 2\ z\ f(z)\ \cos^{-1}\left(\frac{z^2 + \delta^2 - R^2}{2\delta z}\right) dz. \tag{10}$$

Denoting the argument of the arc cosine as $\gamma$ and normalizing the total energy entering the aperture with zero pointing error to unity, the expression for the intercept factor is

$$\Phi = \int_{\delta-R}^{\delta+R} 2\ z\ f(z)\ \cos^{-1}(\gamma)\ dz. \tag{11}$$

The above derivation is for $\delta > R$ or the flux center outside the aperture. Similar techniques can be used to derive an equation for $\delta \leq R$ and the complete expression for $\Phi$ is

$$\phi(R,\delta) = \begin{cases} \displaystyle\int_0^{R-\delta} 2\ \pi\ z\ f(z)\ dz + \int_{R-\delta}^{R+\delta} 2\ z\ f(z)\ \cos^{-1}(\gamma)\ dz, & 0 \leq \delta \leq R \\ \displaystyle\int_{\delta-R}^{\delta+R} 2z\ f(z)\ \cos^{-1}(\gamma)\ dz, & \delta > R \end{cases} \tag{12}$$

where

$$\gamma = \frac{z^2 + \delta^2 - R^2}{2\delta z}. \tag{13}$$

In the above equation, it is necessary to have a description of the flux distribution, f(z), at the focal plane. If the distribution were Gaussian as in Reference 3, f(z) could be expressed analytically as in Equation 2. However, in general, f(z) will not be so simple and a "table look-up"/interpolation scheme employed.

EXPECTED VALUE OF THE INTERCEPT FACTOR

The intercept factors derived above in Equations 3 and 12 gave instantaneous answers for given values of pointing error ($\delta$), aperture radius (R), and flux distributions; but the characterization of the efficiency loss as a function of a wide class of pointing error time histories is desired. It is virtually impossible to predict *a priori* how a specific pointing error time history from a specific configuration would appear because of parameter inaccuracies, cloud shadowing, disturbance torques, *et. al.* Hence, it is necessary to generalize the problem using expected profiles from existing systems or systems closely akin to Solar Collectors. Another method, which is statistical in nature, would assume that the pointing error is a normally distributed random variable with a standard deviation of $\sigma_\delta$. Then the intercept factor could be calculated as a function of $\sigma_\delta$. The first method is made deterministic by assuming the error in the two axes behaves as shown in Figure 4. Assuming the two motions are independent and linear within the deadband, it can be shown that the errors are uniformly distributed between -A and +A and their joint density function $f_{xy}$ (x,y) (x for azimuth, y for elevation) can be drawn as shown in Figure 5.

Because of the circular geometry of the aperture, it is natural to use the Euclidean Norm metric to express the pointing error. This norm is simply

$$r = \sqrt{x^2 + y^2}$$

where r is radial pointing error. It is desired to determine the density function, f(r), from the joint

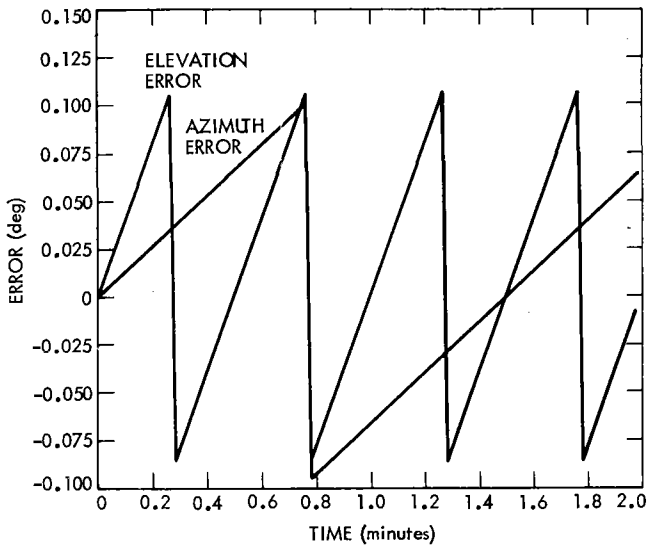


Fig. 4 Typical Error Behaviors-on/off Controller

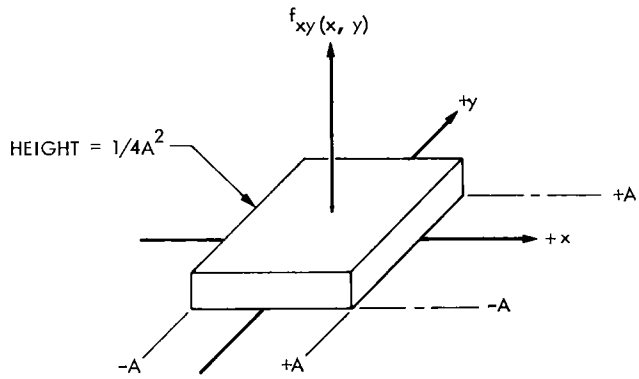


Fig. 5 Uniform Density Function

density, $f_{xy}(x, y)$ in terms of the above metric and is accomplished by methods similar to those used for the intercept factor derivation; namely,

$$f(r) = \iint_{\Delta D} f_{xy}(x,y)\, dx\, dy. \tag{14}$$

For this particular geometry, the determination of the region of integration, $\Delta D$, is slightly more complicated than before. The square region (see Figure 6) within the outer circle representing

$$r = \sqrt{x^2 + y^2}$$

contains the joint density $f_{xy}(x,y)$. The density $f(r)$ is composed of two components - that from 0 to A [called $f_1(r)$] and four shaded regions together [called $f_2(r)$].

First,

$$f_1(r) = \int_0^{2\pi} f_{xy}(x,y)\, r\, d\theta \tag{15}$$

or

$$f_1(r) = \frac{1}{4A^2} * 2\pi * r = \frac{\pi r}{2A} \tag{16}$$

which is simply a linear function of r. For the second function, $f_2$, it is noted that each of the four regions can be divided into two equal areas as shown in Figure 7. Let $\rho$ be the angle from $\theta = 45°$ to 90°. The total density $f_2(r)$ in the eight regions is

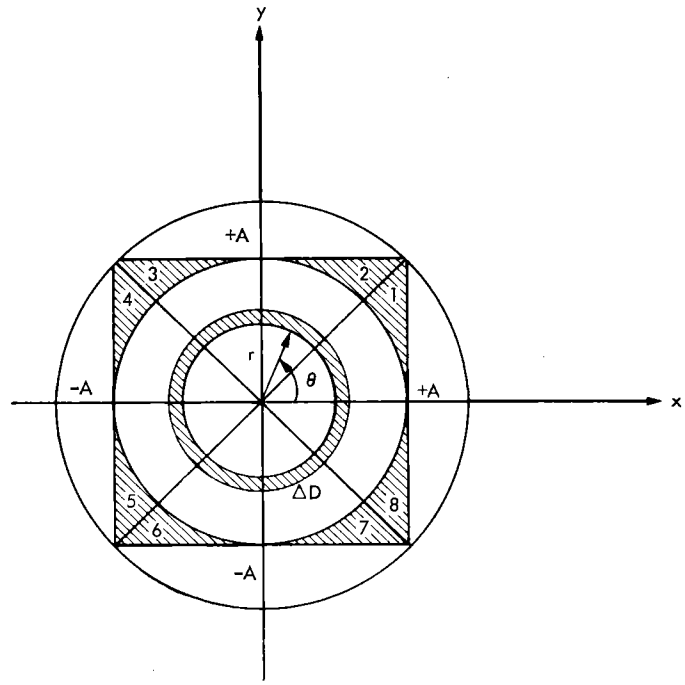


Fig. 6 Joint Density Geometry

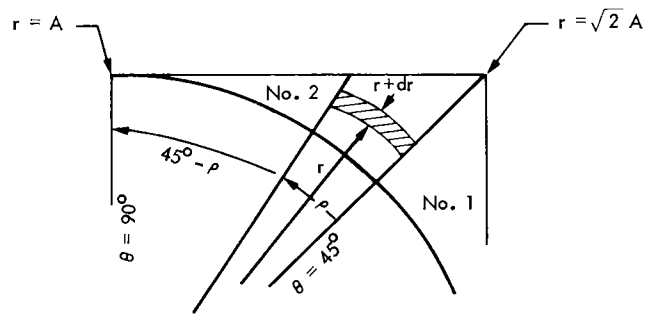


Fig. 7 Region No. 2 Detail

$$f_2(r) = 8\, r\, \rho\, f_{xy}(x,y) = 8\, r\, \rho \frac{1}{4A^2}. \tag{17}$$

Noting that

$$A = r * \cos(45° - \rho), \tag{18}$$

it follows that

$$f_2(r) = \frac{2r}{A^2}\left[\pi/4 - \cos^{-1}(A/r)\right] \tag{19}$$

and hence, the desired expression for the radial pointing error density function is

$$f(r) = \begin{cases} \dfrac{\pi r}{2A^2}, & 0 \le r \le A \\[2ex] \dfrac{2r}{A^2}\left[\pi/4 - \cos^{-1}(A/r)\right], & A < r \le \sqrt{2}A. \end{cases} \tag{20}$$

It is instructive to verify this density expression using a Monte Carlo simulation technique. Here 10,000 random numbers are generated for both x and y, converted by the Euclidean Norm, and then arranged into a histogram "frequency of occurrence" format. The mean of the occurrences is concurrently computed in the simulation. Results of the simulation together with the curve of f(r) (equation 20) are shown in Figure 8, and there is a close similarity between the two.

Also, it is instructive to compare expected values using the basic definition of expected value, *i.e.*

$$E\{f(r)\} = \int_{-\infty}^{+\infty} r\, f(r)\, dr. \tag{21}$$

The expected value of f(r) was numerically calculated to be 0.765 which compares favorably to the Monte Carlo value of 0.762 with A equal to unity.

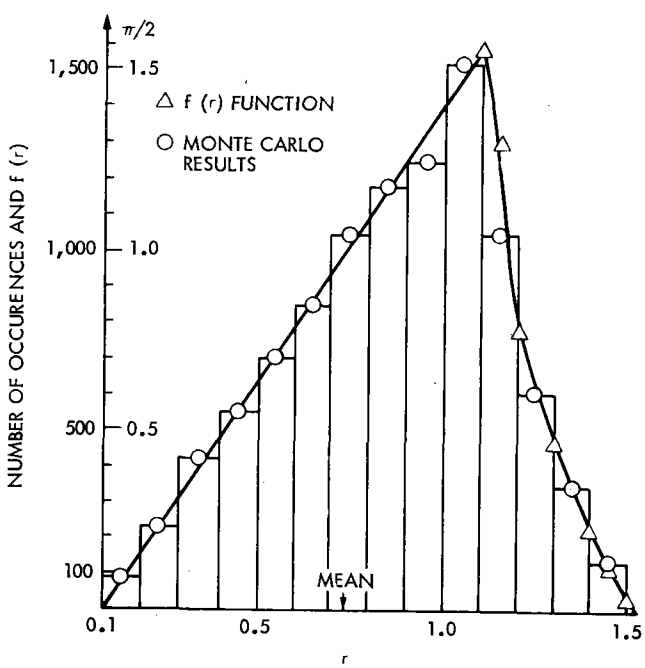


Fig. 8 Frequency Distribution from Monte Carlo Simulation and Plot of Euclidean Norm Density

The above analyses was necessary to arrive at a point where the answer can be given for the following important question, "What is the expected value of the intercept factor function, Φ, for various R, flux distributions f(z) and deadband size, A?" Or, neglecting the first two independent variables (which implies that the concentrator and receiver configurations are specified) the question is "How does Φ change with A?" This is important for it indicates how much energy will be lost due to pointing error. With larger A, both equipment cost and parasitic power consumption will be lower. With smaller A, less energy will be lost. The expected value of the intercept factor can be calculated using

$$E\{\Phi(A)\} = \int_0^{\sqrt{2}A} f(r)\ \Phi\ (r)\ dr \tag{22}$$

where f(r) and Φ(r) are calculated using equations 20 and 12, respectively.

EXAMPLES

Example #1 - Gaussian Distribution

Using the intercept factor function described by Equation 3 the integration of the expected value function (equation 22) was performed numerically for various values of A and R (expressed in σ units). Results are shown in Figure 9. Now let a 12 meter parabolic dish with an f/D ratio of 0.6 have a slope error of 0.1° (*i.e.* standard deviation = 0.1°). From a ray trace analysis, the +3σ value of the flux distribution generated at the focal plane is about 9 cm (1σ is 3 cm) for a total diameter of about

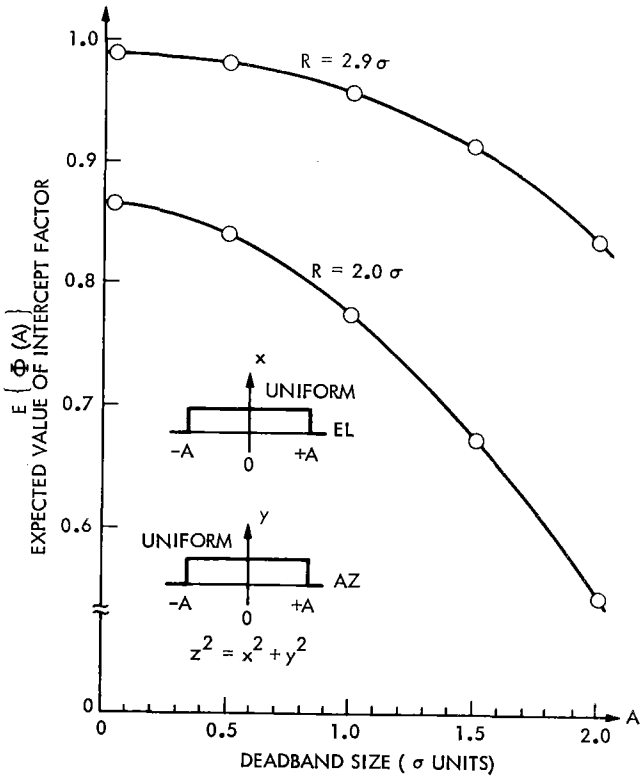


Fig. 9 Expected Value of Intercept Factor for Euclidean Norm of Two-Sided Deadband

18 cm. If the receiver aperture were 18 cm in diameter and if there is no pointing error, then 98.9% (see Figure 2) of the available energy would enter the receiver. But, for purposes of this example, assume the "best" receiver aperture radius was calculated to be 5.7 cm. Therefore,

$$R = \frac{5.7}{3} = 1.9\sigma. \tag{23}$$

Because of this rather small aperture the maximum amount of energy that could enter the receiver would only be 83.5% of the amount available (definition of the intercept factor's upperbound). Now assume there are three options for a deadband size ±0.05° ±0.1°, or ±0.2° which, for this example, correspond to A values of 0.2σ, 0.4σ, and 0.8σ, respectively. These options will have their own individual cost, maintenance, and power consumption characteristics associated with them and can be traded off in a rational manner with the change in performance degradation. Using Figure 9, the values are obtained. Table 1 shows the comparison.

Table 1 Comparison of Different Deadbands

| Option | Dead Band (A) | Upper Bound of Φ(A) | E{Φ(A)} | % Lost |
|---|---|---|---|---|
| A | ±0.05° (0.2σ) | 83.5% | 83.2% | 0.3% |
| B | ±0.1° (0.4σ) | 83.5% | 82.0% | 1.5% |
| C | ±0.2° (0.8σ) | 83.5% | 77.3% | 6.2% |

Example #2 - Radially Symmetric Distribution

Assume the following parameters:

$D = 10$ m

$f/D = 0.604$

$\sigma_s = 2$ mrad (slope error)

$R = 11$ cm (receiver aperture radius)

$A = 0.1°$ (deadband size)

$\sigma_c = 0$ (contour errors)

Corning Silvered Microsheet

For the above parameters, L. Wen in Reference 1 has generated the predicted flux distribution at the focal plane using a cone optics ray tracing computer program and is reproduced in Figure 10. This program considers the sun's finite size, limb darkening effects, and most of the optical errors described previously. Using Equation 12, the intercept factor, Φ, is generated and is shown in Figure 11. Using Equation 22, the expected value of Φ is generated for various deadband sizes and is also shown in Figure 11. For the deadband specified (*i.e.* ±0.1°), a dynamic computer simulation was run: the AZ/EL error behaviors are shown in Figure 4 and the instantaneous intercept factor, Φ(t), together with its running time average intercept factor, $\Phi_{AVG}(t)$, are shown in Figure 12. Note that the average Φ value near the end of the simulation is very near the predicted value of the expected value (E{Φ(0.1°)} in Figure 11). Also note at the start of the simulation when both AZ and EL errors are zero, the intercept factor is at its upper bound.

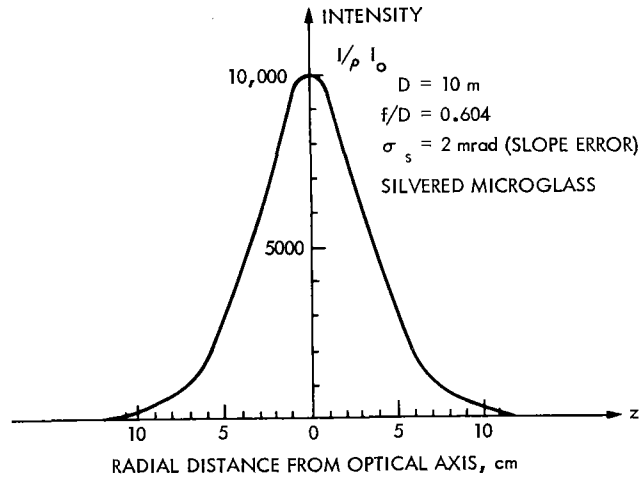


Fig. 10 Predicted Flux Distribution

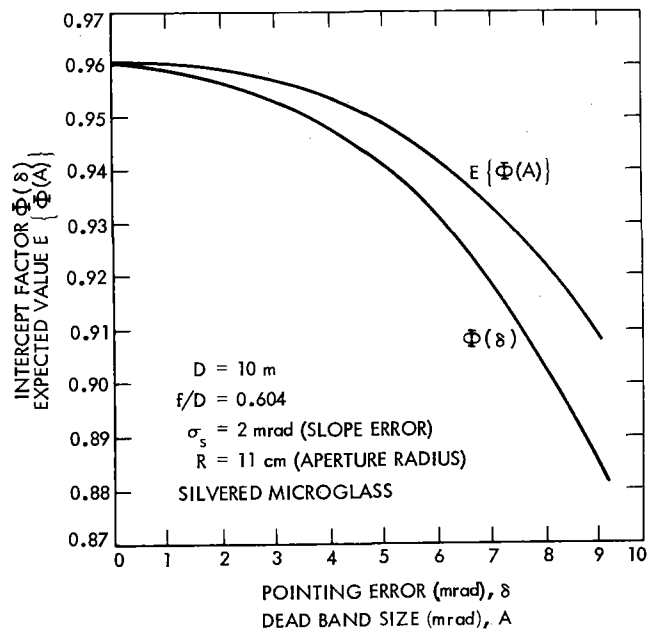


Fig. 11 Expected Value of Intercept Factor

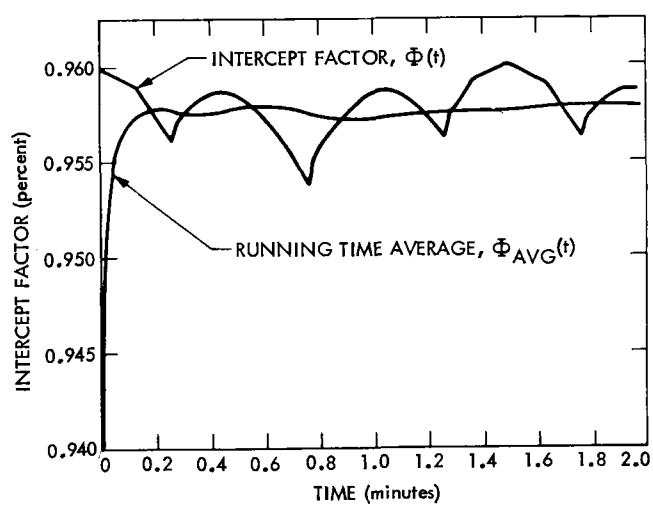


Fig. 12 Intercept Factor Simulation

Example #3 - Uniform Distribution-Model Verification

Because Equations 3 and 12 can only be solved numerically, a method of analytical verification is desired to confirm their validity. If a uniform flux distribution bounded by a circle of radius R is used with a receiver aperture of radius R, a closed form solution can be derived.

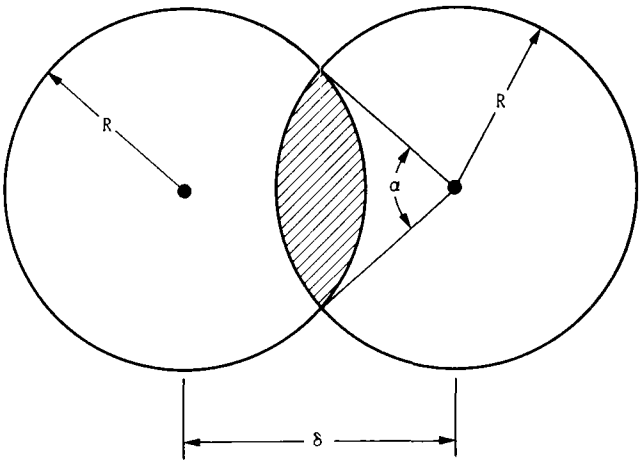


Fig. 13 Analytical Verification Technique

This problem can be visualized as follows: determine the common volume in the intersection of two right circular cylinders of equal radii and known constant heights. Let the heights be unity and the radii equal to R (radius of the aperture). Let $\delta$ (pointing error) be the distance between centers. See Figure 13. The percentage of area is the shaded section and is given by

$$\% = \frac{\alpha - \sin\alpha}{\pi} \tag{24}$$

where $\alpha = 2 \cos^{-1} (\delta/2R)$. Because the uniform distribution has unity value this equation is the intercept factor, $\Phi(\delta)$ and values generated by this equation are virtually identical with those numerically generated by Equation 12.

CONCLUSIONS

The derivation of an expression for the intercept factor for point focusing solar collectors is extended to include radially symmetric flux distributions. A previous study considered only Gaussian flux distributions. The results of the derivation allows for the analysis of a wider range of flux distributions including ones generated by complex ray tracing programs and those generated by actual measurements.

The expected value function of the intercept factor was derived for an on-off type control law as a function of deadband size. This expression is a direct measure of the expected energy input for typical pointing errors resulting from control law design. In other words, the on-off control system currently being used in many solar applications has inherent time varying pointing errors, and the expected value gives a quantitative expression that describes these errors.

A major conclusion of the paper is that errors due to pointing can be separated from those due to optical imperfections (slope, contour, and specular types). These optical errors dictate the final shape of the flux distribution at the focal plane, while the pointing error merely translates it (for small errors) across the aperture, resulting in reduced efficiency. This loss in efficiency is thus directly related to pointing error and serves as a powerful tool in the preliminary design phases of solar thermal power systems.

REFERENCES

1 Wen, L., "Thermal Optical Surface Properties and High Temperature Solar Energy Conversion," 2nd ASME Thermophysics and Heat Transfer Conference, Palo Alto, CA, May 1978.

2 Hughes, R.O., "The Sun Tracking Control of Solar Collectors Using High-Performance Step Motors," Sixth Annual Symposium on Incremental Motion Control Systems and Devices, Champaign, ILL, May 1977.

3 Hughes, R.O., "Optimal Control of Sun Tracking Solar Collectors," International Solar Energy Society Conference, Denver, CO, Aug. 1978.

4 Hughes, R.O., "Effects of Pointing Errors on Receiver Performance for Parabolic Dish Solar Concentrators," 13th IECEC, San Diego, CA, Aug. 1978.

PART II

# OPTIMAL CONTROL OF SUN TRACKING SOLAR COLLECTORS*

Robert O. Hughes
Control and Energy Conversion Division
Jet Propulsion Laboratory
Pasadena, California

ABSTRACT

Using the disciplines of Modern Control Theory, an optimal tracking control for a point focusing solar concentrator is derived. By converting the tracking problem into a regulator problem with a trim rate input a very low pointing error is achieved. A representative example with a corresponding computer simulation is presented.

## 1. INTRODUCTION

A common element in all sun tracking solar collectors (be they troughs, heliostats or parabolic dishes) is the control algorithm that commands the required motion in the articulation axis(es). The algorithm could be "open loop" in which precomputed commands are sent or "closed loop" in which measurements of the desired output are used to generate motion commands. A typical closed loop algorithm in current use is the "on-off" or "bang-bang" type which normally employs threshold sensing to effect required motion. This control law is simple and intuitively appealing, but it does have two drawbacks; namely, pointing inaccuracy and possible instability.

Point focusing parabolic dishes have stringent tracking requirements and are used in this study as the representative type of solar concentrator for discussion and analysis; other concentrator systems can be considered subsets of this basic type. A typical point focusing concentrator concept is shown in Fig. 1, and Refs. [1], [2], and [3] give background information and analytical

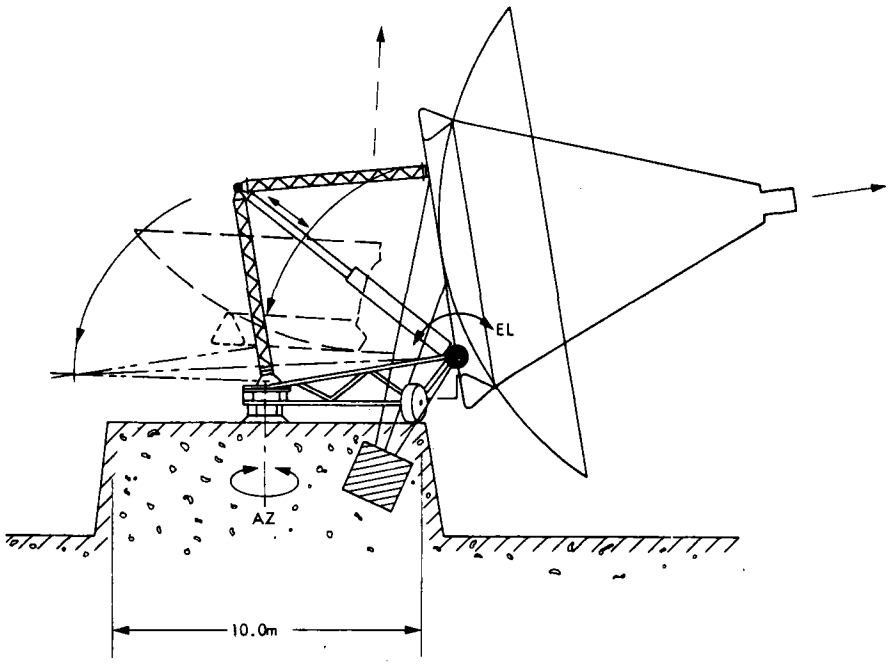


Fig. 1. Raised Mount for Deep Dish Concentrator

*This paper presents the results of one phase of research carried out at the Jet Propulsion Laboratory, California Institute of Technology. The work was jointly sponsored by the Department of Energy and the National Aeronautics and Space Administration under Interagency Agreement and Contract No. NAS7-100.

discussions about typical design and control problems. Note that the axis of the paraboloid must be pointed at the sun in order to produce the required flux densities at the receiver aperture. Whenever there is a pointing error, energy is lost; hence, it is desired, through proper control techniques, to minimize this energy loss.

An attractive method of analysis for this tracking problem is the optimal control formulation, which has been widely used in various applications (usually in the aerospace field). While the optimal control would probably not be implemented in actual practice because of its cost and complexity, it does provide an excellent method of comparison with other types of control algorithms.

## 2. COLLECTOR MODEL

To apply optimal control techniques, a "reasonable" linear model is required to achieve the goal of "minimizing the pointing error in the presence of disturbances without using 'too much' energy and without physical damage to the components." The collector system is nonlinear (as are all real systems) due to factors such as backlash and friction. The control law developed after any linear analysis should always be tested in a real system or simulated using the best nonlinear model available.

As a linear model of a single axis of the collector, let a second order model describe the plant dynamics and a single integrator represent the collector's electric motor. A simple block diagram is shown in Fig. 2, where $\theta_o$ is the collector's line of sight (LOS), $\theta_i$ is the sun's position, e is the difference between $\theta_i$ and $\theta_o$ (i.e., the error), u is command input to the motor, $\omega_n$ is the natural frequency of the plant where

$$\omega_n = \sqrt{\frac{K}{J}} \tag{1}$$

K is the stiffness, J is inertia, $\xi$ is the damping ratio, s is the Laplace operator, and $K_s$ is the system gain.

Letting

$$\begin{cases} x_1 = \theta_o \\ x_2 = \dot{\theta}_o \\ x_3 = \ddot{\theta}_o \end{cases} \tag{2}$$

and assuming that the collectors' position, velocity, and acceleration can be accurately measured, the state space model (required for optimal control analysis) becomes

$$\begin{aligned} \dot{\underline{x}} &= \underline{A}\,\underline{x} + \underline{B}u^* \\ \underline{y} &= \underline{C}\,\underline{x} \end{aligned} \tag{3}$$

where

$$\underline{A} = \begin{bmatrix} 0 & 1 & 0 \\ 0 & 0 & 1 \\ 0 & -\omega_n^2 & -2\xi\omega_n \end{bmatrix}$$

$$\underline{B} = \begin{bmatrix} 0 \\ 0 \\ K_s\omega_n^2 \end{bmatrix} \tag{4}$$

$$\underline{C} = \begin{bmatrix} 1 & 0 & 0 \\ 0 & 1 & 0 \\ 0 & 0 & 1 \end{bmatrix}$$

and $\underline{y}$ is the output vector. Letting $\underline{z}$ be the desired track (the sun's position, velocity, and acceleration) or

$$\underline{z} = \begin{bmatrix} \theta_i \\ \dot{\theta}_i \\ \ddot{\theta}_i \end{bmatrix} \tag{5}$$

the error, $\underline{e}$, can be defined as

$$\underline{e} = \underline{z} - \underline{y} \tag{6}$$

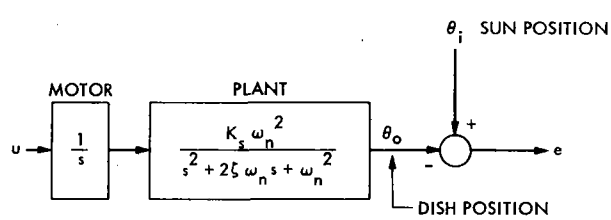


Fig. 2. Linear Model

*Underbars denote matrices and overdots denote differentiation with respect to time.

## 3. OPTIMAL TRACKING PROBLEM

The above model is cast in the form commensurate with that required in Appendix A to achieve theoretical optimal tracking of the sun. As $\underline{z}$ can be accurately predicted through emphemeris data, only the weighting matrices Q and R need be specified. However, a major practical problem exists with this formulation - that of the mechanization of the $\underline{g}[t]$ dynamics (eqn. A-9). Not only must the $\underline{g}$ dynamics reside in the control circuitry, but also the initial value of $\underline{g}$(i.e., $g[t_o]$) must be precomputed each day using "backward integration." A more straightforward and tractable method of analysis and implementation is sought.

## 4. STATE REGULATOR FORMULATION

The optimal tracking solution described above has found use in many areas where high accuracy was required and where the target was moving rapidly (satellite tracking, for example). However, the sun moves very slowly in comparison with such targets and the need for the extreme continuous accuracy is not required. By using a few reasonable assumptions, the tracking problem can be recast into a regulator problem, thereby reducing complexity.

The differential equation that describes the plant/motor in Fig. 2 can be written as:

$$\dddot{\theta}_o + 2\xi\omega_n\ddot{\theta}_o + \omega_n^2\theta_o = K_s\omega_n^2 u \ . \tag{7}$$

By defining the new set of state variables,

$$\begin{aligned} e_1 &= \theta_i - \theta_o \\ e_2 &= \dot{\theta}_i - \dot{\theta}_o \\ e_3 &= \ddot{\theta}_i - \ddot{\theta}_o \end{aligned} \tag{8}$$

and substituting into eqn. (7), the following results:

$$\dddot{e} + 2\xi\omega_n\ddot{e} + \omega_n^2\dot{e} = -K_s\omega_n^2 u + \dddot{\theta}_i + 2\xi\omega_n\ddot{\theta}_i + \omega_n^2\dot{\theta}_i . \tag{9}$$

Now assume that $\dddot{\theta}_i$ and $\ddot{\theta}_i$ are zero. In Fig. 3 the sun's maximum predicted rates for 35°N latitude are shown. At about 11:30 (12:30) local time on summer solstice, a maximum sun acceleration occurs with a value of about 42° $hr^{-2}$ ($3.2 \times 10^{-6}$ deg $sec^{-2}$). This is virtually insignificant compared with the capability of the solar tracking system, and it also indicates that $\dot{\theta}_i$ will remain constant (in a computational sense) for relatively long time intervals (say 1-2 minutes). Therefore, the $\dot{\theta}_i$

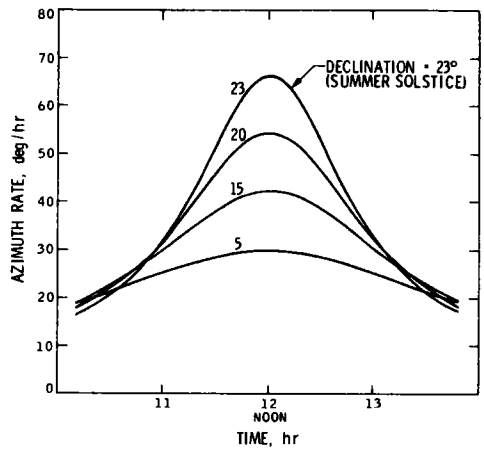


Fig. 3. Sun's Rate in Azimuth for 35° N Latitude and for Various Times of the Year

term acts as a constant bias to drive the collector at the sun's predicted rate.

Transforming eqn. (9) into matrix notation, i.e.,

$$\dot{\underline{e}} = \underline{A}\,\underline{e} + \underline{B}\,u + \begin{bmatrix} 0 \\ 0 \\ \omega_n^2\dot{\theta}_i \end{bmatrix} \tag{10}$$

and noting that this equation (neglecting the bias term) has the structure of a state regulator, i.e., eqn. (A-1), an "error regulator" problem results. This is the desired end result - to constantly drive the error to zero in the presence of disturbances.

General guidelines (a strict methodology does not exist) for selection of the $\underline{Q}$ and $\underline{R}$ matrices in the cost functional (eq. A-2)

$$J = \frac{1}{2}\int_0^\infty (\underline{e}^T\,\underline{Q}\,\underline{e} + u^T\,\underline{R}\,u)\,dt \tag{11}$$

where

$$\underline{Q} = \begin{bmatrix} Q_1 & 0 & 0 \\ 0 & Q_2 & 0 \\ 0 & 0 & Q_3 \end{bmatrix} \tag{12}$$

are given in Ref. [4]. Using $\underline{R}$ = 1, the optimal control (eqn. A-3) can be expressed as

$$u = -\begin{bmatrix} 0 \\ 0 \\ -K_s\omega_n^2 \end{bmatrix}^T \underline{K}\,\underline{e} \qquad (13)$$

or

$$u = K_s\omega_n^2 \,(K_1\, e_1 + K_2\, e_2 + K_3\, e_3) \qquad (14)$$

or, stated simply, the optimal regulating control, u, is a linear combination of the system states.

The complete system is shown in Fig. 4; note the similarity with Fig. 5 from Ref. [1]. This can be visualized as having two input branches: The first is the open loop "sun rate" and the second the optimal regulator feedback control. It can be shown that a very small tracking error will accumulate over a half-day period when trim rate is used exclusively. However, when feedback control is added, this error will be taken as a small disturbance and will be driven to zero. In essence, this control system behaves as a regulator operating about the slowly changing set point.

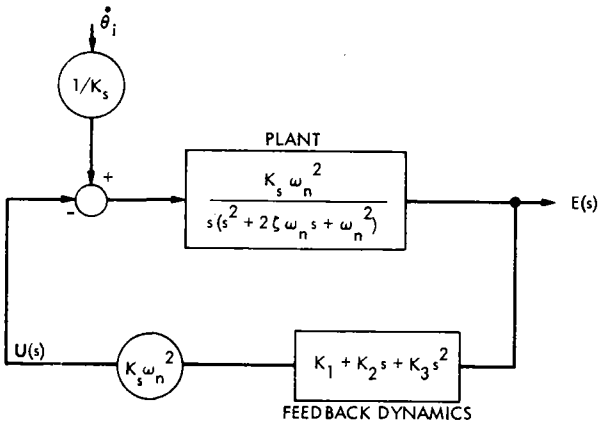


Fig. 4. Optimal Regulator

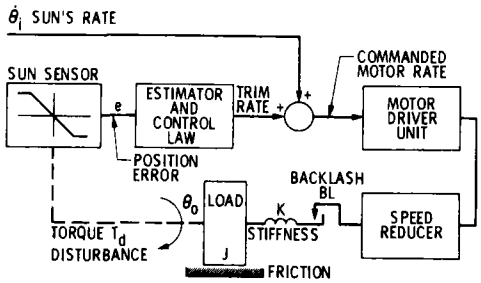


Fig. 5. Nonlinear Block Diagram

## 5. MECHANIZATION OF THE OPTIMAL REGULATOR

To mechanize the optimal control law for the solar tracking application described above, the following procedure would be used:

1. Obtain a good description of the hardware components - generate model - linearize for analysis.
2. Choose $\underline{R}$ and $\underline{Q}$ values.
3. Generate optimal gains: $K_1$, $K_2$, and $K_3$.
4. Calculate sun's rate, $\dot{\theta}_i$, during the given day.
5. Obtain measurements or estimates of the states $e_1$, $e_2$, and $e_3$.
6. Connect elements together as described in Fig. 4.

## 6. EXAMPLE

Representative values of a single axis for an ideal small solar concentrator were used to simulate the performance of the optimal regulator control law using simple linear and nonlinear models. First, the physical model was linearized and an estimate of the damping ratio obtained. Then the optimal gains were calculated (Ref. [5]) for R = 1, $Q_1$ = 1, $Q_2$ = 0.2, $Q_3$ = 0.2. Using 65° $hr^{-1}$ for $\dot{\theta}_i$, the simulation was run using the linear model with a moderate wind disturbance (step function) occurring at time = 5 seconds. The positional error trace is shown in Fig. 6 and has the characteristic exponential (i.e., linear) decay response.

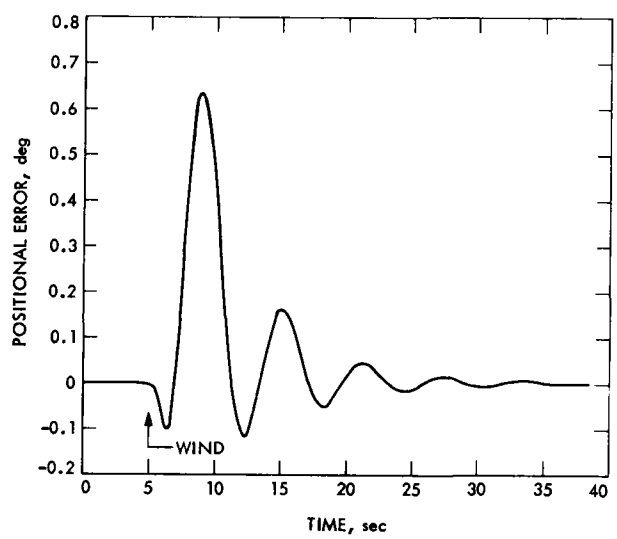


Fig. 6. Linear Response to Wind Disturbance

The same control law and wind disturbance was then implemented on the nonlinear model which simulated the effects of Coulomb friction (backlash was set

to zero), and Figs. 7 and 8 show the results. Note the definite change in the error response due to friction.

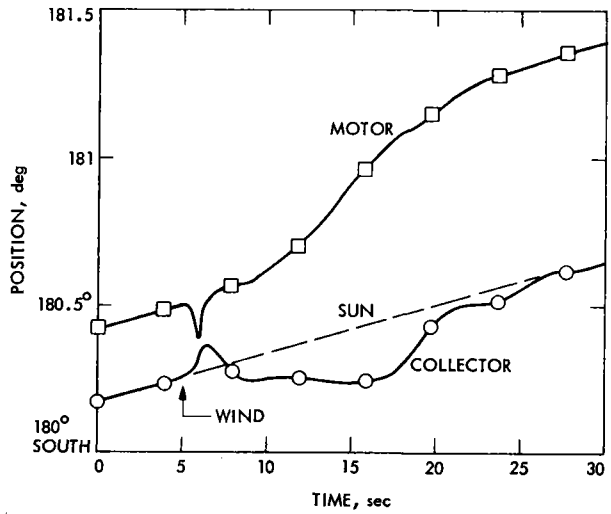


Fig. 7. Positional Response for Nonlinear System

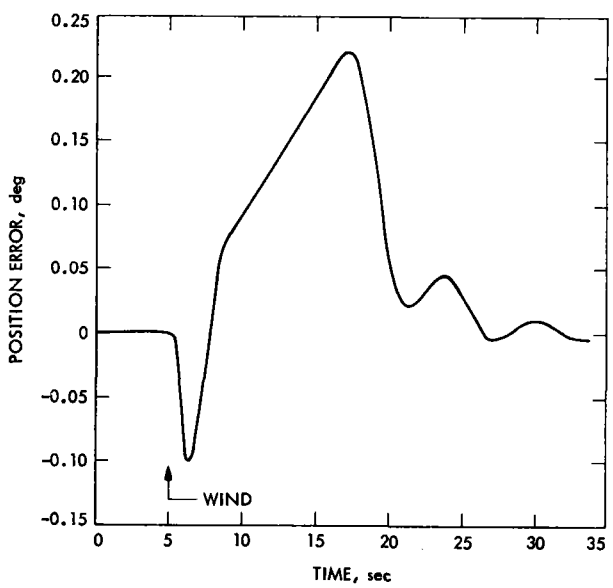


Fig. 8. Error Response for Nonlinear System

## 7. CONCLUSIONS

It is shown that the disciplines of Modern Control Theory and Optimal Control Theory, which are generally reserved for aerospace and large scale systems applications, can be straightforwardly applied to the sun tracking performance of solar concentrators. With the conversion from a standard tracking problem to a regulator problem using the trim rate technique, and with the optimal control formulation, it is shown that an almost zero steady state tracking error can be achieved (even with wind disturbances). This implies less energy will be lost and the entire system will be more cost effective.

The optimal control techniques described herein offer a straightforward, albeit time consuming, methodology for deriving control algorithms. However, as the use of optimal type algorithms requires relatively large computing facilities and because a major goal of the solar thermal power program is minimal cost, such algorithms will probably not be used in commercial endeavors. The most important function of these techniques is that they can serve as comparison standards for other types of control algorithms and aid in their development.

## 8. REFERENCES


1. R.O. Hughes, "The Sun Tracking Control of Solar Collectors Using High-Performance Step Motors," Sixth Annual Symposium on Incremental Motion Control Systems and Devices, Champaign, IL, May 1977.

2. R.O. Hughes, "The Effects of Pointing Errors on Receiver Performance for Parabolic Dish Solar Concentrators," 13th IECEC, San Diego, CA, Aug. 1978.

3. L.Wen, "Thermal Optical Surface Properties and High Temperature Solar Energy Conversion," 2nd ASME Thermophysics and Heat Transfer Conference, Palo Alto, CA, May 1978.

4. D'Azzo and Houpis, Linear Control System Analysis and Design, McGraw-Hill, 1975.

5. D. Wiberg, State Space and Linear Systems, Schaum's Outline, 1971.

6. Athans and Falb, Optimal Control, McGraw-Hill, 1966.


## APPENDIX A. OPTIMAL CONTROL LAWS

Athans and Falb in Ref. [6] derive several control laws which are useful in the operation of sun tracking algorithms. Simplified slightly, two important laws are stated below:

### STATE REGULATOR PROBLEM

Given the linear, constant, completely controllable and observable system:

$$\dot{\underline{x}} = \underline{A}\,\underline{x} + \underline{B}\,\underline{u} \qquad \text{(A-1)}$$

where $\underline{x}$ is the state vector, $\underline{A}$ is the system matrix, $\underline{B}$ is the input matrix and $\underline{u}$ is the control

vector ($\underline{x}$ and $\underline{u}$ are functions of time) and a given cost functional

$$J = \frac{1}{2} \int_0^\infty (\underline{x}^T \underline{Q}\, \underline{x} + u^T R\, u)\, dt \qquad \text{(A-2)}$$

where $\underline{u}$ is unconstrained and $\underline{Q}$, $\underline{R}$ are constant positive definite matrices, then the optimal control law that minimizes J exists, is unique, and is given by

$$\underline{u} = -\underline{R}^{-1}\, \underline{B}^T\, \underline{K}\, \underline{x} \qquad \text{(A-3)}$$

where $\underline{K}$ is a constant positive definite matrix which is a solution of the Riccatic-type matrix equation

$$-\underline{K}\, \underline{A} - \underline{A}^T \underline{K} + \underline{K}\, \underline{B}\, \underline{R}^{-1}\, \underline{B}^T \underline{K} - \underline{Q} = 0 \qquad \text{(A-4)}$$

Ref. [5] documents techniques for the numerical solution of this equation.

TRACKING PROBLEM

Given the linear, constant, completely controllable and observable system

$$\dot{\underline{x}} = \underline{A}\, \underline{x} + \underline{B}\, \underline{u}$$

$$\underline{y} = \underline{C}\, \underline{x}$$

where $\underline{C}$ is the output matrix and $\underline{y}(\underline{y}[t])$ is the output and given $\underline{z}(\underline{z}\,[t])$, the desired trajectory of the output, and defining the error, $\underline{e}(\underline{e}[t])$, as

$$\underline{e} = \underline{z} - \underline{y}\,, \qquad \text{(A-5)}$$

and given

$$J = \frac{1}{2} \int_{t_o}^{t_f} (\underline{e}^T\, \underline{Q}\, e + \underline{u}^T\, \underline{R}\, \underline{u})\, dt \qquad \text{(A-6)}$$

where $t_o$ is time of sunrise and $t_f$ is time of sunset, then the optimal control is

$$\underline{u} = \underline{R}^{-1}\, \underline{B}^T\, [\underline{g} - \underline{K}\, \underline{x}] \qquad \text{(A-7)}$$

where $\underline{K}$ is a solution to

$$-\underline{K}\, \underline{A} - \underline{A}^T \underline{K} + \underline{K}\, \underline{B}\, \underline{R}^{-1}\, \underline{B}^T \underline{K} - \underline{C}^T\, \underline{Q}\, \underline{C} = 0 \qquad \text{(A-8)}$$

and g ($\underline{g}[t]$) is a solution of the differential equation

$$\dot{\underline{g}} = -\left[\underline{A} - \underline{B}\, \underline{R}^{-1}\, \underline{B}^T \underline{K}\right]^T \underline{g} - \underline{C}^T\, \underline{Q}\, \underline{C} \qquad \text{(A-9)}$$

with

$$\underline{g}(t_f) = \underline{C}^T \underline{K}\, \underline{z}(t_f).$$

APPENDIX C

SECTION I

OFFSET PARABOLOIDAL CONCENTRATOR

The basic configuration of an offset paraboloid is obtained by slicing a portion of a primitive paraboloid, i.e., the portion obtained by the intersection of a plane with the usual paraboloid. Note that the primitive paraboloid is an imaginary one while the actual reflector consists of the sliced portion only. The collection system is two-axis tracking with the incoming sunlight in the direction parallel to the optical axis of the original primitive paraboloid. From the diagram, it is readily seen that the sunlight reflected by the offset paraboloid, being a part of the primitive paraboloid, will be directed to the focus. It is necessary to introduce the imaginary primitive paraboloid in order to show the construction of the offset paraboloidal reflector and to define the axis and the focus. The collecting aperture of the offset paraboloid is displaced from the apex of the primitive paraboloid so that it lies outside the shaded area due to the receiver assembly at or near the focus and its supporting structure which is located on the opposite side of the optical axis as the offset paraboloidal reflector. Since the sunlight impinging on the system is parallel to the optical axis, assuming perfect tracking, the aperture of the offset paraboloid is entirely unblocked.

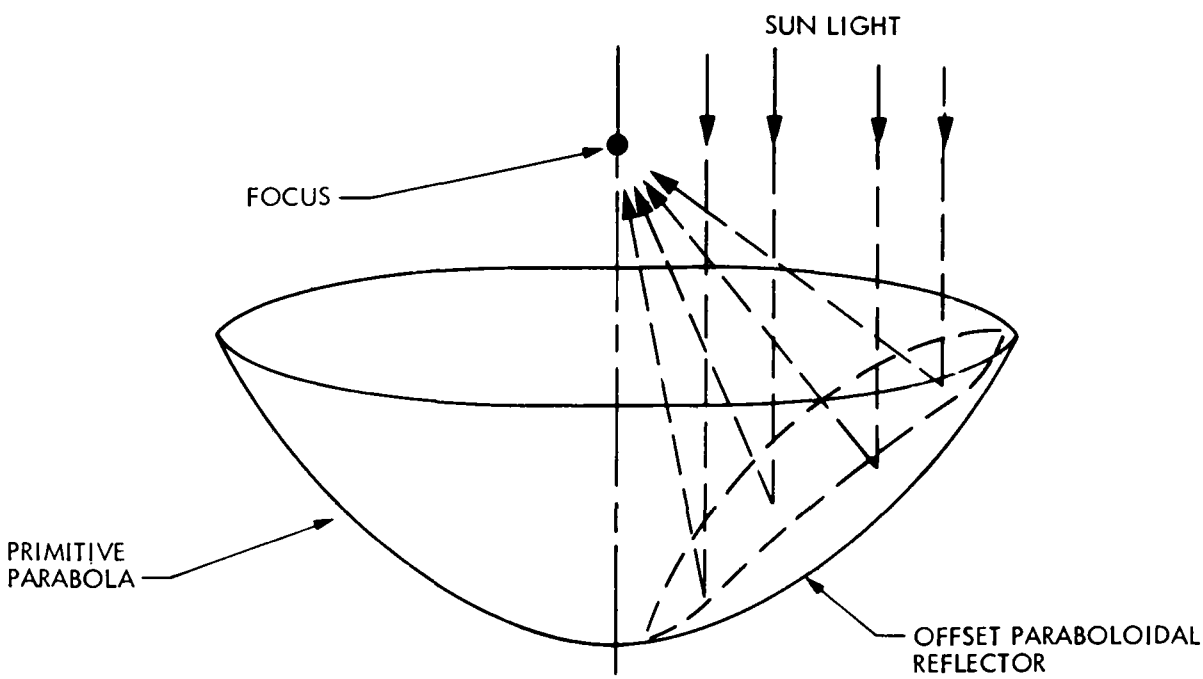


Figure C-1. Basic Configuration of an Offset Paraboloidal Reflector

The equation of the imaginary primitive paraboloid is given by

$$Z = \frac{x^2 + y^2}{4F}$$

where F denotes the focal length.

The equation of the plane is given by $Z = ay + b$ where a is the slope of the plane and b is the intercept on the Z-axis. The domain of intersection between the plane and the paraboloid is described by the following equation:

$$x^2 + (y - 2a\ F)^2 = 4a^2F^2\ [1 + b/(a^2F)]$$

The projected aperture area of the offset paraboloid on the xy plane (normal to the incident direct insolation) is a circle of radius

$$2\sqrt{a^2F^2 + bF}$$

centered at $x = 0$, $y = 2aF$ with area $4\pi(a^2F^2 + bF)$. If we consider the direction normal to the aperture, by using a suitable coordinate transformation (translation and rotation), it can be shown that the aperature is an ellipse. After specifying the region of the offset paraboloid and incorporating the boundary conditions in Schrenk's solar simulation procedures, the flux distributions may be computed for various situations as follows:

(1) Uniform solar disk.

(2) Solar disk with limb darkening (i.e., decreasing brightness from the center of the disk toward the limb)

(3) Different F/D ratios, where F is the focal length and D is the aperture diameter. When specifying the F/D it should be explicitly stated whether it refers to the primitive paraboloid or the offset paraboloid.

(4) Along two perpendicular directions through the focus parallel to the aperture plane of the offset paraboloid.

(5) Different Z-intercepts, i.e., intercept of the aperture plane with the Z-axis as shown in Figure C-2.

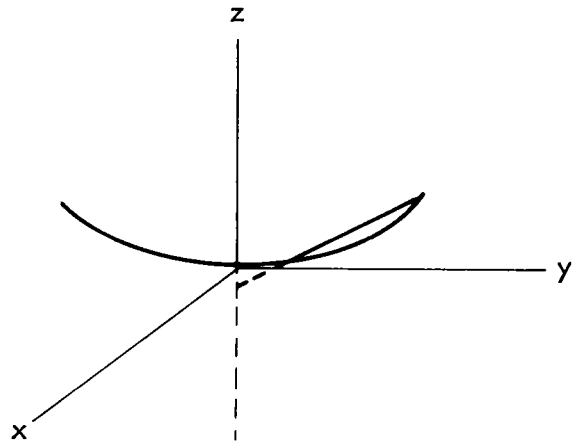


Figure C-2. Coordinate System for an Offset Paraboloidal Reflector

## Results and Discussions for Offset Paraboloid

Figures C-3 and C-4 give the flux distributions along with the x and y directions through the focus for an offset paraboloidal reflector derived from a primitive paraboloid of F/D = 1. The limb darkening effect is modeled in a simplified manner by using a limb darkening coefficient corresponding to 6700 Å. The Z-intercept as defined earlier is -0.0069. The direction of the flux is taken to be normal to the aperture plane of the offset paraboloid. The ordinate is the concentration ratio divided by the specular reflectivity of the reflector. The x- or y-coordinates are distances measured in units of the focal length. Similar results are presented in Figures C-5 and C-6 for flux distributions along the x and y directions through the focus for the case of F/D = 0.5 (F/D refers to the primitive paraboloid) with Z intercept = -0.0079. We may arrive at the following conclusions:

(1) The shading due to the receiver assembly and its supporting structures can be completely eliminated by using the offset paraboloid as solar concentrator. Thus, we have essentially an unblocked aperture.

(2) The flux distribution along the y-direction is slightly more spread out than that along the x-direction. The skewness of the flux distributions is negligible and if a cavity receiver were placed at the focus with the receiver aperture plane parallel to the aperture plane of the reflector, there is no danger of overheating one side of the cavity receiver.

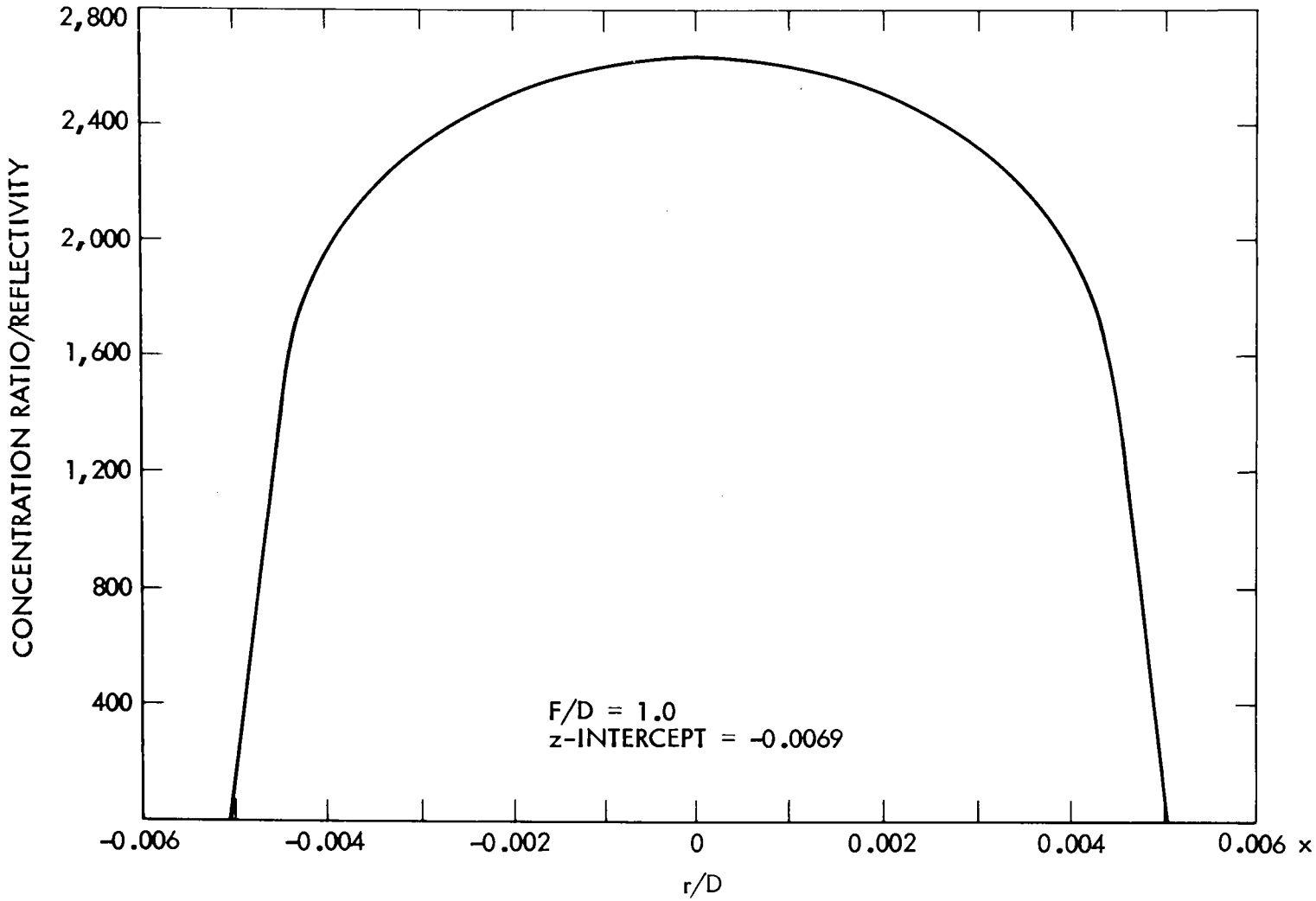


Figure C-3. Distribution of Normalized Concentration Ratio along the x-Axis at the Focal Plane of an Offset Paraboloidal Reflector.

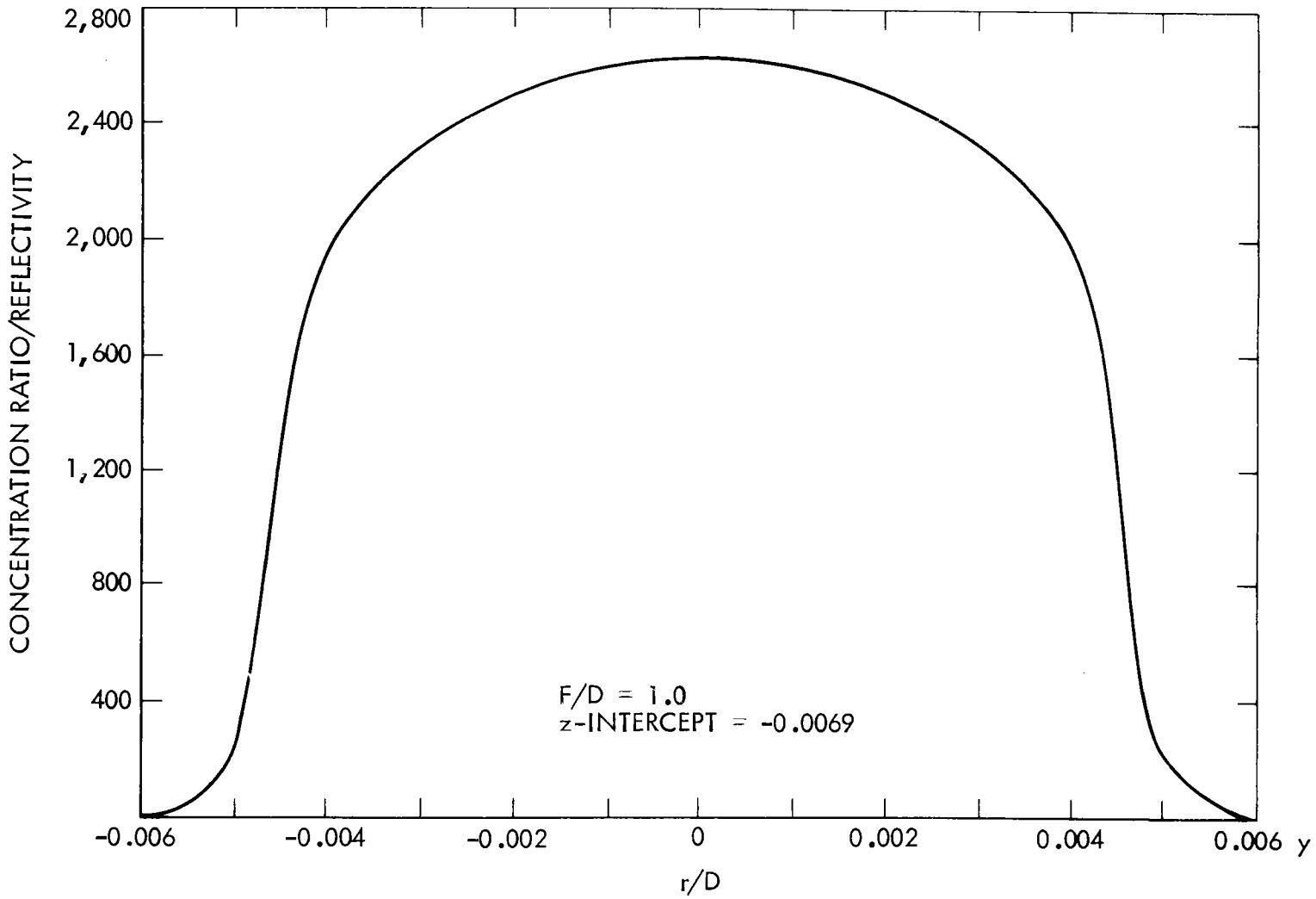


Figure C-4. Distribution of Normalized Concentration Ratio along the y-Axis at the Focal Plane of an Offset Paraboloidal Reflector.

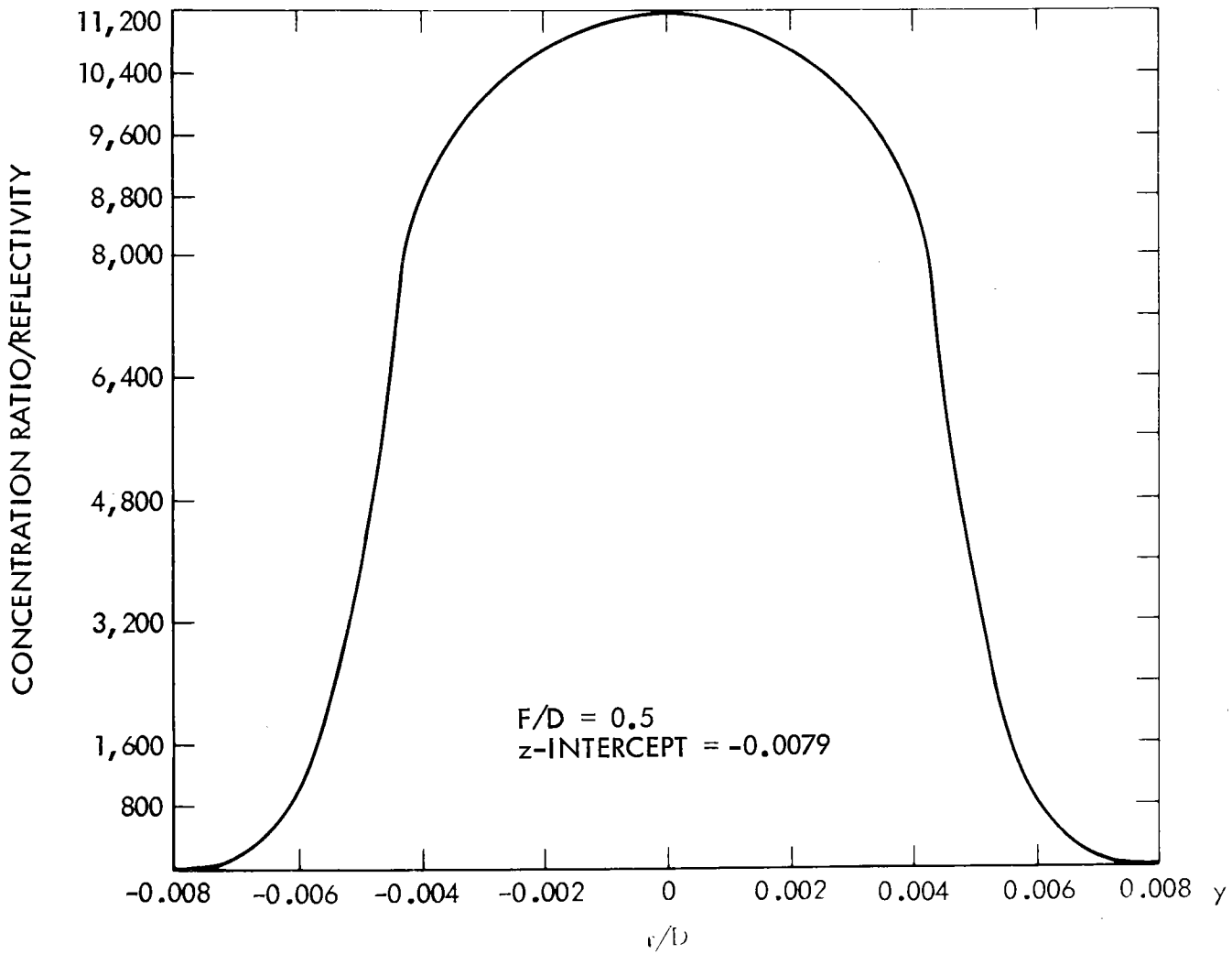


Figure C-5. Distribution of Normalized Concentration Ratio along the y-Axis at the Focal Plane of an Offset Paraboloidal Reflector.

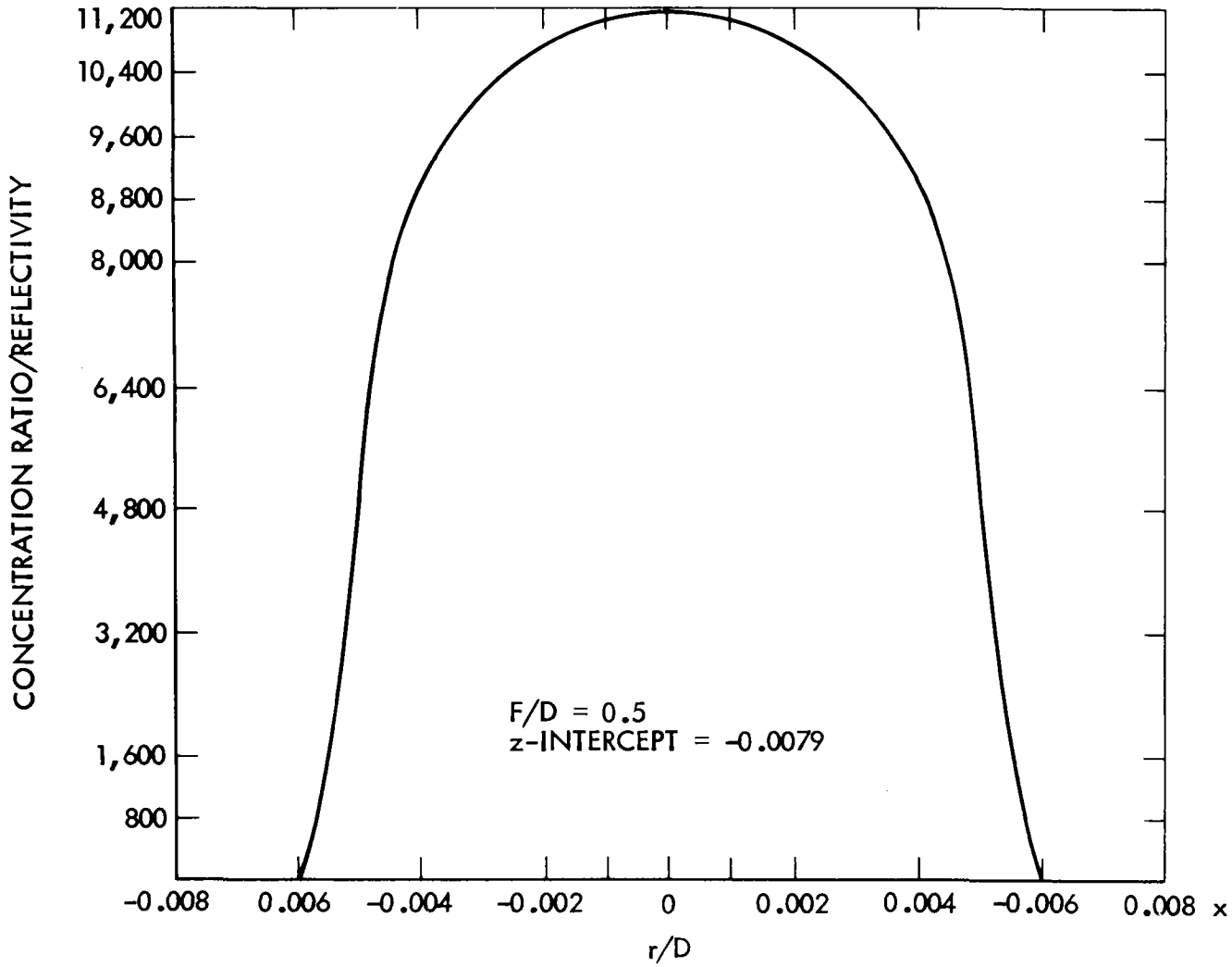


Figure C-6. Distribution of Normalized Concentration Ratio along the x-Axis at the Focal Plane of an Offset Paraboloidal Reflector.

(3) The projected surface area of the offset paraboloid normal to the direct incident insolation is a circle of radius

$$2\sqrt{a^2F^2 + bF}$$

where a, b, and F have been defined previously. When comparing different concentrators, it is essential to use the same projected aperture areas. For an offset paraboloid derived from a primitive paraboloid of F/D = 0.5, the concentration ratio is decreased by 12 percent compared with the simple paraboloid (F/D=1) of equivalent projected aperture areas.

## SECTION II

## CPC - PARABOLOID AND CPC - FRESNEL CONCENTRATOR SYSTEMS

Another design concept under consideration is a Compound Parabolic Concentrator (CPC) located at the focal plane of a simple paraboloid or a Fresnel-type mirror. A two dimensional CPC is shown in Figure C-7. Two parabolic mirrors are situated so that the focus ($f_1$) of one mirror segment ($M_1$) coincides with the lower edge of the other mirror segment ($M_2$). The upper edges of the two mirror segments are parallel to each other and thus parallel to the axis of the CPC. Radiation entering the aperture reaches the absorber only if it is within the acceptance angle ($\theta_{max}$). If a two dimensional CPC is revolved 180 degrees around its principal axis, a three dimensional CPC is obtained. A CPC will serve as a secondary reflector if it is placed at the focal plane of a concentrating reflector. Figure C-8 shows a three dimensional CPC located at the focal plane of a simple paraboloid so that the axis of the CPC and the paraboloid coincide. For a tracking concentrator, the optical axis of the system will coincide with the line joining the vertex of the paraboloid and the center of the solar disk, assuming no tracking errors. The function of the CPC is to further concentrate radiation passing through the focal plane of the primary mirror. Therefore, if a given concentration ratio is to be attained, the primary mirror surface error tolerances may be relaxed if a CPC is used. The results of a preliminary investigation are presented below.

### Results and Discussion

The maximum concentration ratio of the CPC is given by the following:

$$C_{CPC} = \frac{1}{\sin^2 \theta_{max}}$$

For a simple paraboloid the maximum concentration ratio is given by:

$$C_P = \frac{\sin^2 \theta}{\tan^2 \delta}$$

where $\theta$ is the rim angle of the paraboloid and $\delta$ is defined as follows:

$\delta = \alpha + \delta_1 + \delta_2$

$\alpha$ = solar half angle

$\delta_1$ = specular sprading half angle

$\delta_2$ = slope error

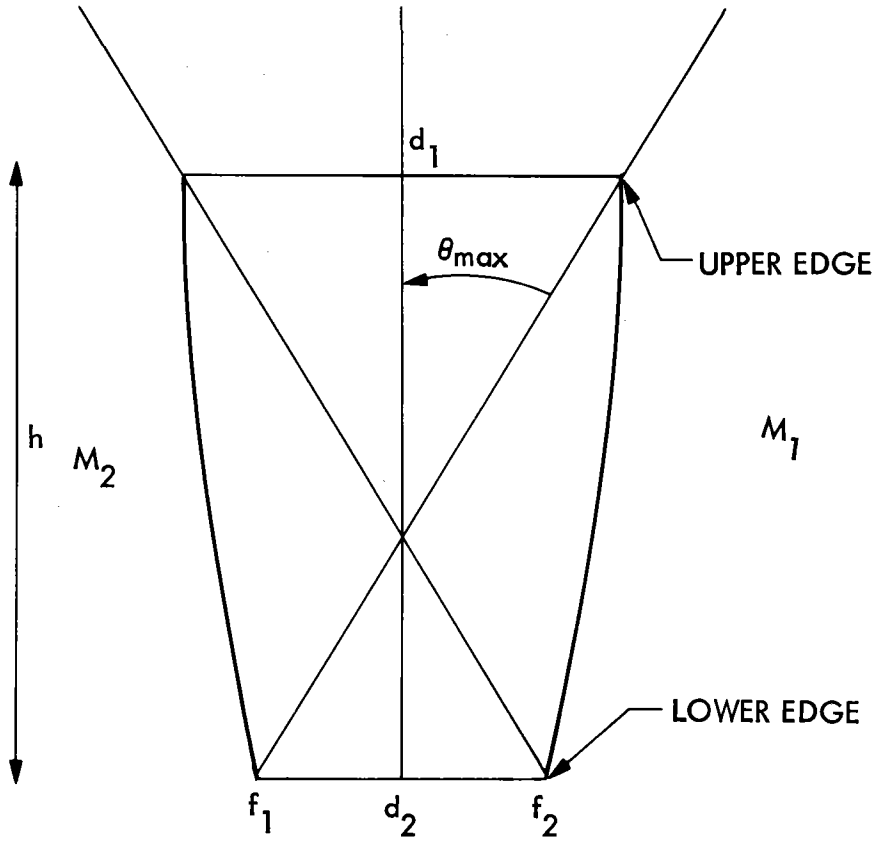


$\theta_{max}$ = ACCEPTANCE ANGLE OF CPC

$d_1$ = DIAMETER OF ENTRANCE APERTURE

$d_2$ = DIAMETER OF EXIT APERTURE

Figure C-7. Compound Parabolic Concentrator (CPC)

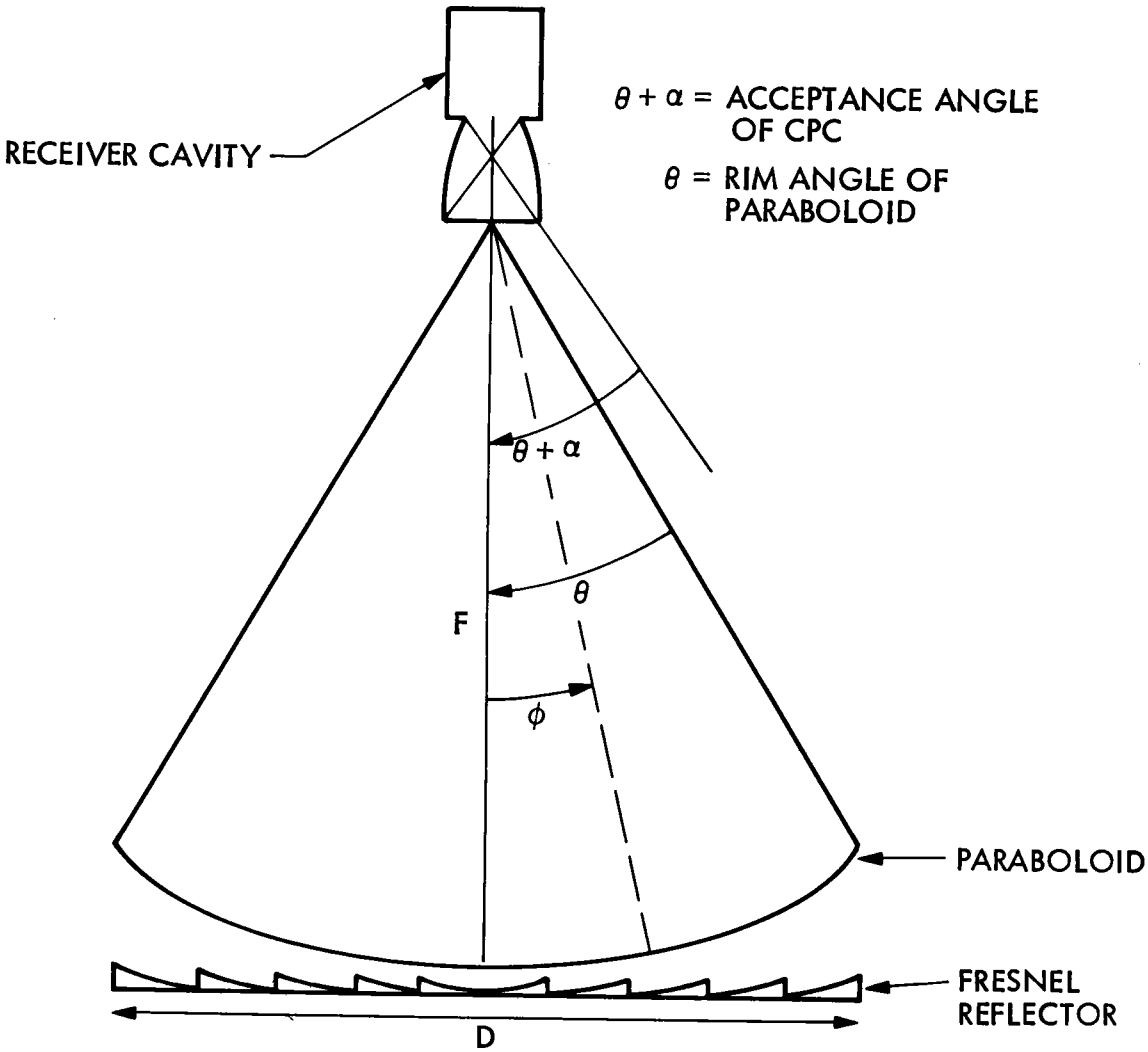


Figure C-8. CPC-Paraboloid System and CPC-Fresnel System

The overall maximum concentration ratio for a CPC - Paraboloid system is then given by

$$C = \rho_P \, \rho_{CPC}^{\langle n \rangle} \frac{\sin^2 \theta}{(\sin^2 \theta_{max}) \tan^2 \delta}$$

To determine <n>, the average number of reflections off the secondary mirror surface, consider Figure C-8. Radiation entering the CPC within the angle $\phi$ reaches the receiver cavity without reflecting from the secondary mirror surface. Radiation which enters the CPC at an angle greater than $\phi$ reflects from the secondary mirror surface only once. Therefore, the average number of reflections may be obtained as follows:

$$\langle n \rangle = \frac{D^2/4 - R^2}{D^2/4} = 1 - \left[ \frac{2F/D \sin \theta_{max} \tan \theta_{max}}{1 + \sin \theta_{max}} \right]^2$$

Figure C-9 shows the maximum concentration ratio of a CPC - Paraboloid system as a function of F/D. Note that for large F/D, the increase in concentration ratio of a CPC - Paraboloid is approximately three times the concentration ratio of a simple paraboloid.

For a Fresnel - CPC System, the loss of projected primary mirror reflector area ($\gamma$) results in a reduction of the overall performance of the system. The maximum concentration ratio of such a system is given by:

$$C = \rho_P \, \rho_{CPC}^{\langle n \rangle} \frac{\sin^2 \theta}{(\sin^2 \theta_{max}) \tan^2 \delta} \left(1 - \frac{4\gamma}{\pi D^2}\right)$$

In this case, <n> is given as:

$$\langle n \rangle = \pi \frac{D^2/4 - \pi R^2 - \gamma'}{\pi D^2/4 - \gamma}$$

where $\gamma'$ is the loss in projected surface area within an annulus from R to D/2. The normalized maximum concentration ratio of a CPC - Fresnel system as a function of F/D is shown in Fig. C-10. The use of a CPC as a secondary reflector is only advantageous for larger F/D ratios.

Figure C-11 shows the maximum concentration ratio of the CPC-Paraboloid system as a function of F/D when slope errors in the primary mirror are introduced. Slope errors significantly degrade the maximum concentration ratio which is almost independent of F/D for F/D greater

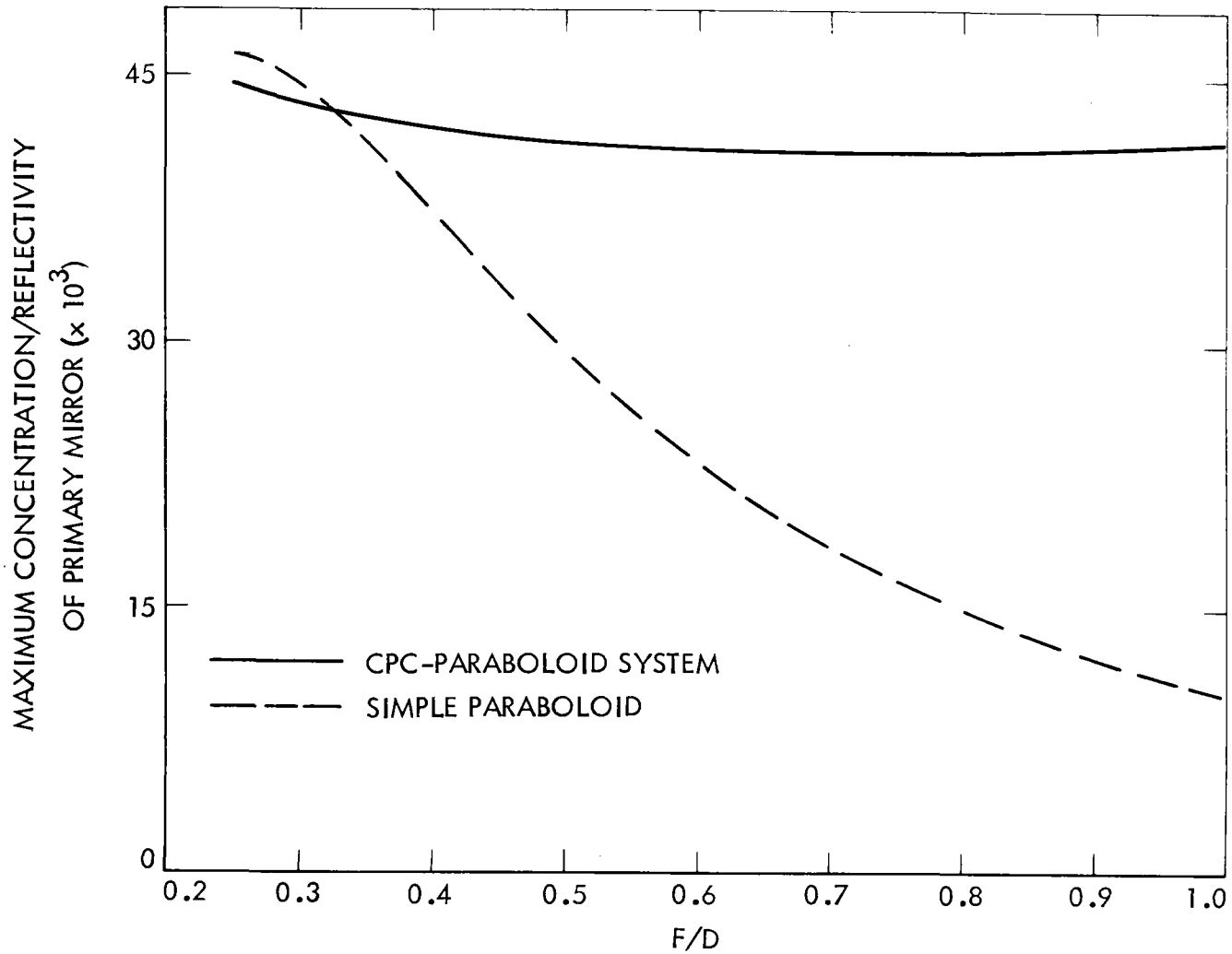


Figure C-9. Maximum Normalized Concentration Ratio of a CPC Paraboloidal System as a Function of F/D Ratio

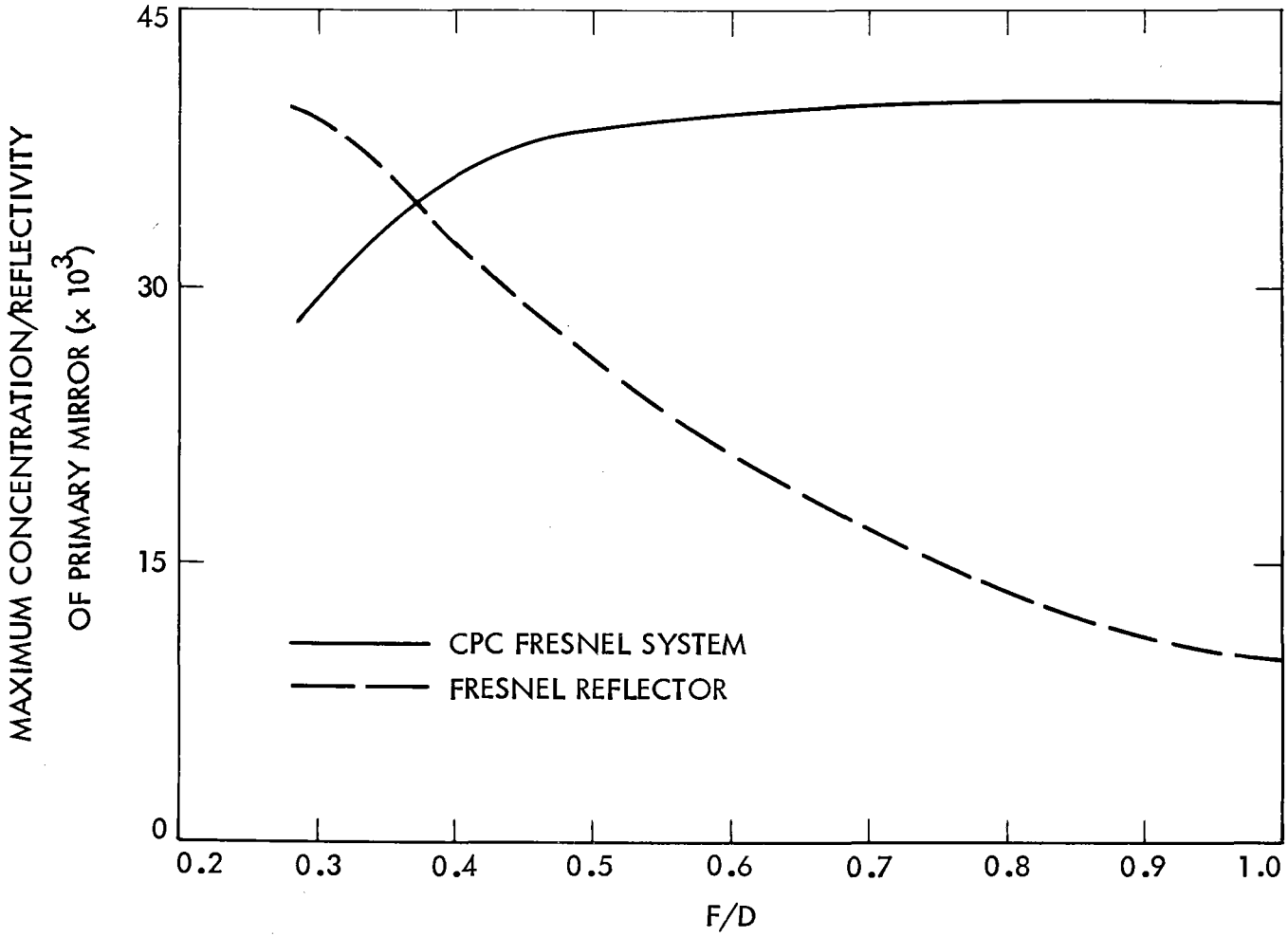


Figure C-10. Maximum Concentration Ratio of a CPC-Fresnel Mirror System as a Function of F/D Ratio

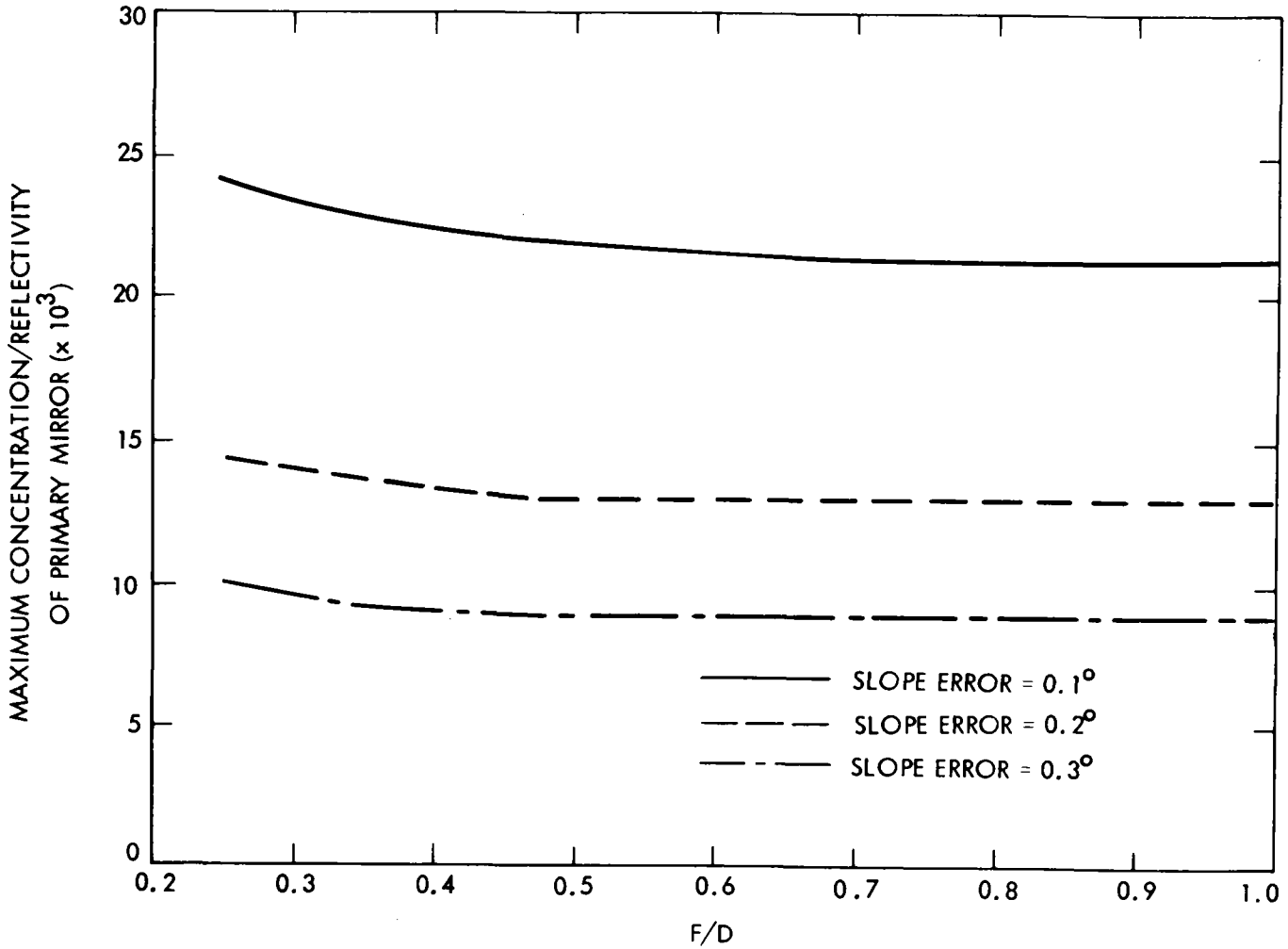


Figure C-11. Maximum Concentration Ratio of a CPC-Paraboloidal System as a Function of F/D and Slope Error.

than 0.45. For a slope error of 0.1° the maximum concentration ratio of a system with F/D equal to one is 21,558. For the same system with slope error equal to 0.3° the maximum concentration ratio is 8,906.

The results for a CPC - Fresnel system with slope errors are shown in Figure C-12.

The results may be summarized as follows:

(1) For smaller F/D the acceptance angle of the CPC is larger and the increase in overall concentration ratio is smaller. Therefore, for F/D equal to 0.25 the CPC-Paraboloid System offers no advantage. However, for an F/D of 1 the increase in maximum concentration ratio may be threefold.

(2) If a maximum concentration ratio of 10,000 is to be obtained the simple paraboloid of F/D equal to 1.0 would have to be an almost perfectly reflecting surface (a perfectly reflecting paraboloid with F/D equal to 1.0 has a maximum concentration ratio of 10,224). If a CPC is introduced as a secondary mirror the requirements for the primary mirror surface slope errors could be relaxed to approximately 0.25°.

(3) In the above analysis tracking or pointing errors have not been considered. Tracking errors may introduce several problems such as hot spots, loss of radiation because it is outside the acceptance angle of the CPC, etc. Therefore, in order to determine if this system is feasible a more detailed analysis must be completed considering the effects of tracking error.

(4) Secondary reflectors, in general, have inherent problems due to the large amount of heat absorbed per unit area. Severe damages such as cracking may occur if the excess heat cannot be disposed of in a suitable manner. For a steam engine the temperature difference between the fluid input and fluid outlet can be as large as 800°F. In this case the excess heat from the secondary reflector could be used for preheating the inlet fluid. However, in the case of the Stirling engine the temperature difference is much smaller ($\Delta T \sim 100°F$) so the excess heat from the secondary reflector would not be effective for preheating and may be completely wasted.

A variation of the CPC - Paraboloid or CPC - Fresnel concentrating system consists of a Compound Elliptic Concentrator (CEC) used as a secondary reflector instead of the CPC. In the CEC-Paraboloid or CEC-Fresnel system, one focus of each elliptical segment is located at the exit aperture of the CEC, while the other focus is located at the edge of the primary reflector. The entrance aperture of the secondary reflector is placed at the focal plane of the primary reflector. Since the rays reflected by the primary mirror are not parallel, and since the CEC appears to have a better capability of focusing non-parallel rays than the CPC, the use of a CEC as a secondary reflector appears to be a more promising concept. Future work will include the investigation of such a concept as well as other variations.

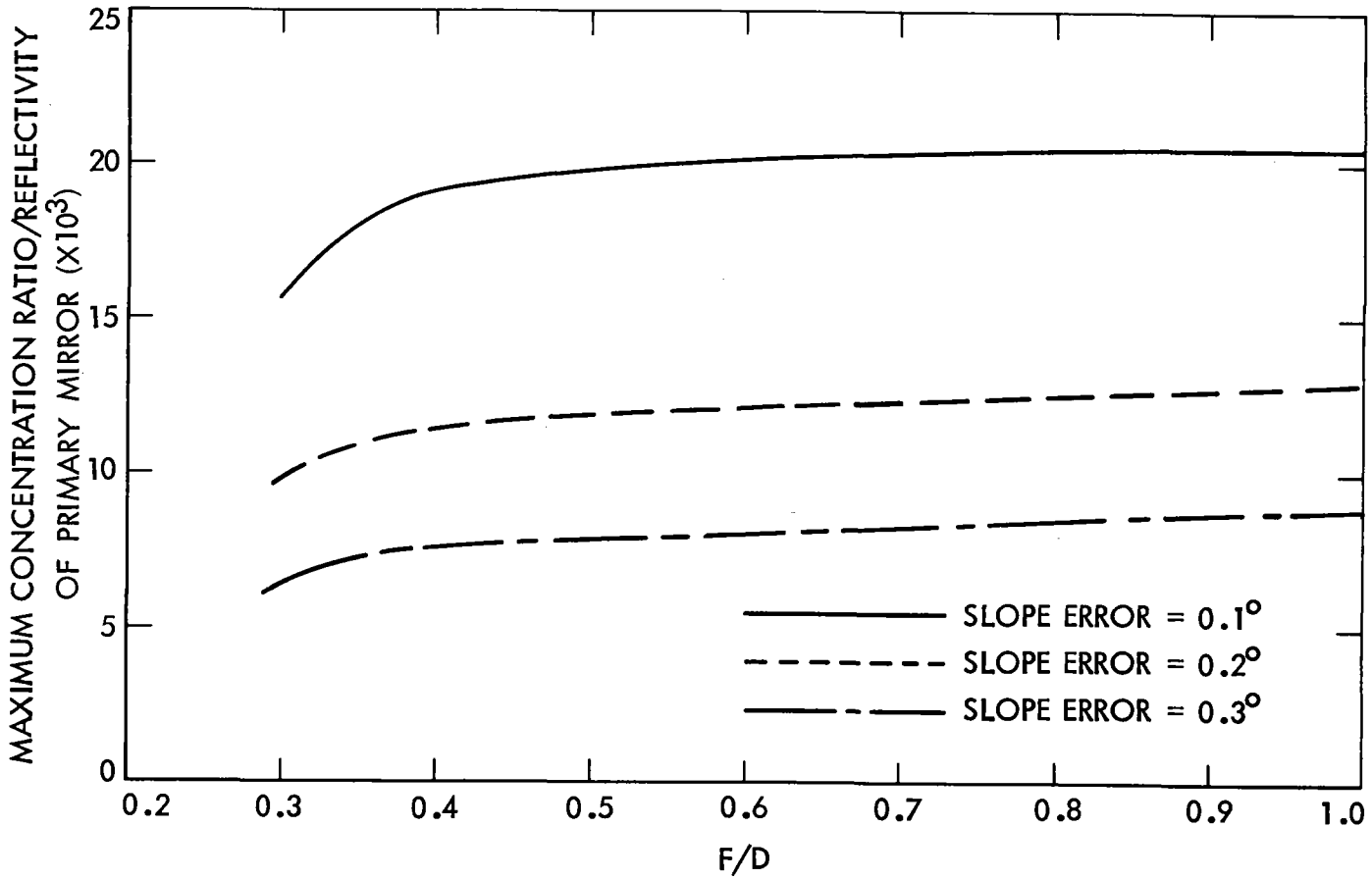


Figure C-12. Maximum Concentration Ratio of a CPC-Fresnel Mirror System as a Function of F/D and Slope Error

## SECTION III

## CASSEGRAINIAN SYSTEM

A Cassegrainian concentrator, shown in Figure C-13, is a two-mirror system with a paraboloidal mirror for a primary mirror and a confocal hyperboloidal mirror as a secondary reflector. The optical axis of the system is pointed toward the sun so that rays impinging on the primary mirror surface are reflected back to the secondary mirror surface. After reflecting off the secondary mirror surface, the rays converge at the vertex of the paraboloid. Thus, the focus of the system is shifted to a more convenient position (i.e., the vertex of the paraboloid).

A preliminary analysis of a Cassegrainian System employing a primary paraboloidal concentrator with a 60° rim angle (F/D = 0.433) and a family of confocal secondary hyperboloidal mirrors has been carried out.

Figure C-14 shows a sketch that defines the parameters involved in this first cut analysis. Note that the focal length (F) of the primary mirror is one unit of length. The parameter A defines the distance between the hyperboloid and the point midway between the vertex of the paraboloid and the focus of the paraboloid. As the position of the hyperboloid is chosen closer to the paraboloid, A decreases and the radius (R) of the hyperboloid increases.

One can imagine a cone of sunlight impinging upon the primary mirror surface a distance x from the optical axis of the system. The center ray which coincides with the axis of the incident cone reaches the vertex of the paraboloid with a total optical path length of $L_1$ and $L_2$. The total optical path length of the center ray is an important parameter since the area over which the reflected energy is spread (the cross-sectional area of the cone when it reaches the plane of the receiver aperture) is roughly proportional to the square of the total optical path length of the center ray. The areal energy spread of a cone when it reaches the receiver plane indicates the size of the solar image at that plane. Figure C-15 shows the total path length of a center ray reaching the receiver plan as a function of x for various positions of the secondary mirror and for a simple paraboloid. The radius of the hyperboloidal mirror is also plotted for each value of A in Figure C-15. From this graph, the percent blockage of the primary mirror due to the presence of the secondary mirror and the percent blockage for various values of A may be determined.

Figure C-16 shows the areal energy spread plotted as a function of x for the simple paraboloid and for Cassegrainian Systems with various positions of the secondary reflector. If we consider the radiation which is reflected from the outer edge of the paraboloid it is apparent that the areal energy spread is greater for the simple paraboloid than for the Cassegrainian System with A = 0.1 or A = 0.2. However, for A = 0.1, the solar image is only about 7% smaller than the solar image of a simple

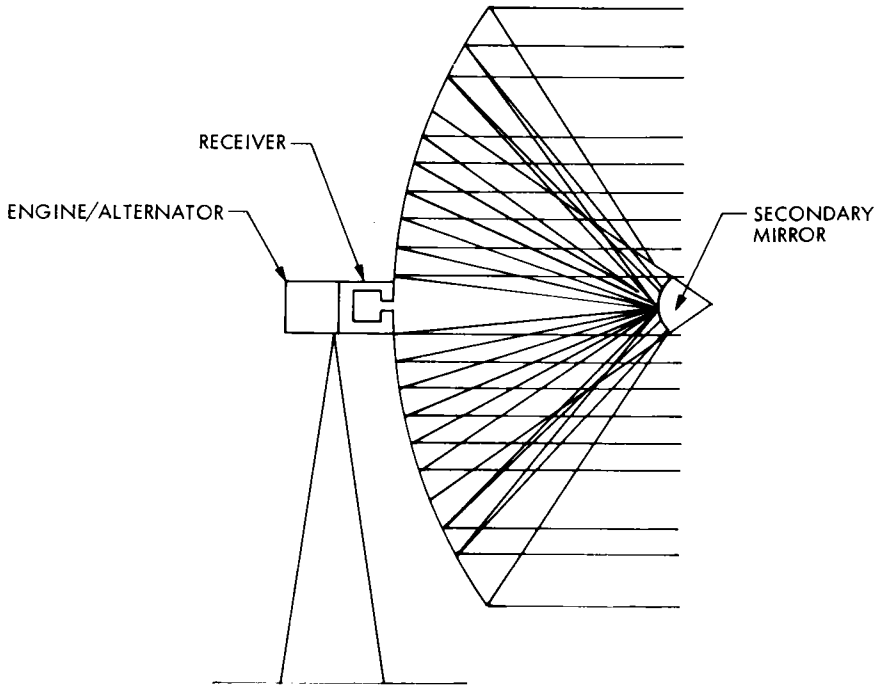


Figure C-13. Cassegrainian System with Paraboloidal Primary Mirror and Hyperboloidal Secondary Mirror

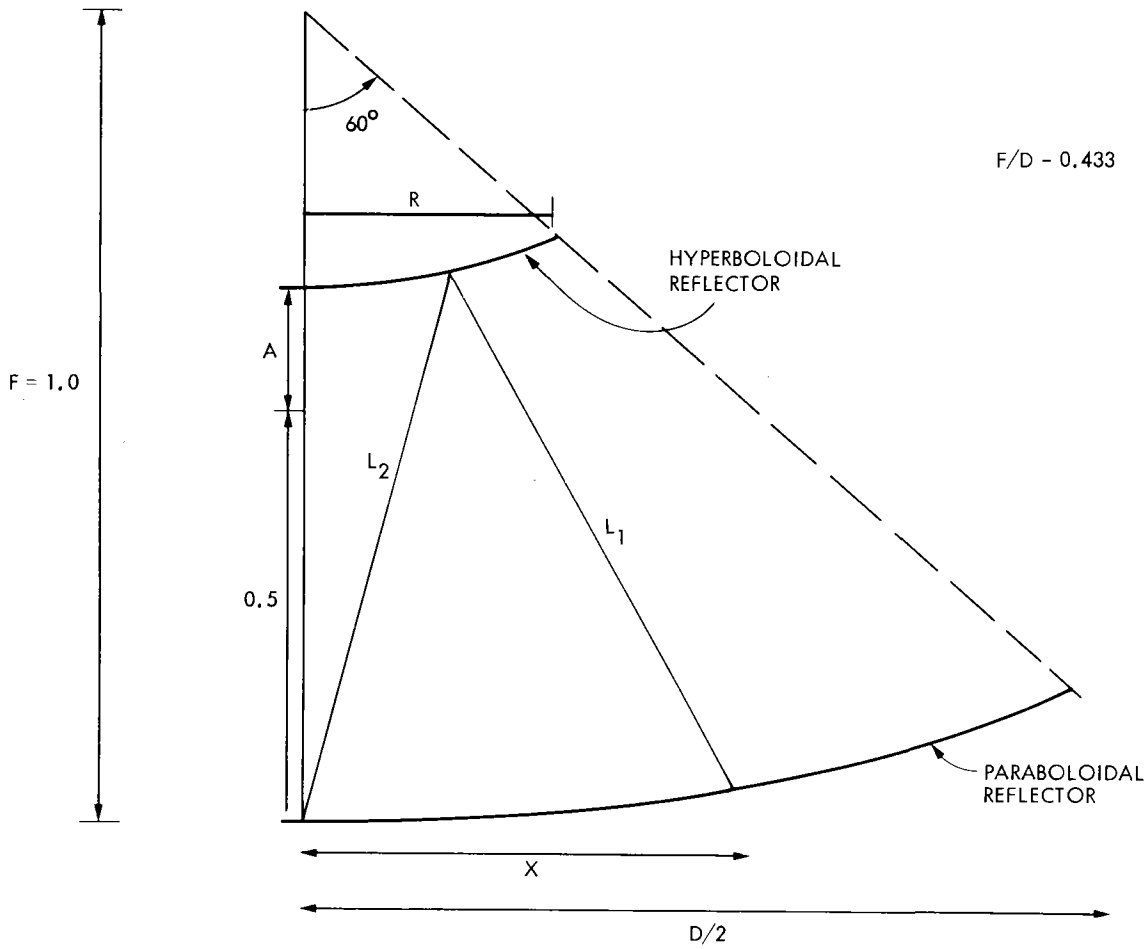


R = RADIUS OF HYPERBOLOID

D/2 = RADIUS OF PARABOLOID

A = DISTANCE BETWEEN CENTER OF HYPERBOLOID AND POINT MIDWAY BETWEEN FOCUS AND VERTEX OF PARABOLOID

$L_1$ = OPTICAL PATH LENGTH FROM PRIMARY MIRROR TO SECONDARY MIRROR

$L_2$ = OPTICAL PATH LENGTH FROM SECONDARY MIRROR TO VERTEX OF PARABOLOID

X = RADIAL DISTANCE TO POINT ON THE PARABOLOID

Figure C-14. Basic Configuration of a Cassegrainian System

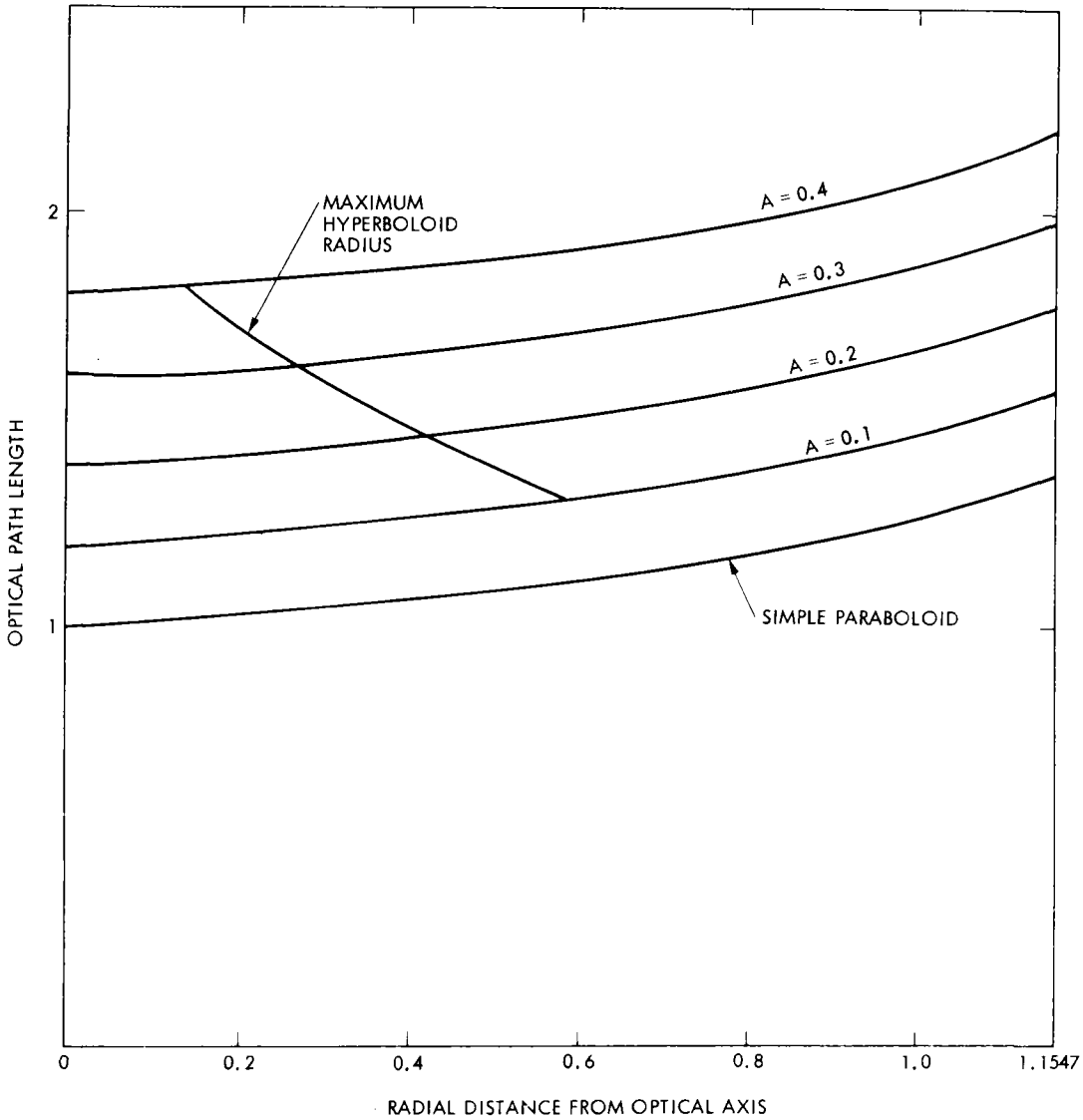


Figure C-15. Total Optical Path Length as a Function of Radial Distance from Optical Axis

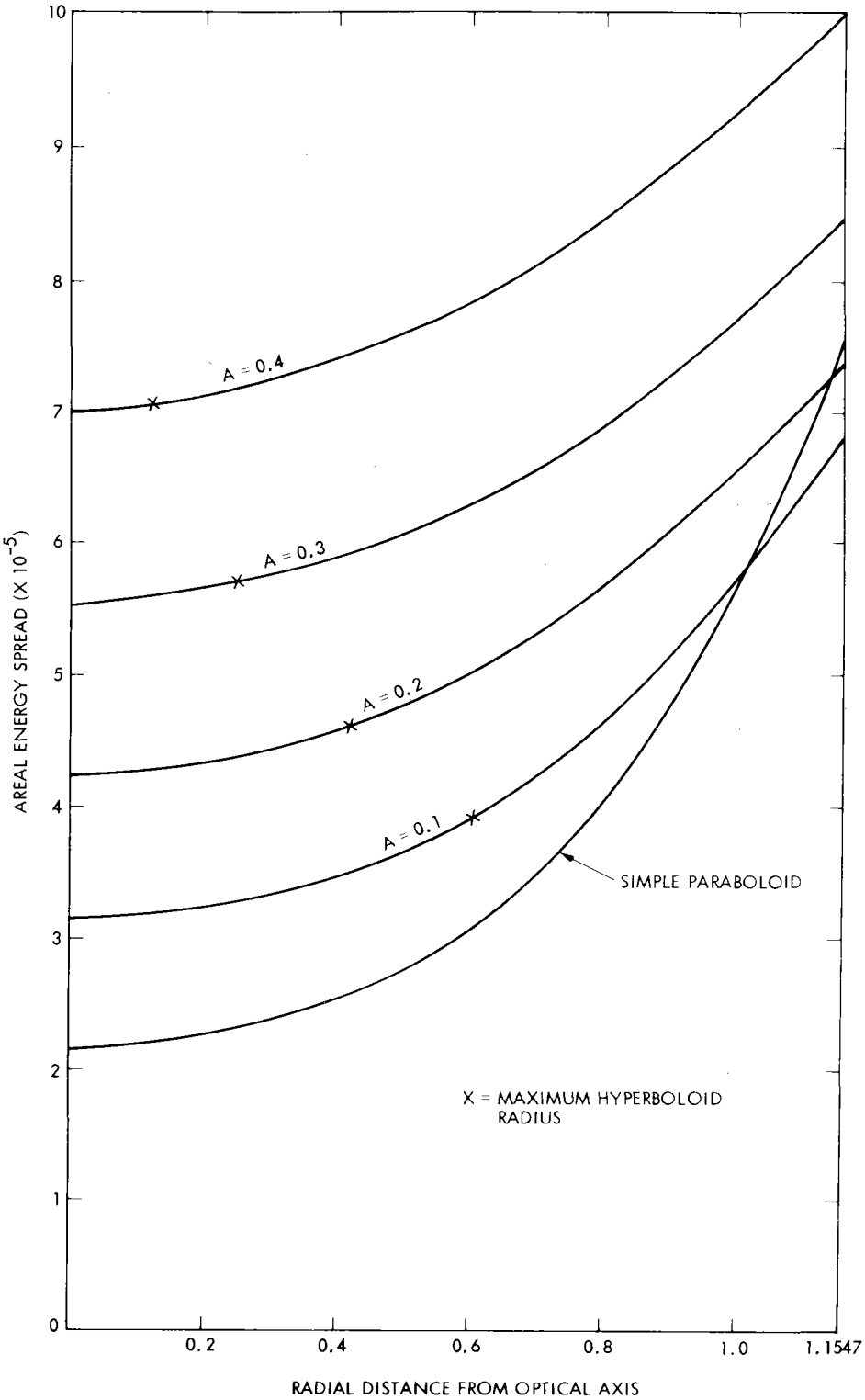


Figure C-16. Areal Energy Spread as a Function of Radial Distance from Optical Axis

Table C-1. Percent Blockage of Primary Mirror Due to Presence of Secondary Mirror

| A | Radius | Percent Blockage |
|---|---|---|
| 0.1 | 0.59855 | 26.80% |
| 0.2 | 0.40949 | 12.58% |
| 0.3 | 0.25762 | 4.98% |
| 0.4 | 0.12596 | 1.19% |

paraboloid with the same F/D value. On the other hand, the loss in primary reflector area due to blockage by the secondary reflector for A = 0.1 is 26.8% as compared to the blockage of a simple paraboloid due to the receiver/engine which is typically 3% to 5%.

## Results and Discussions for Cassegrainian System

The solar image of a Cassegrainian system may be smaller in some cases. However, at the same time the loss in performance due to secondary mirror blockage is very severe. Furthermore, secondary mirrors have several inherent problems such as cracking of the mirror due to the large amount of heat absorbed per unit area. As mentioned earlier (Appendix C.II) the heat taken from the mirror to prevent cracking must be wasted for a Stirling cycle engine due to the small temperature difference between input fluid temperature and output fluid temperature. In addition, the losses at the secondary mirror surface such as absorption and specular spreading will also greatly degrade the performance of a two-mirror system. In order to compare the performance of a Cassegrainian System more accurately, a study, including the above mentioned factors, would have to be conducted.

APPENDIX D

HEAT TRANSFER ANALYSIS

SECTION I

RECEIVER SENSITIVITY ANALYSIS

## A. SENSITIVITY DEFINITION

In order to achieve (1) the highest possible receiver efficiency which is a controlling factor in the overall system efficiency, and (2) the highest possible fluid temperature for maximizing the engine efficiency, the need for a sensitivity analysis was stressed. The receiver sensitivity concept is introduced here to enable the designer to sense the magnitude and directional effect of the various receiver parameters on receiver performance. Note that this sensitivity analysis could be expanded to incorporate the concentrator and the engine-generator in addition to the receiver. However, the present discussion will be focused on solar receiver parameters.

Sensitivity is defined as the measure of the dependency of system characteristics on variations occuring in a particular element or parameter (as shown in Figure D-1). Sensitivity ($S_X$) is expressed as:

$$\left.\begin{aligned} S_X &= \frac{\Delta Y/Y_0}{\Delta X/X_0} \\ S_X &= \left(\frac{dY}{dX}\right)_0 \frac{X_0}{Y_0} \\ S_X &= \left(\frac{d \ln Y}{d \ln X}\right)_0 \end{aligned}\right\} \qquad (1)$$

where X is an arbitrary input element, Y is the system output, $\Delta$ represents a differential change in either X or Y, and the subscript (0) denotes conditions at a reference point.

Equation (1) states that the differential sensitivity of Y with respect to X is the percentage change in Y divided by that percentage change in X which has caused the change in Y, keeping all the other input elements unchanged. The definition is suitable only for small changes. Any system that is operating at an optimum value of one of its elements should have zero sensitivity with respect to this element. The concept of sensitivity has been widely used in studying automatic controls, electric circuits, and many physical systems. Its new application to solar receivers represents a useful tool in the performance optimization, as will be discussed later.

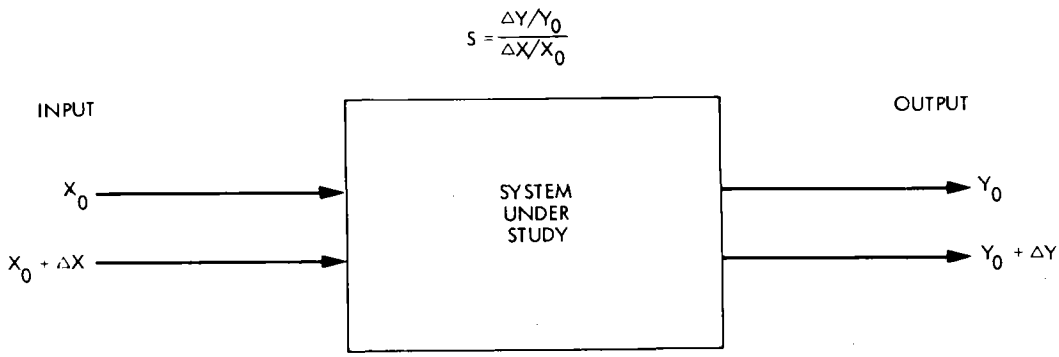


Figure D-1. Sensitivity Definition

In solar receivers, the input element X could be one of the following:

(1) Total solar flux $\sum_i A(i) \cdot I(i)$ falling on receiver walls, where A(i) and I(i) are the ith node surface area and solar irradiation, respectively

(2) Inlet fluid temperature ($T_{in}$)

(3) Wall emissivity in the solar band ($\varepsilon^*$)

(4) Wall emissivity in the infrared region ($\varepsilon$)

(5) Ambient temperature ($T_{amb}$)

(6) Fluid mass flow rate ($m_f$)

The receiver output Y, on the other hand, could be either: the exit fluid temperature ($T_{out}$), or the extracted thermal energy from the receiver ($Q_{ext}$). Since these two output elements are important to the performance evaluation of the energy conversion subsystem, both were considered. In the following subsections, the heat extracted sensitivity

will be denoted by (HES), the exit temperature from receiver sensitivity by (ETS), the receiver efficiency sensitivity by (RES), the concentrator efficiency sensitivity by (CES), the engine efficiency sensitivity by (EES) and the overall efficiency sensitivity by (OES). Note that since the overall efficiency is the triple product of concentrator, receiver, and engine efficiencies, then to any element or parameter

$$OES = CES + RES + EES \tag{2}$$

B. EFFECT OF SOLAR FLUX VARIATIONS

In general, changes in receiver solar flux can happen either due to:

(1) A change in the concentrator efficiency ($\eta_c$) or,

(2) A direct change in the local solar insolation (F). If the concentrator performance is expressed as

$$\eta_c = \sum_i A(i)\ I(i)/(F \cdot A_c) = \phi\ \rho_c \tag{3}$$

where F is the total insolation falling on the concentrator projected area Ac, $\phi$ is the concentrator-receiver intercept factor and $\rho_c$ is the mirror reflectivity, Equation 3 can be rewritten as

$$\sum_i A(i)\ I(i) = \eta_c \cdot F \cdot A_c \tag{3}$$

or

$$(CES)_I = 1$$

which gives the direct one-to-one correspondence between changes in concentrator efficiency or concentrator solar insolation to the receiver flux.

In order to give a quantitative evaluation of the solar flux effect on the overall system efficiency, an appropriate model for the engine has to be included. If for the sake of the present discussion, the engine efficiency ($\eta_e$) is approximated as a constant fraction ($\lambda$) of the ideal Carnot's cycle working between the temperature limits $T_{out}$ and $T_{amb}$, then the following is true:

$$\eta_e = \lambda \left(1 - \frac{T_{amb}}{T_{out}}\right) \tag{4}$$

where $T_{out}$ is the fluid exit temperature from the receiver.

By differentiation of Equation (4) the percentage change in engine efficiency resulting from a percentage change in the receiver outlet temperature, keeping all the other parameters the same, is given at constant ambient temperature by

$$(EES)_I = \left(\frac{T_{amb}}{T_{out} - T_{amb}}\right)_0 (ETS)_I \tag{5}$$

where subscript (I) refers to the sensitivity due to solar flux variations, and using the definition in Equation 1.

The relationship between $(ETS)_I$ and $(HES)_I$ could be simply derived by differentiating the energy extracted equation written as:

$$Q_{ext} = m_f \, c_f (T_{out} - T_{in}) = \eta_R \sum_i A(i) \, I(i) \tag{6}$$

where $c_f$ is the specific heat of the receiver fluid.

Accordingly, keeping $T_{in}$ and $m_f c_f$ unchanged, then

$$(HES)_I = (ETS)_I \left(\frac{T_{out}}{T_{out} - T_{in}}\right)_0 \tag{7}$$

On the other hand, the relationship between (RES) and (HES) can be derived from Equation (6) also by differentiation,

$$(HES)_I = 1 + (RES)_I \tag{8}$$

Combining Equations (2), (3), (5), (7), and (8), the general sensitivity expressions due to receiver solar flux variations are written as:

$$
\left.
\begin{aligned}
(CES)_I &= 1 \\
(RES)_I &= (HES)_I - 1 \\
(EES)_I &= \left(1 - \frac{T_{in}}{T_{out}}\right)_0 \left(\frac{T_{amb}}{T_{out} - T_{amb}}\right)_0 (HES)_I \\
(OES)_I &= (HES)_I \left[\frac{1 - (T_{in} - T_{amb}/T_{out}^2)}{1 - (T_{amb}/T_{out})}\right]
\end{aligned}
\right\} \quad (9)
$$

The heat extracted sensitivity $(HES)_I$ can be proven to be always greater than one for any solar receiver. Accordingly, the overall efficiency sensitivity $(OES)_I$ using Equation (9) will be always greater than unity for all solar receivers. This conclusion has been verified for the example cavity receiver where at a given reference state, the values of (RES), (HES), (EES), and (OES) were found to be 0.09, 1.09, 0.08, and 1.17 respectively.

## C. EFFECT OF INLET FLUID TEMPERATURE ($T_{in}$)

Increasing the inlet fluid temperature is known to have an adverse effect on both receiver efficiency and energy extracted due to the increase in thermal losses, while it produces hotter exit temperature to the engine. Numerically, the receiver performance sensitivity was tested for the example receiver at different inlet fluid temperatures, and the results can be generalized as will be shown in Section II of Appendix D.

The receiver efficiency sensitivity, $(RES)_{T_{in}}$, is identical to $(HES)_{T_{in}}$ since the solar flux is kept unchanged, i.e.,

$$(RES)_{T_{in}} = (HES)_{T_{in}} \quad (10)$$

On the other hand, the relationship between $(HES)_{T_{in}}$ and $(ETS)_{T_{in}}$ could be derived by differentiating Equation (6) keeping $m_f c_f$ unchanged. Accordingly,

$$(ETS)_{T_{in}} = (HES)_{T_{in}} \left\{1 - \frac{T_{in}}{T_{out}}\right\}_0 + \left(\frac{T_{in}}{T_{out}}\right)_0 \quad (11)$$

The effect on the overall system efficiency will then follow using the same engine efficiency expression, Equations (4) and (5). To properly evaluate the effect of the inlet fluid temperature to the receiver on the overall system efficiency, two regions must be identified as shown in the efficiency trend sketched in Figure D-2.

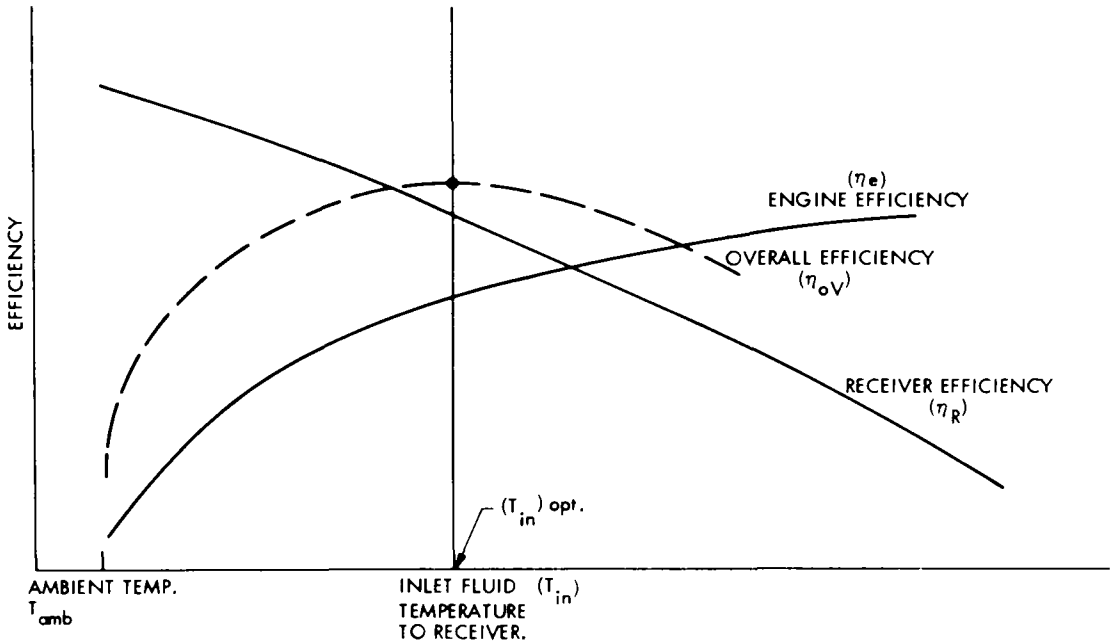


Figure D-2. Effect of Inlet Fluid Temperature to Receiver on Receiver-Engine Performance

If the reference point was located on the left hand side of the optimum inlet temperature (which corresponds to the maximum overall efficiency $\eta_{ov,max}$) then the sensitivity of the overall efficiency is positive. Adversely, the sensitivity of the overall efficiency will be negative if $(T_{in})$ is on the right hand side of the $T_{in,opt}$.

In the neighborhood of the optimum inlet fluid temperature, the sensitivity of the overall efficiency $(\eta_{ov})$ is zero.

The search for the optimum inlet temperature to the receiver was discussed in Section II of this Appendix. However, general sensitivity expressions could be made to summarize the above finding using Equations (2), (3), (4), (5), (10), and (11).

$$\left.\begin{aligned}
(CES)_{T_{in}} &= 0 \\
(RES)_{T_{in}} &= (HES)_{T_{in}} \\
(EES)_{T_{in}} &= \left[(HES)_{T_{in}} \cdot \left(1 - \frac{T_{in}}{T_{out}}\right)_0 + \left(\frac{T_{in}}{T_{out}}\right)_0\right]\left(\frac{T_{amb}}{T_{out} - T_{amb}}\right)_0
\end{aligned}\right\} \quad (12)$$

At the optimum inlet fluid temperature, $T_{in,opt}$

$$\left.\begin{aligned} (RES)_{T_{in,opt}} &= -(EES)_{T_{in,opt}} \\ \text{or when} \\ (T_{out})^2 &= T_{in} \cdot T_{amb} \left[ 1 - \frac{1}{(HES)_{T_{in}}} \right] \end{aligned}\right\} \quad (13)$$

D. EFFECT OF WALL-SOLAR ABSORPTIVITY ($\alpha^*$)

The solar absorptivity vector (ESOL) or ($\alpha^*$) plays a significant role in the receiver performance improvement. Increasing the solar absorptivity always increases the energy extracted, efficiency, exit fluid temperature and engine efficiency.

It is always recommended for the materials used for interior surfaces (for cavity receivers) or exterior surfaces (for external receivers) to have the highest possible absorptivity in the solar band ($\alpha^*$).

The receiver efficiency sensitivity $(RES)_{\alpha*}$ is identical to $(HES)_{\alpha*}$ in this case since the solar flux is kept unchanged. On the other hand, the relationship between $(HES)_{\alpha*}$ and $(ETS)_{\alpha*}$ is similar in form to Equation 7. The effect on the engine sensitivity $(EES)_{\alpha*}$ is similar in form to Equation 5. In general, for any advanced solar receiver, the sensitivity expressions become:

$$\left.\begin{aligned} (CES)_{\alpha*} &= 0 \\ (RES)_{\alpha*} &= (HES)_{\alpha*} \\ (EES)_{\alpha*} &= \left( \frac{T_{amb}}{T_{out} - T_{amb}} \right)_0 \left( 1 - \frac{T_{in}}{T_{out}} \right)_0 (HES)_{\alpha*} \\ (OES)_{\alpha*} &= \left[ 1 + \left( \frac{T_{amb}}{T_{out} - T_{amb}} \right)_0 \left( 1 - \frac{T_{in}}{T_{out}} \right)_0 \right] (HES)_{\alpha*} \end{aligned}\right\} \quad (14)$$

For example, the Table Mountain receiver gave the values of 0.1, 0.06, and 0.106 for the sensitivities $(HES)_{\alpha*}$, $(EES)_{\alpha*}$ and $(OES)_{\alpha*}$ respectively.

Variations of optical properties can occur during receiver operation due to either temperature fluctuations or weather effects on surface texture.

## E. EFFECT OF WALL-EMISSIVITY ($\varepsilon$) IN THE INFRARED REGION

The nodal emissivity vector (EIR) or ($\varepsilon$) in the infrared region is one important parameter in the receiver performance. Increasing the emissivity ($\varepsilon$) for a cavity-type receiver, tends to increase the receiver efficiency energy extracted and exit temperature contrary to the common intuition that selective surfaces are also good for cavity receivers. This is because the high emissivity in the IR band means higher absorptivity in the IR band and small reflections which tend to reduce reflection losses through the receiver aperture to approach the black body characteristics. For external receivers or non-cavity types, smaller IR emissivity or selective surface property tends to improve the performance. Therefore, the sensitivity trends will be subject to receiver geometry.

The receiver efficiency sensitivity (RES) is identical to (HES) in this case since the solar flux is kept unchanged, i.e.,

$$(RES)_\varepsilon = (HES)_\varepsilon \tag{15}$$

On the other hand, the relationship between $(HES)_\varepsilon$ and $(ETS)_\varepsilon$ is similar to what was derived in Equations (6) and (7), or

$$(HES)_\varepsilon = (ETS)_\varepsilon \left( \frac{T_{out}}{T_{out} - T_{in}} \right)_0 \tag{16}$$

The effect on the engine efficiency will be followed using Equations (4) and (5) expressed as

$$(EES)_\varepsilon = (ETS)_\varepsilon \cdot \left( \frac{T_{amb}}{T_{out} - T_{amb}} \right)_0 \tag{17}$$

In general, the sensitivity expressions can be written as:

$$\left.\begin{aligned}
(CES)_\varepsilon &= 0 \\
(RES)_\varepsilon &= (HES)_\varepsilon \\
(EES)_\varepsilon &= \left( \frac{T_{amb}}{T_{out} - T_{amb}} \right)_0 \left( 1 - \frac{T_{in}}{T_{out}} \right)_0 (HES)_\varepsilon \\
(OES)_\varepsilon &= \left[ 1 + \left( \frac{T_{amb}}{T_{out} - T_{amb}} \right)_0 \left( 1 - \frac{T_{in}}{T_{out}} \right)_0 \right] (HES)_\varepsilon
\end{aligned}\right\} \tag{18}$$

## F. EFFECT OF AMBIENT TEMPERATURE

Increasing the ambient temperature ($T_{amb}$) tends to increase both the receiver efficiency and the energy extracted from the receiver since the heat losses are reduced. The receiver efficiency sensitivity (RES) is identical to (HES) in this case since the solar flux is kept unchanged, i.e.,

$$(RES)_{T_{amb}} = (HES)_{T_{amb}} \tag{19}$$

On the other hand, the relationship between $(HES)_{T_{amb}}$ and $(ETS)_{T_{amb}}$ will be identical to the expression given in Equations (6) and (7). Hence,

$$(ETS)_{T_{amb}} = (HES)_{T_{amb}} \left(1 - \frac{T_{in}}{T_{out}}\right)_0 \tag{20}$$

The effect on the engine efficiency will be in two ways. First, an increase in the outlet temperature ($T_{out}$) will increase the engine efficiency. Second, an increase in the ambient temperature would decrease the engine efficiency. By differentiating Equation 4 around the reference state, one can prove that,

$$(EES)_{T_{amb}} = \left(\frac{T_{amb}}{T_{out} - T_{amb}}\right)_0 \left[(ETS)_{T_{amb}} - 1\right] \tag{21}$$

In general, the above equations can be written at any reference point

$$\left.\begin{aligned} (CES)_{T_{amb}} &= 0 \\ (RES)_{T_{amb}} &= (HES)_{T_{amb}} \\ (EES)_{T_{amb}} &= \left(\frac{T_{amb}}{T_{out} - T_{amb}}\right)_0 \left[(HES)_{t_{amb}} \cdot \left(1 - \frac{T_{in}}{T_{out}}\right)_0 - 1\right] \end{aligned}\right\} \tag{22}$$

## G. EFFECT OF RECEIVER MASS FLOW RATE

Changing the fluid mass flow rate in the receiver changes the convective heat transfer coefficient between the fluid and the interior walls and gives rise to changes in the temperature pattern. The receiver efficiency sensitivity (RES) is identical to (HES) in this case since the solar flux is kept unchanged, i.e.,

$$(RES)_{m_f} = (HES)_{m_f} \tag{23}$$

On the other hand, the relationship between (HES) and (ETS) will be derived from Equation (6) by differentiation as follows:

$$(HES)_{m_f} = 1 + \left[ \left( \frac{T_{out}}{T_{out} - T_{in}} \right)_0 (ETS)_{m_f} \right] \tag{24}$$

The effect on the engine efficiency will follow using Equations (4) and (5) where

$$(EES)_{m_f} = \left( \frac{T_{amb}}{T_{out} - T_{amb}} \right)_0 (ETS)_{m_f} \tag{25}$$

In general, the overall efficiency sensitivity at any reference state is expressed as:

$$\left.\begin{aligned} (CES)_{m_f} &= 0 \\ (RES)_{m_f} &= (HES)_{m_f} \\ (EES)_{m_f} &= \left( \frac{T_{amb}}{T_{out} - T_{amb}} \right)_0 \left( 1 - \frac{T_{in}}{T_{out}} \right)_0 \left( (HES)_{m_f} - 1 \right) \end{aligned}\right\} \tag{26}$$

The conclusion that can be drawn from the above is that though the increase of mass flow rate increases slightly the receiver efficiency, it has a reducing effect in the exit fluid temperature which in turn lowers the engine efficiency. The net effect is the lowering of the overall thermal efficiency.

A generalized format for solar receivers is presented in Section II of this appendix.

## SECTION II

## GENERALIZED FORMAT FOR SOLAR RECEIVERS

### A. STRAIGHT LINE FORMAT FITTING

Similar to the analytical formats generally used in solar collectors, the heat extracted by the fluid ($Q_{ext}$) is expressed as the result of a subtraction between two macro-heat transfer terms.

The first term would be the net absorbed part of the receiver solar flux [$\sum_i A(i)\ I(i)$] multiplied by some effective solar absorptance $\alpha_e^*$ and the second term would be the net heat loss to the surroundings by all modes of heat transfer. The second term could be presented by different, but analogous forms, in terms of inlet fluid temperature ($T_{in}$), outlet fluid temperature ($T_{out}$) or average receiver wall temperature.

The most convenient one is represented here as the product [$U_L A_L\ (T_{in} - T_{amb})$] , where $U_L$ is an effective heat loss coefficient, and $A_L$ is an effective surface area from which the receiver loses energy to the surrounding ambient conditions. Accordingly, the thermal energy extracted by the flowing fluid out from the receiver, can be written as:

$$Q_{ext} = \alpha_e^* \left[ \sum_i A(i)\ I(i) \right] - U_L A_L\ (T_{in} - T_{amb}) \qquad (27)$$

The receiver efficiency ($\eta_R$) can thus be written as:

$$\eta_R = \alpha_e^* - U_L A_L \frac{(T_{in} - T_{amb})}{\sum_i A(i)\ I(i)} \qquad (28)$$

Equation 28 can be considered a general form suitable for expressing the receiver behavior under varying conditions of ambient temperature, solar flux and inlet temperatures. To test this hypothesis, the JPL-Table Mountain receiver performance was considered using the HEAP simulation program. The results were also plotted in Figure D-3 where the receiver efficiency ($\eta_R$) is the ordinate and the parameter ($T_{in} - T_{amb}$)/[$\sum_i A(i)\ I(i)$] is the abscissa. The straight line equation that fits these results was obtained by curve fitting using the least squares method. The straight line intersects the ordinate giving $\alpha_e^*$ as 0.87837. The slope of the straight line gives the product ($U_L A_L$) as 1.7762 Btu/hr°F The percentage error is ±2%.

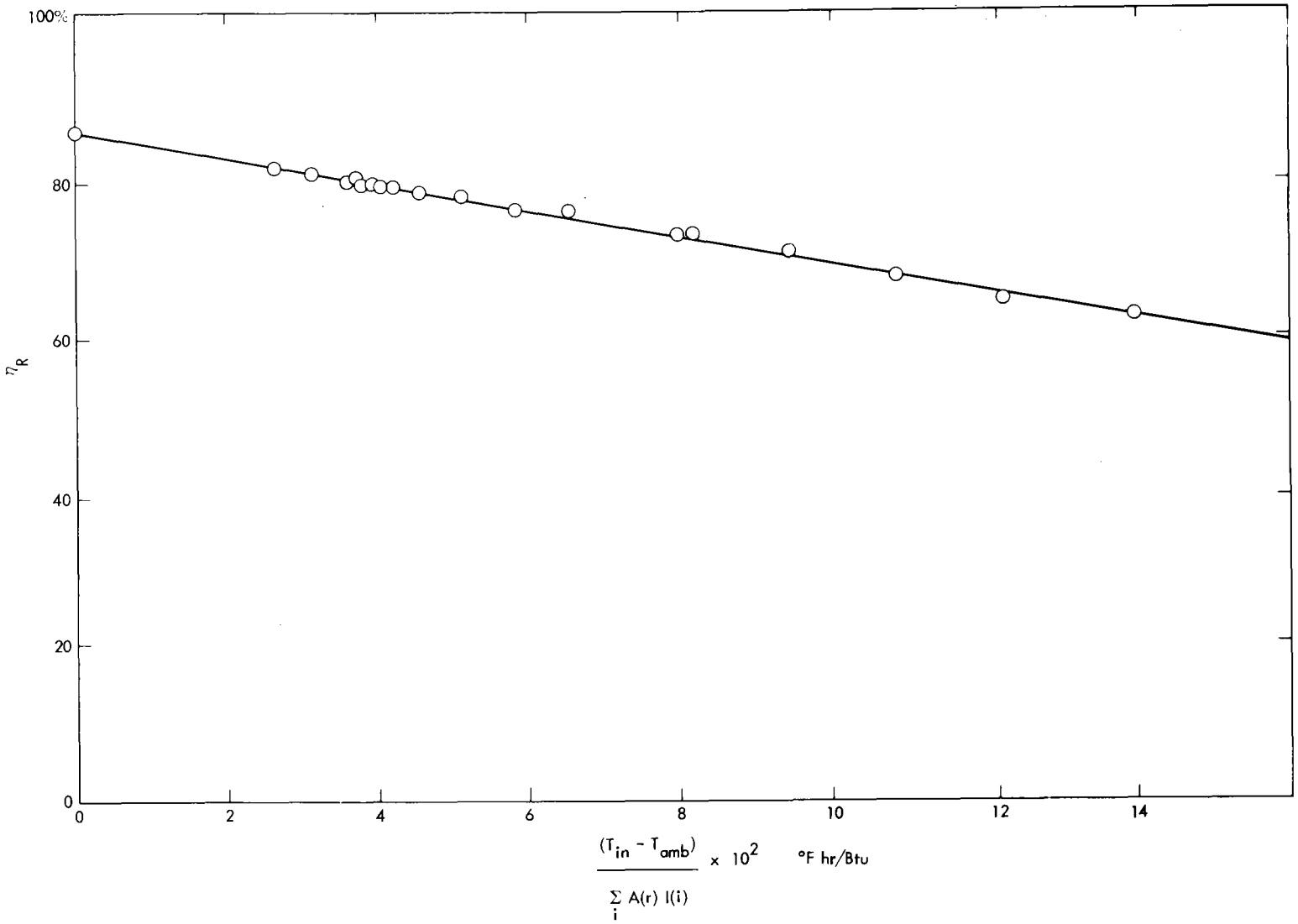


Figure D-3. Receiver Straight-Line Performance for Table Mountain Receiver

## B. CHECK ON RECEIVER SENSITIVITY ANALYSIS USING THE GENERALIZED RECEIVER FORMAT

The sensitivity analysis presented in Section I of this Appendix could have been derived in an approximate manner if Equation (27) was available in advance. The constants in Equation (27) for any receiver could be derived either using experimental values or using simulated HEAP values. In either case, the straight line format approximating the receiver performance will be shown next to be a useful tool in receiver analysis and the receiver-engine optimization process.

### 1. Check on Receiver Sensitivity to Solar Flux Variations

Using the straight line approximation for the receiver efficiency, the heat extracted sensitivity $(HES)_I$ can be simply derived by differentiating Equation (27) with respect to the flux $\sum_i A(i)\ I(i)$. After rearrangement of terms, $(HES)_I$ can be written as

$$(HES)_I = 1 + \left[ \frac{U_L A_L\ (T_{in} - T_{amb})}{\alpha_e^* \sum_i A(i)\ I(i) - U_L A_L\ (T_{in} - T_{amb})} \right]_0 \qquad (29)$$

Equation (29) gives directly a numerical value for $(HES)_I$ once the receiver characteristic constants $\alpha_e^*$ and $U_L A_L$ are given. It also explains why $(HES)_I$ must be larger than unity for all receivers.

For the values given in Section II.A for $\alpha_e^*$ and $U_L A_L$, $(HES)_I$ can be calculated as 1.091. The latter agrees with the value given in Section I.B. The rest of the sensitivity factors such as $(RES)_I$ and $(ETS)_I$ can be then calculated using $(HES)_I$ in Equation (29) together with Equation (9).

### 2. Check on Sensitivity to Inlet Fluid Temperature ($T_{in}$)

By differentiating Equation (27) with respect to $T_{in}$, keeping all the other parameters unchanged, the heat extracted sensitivity $(HES)_{T_{in}}$ could be written as:

$$(HES)_{T_{in}} = \frac{-U_L A_L\ (T_{in})_0}{\left[\alpha_e^* \sum_i A(i)\ I(i) - U_L A_L\ (T_{in} - T_{amb})\right]_0} \qquad (30)$$

Equation (30) explains why $(HES)_{T_{in}}$ is always negative. The other sensitivity factors, $(RES)_{T_{in}}$ and $(ETS)_{T_{in}}$ can be then computed using Equations (12) and (13).

If the reference point was selected to be the optimum conditions corresponding to the maximum overall efficiency, the overall efficiency sensitivity is zero.

In general, at the optimum inlet temperature, Equations (13) and (30) could be combined to give the optimum outlet temperature corresponding to zero $(OES)_{T_{in}}$ as:

$$(T_{out})_{opt} = \sqrt{(T_{amb})^2 + \frac{\alpha_e^* T_{amb} \sum_i A(i)\ I(i)}{U_L A_L}} \tag{31}$$

For the Table Mountain receiver, $(T_{out})_{opt}$ was found to be about 2000°F (1540°F).

3. Sensitivity to Receiver Optical Properties: $\alpha^*$(ESOL) and $\varepsilon$(EIR)

There is no explicit existence for the optical properties (ESOL) and (EIR) in the straight line expression of solar receivers. However, they affect both the intercept ($\alpha_e^*$) and the heat loss slope ($U_L A_L$). If the characteristic constants sensitivity, $S_{\alpha_e^*}$ and $S_{U_L A_L}$, were known as a result of changing either (EIR) or (ESOL), then

$$(HES)_{\substack{EIR \\ or\ ESOL}} = \frac{S_{\alpha_e^*}\left[\alpha_e^* \sum_i A(i)\ I(i)\right]_0 - S_{U_L A_L}\left[U_L A_L\ (T_{in} - T_{amb})\right]_0}{\left[\alpha_e^* \sum_i A(i)\ I(i) - U_L A_L\ (T_{in} - T_{amb})\right]_0} \tag{32}$$

4. Sensitivity to Ambient Temperature $(T_{amb})$

The sensitivity $(HES)_{T_{amb}}$ could be derived simply from Equation (27) by differentiation. Accordingly,

$$(HES)_{T_{amb}} = \frac{U_L A_L\ T_{amb}}{\left[\alpha_e^* \sum_i A(i)\ I(i) - U_L A_L\ (T_{in} - T_{amb})\right]_0} \tag{33}$$

Equation (33) shows that $(HES)_{T_{amb}}$ is always positive at any selected reference point.

5. Sensitivity to Mass Flow Rate

Again, there is no explicit existence of the mass flow rate in the straight-line expression. However, the flow rate affects both the line intercept and slope by a negligible weight. However, if the characteristic constants sensitivity $S_{\alpha^*}$ and $S_{U_L A_L}$ were given as a result of changing the fluid rate, the heat extracted sensitivity $(HES)_{m_f}$ will be given by the same expression in Equation (32).

## SECTION III

## RECEIVER - ENGINE COUPLING OPTIMIZATION

Having established the sensitivity and weighting factors for each parameter affecting the receiver performance, the next step is to find the optimum set of conditions at which the system as a whole gives its highest performance. The system here is referred to as that control volume surrounding the concentrator, receiver and the engine.

First, the concentrator role in the solar collection subsystem is implied in its name, i.e., it has to redirect and concentrate the solar irradiation falling on the curved mirror to the receiver aperture following the real optics formula. The concentrator efficiency is defined as the ratio of the solar flux inside the receiver walls $[\sum_i A(i)\ I(i)]$ divided by the total solar irradiation falling on the mirror projected area $(F \cdot A_c)$. Accordingly, the concentrator efficiency includes all the attenuation factors that prevent ideal redirection and aiming of all the solar energy falling on the mirror from passing all through the receiver aperture. These factors are typically the intercept factor ($\phi$) and the mirror reflectivity ($P_c$) as previously given in Equation (3).

A high-quality mirror with a high intercept factor (made possible by small errors in mirror surface slope, tracking mechanism, mirror specularity, etc.) would yield only a high solar flux to the receiver.

Second, the receiver interfaces with the concentrator only through the magnitude of the solar flux $[\sum_i A(i)\ I(i)]$. The receiver responds to the variations of this solar flux as given earlier in the discussion in Sections I and II. The inlet fluid temperature, on the other hand, plays a significant role in controlling both the outlet temperature ($T_{out}$) and the receiver efficiency as discussed in Section I. The approximation made earlier in Section II to solar receivers, in which the efficiency $\eta_R$ is given by a straight line form in the parameter $(T_{in} - T_{amb})/\sum_i A(i)\ I(i)$ has proved to be a useful tool in predicting and analyzing the receiver sensitivity. This approximate model would group the effects of receiver geometry, optical and physical properties, etc., into two characteristic quantities. These quantities are:

(1) Ordinate intersect ($\alpha_e^*$) at zero abscissa and,

(2) Line slope ($U_L A_L$) which represents the energy losses per unit temperature difference ($T_{in} - T_{amb}$).

Third, the engine efficiency is assumed for this discussion to be a constant fraction of the ideal Carnot's cycle working between the receiver exit temperature $T_{out}$ and the ambient temperature $T_{amb}$, as given earlier in Section I. Since the ambient temperature is beyond the control strategy of the power plant, the engine efficiency, according to the above assumption, is only affected by the temperature $T_{out}$ in this optimization study, if the ambient temperature is unchanged.

The dependency of each component performance on external weather parameters and other inputs from neighboring component is depicted in Figure D-4. For a given weather pattern, the average solar insolation and ambient temperature are considered constants. For a given set of components (i.e., a specific concentrator, a specific receiver, and a specific engine), the only operating condition that needs optimization is the inlet fluid temperature which should correspond to a maximum overall solar-to-electric efficiency. This is what will be explained next. No attempt is made, in this report, to show how the optimized set of conditions change with different types of components.

## A. PERFORMANCE OPTIMIZATION USING THE GENERAL RECEIVER EQUATION

Let the receiver performance be expressed by the straight line equation, as stated earlier in Section IX.C in the form

$$\eta_R = \alpha_e^* - U_L A_L \left[ \frac{T_{in} - T_{amb}}{\sum_i A(i)\ I(i)} \right] \tag{33}$$

Accordingly, the outlet fluid temperature $T_{out}$ will be given as

$$T_{out} = T_{in} + \frac{\alpha_e^* \sum_i A(i)\ I(i) - U_L A_L\ (T_{in} - T_{amb})}{\dot{m}_f\ c_f} \tag{34}$$

The engine efficiency, on the other hand, will be idealized as

$$\eta_e = \lambda \left( 1 - \frac{T_{amb}}{T_{out}} \right) \tag{35}$$

where $\lambda$ a fraction that is practically 0.5 at full load. Let us consider further that the free basic system components; the concentrator, the receiver, and the engine, are well defined and their characteristics given. This means that $\eta_c$, $U_L A_L$, $\alpha_e^*$ and $\lambda$ are given. For the weather conditions, the solar insolation F falling on the mirrors projected area $A_c$ and the ambient temperature $T_{amb}$ all will be assumed given and unchanged for the moment. To find the optimum $(T_{in})_{opt}$ in this case, Equations. 33, 34, and 35 are re-written in terms of the dimensionless factors "a" and "b" where

$$\left.\begin{aligned} a &= U_L A_L / m_f\ c_f \\ b &= \frac{\eta_c\ F\ A_c\ \alpha_e^*}{m_f\ c_f\ T_{amb}} = \frac{\alpha_e^* \sum_i A(i)\ I(i)}{m_f\ c_f\ T_{amb}} \end{aligned}\right\} \tag{36}$$

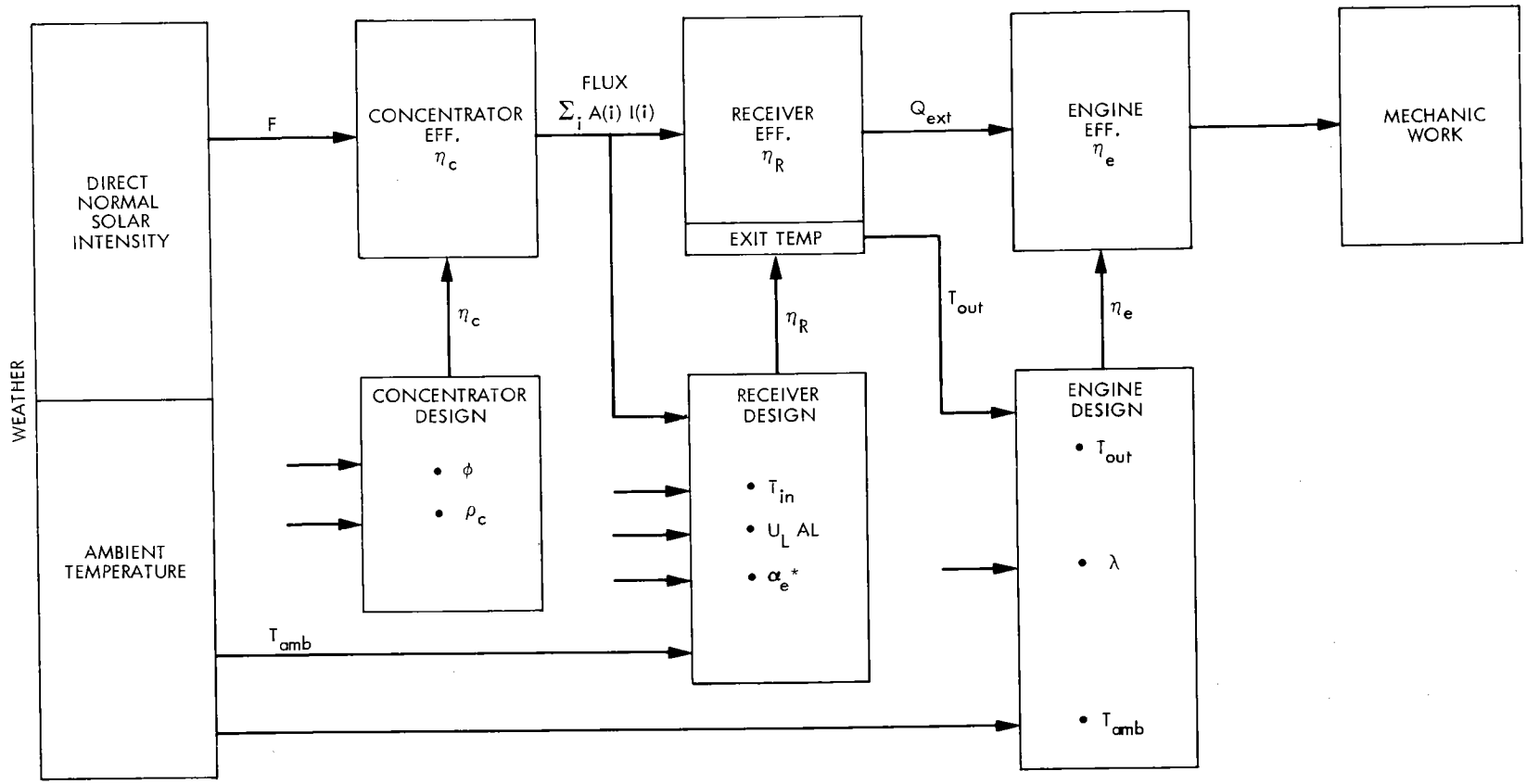


Figure D-4. Interdependence of Subsystem Parameters

Hence, Equations (33) and (34) are reduced to

$$\eta_R = \left(1 + \frac{a}{b} - \frac{a}{b}\frac{T_{in}}{T_{amb}}\right) \alpha_e^* \tag{37}$$

$$T_{out} = (1 - a)\ T_{in} + (a + b)\ T_{amb} \tag{38}$$

The overall efficiency $\eta_{ov}$ is then differentiated with respect to $(T_{in})$ to find its maximum value. After equating to zero, solving the quadratic form and rearrangement of terms, $(T_{in})_{opt}$ can be computed from

$$(T_{in})_{opt} = T_{amb} \frac{\sqrt{1 + \frac{b}{a}} - (a + b)}{(1 - a)} \tag{39}$$

It can be concluded, that whether experimental results are collected or analytical simulation is made to enable the designer to estimate the slope and intercept of the receiver performance, the straight line method is extremely valuable in determining the optimum conditions at first sight. Besides, Equation (39) could be further evaluated to investigate the system sensitivity to the two dimensionless groups "a" and "b" that include all the operational characteristics of the various components. However, this point will be addressed in the future and will not be included in this report.